Zooming in on Star-formation in the Andromeda Galaxy:

Molecular Clouds Resolved with Wideband Millimeter Interferometry and Chemical Abundances of H ii Regions

Author:
Chloe Bosomworth

Supervised by:
Dr. Jan Forbrich
Secondary Supervisor:
Prof. Daniel Smith

Centre for Astrophysics Research
School of Physics, Astronomy and Mathematics
University of Hertfordshire

Submitted to the University of Hertfordshire in partial fulfilment of the requirements of the degree of Doctor of Philosophy.

February 2025
Final Version: January 2026

Abstract

The Andromeda Galaxy (M31), the nearest neighbouring large spiral galaxy to the Milky Way, provides a unique external perspective on star formation and the interstellar medium (ISM). Molecular gas is the primary fuel for star formation and is largely contained within giant molecular clouds (GMCs). Observing GMCs with a wide range of properties is more difficult in the Milky Way, due to our position within the Galactic disc and uncertainties in distance measurements. For this, M31 becomes an ideal laboratory. This thesis presents three studies, which together characterise dust and gas properties of M31 GMCs including metallicity, CO conversion factor and the forces acting on cloud and subcloud scales. provide insight into the initial conditions of star formation.

Optical spectroscopy of H II regions is used to measure elemental abundance (metallicity) variation across the disc of M31. Metallicity generally decreases with galactocentric radius, however, significant scatter around this gradient indicates local variation in star formation conditions suggesting M31 has a recent history of galaxy interactions and mergers. Comparing H II region metallicities with properties of their associated GMCs provides further insight into how cloud properties correlate with local chemical enrichment.

Simultaneous submillimetre observations of thermal dust emission and CO isotopologues help constrain the CO-to-H_2 conversion factor, $\alpha_{\rm CO}$, in M31 GMCs. Dust continuum accurately traces H_2 properties, enabling a direct measurement of $\alpha'_{\rm CO}$, the factor relating CO luminosity to dust mass, independent of H_2 measurements. $\alpha'_{\rm CO}$ is converted to $\alpha_{\rm CO}$ by the gas-to-dust ratio. Results indicate that $\alpha'_{\rm CO}$ is approximately constant for M31 GMCs, and does not vary significantly with metallicity. Additionally, an assessment of the dynamical state of these GMCs provides further evidence that while GMCs are bound by external forces and not self-gravity, these observations trace dust emission from dense, gravitationally bound regions.

Lastly, the nitrogen-to-oxygen abundance ratio (N/O) is examined for the same H II region sample. Oxygen and nitrogen have different nucleosynthetic origins, and their ratio provides insight into the relative nucleosynthesis rates of stars with different masses. Our findings support recent evidence from observations and simulations suggesting that the M31 disc formed from a more intense and rapid burst of star formation than the Milky Way disc. The derived $\mathrm{N/O} - \mathrm{O/H}$ relationship for M31 shows that at high metallicities, N/O increases with increasing O/H, as theory predicts. However, the trend is significantly steeper than the general Milky Way relation for this metallicity range. Altogether these studies reveal that M31's chemical evolutionary history differs from that of the Milky Way's, and that star formation occurs in gravitationally bound regions of GMCs.

Declaration

I declare that no part of this work is being submitted concurrently for another award of the University or any other awarding body or institution. This thesis contains a substantial body of work that has not previously been submitted successfully for an award of the University or any other awarding body or institution.

The following parts of this submission have been published previously and/or undertaken as part of a previous degree or research programme:

1. Chapter 2: Published as Bosomworth, Forbrich, Lada, Caldwell, Kobayashi, Viaene, 2025. Cloud-scale elemental abundance variations and the CO-to-dust-mass conversion factor in M31, *Monthly Notices of the Royal Astronomical Society*, 536, 3803.

2. Chapter 3: Submitted for publication as Bosomworth, Forbrich, Lada. Resolved Dust Emission and CO Isotopologues in Giant Molecular Clouds of the Andromeda Galaxy, *Astrophysical Journal*, 2025.

3. Chapter 4: In preparation for submission as a standalone publication in a refereed journal as Bosomworth, Forbrich, Lada, Kobayashi, Bhattacharya, Caldwell, Variation of the Nitrogen-to-Oxygen ratio in H II regions across the disk of M31, 2025.

Except where indicated otherwise in the submission, the submission is my own work and has not previously been submitted successfully for any award.

Acknowledgements

First and foremost, I would like to express my deepest gratitude to my supervisor, Dr. Jan Forbrich, for his continuous support and confidence in my ability to complete this thesis. From the outset, Jan has provided invaluable guidance and insight, without which the work presented in this thesis would not have been possible. I have been extremely fortunate to have a supervisor whose kindness and enthusiasm have allowed me to pursue research in a subject that has fascinated me for as long as I can remember.

I would also like to express my sincere thanks to Prof. Charles J. Lada, who supervised me during my predoctoral fellowship at the Center for Astrophysics | Harvard and Smithsonian. Working with him on my research was an exceptional opportunity, and his insightful discussions and guidance during our collaborations helped shape the direction of this thesis and my growth as a researcher.

I would also like to thank my collaborators at the University of Hertfordshire, Prof. Chiaki Kobayashi and Dr Souradeep Bhattacharya, whose suggestions and insights into my research on chemical abundances have helped to strengthen the quality of these chapters. I am grateful to my secondary supervisor, Prof. Daniel Smith, for many insightful and educational discussions over the last four years.

I am grateful to the members of *The Orion-Andromeda Conspiracy*, Jaime Vargas González, Jonathan Toomey, Eoin O'Kelly and James Appleton, for the engaging weekly discussions and creating such a supportive research environment. I would also like to thank Dr. Dyna Ibrahim, with whom I have shared this PhD journey, for her friendship and constant encouragement.

Additional thanks to my examiners and members of my Viva committee, Dr. Rob Yates and Prof. Martin Bureau for providing constructive comments that were valuable in strengthening the final version of this thesis.

Finally, I am deeply grateful to my family and friends, for constant support and encouragement. I am especially thankful to my parents, my sister Kelly, and to Smartie, Peach, and Willow whose company made even the challenging days easier.

Contents

List of Figures

List of Tables

Chapter 1

Introduction

Almost everything we see in the cosmos is due to galaxies and the gas, dust and stars they contain. These components fuel and are the product of many cycles of star formation, taking place largely within giant molecular clouds and we can uncover these processes in exquisite detail within individual galaxies. Observational studies towards very local molecular clouds within the Milky Way (MW) provide these detailed insights on sub-molecular cloud scales. However, uncertainties due to distance estimates and line-of-sight extinction tied to our own position within the MW mean that we can only study this in detail in very few local clouds. The recent advancements in observational capabilities have allowed us to extend these studies to nearby galaxies. The Andromeda Galaxy, in particular, stands out as an ideal laboratory for this, as the MW's most nearby large spiral galaxy. For these reasons, the key aim of this thesis is to "zoom-in" on star formation in Andromeda. Taking advantage recent advances in observational capabilities, we investigate key concepts tied to dust and the interstellar medium (ISM), including metallicity, chemical abundances, and CO-to-molecular-mass conversion factors on individual cloud scale and smaller. This work builds on previous small-scale studies in M31, including analyses of dust-extinction (Dalcanton et al. 2015; Dong et al. 2016) and the electron-temperature (T_e)-derived metallicities derived by (Zurita and Bresolin 2012).

In this introductory chapter, we outline the relevant background for the study. This chapter is structured as follows. We introduce the ISM and its various complex phases in Section 1.1, as well as introducing CO as the easiest, but not the only, molecular tracer to measure the physical properties of molecular hydrogen (H_2) in extragalactic studies. The role of thermal dust emission as a dense gas tracer is also highlighted. Section 1.2 focuses on giant molecular clouds (GMCs),

the primary sites of star formation, introducing key surveys and concepts that are central to this thesis. In Section 1.3 we introduce the Andromeda galaxy, uncovering its intricate structure based on tracers introduced in previous sections, including the star-forming "Ring of Fire", and its history of collisions and mergers. Section 1.4 discusses massive star formation, which heavily influences the ISM, dissociating H_2 and ionising atomic hydrogen (H I) to form H II regions. We investigate the importance of measuring the abundance of heavy elements, referred to as 'metals', in astronomy, in Section 1.5. Section 1.6 outlines the two observational methods utilised in this work: optical spectroscopy and submillimetre (sub-mm) observations. Finally, Section 1.7 provides a roadmap for the subsequent science chapters of this thesis.

1.1 The Interstellar Medium

The ISM is the material between stars inside of galaxies, made up of gas and dust. Studying the ISM is essential to understanding galaxy evolution and star formation history (SFH), as it is from this material that stars are formed. Stars also return much of their mass to the ISM through supernova (SN) explosions and winds, enriching the ISM with metals formed via nucleosynthesis (see Section 1.5.1). In astronomy, 'metals' refers to elements heavier than Helium (He). This material then forms the ISM for the next generations of star formation. Thus, star formation determines the structure, composition and properties of the ISM.

Our understanding of the ISM began with the identification of interstellar dust via stellar reddening (Trumpler 1930) and the detection of interstellar absorption lines (e.g., Swings and Rosenfeld 1937). The H I line at 21 cm was detected in the 1950s (Ewen and Purcell 1951), tracing the atomic component of interstellar gas. The first detection of H_2 was made at ultraviolet (UV) wavelengths (Carruthers 1970); however, dust extinction often prevents UV observations, making H_2 difficult to detect in dense regions (see below). Utilising mm-wavelength observations of CO emission to derive the H_2 distribution in the MW was first employed by Scoville and Solomon (1975) and Gordon and Burton (1976), following the discovery of the CO$(1-0)$ line at 2.6 mm by Wilson et al. (1970). Subsequently, large CO surveys (e.g., Solomon et al. 1979; Solomon and Sanders 1980) demonstrated that molecular gas in the MW is confined within GMCs, the primary sites of star formation in galaxies (e.g., McKee and Ostriker 2007; Heyer and Dame 2015).

The gas and dust of the ISM accounts for only $\approx 10-15\%$ of the luminous mass of the Galactic disc, and comparable fractions are found in typical spiral galaxies (Young and Scoville 1991). In spiral/disc galaxies, it is primarily concentrated along the galactic plane and spiral arms, where the majority of star formation takes place. The basic mass composition of the ISM is as follows: 70% Hydrogen (H), 28% He and 2% metals. 30-50% of these heavier elements are predicted to be depleted into dust grains (Draine et al. 2007). The majority of the ISM volume is low-density; however, it spans a wide range of temperatures, densities and ionisations across its phases described in this section. Draine (2011) identify seven distinct ISM phases that account for the majority of the mass and volume of the ISM in the MW:

- **Coronal gas/hot ionised medium (HIM):** Collisionally ionised gas heated by SNe explosions. Low density and high volume, making up approximately half of the volume of the Galactic disc, as well as most of the volume above and below the disc.
- **H II gas:** Gas photoionised by ultraviolet (UV) photons from hot stars, mostly by massive O stars. When the H II gas is extended and low-density 'intercloud' medium, this is called diffuse H II/warm ionised medium (WIM). When dense gas, such as from a nearby molecular cloud, is photoionised, an H II region is formed. Photoionised gas is also found in planetary nebulae (PNe).
- **Warm H I/warm neutral medium (WNM):** Atomic gas heated by photoelectrons from dust ionisation, starlight, and cosmic rays, and additionally cooled by optical and fine structure line emission. ≈ 40 % of the disc volume is warm H I, primarily traced by H I 21 cm absorption/emission and absorption lines in the optical and UV.
- **Cool H I/cold neutral medium (CNM):** Atomic gas also heated by the same mechanisms as the WNM and cooled by fine structure line emission. Cool H I fills only $\approx$1 % of the local ISM volume and is traced by the same mechanisms as the WNM.
- **Diffuse H_2:** Similar to clouds of cool H I but with higher density and can additionally be observed by the lowest rotational CO transition, $CO(1-0)$.
- **Dense H_2:** Contained in molecular clouds (MCs) where star formation primarily takes place (see Section 1.2). Gas is heated and ionised by cosmic rays and UV photons and cooled through CO line emission and C I fine structure line emission. Molecular clouds are observed from their molecular line (e.g., $CO(1-0)$) emission and dust emission in the far-IR (FIR) and sub-mm.

Phase	T (K)	$n_{\rm H}$ (cm^{-3})	f_ν	$\langle n_{\rm H}\rangle f_\nu$ (cm^{-3})
Coronal gas	$\lesssim 10^{5.5}$	≈0.004	≈ 0.5	≈ 0.002
H II gas	10^4	$0.3 - 10^4$	≈ 0.1	≈ 0.02
Warm H I	≈5000	0.6	≈ 0.4	≈ 0.2
Cold H I	≈100	30	≈ 0.01	≈ 0.3
Diffuse H_2	≈50	≈100	≈ 0.001	≈ 0.1
Dense H_2	10 – 50	$10^3 - 10^6$	≈ 10^{-4}	≈ 0.2
Cool stellar outflows	$50 - 10^3$	$1 - 10^6$		

TABLE 1.1: Properties of the phases of the ISM as defined by Draine (2011).

- **Cool stellar outflows:** Low-velocity ($\lesssim$ 30 km s^{-1}) and high-density outflows from cool, evolved stars. Additionally, high-velocity outflows of much lower densities come from hot stars (e.g., Li and Bryan 2020). Stellar outflows are detected by absorption lines (optical and UV), dust IR, H I, CO and OH radio emission.

Table 1.1 gives the properties of the ISM phases as defined by Draine (2011). $n_{\rm H}$ is the number density of H atoms, f_ν is the volume filling factor (the fraction of ISM volume) and $\langle n_{\rm H}\rangle f_\nu$ is the mean $n_{\rm H}$ over total volume.

Approximately 50% of the interstellar gas mass is contained within 1-2% of the ISM volume, within molecular clouds (Klessen and Glover 2016). Although these established phases exist, the ISM is extremely dynamic and is converted to different phases through ionisation and radiative cooling.

In this thesis we primarily focus on H II regions (see Section 1.4.1), and GMCs formed of dense H_2 (see Section 1.2). In the following subsections, we will cover how H_2 gas properties are derived from observations using different tracers. Abundances of heavy elements, specifically in H II regions, is discussed in Section 1.5.

1.1.1 Tracing Molecular Gas

Now that we have discussed the phases of the ISM, highlighting those most relevant for studying star formation, we can delve deeper into observational methods used to trace H_2, by far the most abundant molecule in interstellar gas, making up ≈ 90% of the ISM by mass. This makes H_2 the primary fuel for star formation. Despite being the most abundant molecule, H_2 is extremely difficult to observe in the cold ISM. This is because it lacks a permanent dipole moment and hence has no dipole rotational transition. The quadrupole rotational transitions exhibited by H_2 require high excitation temperatures and are therefore highly unlikely to occur in the cold ISM.

Although CO is much less abundant in interstellar gas (0.03% by mass; Heyer and Dame 2015), it displays the brightest emission in molecular clouds at mm/sub-mm wavelengths and is the most commonly used tracer of H_2. CO molecules have a weak permanent dipole moment and low excitation energy; therefore, they experience collisional excitation in the cold ISM. The strong emission lines of CO can be detected at great distances and so are extremely useful in extragalactic observations. Measurements of CO emission can be used to derive the H_2 mass and density, providing insights into the molecular gas reservoir that fuels star formation.

The column density of H, $n_{\rm H}$, corresponds to the total number of H nuclei (H I + H_2) along the line of sight. Therefore, $n_{\rm H}$ is highest in the densest regions of a molecular cloud. The lowest rotational transitions of CO (see the following subsection) generally become optically thick at high $n_{\rm H}$. The optical thickness of emission measures the fraction of emitted photons which are absorbed or scattered as they pass through a medium. A transition becomes optically thick when the majority of the emission is absorbed or scattered. This means that the CO emission observed arises primarily from the envelope of the molecular cloud, which has lower $n_{\rm H}$. This can lead to underestimations of $M_{\rm H_2}$ that reflect the diffuse envelopes of molecular clouds and not the dense regions where stars are most likely to form.

SFR is more tightly correlated with gas mass at high $n_{\rm H}$ than with the total cloud mass (Lada et al. 2010). Therefore, it is important to accurately measure $M_{\rm H_2}$ of these regions. In particular, we will explore the use of dust as a tracer of dense gas in this thesis. Thermal dust continuum emission is observed at FIR and sub-mm wavelengths (see below). In addition, molecules such as HCN and HCO+ have higher dipole moments than CO. This means that higher densities are required to excite these molecules. HCN and HCO+ are therefore less optically thick than CO, which becomes saturated. However, their lower abundance and weaker emission lines make them difficult to detect in extragalactic observations. For this reason, CO is essential to trace H_2 in many extragalactic studies. To measure $M_{\rm H_2}$ from CO observations, we require the CO-to-H_2 conversion factor, $X_{\rm CO}$ or $\alpha_{\rm CO}$, which is discussed below. Therefore, calibrating $\alpha_{\rm CO}$ using optically thin gas tracers is extremely important for extragalactic astronomy when weaker molecular emission lines, or thermal dust emission, cannot be detected.

The proximity of M31 enables GMCs to be observed down to pc scale in our Submillimeter Array (SMA) survey by CO (Lada et al. 2024) and dust continuum (Viaene et al. 2021). Also, HCN, HCO^+, and HNC have been observed in a sample of GMCs with the Northern Extended Millimeter Array (NOEMA) (Forbrich et al. 2023). Figure 1.1 displays the emission from three

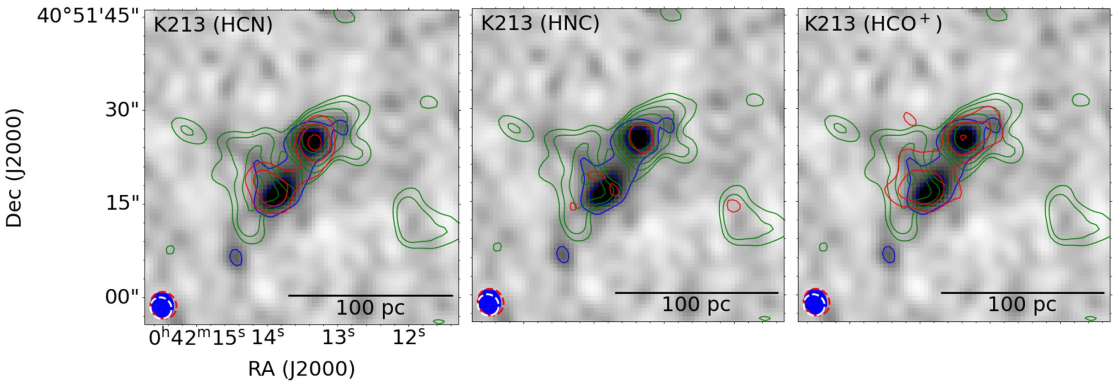

FIGURE 1.1: SMA 230-GHz continuum image of M31 GMA K213 from Kirk et al. (2015). Contour lines represent the following at 3, 6, 12, ...σ: (green) ^{13}CO(1−0) from NOEMA, (blue) 230-GHz continuum emission, and (red, left-to-right) HCN, HNC and HCO$^+$ from NOEMA. The synthesized beam sizes are displayed in the bottom-left for 230-GHz continuum (blue), ^{13}CO(1 − 0) (white dashed) and HCN, HNC, and HCO$^+$ (red dashed, left-to-right). Credit: Forbrich et al. (2023).

individual M31 GMCs as probed by different tracers, using 230-GHz continuum from the SMA as a background image. Contours from NOEMA observations of the CO isotopologue (see below) ^{13}CO(1 − 0), HCN, HCO$^+$, and HNC in the three M31 giant molecular associations (GMAs; Kirk et al. 2015) are overlaid on the image, along with contours of the 230-GHz continuum. At this frequency, Forbrich et al. (2023) found that free-free emission contributes only ≈ 13%. Synchrotron emission is expected to be negligible at 230-GHz because it is well approximated by a power law at millimetre (mm) wavelengths (Planck Collaboration et al. 2016). Therefore, the continuum emission is expected to be dominated by thermal dust. Figure 1.1 highlights the extent of emission probed by different tracers of the same GMCs. In these observations, thermal dust emission is spatially aligned with both HCN and HCO$^+$, and its contours are tracing more dense material than ^{13}CO(1 − 0), highlighting its usability as a dense gas tracer in this work.

1.1.2 CO Isotopologues

The most abundant CO isotopologue is ^{12}CO, and emission from its lowest rotational transition, ^{12}CO(1−0), is the most commonly used tracer of H_2. ^{12}CO(1-0) and the second lowest rotational transition, ^{12}CO(2-1), emit at rest wavelengths 2.6 mm and 1.3 mm respectively, making them detectable in mm observations. Additional, less abundant CO isotopologues are ^{13}CO and C^{18}O. Their lower abundances result in less optically thick emission lines, and so their emission is less saturated than that of ^{12}CO. As a result, observations of these isotopologues can probe higher $n_{\rm H}$ than ^{12}CO emission. By comparing cloud properties using ^{12}CO, ^{13}CO and the extremely rare C^{18}O, we can investigate diffuse to dense structure within GMCs. However, their emission lines

are weak compared to ^{12}CO, making them more difficult to observe in extragalactic molecular clouds. The abundance ratio $[^{12}\mathrm{CO}]/[^{13}\mathrm{CO}] = 77 \pm 7$ in the local ISM (Wilson and Rood 1994), and $[^{13}\mathrm{CO}]/[\mathrm{C}^{18}\mathrm{O}] = 6.7 \pm 2.9$ was found for M31 GMCs (Viaene et al. 2021). This means that C^{18}O is only detected in a fraction of M31 GMCs compared to ^{12}CO and ^{13}CO and so, unfortunately, cannot yet provide the same insights from a significant sample of GMCs in M31.

As previously mentioned, using CO as a tracer of H_2 requires an accurate estimate of α_{CO}, which can be calibrated from dust emission. The wideband-receiver upgrade to the SMA (Grimes et al. 2016) has enabled resolved detections of dust continuum emission from M31 GMCs, obtained simultaneously with CO(2-1) isotopologues (Forbrich et al. 2020; Viaene et al. 2021). In Chapter 3 we build on these works by analysing CO and dust emission from the now completed SMA survey.

1.1.3 Thermal Dust Emission

Interstellar dust grains absorb energy in the form of UV and optical light, which is re-emitted at longer (IR and sub-mm) wavelengths corresponding to the dust's temperature (T_{dust}). In most galaxies, cold dust is heated by evolved stellar populations. UV radiation from young stars is the predominant heating mechanism for warmer dust. In most galaxies, both mechanisms contribute to dust heating (e.g., Bendo et al. 2015). We can begin to derive dust properties of clouds by starting with the emission spectrum of a blackbody, B_ν, according to Planck's radiation law (Planck 1900). As a function of frequency, B_ν is given by equation 1.1,

$$B_\nu = \frac{2h\nu^3}{c^2} \frac{1}{e^{h\nu/k_{\mathrm{B}}T} - 1}, \tag{1.1}$$

where h is Planck's constant, c is the speed of light in a vacuum, and k_{B} is the Boltzmann constant. The flux density of thermal dust emission is expressed by a modified blackbody, or a greybody model, assuming optically thin dust emission ($\tau_\nu \ll 1$), by

$$S_\nu \simeq B_\nu(T)\, \tau_\nu \Omega, \tag{1.2}$$

where S_ν represents the flux density at a specific ν. τ_ν is the optical thickness/depth and Ω_{beam} is the beam solid angle. The optical depth of dust emission is determined by its opacity, κ_ν, a

measurement of how much radiation is absorbed or scattered by dust at a particular ν, following equation 1.3:

$$\tau_\nu = \kappa_\nu \Sigma_{\rm dust} \tag{1.3}$$

where $\Sigma_{\rm dust}$ is the dust surface density Draine (2011). Thus, optical depth increases with increasing opacity for a given $\Sigma_{\rm dust}$. Thermal dust emission depends only on two parameters: dust opacity and $T_{\rm dust}$, unlike molecular emission lines, which also depend on excitation conditions. Dust makes up approximately 1% of the ISM by mass, compared to CO which makes up 0.03% (values typical of the MW; Heyer and Dame 2015). Dust emission is typically more optically thin than CO line emission and is well-mixed with molecular gas (with H_2 forming on the surfaces of dust grains; e.g., Wakelam et al. 2017), it is a more direct tracer of H_2 column density than CO (e.g., Bolatto et al. 2013).

From the thermal dust emission, dust mass, $M_{\rm dust}$, can be calculated following equation 1.4:

$$M_{\rm dust} = \frac{S_\nu d^2}{\kappa_\nu B_\nu(T_{\rm dust})}, \tag{1.4}$$

where d is the distance to the source. κ_ν can be obtained from a dust model. The radiative transfer model of M31 (Viaene et al. 2017) has been shown to reproduce the observed flux density of M31 from FUV to sub-mm wavelengths using the using the THEMIS (The Heterogeneous dust Evolution Model for Interstellar Solids) dust model of Jones et al. (2017). The Viaene et al. (2017) 3-dimensional (3D) radiative transfer model is based on observed properties of M31. This model revealed that in M31, 91% of the stellar radiation absorbed by dust comes from evolved stars. This radiation is mainly absorbed within the bright central bulge out to 10 kpc.

1.1.4 Dust Extinction

Dust extinction refers to the combination of absorption and scattering of light by dust grains along the line of sight. The presence of thermal dust emission in the FIR and sub-mm discussed above is only possible because of dust extinction at optical and UV wavelengths. Therefore, it is essential to correct spectra for dust extinction, particularly in dusty regions, to accurately measure emission line fluxes.

Following Cardelli et al. (1989), extinction corrections to optical spectra are typically applied using the colour excess between the B and V bands, E_{B-V}, which quantifies nebular reddening due to dust along the line of sight (Cardelli et al. 1989). Interstellar reddening occurs because dust grains absorb blue light more than red light, resulting in the sources appearing redder than it is. E_{B-V} (nebular) can be calculated from the observed intensity ratio I(Hα)/I(Hβ) by comparing the observed value to the expected value of 2.86 for case B recombination in physical conditions typical of the MW (Osterbrock and Ferland 2006). Visual extinction, $A_{\rm V}$, is related to E_{B-V} by a proportionality constant, R_V (the ratio of the total to selective extinction):

$$A_V = R_V \times E_{B-V} \tag{1.5}$$

The standard value for the diffuse ISM from MW observations is $R_V \approx 3.1$ (Seaton 1979). An extinction curve such as that of Cardelli et al. (1989) can then be applied to spectroscopic observations to correct for dust extinction.

The wavelength dependence of extinction is displayed in Figure 1.2 in terms of the extinction cross-section per H atom, σ. Below the Lyman limit (λ = 91.2 nm), extinction is no longer dominated by the scattering and absorption of radiation by dust, but by the photoionisation of atoms. The shape of the graph at $\lambda > 91.2$ nm can be explained by the efficiency of dust grains of different sizes at scattering light of specific wavelengths. Dust grains with diameters comparable to the wavelengths of optical and UV light scatter light extremely efficiently, reducing the luminosity in the original direction of propagation.

The dotted lines at λ>91.2 nm indicate extinction curves with different assumptions for R_V. This is further highlighted in Figure 1.3 which provides a closer look at the Cardelli et al. (1989) extinction curve for FIR-UV wavelengths, also showing the most 'extreme' cases of R_V from their observations.

Although the extinction curve in the IR/optical is approximately a constant power law relation that is independent of R_V, the UV range is sensitive to strong radiation fields, in particular around the 'UV bump' at 220 nm. We used the optical extinction curve shown above to correct our spectra for dust extinction in Chapter 2.

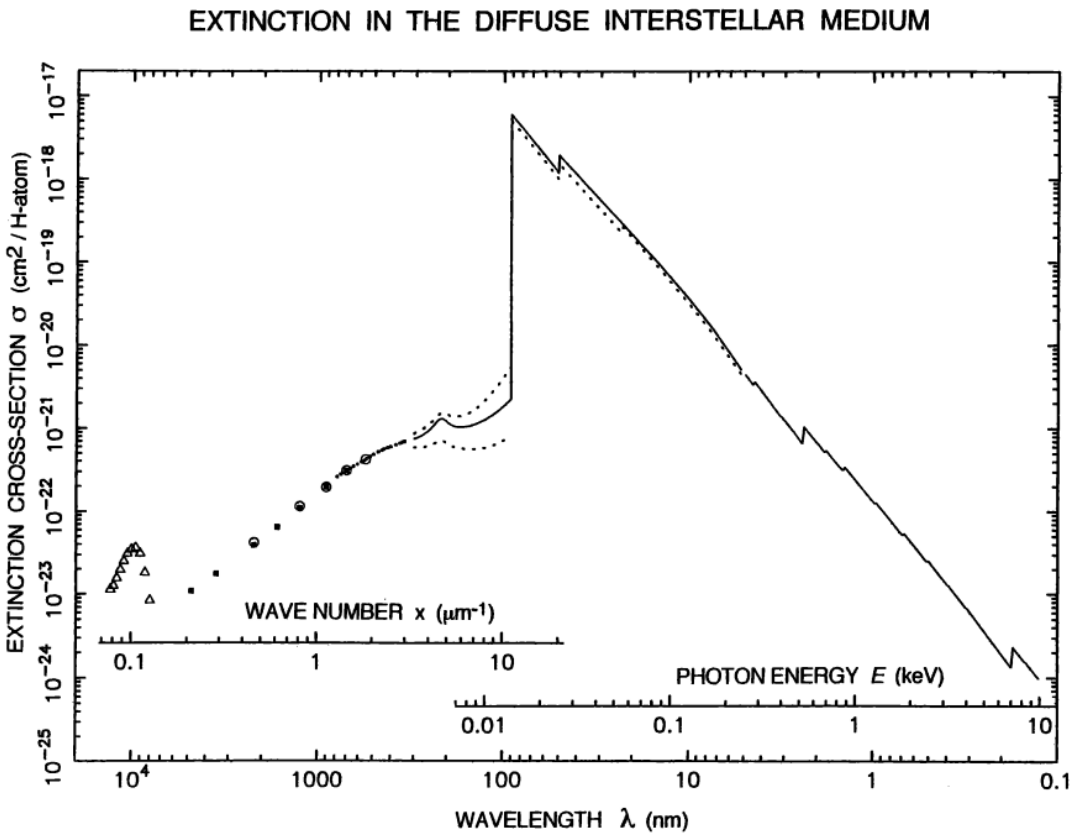

FIGURE 1.2: Extinction cross-section (normalised per H atom) in the diffuse ISM as a function of wavelength, ranging from far infrared to X-rays. Above the Lyman limit, dotted lines represent two extreme cases of extinction along the line of sight. Credit: Ryter (1996).

1.1.5 CO Conversion Factors

As previously mentioned, to accurately calculate the mass of a GMC from CO observations, we require an accurate estimate of the CO-to-H_2 conversion factors for column density or mass, $X_{\rm CO}$ or $\alpha_{\rm CO}$, respectively. This arises from the relation between H_2 column density ($N_{\rm H_2}$) and the integrated line intensity of CO$(1-0)$, $W_{\rm CO(1-0)}$, as given by equation 1.6 (e.g., Bolatto et al. 2013):

$$N_{\rm H_2} = X_{\rm CO} W_{\rm CO(1-0)}. \tag{1.6}$$

Note that $N_{\rm H_2}$ is the column density of H_2, and $X_{\rm CO}$ typically has units of $\rm cm^{-2}\,(K\,km\,s^{-1})^{-1}$. $W_{\rm CO(1-0)}$, is given in units of $\rm K\,km\,s^{-1}$. $M_{\rm mol}$ is then calculated by integrating over the emitting area. The conversion factor for the CO$(1-0)$ luminosity, $L_{\rm CO(1-0)}$, to $M_{\rm mol}$ is derived by integrating over the emitting area, and converting column density to mass (Bolatto et al. 2013),

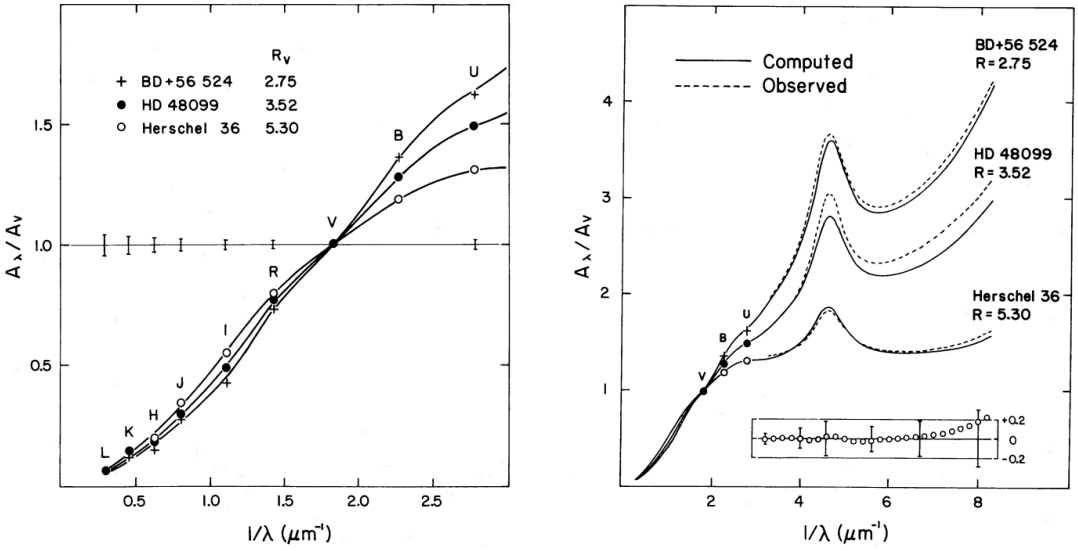

FIGURE 1.3: Extinction curves for *left* IR and optical and *right* UV wavelengths under different assumptions of R_V. Credit: Cardelli et al. (1989)

$$M_{\rm mol} = \alpha_{\rm CO} L_{\rm CO(1-0)} \tag{1.7}$$

with typical units of $M_\odot$(K km s^{-1}pc^2)$^{-1}$. To account for He mass as well as H_2 mass, $M_{\rm mol} \approx 1.36 \times M_{\rm H_2}$. CO conversion factors are essential to produce accurate measurements of both $N_{\rm H_2}$ and $M_{\rm H_2}$ from CO observations.

From different methods, a constant value of $\alpha_{\rm CO} \approx 4.3\ M_\odot$(K km s^{-1}pc^2)$^{-1}$ has been obtained for MW GMCs for ^{12}CO(1 − 0) (Bolatto et al. 2013). The corresponding value for ^{12}CO(2 − 1) is $\approx 6.1\ M_\odot$(K km s^{-1}pc^2)$^{-1}$ assuming an intensity ratio $I_{CO(2-1)}/I_{CO(1-0)} = 0.7$ (Bolatto et al. 2013; Nishimura et al. 2015, and references therein). In the MW, there is little evidence for variation in $\alpha_{\rm CO}$. However, Shetty et al. (2011) conclude that this is due to the limited ranges of column densities, temperatures, and CO linewidths that characterise MW GMCs. Extragalactic studies observe molecular clouds with different physical properties and have identified large variations in $\alpha_{\rm CO}$ and $X_{\rm CO}$ throughout galaxy discs (e.g., Leroy et al. 2011; Sandstrom et al. 2013). Therefore, obtaining $\alpha_{\rm CO}$ measurements from GMCs beyond the MW is essential to calibrating $\alpha_{\rm CO}$ for use in extragalactic astronomy.

Measuring $\alpha_{\rm CO}$ directly in extragalactic GMCs using observations of optically thin emission is difficult. However, the improvement in observational capabilities from the SMA wideband receiver upgrade has enabled $\alpha_{\rm CO}$ calibration from dust (Forbrich et al. 2020; Viaene et al. 2021) to be performed in M31. Additionally, $\alpha_{\rm HCN}$ and $\alpha_{\rm HCO^+}$ have been measured in a subsample of

these GMCs (Forbrich et al. 2023). In the following subsection we will discuss measuring the CO conversion factor from measurements of $M_{\rm dust}$.

1.1.6 Calibrating $\alpha_{\rm CO}$ from Dust Emission

As mentioned in Section 1.1.3, using dust continuum emission to measure $\alpha_{\rm CO}$ can provide a conversion factor that reflects the dense gas of molecular clouds. Therefore, to calculate $M_{\rm mol}$ of the cloud and subsequently $\alpha_{\rm CO}$ from a measurement of $M_{\rm dust}$, we must assume a gas-to-dust mass ratio ($R_{\rm g/d}$). We note that on the scales of individual molecular clouds, the mass of H I contributes negligibly (e.g., Wolfire et al. 2010) and therefore $R_{\rm mol/d} \simeq R_{\rm g/d}$, or $M_{\rm gas} \simeq M_{\rm mol}$. The typical MW $R_{\rm g/d} \approx 136$, including a factor of 100 to account for the ISM being 1% dust compared to 99% gas by mass, and 1.36 to account for He (Draine et al. 2007). However, chemical evolution models (e.g., Mattsson and Andersen 2012; Hirashita and Harada 2017) and observations (e.g., Sandstrom et al. 2013; Giannetti et al. 2017) have shown that $R_{\rm g/d}$ can vary depending on dust properties such as grain size and metallicity (the abundance of elements heavier than He, see Section 1.5.6).

To exploit the full capabilities of dust as a tracer of molecular gas, we need a direct comparison of observations for GMCs with a range of physical properties than we can probe locally. However, for M31 a significant sample of dust detections from GMCs at approximately the same distance has been obtained (Forbrich et al. 2020; Viaene et al. 2021). To obtain a direct conversion factor measurement without assuming a $R_{\rm g/d}$, from sub-mm observations of dust emission from M31 GMCs, Forbrich et al. (2020) derived the CO-to-$M_{\rm dust}$ conversion factor, $\alpha'_{\rm CO}$, given by Equation 1.8:

$$\alpha'_{\rm CO} = \frac{M_{\rm dust}}{L_{\rm CO}} = \frac{\alpha_{\rm CO}}{R_{\rm g/d}}. \tag{1.8}$$

The M31 values of $\alpha_{\rm CO}$ for both ^{12}CO(2 − 1) and ^{13}CO(2 − 1) are consistent with the MW if $R_{\rm g/d} \approx 136$ is assumed when converting from $\alpha'_{\rm CO}$ (Viaene et al. 2021). However, significant scatter was present around the median, indicating possible variation with cloud properties. In Chapter 3 we present results for the now completed SMA survey and produce a direct test of the metallicity dependence of $\alpha'_{\rm CO}$.

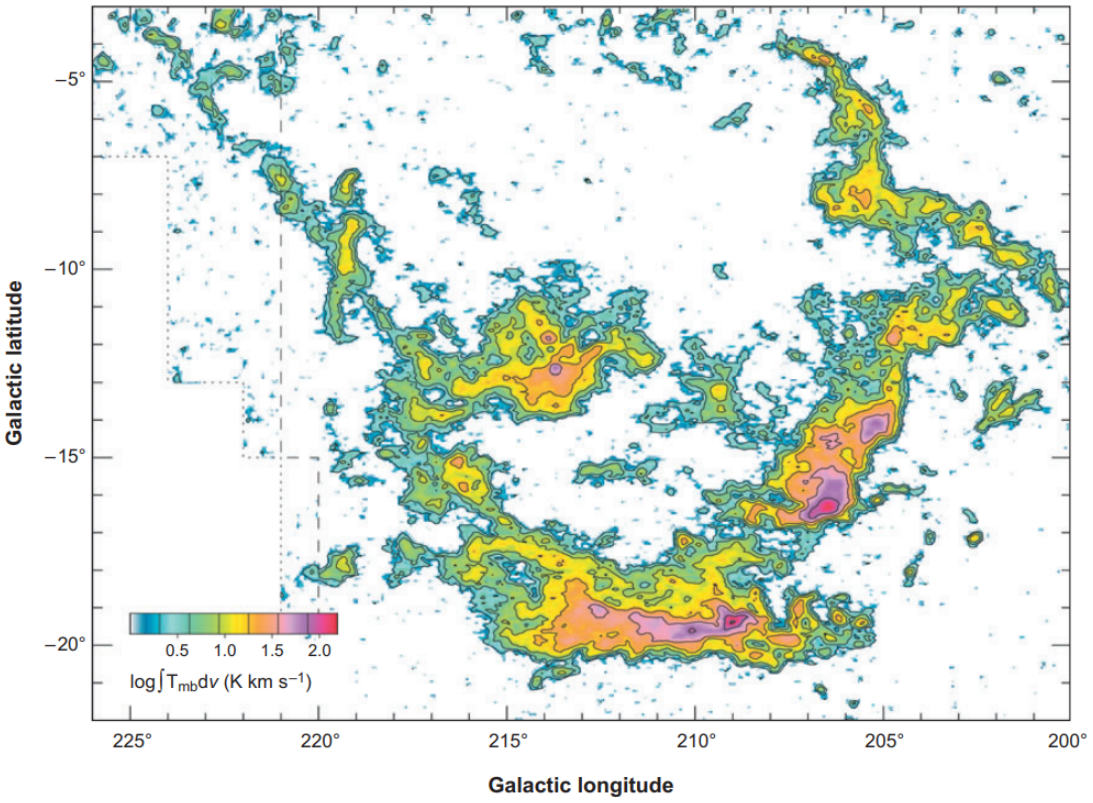

FIGURE 1.4: Molecular gas map of the Orion-Monoceros region. Three GMCs can be seen; Orion A (lower centre), Orion B (middle right) and Monoceros R2 (slightly left of centre). The colourscale displays the CO(1-0) velocity-integrated intensity from Wilson et al. (2005). Credit: McKee and Ostriker (2007).

1.2 Giant Molecular Clouds

In the previous section, we established that the primary constituent of the cold, dense ISM from which stars form is H_2. Star formation requires cold and dense gas which is typically contained in molecular clouds. GMCs are characterized by masses $\gtrsim 10^4 M_\odot$ and diameters > 20 pc (Solomon et al. 1979) but they can be as large as 100 pc. GMC structure is very complex, made up of dense clumps and filaments with surrounding gas of lower density. Star formation occurs when the dense material undergoes gravitational collapse (see Section 1.4). From measurements of GMC properties including mass, density and α_{CO}, we can gain insight into the environments of star formation.

To visualise the complex structures of GMCs, a molecular gas map of molecular clouds in the Orion-Monoceros region is shown in Figure 1.4. This region contains three GMCs (Orion A, Orion B and Monoceros R2) which are shown by the colourscale to have internal density variations based on observations of $CO(1-0)$ emission by Wilson et al. (2005).

Another characteristic of GMCs is that they are assumed to be bound by self-gravity, whereas molecular clouds of $M < 10^3 M_\odot$ require external forces to maintain gravitational equilibrium (e.g., Heyer et al. 2001). The scaling relations of Larson (1981) link the fundamental physical properties of GMCs-mass, size, and velocity dispersion as follows,

- The **linewidth-size (l-s) relation** states that the velocity dispersion, σ, of the CO emission line is proportional to the cloud size by the following relation:

$$\sigma \propto R^{\mathrm{p}}, \tag{1.9}$$

  where the cloud radius, $R = \sqrt{\mathrm{Area}/\pi}$, and $p = 0.38$ (Larson 1981). More recently, observational studies of Galactic molecular clouds and theoretical models have calculated $p \approx 0.5$ (e.g., Solomon et al. 1987; Passot and Vázquez-Semadeni 2003; Kudoh and Basu 2003; Rice et al. 2016).

- The **mass-size (m-s) relation** links cloud mass to R according to

$$M \propto R^2. \tag{1.10}$$

  When equation 1.10 is satisfied, clouds have approximately constant surface densities, $\Sigma = M/\pi R^2$.

- Combining the l-s and m-s relations leads to a relation between cloud mass (or L_{CO}) and velocity dispersion (σ). For a given size, a positive correlation between mass and σ implies that an object is approximately in virial equilibrium.

The virial theorem states that for a gravitationally bound system in equilibrium, the kinetic energy (KE) is twice the absolute value of the gravitational potential energy (GPE), i.e.,

$$2\mathrm{KE} + \mathrm{GPE} = 0. \tag{1.11}$$

A body is bound by self-gravity when the magnitude of the GPE exceeds the internal KE.

Observations of MW GMCs have validated Larson's relations (e.g. Solomon et al. 1987; Heyer et al. 2009). However, their validity is questioned from observations of extragalactic GMCs (e.g. Hughes et al. 2013; Colombo et al. 2014; Evans et al. 2021; Lada et al. 2024).

1.2.1 Are GMCs Gravitationally Bound?

If a GMC is indeed bound by self-gravity, it can be viewed as an isolated system with forces acting upon it as follows. On one hand, GPE is driving the material towards gravitational collapse (see Section 1.4). On the other hand, the KE of the system due to turbulence and pressure within the cloud (see Section 1.5.4) is resisting gravitational collapse.

Larson (1981) proposed that molecular clouds are gravitationally bound and approximately satisfy the virial theorem. The virial parameter, $\alpha_{\rm vir}$, measures the gravitational boundness of an object from the ratio of KE to GPE. Assuming a constant density cloud, Bertoldi and McKee (1992) derived the following for $\alpha_{\rm vir}$:

$$\alpha_{\rm vir} = \frac{5\sigma^2 R}{GM}. \tag{1.12}$$

However, GMCs have complicated internal density structures highlighted by Figure 1.4. Therefore, a power-law density distribution, $\rho(r) \propto r^{-1}$ (Solomon et al. 1987) is often assumed (e.g., Lada et al. 2024). The corresponding $\alpha_{\rm vir}$ is then

$$\alpha_{\rm vir} = \frac{4.5\sigma^2 R}{GM}. \tag{1.13}$$

Equation 1.13 is derived by assuming a stratified cloud. This assumes an ellipsoidal cloud with concentric, ellipsoidal layers of equal density (e.g., Bertoldi and McKee 1992). A cloud is virialized when $\alpha_{\rm vir} = 1$, and so the mass of a virialized cloud, $M_{\rm vir}$, from 1.13 is

$$M_{\rm vir} = \frac{4.5R\sigma^2}{G}. \tag{1.14}$$

However, Maloney (1990) found that the masses of clouds with lower luminosity can be overestimated by assuming virial equilibrium. If the mass of a cloud or region is measured from $\alpha_{\rm CO} \times L_{\rm CO}$ (equation 1.7) then the virial and bound nature of the region can be inferred from the relationship between $M_{\rm vir}$ and luminous mass, $M_{\rm lum}$.

In a plot of $M_{\rm vir}$ vs $M_{\rm lum}$, the virial condition is represented by a 1:1 relationship. Earlier we established that a cloud is gravitationally bound when |GPE| > KE, or KE + GPE < 0.

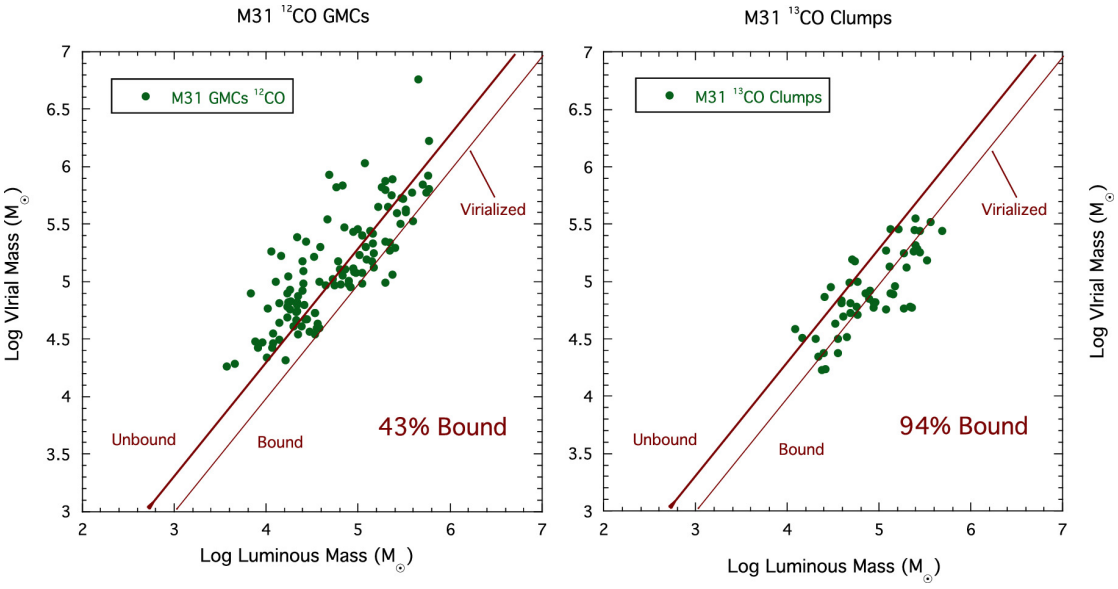

FIGURE 1.5: $M_{\rm vir}$ vs $M_{\rm lum}$ for: M31 GMCs defined by ^{12}CO emission (left) and ^{13}CO clumps (right) associated with M31 GMCs. The thin solid line represents the virial condition, when $\alpha_{\rm vir} = 1$ and the thick solid line separates the bound and unbound sources, when $\alpha_{\rm vir} = 2$. Credit: Lada et al. (2024).

Comparing this with equation 1.11, this corresponds to $M_{\rm lum} > \frac{1}{2}M_{\rm vir}$. An example of a $M_{\rm vir}$ vs $M_{\rm lum}$ diagram is shown in Figure 1.5, using a sample of GMCs in M31 (Lada et al. 2024).

.

The sensitivity required to obtain resolved dust continuum detections in our SMA survey resulted in entire GMCs traced from ^{12}CO$(2-1)$ at 3σ (Viaene et al. 2021), which was observed simultaneously. 162 GMCs and 85 ^{13}CO-emitting GMC regions (clumps) were identified (Lada et al. 2024). Only 43% of M31 GMCs were found to be gravitationally bound, however, 94% of ^{13}CO clumps were shown to be gravitationally bound and approximately virialized. This challenges the long-accepted theory that GMCs are bound by self-gravity. However, this result supports a recent study of MW GMCs by Evans et al. (2021) which found that only 22% of GMCs are bound but that most ^{13}CO clumps are bound (60%).

A key conclusion from these results is that, whilst most GMCs are not necessarily gravitationally bound or virialized, the majority of the $M_{\rm mol}$ of a GMC is contained within dense regions which are bound and approximately in virial equilibrium: the spatial extent of ^{13}CO is 25% that of ^{12}CO in these observations (Viaene et al. 2021), however, the derived masses of these regions are of similar orders of magnitude (see Figure 1.5). In Chapter 3 we expand on this research, following Lada et al. (2024) by analysing the gravitational and virial bound states of regions of these GMCs

traced by dust emission from the same SMA survey. This enables us to both evaluate dust as a tracer of dense gas and compare this to the structures probed by CO isotopologues.

1.2.2 Giant Molecular Associations in M31

To observe M31 at the required resolution and sensitivity, to detect resolved thermal dust emission, integration times of $\approx$ 6 hours per target were required (Forbrich et al. 2020). The angular size of M31 is $\approx 200' \times 70'$ (Paturel et al. 2003), and the average synthesized beam of the SMA in subcompact configuration is $4.5'' \times 3.8''$. Therefore, it would be impossible to observe the entire galaxy in this way, and a targeted survey was required. Targets were chosen based on the *Herschel* Exploitation of Local Galaxy Andromeda (HELGA) survey (Fritz et al. 2012; Kirk et al. 2015). *Herschel* 350 μm observations identified 326 giant molecular associations (GMAs) in M31: associations because the substructures are not resolved by *Herschel* Spectral and Photometric Imaging Receiver (SPIRE; Griffin et al. 2010) observations. The angular resolution of SPIRE at 250 μm, 350 μm, and 500 μm is 18.2$''$, 24$''$ and 36 $''$, respectively ($\approx$ 54 pc, 90 pc and 136 pc), and these lower resolutions (compared to the SMA observations) enabled M31 to be mapped out to a galactocentric radius (GCR) of $\approx$ 26 kpc. These GMAs, identified from the 350 μm data from pixels with a signal-to-noise ratio (S/N) of $\mathrm{S/N} > 5$, have projected sizes of $\approx 750 - 950$ pc, and thus many encapsulate associations of several individual GMCs. The locations of the 326 GMAs overlaid on a deprojected image of M31 are displayed in the left-hand panel of Figure 1.6.

Figure 1.6 shows that GMAs are distributed throughout the entire disc of M31 out to GCR $\approx$ 22 kpc. The right-hand panel of Figure 1.6 shows the number of clouds per kpc^2 with galactocentric distance. There is a clear decrease in the number density of GMAs with increasing GCR. The series of peaks at $\approx 5, 11$ and 15 kpc coincide with the previously identified rings in M31 (see Section 1.3.1). Kirk et al. (2015) found that the total mass of GMAs associated with the 10 kpc ring is 6.5×10^7 M$_\odot$, which is $\approx$ 25% of the total gas mass of M31 (2.6×10^8 M$_\odot$; Fritz et al. 2012). This suggests that, if the star formation efficiency (SFE) is constant across the disc, a large fraction of the star formation in M31 takes place within the 10 kpc ring.

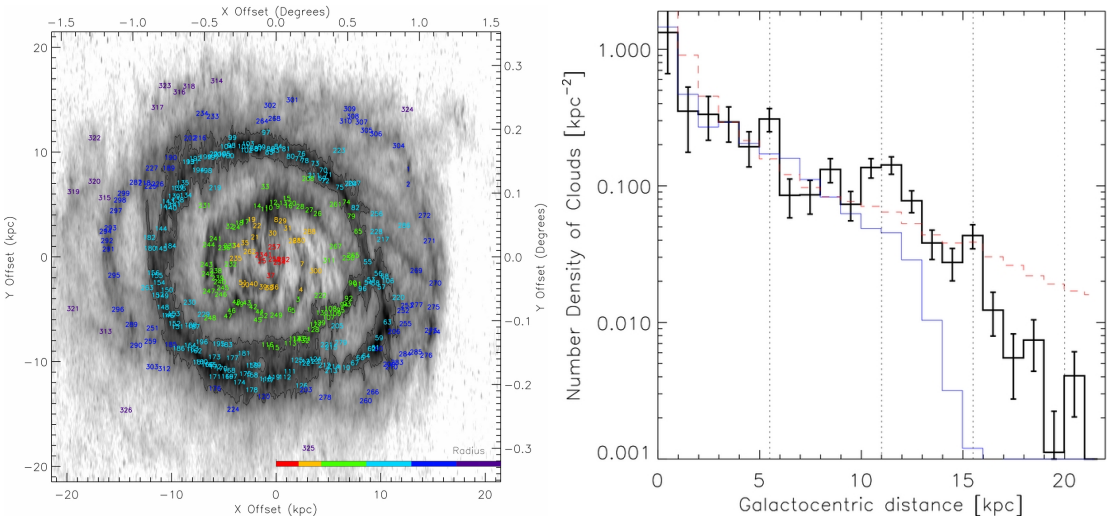

FIGURE 1.6: *Left:* Positions of *Herschel* 250 μm-identified GMAs, plotted over a map of SPIRE 250 μm intensity. The contour shows the 10 kpc star-forming ring. Source labels are coloured by their respective GCR, displayed by the colourbar, the scale of which is denoted by the x-axis of the plot. *Right:* Number density of GMAs (here referred to as clouds) with galactocentric distance. Dotted vertical lines display the GCR of previously identified ring structures in M31 (Haas et al. 1998; Gordon et al. 2006). The dashed red line shows the surface brightness profile of M31 at 3.6 μm. The number density of dark nebulae from Hodge (1980) is displayed as a blue solid line. Credit: Kirk et al. (2015).

1.3 The Andromeda Galaxy

The Andromeda Galaxy, also known as Messier 31 (M31), is our most nearby large spiral galaxy and is part of the Local Group. M31 is $\approx$ 780 kpc away from the MW (Stanek and Garnavich 1998; McConnachie et al. 2005). Observations from an external vantage point provide insights into spiral galaxies that are impossible for the MW due to our position within the Galactic disc. With a disc scale length of $r_{\rm d} \approx 5.5\ kpc$, the disc of M31 is $\approx 2.4\times$ larger than the MW disc. Additionally, M31 has a total disc mass of $M_{\rm tot} = 7 \times 10^{10}$ M$_\odot$, made up of a stellar mass of $5.9 \times 10^{10} M_\odot$ and a gas mass of 6×10^9M$_\odot$, thus the disc of M31 is $\approx 2\times$ more massive than the MW disc (Yin et al. 2009).

The inclination angle of M31 is $i = 12.5°$, making it close to edge-on along the line of sight. This has previously caused some complications in unveiling its morphology and classification beyond a spiral (S) galaxy. First classified as a "normal" spiral galaxy (SA; Hubble 1927), M31 was later shown to be a barred spiral galaxy (SB) through infrared (IR) imaging e.g. with the *Spitzer Space Telescope* (Gordon et al. 2006). In the updated classification system of de Vaucouleurs et al. (1991), M31 was classified as type SA(s)b, where 'b' indicates moderately tight spiral arm

structure. However, near-IR imaging by the Two Micron All-Sky Survey (2MASS) has allowed it to be reclassified as SBb type (Skrutskie et al. 2006).

Spiral galaxies have a central 'bulge', highly concentrated with stars, from which the spiral arms extend from. Central bar structures, such as the one in M31, also contain high concentrations of stars and spiral arms extend from the bars' ends. Spiral arms are the primary sites of recent star formation, inhabited by young, hot OB stars. Deciphering the morphology of M31 is further complicated by its deviation from a "normal" spiral structure. Ring-like dust structures in M31 were first identified in 1998 from IR observations by the *Infrared Space Observatory* (*ISO*; Haas et al. 1998). Later, IR observations with the *Spitzer Space Telescope* (Gordon et al. 2006) revealed its more detailed structure, with its main ring-like component at a GCR of $\approx$ 10 kpc, but also fainter rings at $\approx$ 5 kpc and 14 – 15 kpc. In the following sub-sections, the formation and observational history of M31's rings and the surveys in which these were observed are discussed in more detail.

1.3.1 Introducing the *Ring of Fire*

The observational wavelengths which trace dust emission (IR and sub-mm; see Section 1.1.3) are perhaps the best at unveiling a galaxy's ISM structure. In comparison, optical tracers are overwhelmed by the brightness of the bulge. The main component of the "Ring of Fire" (RoF) is the ring at a radius of $\approx$ 10 kpc. The RoF is the most prominent feature in FIR images of M31, the first of which were obtained by the *Infrared Astronomical Satellite (IRAS)* at $\approx 1'$ (227 pc) resolution at wavelengths 12, 25, 60, and 100 μm (Xu and Helou 1996), thus tracing both warm and cold dust. Also, both the brightest ring and the fainter outer ring were seen in *ISO* observations at 175 μm with $\approx 1.3'$ (295 pc) resolution, which traces cold dust (Haas et al. 1998). The resolution of the *IRAS* and *ISO* observations are sufficient to reveal the general morphology of M31, but not to resolve spiral structure.

One of the most prominent surveys to unveil the galactic structure of M31 is the *Spitzer* Multi-band Imaging Photometer (MIPS; Rieke et al. 2004) IR imaging survey (Gordon et al. 2006). MIPS imaged M31 at wavelengths of 24, 70, and 160 μm (see Figure 1.7) achieving spatial resolutions of $6''$, $18''$, and $40''$ ($\approx$ 23, 68 and 151 pc), respectively, enabling more detailed spiral and ring structure to be unveiled. The MIPS images show the RoF to split into two over approximately a quarter of the galaxy, nearest to the position of the satellite galaxy M32 (south-west, corresponding to the lower-right in Figure 1.7).

FIGURE 1.7: The *National Aeronautics and Space Administration (NASA)*'s *Spitzer Space Telescope*'s multi-wavelength view of M31, combining images at 24 (blue), 70 (green), and 160 (red) μm. Image credit: NASA/JPL-Caltech/K. Gordon, University of Arizona.

A deprojected version of the *Spitzer* MIPS image enabled the morphology of M31 to be further revealed from these observations. Shown in Figure 1.8, compact IR objects (likely star-forming regions, see Section 1.4.1) detected in all three MIPS bands are plotted at 40″ resolution (matching the 160 μm band). The right-hand panel of Figure 1.8 displays a deprojected M31 with Cartesian coordinates. Within the main RoF (highlighted by a black dashed circle), the morphology appears to be spiral-like (beginning at the bar ends), largely following the spiral features marked in green. It is at a radius of $\approx$ 10 kpc that the galaxy appears "disturbed" and the morphology of M31 no longer traces the spiral pattern as closely. The offset of the centre of the RoF from the nucleus by 5′.5, 3′.0 (1.25 kpc, 0.68 kpc), along with its remarkable circularity (Gordon et al. 2006) hints that this is not made up of spiral arm segments.

The asymmetric shape of the RoF is better seen in polar coordinates (Figure 1.8 left-hand panel). A perfectly circular ring would be represented by a horizontal line. A ring at GCR $\approx$ 10 kpc (3.8 arcmin) represents the RoF relatively well, apart from at a position angle (PA) of $\approx$ 200° where the ring splits. This may or may not be coincidentally closest to the position of the satellite galaxy M32 (Gordon et al. 2006).

The chemical evolution model of Yin et al. (2009) showed that M31 has a lower gas mass ($\approx 6 \times 10^9 M_\odot$ vs $\approx 7 \times 10^9 M_\odot$) than the MW. The model showed that, when both galaxies are the same age, M31's SFE (= SFR per unit gas mass) is 2 × higher than the MW's. The main RoF at a radius of 10 kpc is the primary reservoir for star formation in M31 (see Section 1.3.3) and therefore contains the majority of H II regions (see Section 1.4.1) as well as the brightest dust emission. The origin of the RoF and its inner and outer components is one of the key questions in studies of M31. The position of the split within the ring hints that this was caused by a collision

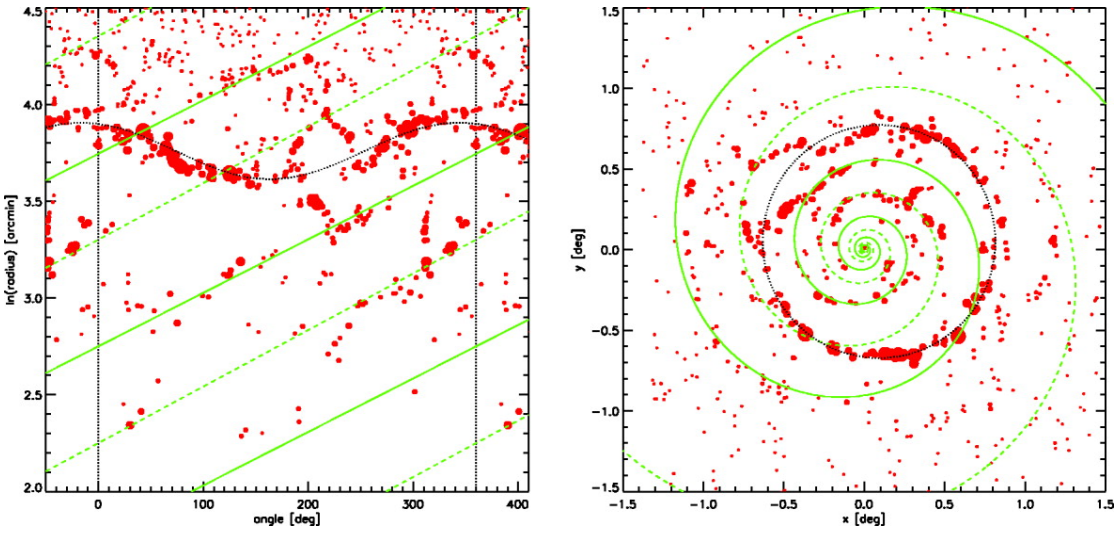

FIGURE 1.8: The *Spitzer Space Telescope*'s deprojected view of M31 point sources at 40″ resolution in polar (left) and cartesian (right) coordinates. Green lines show two simple logarithmic spiral patterns. The RoF at a radius of approximately ≈10 kpc, offset from the galactic center by (5.5′, 3.0′), is displayed by a black dashed line. From Gordon et al. (2006).

between M31 and one of its satellite galaxies, M32, which we discuss in detail in the following section.

1.3.2 Interactions with Satellite Galaxies

Interactions between M31 and its two nearest satellite galaxies, M32 and NGC 205, have long been speculated (e.g. Schwarzschild 1954) to be related to the atypical spiral structure of M31. The higher mass and position close to the split within the RoF makes M32 the most likely culprit. Block et al. (2006) interpret the presence of the main RoF and outer ring at GCR ≈ 15 kpc as evidence of a nearly central, head-on collision between M31 and M32, taking place ≈ 200 Myr ago. The top panels of Figure 1.9 display the differences in gas density ($\Sigma_{\rm gas}$) profiles of the MW and M31, highlighting that whilst the MW has more gas in its inner regions (GCR < 7 kpc), M31 has most of its gas at GCR ≈ 10 – 15 kpc. Here we refer to the total gas surface density, the material traced by H I and H_2 separately is discussed in Section 1.1 and here we refer to the total gas density.

Another indication that an interaction was the cause of the ring formation is that the SFR radial profile of M31 does not obey the classical Kennicutt-Schmidt (KS; Kennicutt et al. 1998) total-gas star-formation law (e.g., Yin et al. 2009). The expected behaviour, according to the KS law, is displayed in the bottom panels of Figure 1.9 for both the MW and M31. Figure 1.9 clearly

shows that neither the KS law nor the M-KS law that describes the MW SFR profile describe the SFR profile of M31. This further indicates that star formation in M31 may have been disturbed by an external source, such as a collision with M32.

The KS law defines SFR surface density, $\Sigma_{\rm SFR}(r)$, depending only on $\Sigma_{\rm gas}$ according to the following formula (Kennicutt et al. 1998):

$$\Sigma_{\rm SFR} = A\Sigma_{\rm gas}^{n}, \tag{1.15}$$

where units of $\Sigma_{\rm SFR}(r)$ are $\mathrm{M_\odot\ yr^{-1}\ pc^{-2}}$ and $\Sigma_{\rm gas}$ has units of $\mathrm{M_\odot pc^{-2}}$. The normalisation constant, $A \approx (2.5 \pm 0.7) \times 10^{-4}\ \mathrm{M_\odot\ yr^{-1}\ kpc^{-2}}$, and the power-law index, $n \approx 1.4 \pm 0.15$. The second star formation law displayed in Figure 1.9 is a modified, KS (M-KS) law that is also radial-dependent, producing the SFR (Ψ) at radius (r; Yin et al. 2009), given by:

$$\Psi(r) = \alpha\Sigma_{\rm gas}^{1.5}\frac{r_{\rm eq\odot}}{r}, \tag{1.16}$$

where α is a coefficient related to SFE and $r_{\rm eq\odot}$ is a reference distance, and for the MW the distance to the Sun (≈ 8 kpc) is used.

However, when only the molecular gas component is considered, the star-formation relation in M31 is broadly consistent with the molecular KS law measured by Bigiel et al. (2008) at GCR>5 kpc (Tabatabaei and Berkhuijsen 2010). Both the power-law relations between the molecular gas surface density ($\Sigma_{\rm H_2}$) and total gas surface density ($\Sigma_{\rm H_1 + H_2}$) with SFR found by Tabatabaei and Berkhuijsen (2010) agree with the best-fit molecular KS law of Bigiel et al. (2008) derived from seven nearby galaxies which are much brighter than M 31.However, large intrinsic scatter around the relations mean that neither the present-day SFR nor the SFE in M31 are well-correlated with the total or molecular gas surface density. This indicates that factors other than gas density (e.g., the structure and physical conditions of the ring) play an important role in regulating star formation in M31.

More recently, the HASHTAG (HARP and SCUBA-2 High-Resolution Terahertz Andromeda Galaxy Survey; Li and Bryan 2020) project mapped M31 in CO$(3-1)$, observing selected fields covering the GCR range $2-14$ kpc. From a comparison between these JCMT (James Clerk Maxwell Telescope) observations and IRAM (Institut de Radioastronomie Millimetrique) 30 m observations of CO$(1-0)$, Li and Bryan (2020) found that the correlation between $\Sigma_{\rm SFR}$ and

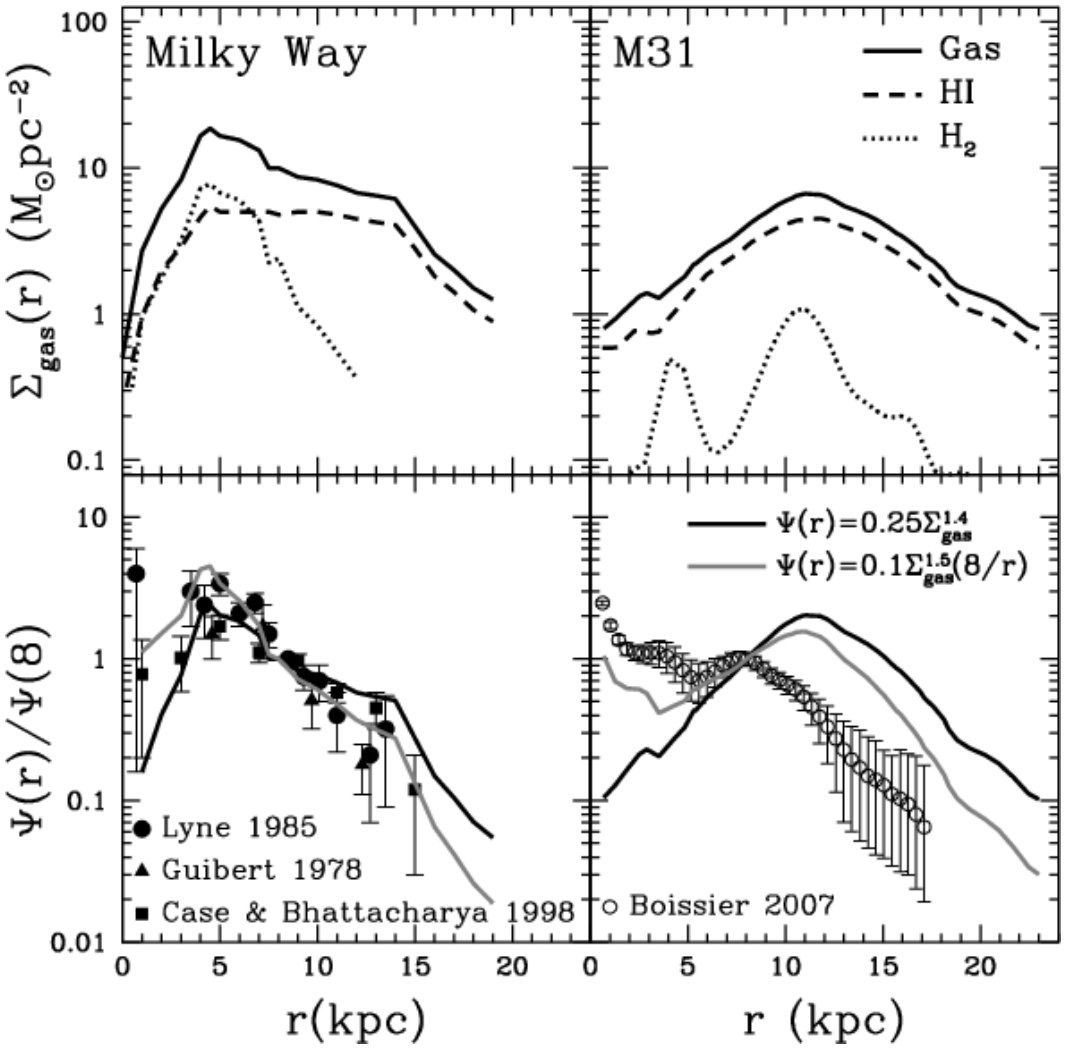

FIGURE 1.9: *Upper panels*: Gas density profiles (total gas, H I and H_2) of *left* the MW and *right* M31. *Lower panels*: SFR profiles of *left* the MW and *right* M31. Lines indicate the results calculated according to KS and M-KS star formation laws. Credit: Yin et al. (2009).

line intensity is significantly stronger for $CO(3-1)$ than $CO(1-0)$, suggesting that $CO(3-1)$ is a better tracer of dense, star-forming gas. Additionally, they find that the $CO(3-1)/CO(1-0)$ intensity ratio is significantly higher in the nuclear ring at ≈ 1 kpc GCR, and the RoF at ≈ 10 kpc, indicating that Σ_{SFR} is higher in these regions.

The length of time since the last major interaction between M31 and M32 has a variety of estimates in the literature, ranging from 200 Myr (e.g., Block et al. 2006; Gordon et al. 2006) to 2 Gyr (e.g., D'Souza and Bell 2018). Observational results include the Panchromatic *Hubble* Andromeda Treasury (PHAT) survey, which estimated that the RoF is ≈ 500 Myr old based on its SFH (Lewis et al. 2015).

To try to estimate how long ago the last galaxy collision with M31 occured and if this, or

previous collisions could have formed the RoF, these interactions have also been investigated in models. For example, Gordon et al. (2006) used numerical simulations of the M31-M32 and M31–NGC 205 interactions. By treating M32 as a point particle with a mass of $1 \times 10^{10} M_{\odot}$, they found that the collision occured $\approx$ 200 Myr ago.

More recent N-body hydrodynamical simulations of the M31-M32 interaction have estimated that the collision occured > 500 Myr ago (Davidge et al. 2012). In particular, the high-resolution simulation of Dierickx et al. (2014) reproduced the gas and stellar morphologies of M31. In their simulation, the interaction resulted in "pseudo-rings" which are expanding spiral arms that appear ring-like due to the high inclination of M31. M32 passes through the south-west side of M31 in the Dierickx et al. (2014) simulation, and this could be related to the below-average gas density at this position, in agreement with the lower abundance of dust at this position seen in IR imaging (see Section 1.3.1). Simulations of Dierickx et al. (2014) estimated that the M31-M32 collision took place $\approx$ 800 Myr ago.

In contrast, from cosmological models, D'Souza and Bell (2018) found that M31's high stellar metallicity and large accreted component indicate the collision took place $\approx$ 2 Gyr ago. Williams et al. (2015) outline three scenarios that could lead to a burst of star formation in M31 2 – 4 Gyr ago, during which approximately one fifth of its stars formed. This includes a tidal interaction with M33 proposed by Bernard et al. (2015), these simulations reproduce the current positions and velocities of M31 and M33 (McConnachie et al. 2005; 2009) and suggest a close passage 2 – 3 Gyr ago. However, the present-day masses and morphologies of M31 and M33 are not consistent with having experienced a strong interaction (Williams et al. 2015).

Secondly, this burst of star formation may be linked to gas accretion during a collision with a metal-rich progenitor, potentially M32. Although M32 is currently a gas-poor dwarf elliptical galaxy (Wirth and Gallagher 1984; Kormendy et al. 2009; Young et al. 2011), its relatively high stellar metallicity suggests that that it is the remnant core of a once more massive galaxy that underwent substantial chemical enrichment before losing much of its stellar and gaseous disc through tidal stripping by M31 (D'Souza and Bell 2018). Tidal stripping preferentially removes the less-bound gas from the outer disc, which is expected to be of lower metallicity than the remnant core. Nevertheless, this stripped gas could still have been more metal-rich than the M31 disc at the time of interaction, providing a plausible explanation for the observed burst of star formation.

On one hand, the simulations of Bekki et al. (2001) support this theory, predicting that M32 began as a low-luminosity spiral galaxy which passed through the central regions of M31, stripping most of its outer disc. Because the central bulge is compact, it is less affected by the tidal field of M31, and its morphology remains after the interaction. On the other hand, simulations of Choi et al. (2002) suggest that M32's precursor was intrinsically compact and rather than the core of a larger spiral galaxy. However, they find that both NGC 205 and M32 exhibit features of tidal interaction with M31. Therefore, whether M32 could provide this metal-rich accreted gas, leading to a large burst of star formation in M31, remains an open question.

Finally, M31 may have experienced a relatively major merger, where the progenitor has completely coalesced into M31. The most consistent progenitor with merger simulations (e.g., Cox et al. 2008; Moreno et al. 2015) is a progenitor galaxy of mass $\gtrsim$ 20% that of M31 pre-merger. Both Cox et al. (2008) and Moreno et al. (2015) show that this merger would trigger a starburst $\approx 2-4$ Gyr ago.

A recent collision between M31 and e.g., M32 (as well as tidal interactions with both M32 and NGC 205) would additionally affect the chemical composition of both the interstellar medium (ISM) of M31 and any subsequent generations of stars. The length of time since the most recent major galaxy interaction, as well as the effects of this, can be investigated by the radial metallicity profile of the ISM and how well-mixed this material is. This is one of the main topics under investigation in Chapter 2 of this thesis. These concepts are discussed in detail in Section 1.5.

1.3.3 Recent Star Formation History

Surveys such as PHAT use optical images taken with the *Hubble Space Telescope* (HST; Lewis et al. 2015) to uncover the recent SFH across M31. PHAT specifically observed a 0.5 square degree area (corresponding to ≈ 380 kpc^2 deprojected) in the north-east (NE) quadrant of M31. Key results of the PHAT survey include galaxy-wide fluctuations in SFH back to $\approx$ 500 Myr ago, predominantly in the RoF. Also, concentrated star formation appears to have begun in the $\approx$ 15 kpc GCR ring $\approx$ 80 Myr ago. Significant variations also occur between 100×100 pc regions (Lewis et al. 2015). The average SFR over the last 100 Myr calculated from this survey is ≈ 0.7 M$_\odot$ yr^{-1} and was found to be approximately constant apart from a small increase by a factor of $\approx 1.3-50$ Myr ago. Finally, over the last $\approx$ 500 Myr, $\approx$ 60% of all star formation in M31 has taken place in the RoF.

The work presented in this thesis complements these PHAT results by focusing on present-day, high-mass star-formation traced by H II regions (see Section 1.4.1). Compared to PHAT, which uncovered the SFH over the past $\approx$ 500 Myr from resolved stellar populations in the NE quadrant of M31, we analyse spectra from individual sources corresponding to candidate H II regions (Azimlu et al. 2011). Since H II regions have ages of $\lesssim$ 10 Myr, they trace the most recent star-formation in M31. Additionally, the spatial coverage is extended to the entire disc. Therefore, we compare current star formation conditions in M31 with the longer-term SFH uncovered by Lewis et al. (2015).

1.4 Massive Star Formation

Although massive stars are relatively rare (Salpeter 1955), they are crucial chemical and dynamical inputs to the ISM via SN and stellar outflows. Massive stars are formed within GMCs, when gravitational equilibrium is disturbed such as by nearby SN explosions or the accretion of external gas. Massive stars (OB) emit UV photons with sufficient energy to ionise H, creating H II regions close to the star-formation site. Massive stars have relatively short lifetimes of order $\approx$ 10 Myr (e.g., Ekström et al. 2012; Langer 2012), and so H II regions trace very recent star formation. H II regions serve as lighthouses of star formation due to their bright emission lines in the UV and optical.

Much of our knowledge of massive star formation comes from observations at IR, mm/sub-mm and radio wavelengths (e.g., Condon 1992; Kennicutt et al. 1998), tracing molecular gas (e.g., CO), thermal dust emission, free-free emission, and H recombination lines in the Paschen series (e.g., Brocklehurst and Seaton 1972). This is to avoid the effects of dust extinction which primarily affects optical and UV observations, as discussed in Section 1.1.4. However, optical spectroscopy of H II regions is particularly useful to probe the chemical properties of recent massive star formation and the chemical enrichment of the ISM.

1.4.1 H II Regions

As highlighted above, H II regions are signposts of recent, massive star formation. Their formation occurs when H I gas surrounding recently formed massive (OB) stars is ionised to H II gas by UV radiation from the star. Figure 1.10 (*left*) displays a schematic representation of a recently formed OB star within a dense clump, with arrows indicating GPE > KE initiating

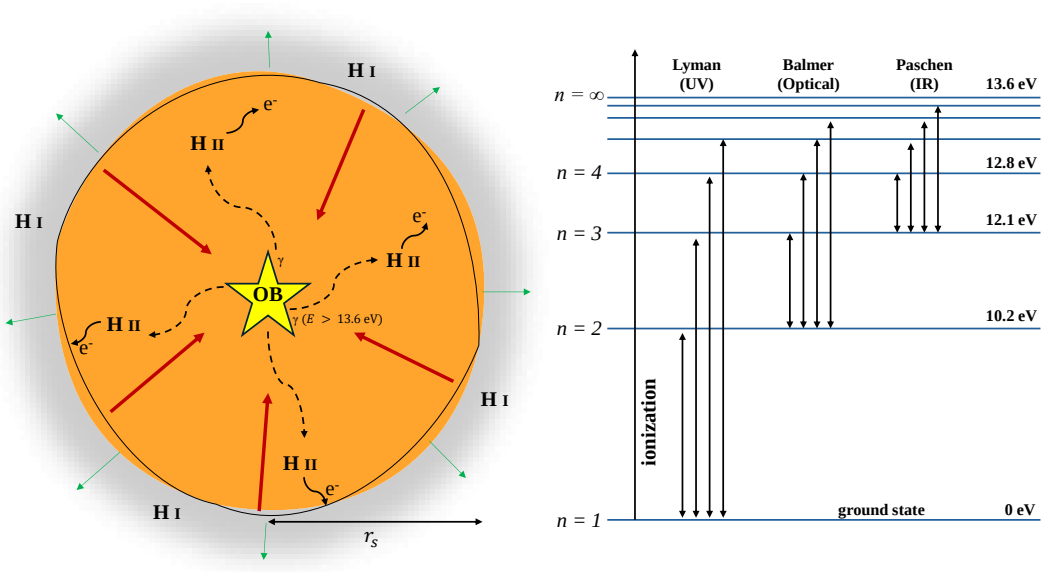

FIGURE 1.10: *Left*: Schematic diagram showing ionisation of an H II region by an OB star. The H I gas surrounding the star is ionised (the electrons are removed from the atoms) by UV photons of energy > 13.6 eV, becoming H II gas. r_s represents the Strömgren radius of the H II region (see Section 1.4.2). *Right*: Electron energy levels (n) of the H atom, displaying the absorption and emission processes that produce lines detectable at varying wavelengths.

gravitational collapse. This ionisation can happen due to one or multiple massive stars, or even clusters.

The H atom is composed of one proton and one electron, with the electron orbiting the proton nucleus in one of the quantised energy states (Bohr 1913). Figure 1.10 (*right*) shows the energy levels of the H atom according to Bohr (1913). When the atom absorbs a photon of sufficient energy, the electron moves up the energy levels. The 'ionisation' arrow represents the electron being removed from the atom when a photon of energy > 13.6 eV is absorbed. Free elections in the ionised gas recombine with H II, and transition between energy levels, emitting photons corresponding to recombination lines in the UV-IR. Electrons which do not recombine produce free-free (bremsstrahlung) radiation at radio wavelengths. Hα emission, corresponding to the transition from $n = 3$ to $n = 2$, is the strongest emission line, due to H being the most abundant atom and Hα the most easily excited state. Hα flux/luminosity is therefore a common tracer of massive star formation in galaxies (e.g., Kennicutt et al. 2008). The ratio of Hα to Hβ is used to correct for visual extinction in optical spectra (see Section 1.1.4).

Free electrons from H ionisation can also collide with atoms of other elements, exciting them to higher energy states, which emit photons of corresponding wavelengths when returning to lower energy states. The primary cooling mechanism of ionised gas is the emission of radiation

through forbidden transitions of collisionally excited atoms (Spitzer 1954). Emission lines at optical wavelengths can be used to robustly identify H II regions. Whilst H II regions are often identified based on their Hα image morphology, compact H II regions can be misclassified as PNe. H II regions and PNe display many of the same optical emission lines, however, their different ionisation mechanisms result in differences in the relative strength of these emission lines.

As discussed, H II regions are ionised by massive stars. PNe ionisation, on the other hand, occurs due to the radiation emitted during the evolution of an intermediate mass star from a cool red giant to an extremely hot white dwarf. Emission lines from low ionisation species (e.g., Hα and Hβ) dominate H II regions, whereas PNe display strong emission lines from high-ionisation species such as [O III] and [N II] (e.g., Draine 2011). Therefore, the flux ratios [N II]/Hα and [O III]/Hβ are commonly plotted on a BPT (Baldwin, Phillips, Telervich) diagram (Baldwin et al. 1981) to differentiate H II regions from PNe. The BPT diagram was originally created to differentiate star-forming galaxies from active galactic nuclei (AGN). Because PNe and AGN produce harder ionising radiation fields than massive star formation, both produce elevated [O III] and [N II] and thus occupy the same region of the BPT diagram (e.g., Kewley et al. 2001; Kauffmann et al. 2003).

1.4.2 Photoionisation Modelling

H II regions can be represented by a Strömgren sphere: the theoretical result of Strömgren (1939) for an ionising source (OB star) embedded within neutral atomic H gas (H I). The Strömgren sphere represents the boundary where photoionisation and recombination balance, creating a narrow transition zone between the H II gas surrounding the ionising source and the H I surroundings (Strömgren 1939). The Strömgren radius (r_s) depends on the rate of ionising photons (

$$r_s = \left(\frac{3\, Q_H}{4\pi\, n_e^2\, \alpha_B} \right)^{1/3}, \tag{1.17}$$

where n_e is the electron number density, and α_B is the recombination coefficient. In H II regions, case B recombination is usually assumed, which states that in an optically thick nebula, all recombination to the ground state ($n = 1$) is cancelled out by subsequent ionisation, thus only ionisation to states $n \geq 2$ are accounted for (e.g., Peimbert et al. 2017). More recent

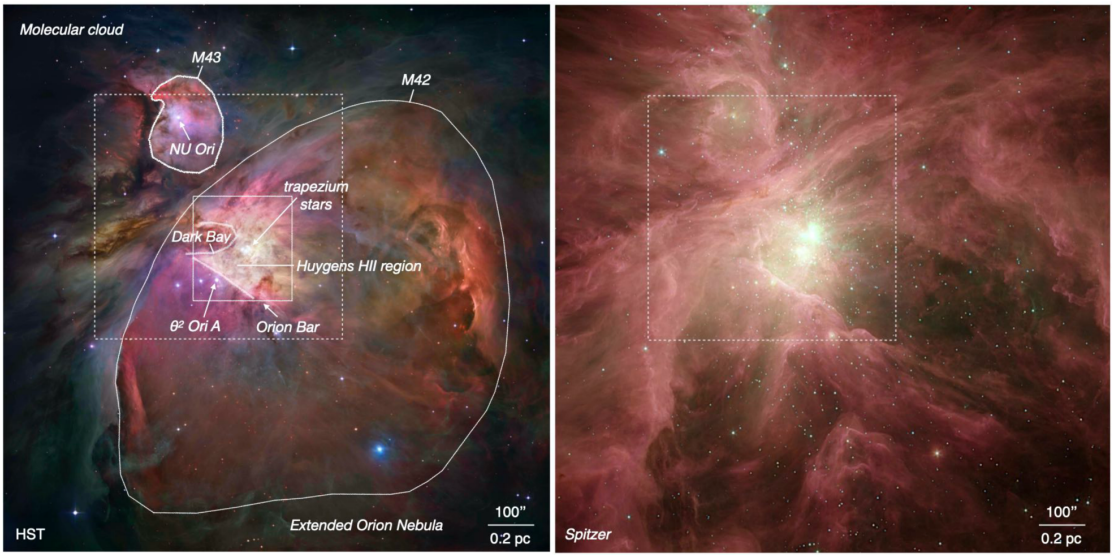

FIGURE 1.11: M42 and M43 of the Orion Nebula in *Hubble* (left) and *Spitzer* (right) observations. Credit: (Habart et al. 2024)

photoionisation models use a modified Strömgren sphere to produce model H II region spectra that replicate observed H II regions. These models typically require the following inputs. Stellar atmosphere models to input the spectral energy distribution (SED) of the ionising source (e.g., Ferland et al. 1998), a gas density distribution, and heating and cooling from photoionisation and collisional excitation respectively. These models are able to produce estimates of emission lines which can be used to calibrate diagnostics for electron temperature (T_e) and chemical abundances (see Section 1.5.5).

1.4.3 The Orion Nebula

In 1656, Christiaan Huygens recorded the first H II region: the Orion Nebula (M42), containing the Orion Nebula Cluster (ONC). M42 is located approximately 414 pc away and has a diameter of $\approx$ 7.8 pc (Menten et al. 2007). It contains $\approx$ 3500 stars that formed within the last $<$ 2 Myr (Hillenbrand et al. 2013). Since then, it has become the most well-studied H II region (e.g., Genzel and Stutzki 1989). The primary ionisation sources of the Huygens H II region are the massive stars of the Trapezium Cluster, which come with a cluster of many low-mass stars.

M42 has an estimated diameter of 7.8 pc (Menten et al. 2007). Much larger Galactic and extragalatic H II regions have been identified, for instance, 30 Doradus of the Large Magellanic Cloud (LMC) has a size of $\approx$300 pc and is 200 times more luminous than M42 (Kennicutt 1984). Observations of nearby H II regions such as M42 enable internal H II region kinematics

to be studied in detail not achieved in extragalactic studies. But it is also crucial to investigate galaxy-wide star formation from optical spectroscopy of H II regions with different properties. This is difficult in the MW, as Galactic H II regions located further away are heavily affected by dust extinction and distance measurements are uncertain. M31 is an excellent candidate for H II region optical spectroscopy and is nearby enough to observe emission from individual sources with the MMT/Hectospec (see Section 1.6.1). Our H II region survey enables us to identify the locations of recent massive star formation, which can be compared to Very Large Array (VLA) observations of M31 GMCs (Toomey et al., in prep,) to infer the ionisation source.

Although the internal structures of H II regions in M31 cannot be resolved to the level achieved in observations of the Orion Nebula, M31 provides the advantage of an H II region sample with consistent spatial resolution across the entire disc. Studies have shown that H II region properties may vary with differences in physical environment (e.g., Kaufman et al. 1987). For instance, the radio map of M81 by Kaufman et al. (1987) showed that giant H II regions are concentrated along spiral arms in this galaxy. This makes our uniform sample of optical spectroscopy towards an individual galaxy particularly valuable. In Chapters 2 and 4, we use a survey of M31 H II regions to evaluate elemental abundances across the galaxy disc (see Section 1.5). As was the case for our SMA survey (see Section 1.2.2), the proximity of M31 means that a targeted survey is required to observe individual sources. We mainly selected observational positions based on the Azimlu et al. (2011) catalog of candidate H II regions discussed below, combined with Hα sources from the aforementioned VLA survey.

1.4.4 Survey of Candidate H II regions in M31

The narrowband Hα imaging survey of Azimlu et al. (2011) covered the entire M31 disc out to GCR $\approx$ 24 kpc, with spatial resolution $\approx$ 3.8 pc. Observations were part of the Survey of Local Group Galaxies using the Mayall 4 m telescope (Massey et al. 2006). The resulting sample consists of 3691 possible H II regions identified from Hα photometry. We refer to these sources as H II region "candidates" because these are identified from Hα emission only, which potentially contaminates the sample with PNe. Candidate H II region sizes range from 16 - 190 pc, comparable to Galactic and M51 H II regions (e.g., Lee et al. 2011).

The positions of the flux peaks of all 3691 Azimlu et al. (2011) sources are shown in Figure 1.12. The more luminous sources trace the spiral arms and star-forming rings of M31, highlighting that star formation primarily occurs there (see Section 1.3). This indicates that in M31, H II

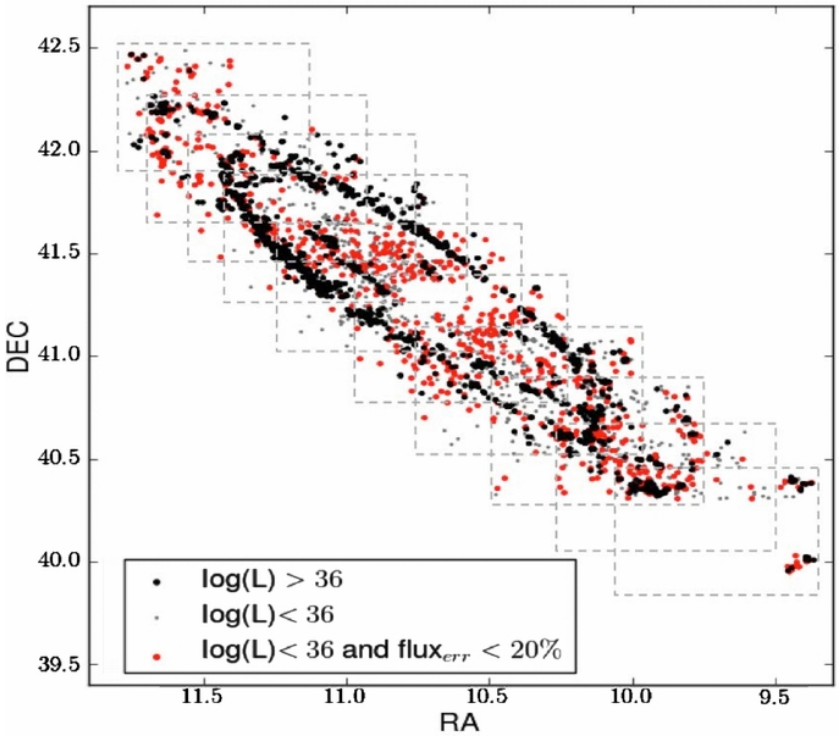

FIGURE 1.12: Candidate H II regions identified from Hα photometry, coloured according to their corresponding Hα luminosity (in $\log(L_{\mathrm{H}\alpha}/\mathrm{erg\ s^{-1}})$ and flux uncertainty. Axes show Right Ascension (RA) and Declination (DEC) in degrees using the J2000 coordinate system. Credit: Azimlu et al. (2011).

region properties may be different for spiral arm and inter-arm environments. Ultimately, optical spectroscopy is needed to robustly identify H II regions in M31 and measure their chemical abundances, discussed in the following section, which infers the chemical enrichment history of the galaxy.

1.5 Metallicity and Chemical Abundance

The majority of elements heavier than He (metals) are synthesised in the cores of stars and returned to the ISM through stellar winds or SNe. The majority of the mass in metals is produced in massive stars via the α-process (e.g., Woosley and Weaver 1995; Maiolino and Mannucci 2019). However, not all heavy elements are produced in stellar cores. Many intermediate-mass elements are produced in AGB star envelopes via the s-process (e.g., Herwig 2005; Karakas and Lattanzio 2014). Approximately half of all elements beyond iron (Fe) are produced during neutron star mergers via the r-process (e.g., Burbidge et al. 1957; Matteucci 2012; Thielemann et al. 2017).

Metallicity (Z) is a measurement of the abundance of these metals, typically expressed as a ratio to H. Measurements of metallicity distribution across the disc of a galaxy provide insight into the history of ISM enrichment from star formation. Therefore, metallicity is a vital parameter for understanding galaxy evolution.

Gas-phase metallicity is a measure of the abundance of heavy elements present in the gaseous component of the ISM. A significant fraction of metals is "depleted" from the gas-phase and is presumed to be locked-up inside solid dust grains (e.g., Savage and Sembach 1996). However, O abundance is significantly less affected by dust depletion than that of other heavy elements (Jenkins 2009; Peimbert and Peimbert 2010). Also, O is the most abundant metal produced by massive stars and exhibits strong emission lines from H II region optical spectra. Therefore, the ratio of oxygen-to-hydrogen, expressed in the form log(O/H) + 12 (hereafter O/H), is typically used as a gas-phase metallicity tracer (e.g., Zaritsky et al. 1994; Kewley and Dopita 2002; Pilyugin et al. 2010). Chemical properties of the ISM can be inferred through O/H of H II regions and PNe, with H II tracing chemical properties of recent star formation and PNe tracing chemical properties at the time of formation of the progenitor star.

Alongside O, Nitrogen (N) experiences negligible dust depletion. Therefore, O/H and log(N/H) + 12 (hereafter N/H) are useful for tracing the enrichment history of the ISM (e.g., Pilyugin and Thuan 2011). Additionally, comparing elements of different nucleosynthetic origins such as O and N (see below) provides insight into the contribution to chemical enrichment from stars of different masses (e.g., Vila-Costas and Edmunds 1993; Pilyugin and Thuan 2011; Vincenzo and Kobayashi 2018).

1.5.1 Nucleosynthesis of Elements

The elements and their yields returned to the ISM depend on the initial stellar mass. The α-elements are elements with even atomic numbers from O up to Calcium (Ca). Neon (Ne), magnesium (Mg), silicon (Si), and sulfur (S), are also α-elements. α-elements are predominantly nucleosynthesised in massive stars through the α-process, where He nuclei (α particles) are captured by atoms of heavy elements. These are then ejected back into the ISM through core-collapse SN. Because massive stars have relatively short lifetimes, enrichment of the ISM from α-elements is relatively fast.

The Fe-peak elements include Fe, chromium (Cr), manganese (Mn), nickel (Ni), cobalt (Co), copper (Cu), and zinc (Zn). These are synthesised in both core-collapse SNe (CCSNe) and Type Ia SNe (SNe Ia); e.g., Arnett 1973; Tinsley 1980; Mernier et al. 2016). Significant amounts of Fe-peak elements are produced during Si burning when massive stars explode as CCSNe (e.g., Arnett and Chevalier 1996; Trimble 1975; Nomoto et al. 2013). In a classical SNe-Ia, the CO (carbon-oxygen) white dwarf in a binary system approaches the Chandrasekhar limit (≈ 1.4 $M_{\odot}$; e.g., Whelan and Iben 1973; Hillebrandt and Niemeyer 2000) and Fe-peak elements are returned to the ISM by thermonuclear SNe-Ia explosions. Sub-Chandrasekhar SNe-Ia explosions (from e.g., violent white dwarf mergers; Pakmor et al. 2012; Ruiter et al. 2013) also occur, but these are not a dominant channel for SN-Ia progenitors (Seitenzahl et al. 2013; Mernier et al. 2016). Stars of masses below the Chandrasekhar limit have longer lifetimes than massive stars, thus ISM enrichment of Fe-peak elements through SNe Ia is slower.

Elements heavier than Fe are produced during the s-process (slow neutron capture process) and the r-process (rapid neutron capture process; see review by Meyer 1994). The s-process occurs in low-mass and intermediate-mass stars, mainly AGB stars, and elements are released by stellar winds (e.g., Busso et al. 1999; Herwig 2005. The r-process takes place in explosive environments such as CCSNe or neutron star mergers (e.g., Symbalisty and Schramm 1982; Thielemann et al. 2017).

N nucleosynthesis is more complicated than O nucleosynthesis, with primary and secondary components. N is produced in the CNO cycle, in which stars fuse H into He through a sequence of six reactions, four proton capture reactions and two positron decays. A simple explanation of the process is that through proton capture, C is converted to N, which is converted to O, and O is converted to C by emitting an α-particle (e.g., see the review by Wiescher 2018). The nuclear reactions are as follows:

$$^{12}\mathrm{C} + {}^{1}\mathrm{H} \longrightarrow {}^{13}\mathrm{N} + \gamma, \quad {}^{13}\mathrm{N} \longrightarrow {}^{13}\mathrm{C} + \mathrm{e}^{+} + \nu, \quad {}^{13}\mathrm{C} + {}^{1}\mathrm{H} \longrightarrow {}^{14}\mathrm{N} + \gamma,$$

$$^{14}\mathrm{N} + {}^{1}\mathrm{H} \longrightarrow {}^{15}\mathrm{O} + \gamma, \quad {}^{15}\mathrm{O} \longrightarrow {}^{15}\mathrm{N} + \mathrm{e}^{+} + \nu, \quad {}^{15}\mathrm{N} + {}^{1}\mathrm{H} \longrightarrow {}^{12}\mathrm{C} + {}^{4}\mathrm{He}.$$

When the seed C is produced within the star itself, a massive (4–8 $M_{\odot}$) AGB or rotating star, the N produced is primary. AGB stars have longer lifetimes than more massive stars, and so this primary N is delayed (Kobayashi et al. 2023). Secondary N is produced when CNO are already present in the progenitor star, thus the yield depends on the initial metallicity of the star (Clayton

1983; Arnett and Chevalier 1996). The contributions of primary and secondary N will be further explored in Section 1.5.3.

1.5.2 Radial Metallicity Gradients

In spiral galaxies, metallicity decreases with increasing GCR (Tinsley 1980). This is a consequence of inside-out galaxy formation, as predicted in chemical evolution models (e.g., Chiappini et al. 2001). Inside-out galaxy formation predicts that star forming disc galaxies begin with the formation of a central bulge which acts as a gravitational potential well, onto which cold gas accretes from the surroundings, forming the disc (e.g., Mo et al. 1998). Typically, the bulge and central regions are assembled on much shorter timescales than the outermost regions (e.g., Chiappini et al. 2001).

As gas provides the 'fuel' for star formation, star formation begins in the bulge and gradually progresses outwards (e.g., Kepner 1999). The higher concentration of gas in the central regions means that SFR is higher closer to the galaxy centre and decreases with GCR. With the inner regions undergoing more cycles of star formation, this scenario predicts that the radial metallicity gradient initially steepens with time, for example in the Galactic model of Chiappini et al. (2001). At later stages of galaxy evolution, the radial metallicity gradient flattens over time due to the following processes (e.g., Pilkington et al. 2012; Bresolin 2017; Vincenzo and Kobayashi 2018).

Radial metallicity gradients are influenced by gas inflow, outflow, and the mixing of metals, all processes that govern galaxy evolution through the baryon cycle. On the one hand, gas acquired through mergers or interactions with other galaxies will typically have a different metallicity to that present in the galaxy beforehand. Radial mixing (see Section 1.5.4) of the ISM transports this usually lower-metallicity gas from the outskirts to the inner regions, diluting the central metallicity (Montuori et al. 2010). On the other hand, SN driven outflows preferentially remove higher-metallicity gas (Dalcanton 2007; Chisholm et al. 2018). Some of this material can later be re-accreted at larger radii through galactic fountains (e.g., Shapiro and Field 1976; Bregman 1980; Fraternali and Binney 2008). Also, galaxies can accrete secular pristine gas from the intergalactic medium (IGM; Kereš et al. 2005; Birnboim and Dekel 2003).

Elements produced over longer timescales (e.g., Fe and N) typically produce steeper gradients than the α-elements (Chiappini et al. 2001). Comparing the radial abundance gradients of different elements is crucial to infer influences on the radial profile from various stellar populations

of different masses. The variations of the ratios of elements with different nucleosynthetic origins with total metallicity additionally uncovers information on the contribution of these nucleosynthesis methods.

1.5.3 Chemical Abundance Scaling Diagrams

Radial abundance gradients provide an overall picture of galaxy chemical evolution and star formation timescales. However, chemical abundance scaling diagrams can provide insight into the relative contributions of stars of different masses. For example, the diagnostic diagram $\log[\alpha/\mathrm{Fe}] - \log[\mathrm{Fe/H}]$ (e.g., Tinsley 1980) analyses the contribution of $\alpha-$elements with increasing Fe abundance. Another example is $\log[\mathrm{N/O}] - 12 + \log[\mathrm{O/H}]$ (hereafter N/O-O/H), which investigates the contribution of both primary and secondary N nucleosynthesis with increasing O abundance (e.g., Mollá et al. 2006; Dopita et al. 2016; Vincenzo et al. 2016). Figure 1.13 displays an N/O-O/H diagram derived from stellar spectra (Israelian et al. 2004; Spite et al. 2005; Nieva and Przybilla 2012) and nebular data (Izotov and Thuan 1999). Combining these datasets enabled Nicholls et al. (2017) to derive abundance scaling relations over a range of metallicities.

As discussed in Section 1.5.1, the CNO cycle produces primary C, N and O, and secondary C and N. The overall relation seen when scaling N/O with O in Figure 1.13 was first explained by Vila-Costas and Edmunds (1993), stating that primary N is constant as a fraction of O with increasing O abundance, and the fraction of secondary N increases linearly with O abundance in log space. Because secondary N nucleosynthesis is delayed, this occurs at higher metallicities than primary nucleosynthesis. Recently, models have shown that the linear increase of N/O with O/H is also due to primary N from AGB stars, because their nucleosynthesis is also delayed due to their lifetimes being longer than those of massive stars (Kobayashi et al. 2020). How the N/O-O/H diagram compares for M31 H II regions is presented in Chapter 4.

1.5.4 Mixing of Metals

The radial metallicity gradient provides an overall picture of star formation throughout a galaxy. However, it has recently become clear that the radial gradient alone is not sufficient to describe the gas-phase metallicity profiles of spiral galaxies. Non-negligible scatter has been identified around the radial gradients of galaxies in multiple surveys (e.g., Kreckel et al. 2019; Bosomworth

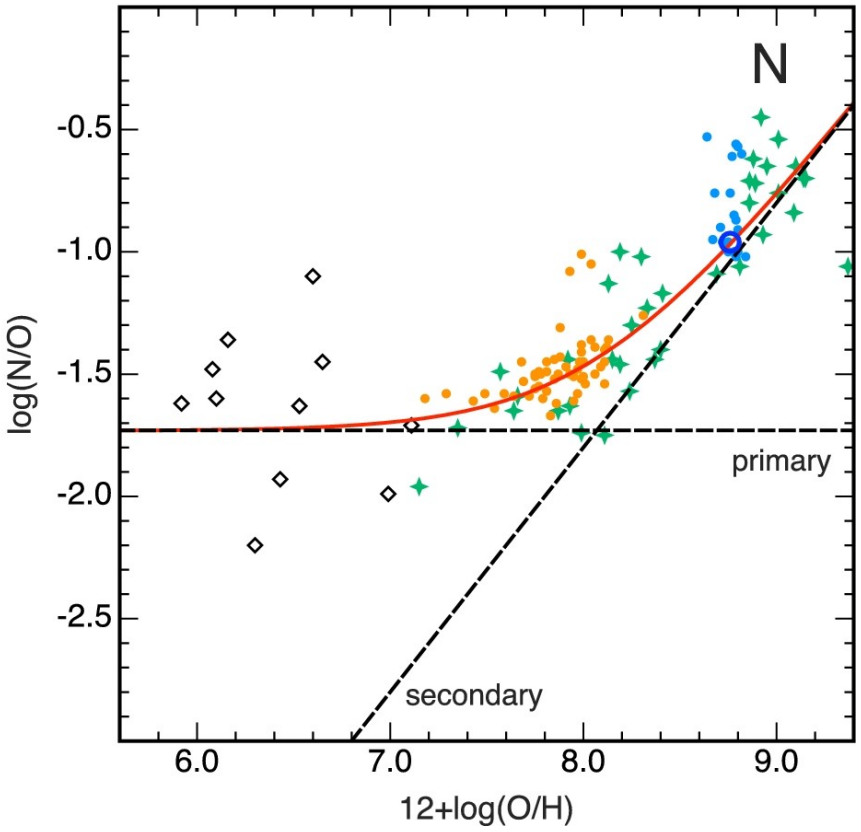

FIGURE 1.13: Relation of the N/O ratio with O abundance, 12 + log(O/H), derived from observational datasets (see text). This includes nebular data from Izotov and Thuan (1999). The dashed lines represent the relative contributions of primary and secondary N nucleosynthesis (and delayed AGB primary). The red solid line shows the total fit to the stellar data, with primary and secondary fits shown as black-dashed lines. Credit: Nicholls et al. (2017).

et al. 2025). This prompts the question of systematic trends in metallicity beyond the well-established radial gradient. Galaxy-wide trends have been identified in observations, in the form of azimuthal variations where enriched material traces spiral arms (e.g., Ho et al. 2017, 2018). Local enrichment of the ISM can also occur on small scales due to nearby star formation and SN resulting in differences in local ISM physical conditions (Kreckel et al. 2019; Groves et al. 2023).

The homogenity of a galaxy's ISM from local (i.e. between individual clouds) to galaxy-wide (i.e. enrichment along spiral arms or bars) scales depends on how efficiently metals are redistributed across the galaxy by mixing. Drivers of mixing include those applicable to isolated systems, like turbulence, and galaxy interactions and mergers. Effective drivers of gas flows and hence mixing include:

- **Radial migration of gas** - Transportation of high-metallicity material from the inner to the outer disc contributes to increasing homogeneity over large spatial scales and leads to

the flattening of the radial gradient over time (e.g., Sánchez et al. 2014; Zinchenko et al. 2021), driven by gravitational interactions with potential spiral arms and bars.

- **Large-scale galaxy structures -** Bars and spiral arms are non-symmetric around the rotation axis, leading to redistribution of angular momentum, driving gas flows and mixing azimuthally.
- **Interstellar turbulence -** Small-scale mixing driven by SN explosions, stellar winds, and cloud interactions.

Investigating how well-mixed the ISM of a galaxy provides valuable insight into the evolutionary history of the disc, such as by indicating the presence of accreted material which is not yet mixed. From the chemical abundances of a large sample of individual H II regions distributed across the galaxy disc, we can investigate the current ISM homogeneity. The two-point correlation function of metallicity, presented below, developed by Kreckel et al. (2020) and utilised by Williams et al. (2022) and Bosomworth et al. (2025), is one method that can provide insight into how well-mixed the ISM is over varying spatial scales. The two-point correlation function (Equation 1.18 is traditionally used in cosmology to provide information on the distribution of galaxies,

$$\xi_2 \left(|\mathbf{x}_1 - \mathbf{x}_2| \right) = \langle \delta \left(\mathbf{x}_1 \right) \delta \left(\mathbf{x}_2 \right) \rangle \, , \tag{1.18}$$

where $\delta \left(\mathbf{x} \right)$ is the overdensity at a particular point, and $\mathbf{x}_1 - \mathbf{x}_2$ is a scalar distance. Equation 1.19 (Kreckel et al. 2020) is used to apply this to large samples of individual sources across the disc of an individual galaxy, and quantifies the correlation between individual metallicities with increasing spatial separation:

$$\xi(r) = \left\langle \frac{\overline{S_X \left(\boldsymbol{r_1} \right) S_X \left(\boldsymbol{r_2} \right)} - \overline{S_X}^2}{\overline{\left(S_X - \overline{S_X} \right)^2}} \right\rangle , \tag{1.19}$$

where S_X is the 2-dimensional (2D) gas-phase abundance field, and $S_X \left(\boldsymbol{r} \right)$ is the abundance at a specific position. By applying this to radial-gradient-subtracted metallicity, we can investigate mixing by quantifying the ISM homogeneity over varying spatial scales. The two-point correlation functions of samples of PHANGS-MUSE spiral galaxies by Kreckel et al. (2020)

and Williams et al. (2022), using the same methodology, have enabled these to be compared for individual galaxies. We compare these to M31 in Chapters 2 and 4 of this thesis.

1.5.5 Measuring Abundances from Emission Lines

As discussed in Section 1.4.1, H II region spectra exhibit emission lines produced through collisional excitation of atoms and ions. Generally, the fluxes of these emission lines are expected to be higher for the most abundant elements, making them tracers of elemental abundances. However, emission lines strengths also depend on the nebular excitation conditions, in particular the electron density (n_e), T_e, and the ionisation parameter (U). Metals act as the primary cooling mechanisms in emission nebulae by emitting radiation. The T_e of a nebula depends on its total metallicity, since higher metallicity nebulae experience more cooling (e.g., Draine 2011).

Emission lines from atoms and ions of elements can be divided into two categories. Auroral lines require higher excitation energies and therefore are stronger in higher T_e regions. Nebular lines require lower excitation energies and thus are less sensitive to T_e and depend primarily on total metallicity. Elemental abundances of emission nebulae can be determined from the ratio of their auroral lines, including [O III]λ4363 and [N II]λ5755, to their respective nebular lines, including [O III]λ5007 and [N II]λ6584 (e.g., Pérez-Montero and Contini 2009). High-metallicity nebulae are cooled more efficiently, therefore their auroral lines are weaker (e.g., Pilyugin et al. 2009).

As they reflect the current ISM which has experienced more enrichment, H II regions typically have higher metallicities than PNe, and so their auroral lines are weaker. This makes the T_e-method difficult, especially in high metallicity, extragalactic H II regions. Therefore, stronger emission lines are often used to indirectly calculate elemental abundances and metallicities, referred to as the strong-line method. The use of nebular and Balmer line measurements to infer elemental abundances from external galaxies dates back to the 1940s (Aller 1942). Strong-line diagnostics (SLDs) can be calibrated empirically or theoretically.

Empirical diagnostics are derived from the relationship between T_e and strong emission line ratios in spectra. The ratio of nebular lines to Balmer lines (Hα, Hβ) depends on metallicity (Alloin et al. 1979), with nebular lines expected to be stronger at higher metallicity. Therefore, these ratios are often used to calibrate SLDs (e.g., Pilyugin and Thuan 2005, 2010, 2016). The theoretical approach uses photoionisation models (see Section 1.4.2) to simulate emission lines

from H II regions of different metallicities (e.g. Kewley and Dopita 2002; Pérez-Montero et al. 2010; Morisset et al. 2016), including high metallicities when auroral lines cannot be detected.

A widely used ratio for empirical and theoretical SLDs is R_{23}, defined as

$$R_{23} = \frac{[\text{O II}]\ \lambda 3727 + [\text{O III}]\ \lambda\lambda 4959, 5007}{\text{H}\beta},$$

which estimates the total cooling due to O and is therefore linked to O abundance (Pagel et al. 1979; Zaritsky et al. 1994; Pilyugin 2001). However, there is a degeneracy between the "upper" and "lower" metallicity branches for R_{23}, making it double-valued with metallicity. At low metallicities, the intensity of the line scales approximately with O abundance, whereas at high metallicities, nebula cooling is dominated by the infrared fine-structure lines. Here, T_e is too low to produce collisionally excited optical emission lines, thus R_{23} decreases with metallicity.

SLDs of low dimensionality, such as those calibrated on the R_{23} ratio only, have been shown to depend strongly on U leading to scatter in metallicity measurements (Pilyugin 2001; Kewley and Dopita 2002). Since O^+ and N^+ have similar ionisation potentials, diagnostics using both [O II] and [N II] are expected to be significantly less dependent on U. In particular, the 3D O abundance diagnostics of Pilyugin and Grebel (2016) have discrepancies from T_e-based abundances of ≈ 0.1 dex (Ho 2019) and depend on [O III], [N II] and [O II] or [S II] and therefore have little dependence on U.

The choice of SLD must be considered carefully. In addition to their sensitivity to U, SLDs can be The depend on the ratio of the local ionising photon flux to n_H (e.g., Dopita et al. 2000; Kewley et al. 2019). Metallicities for the same H II regions estimated from different SLDs can have discrepancies up to ≈ 0.6 dex (Kewley and Ellison 2008). Empirical SLDs generally agree better with direct metallicities based on T_e than theoretical SLDS, but T_e fluctuations within H II regions can cause the true metallicity to be underestimated by the T_e-method and empirical SLDs (Garnett 1992; Stasińska 2005).

When comparing metallicities of H II regions using a consistent diagnostic, the relative scatter can be reduced to ≈ 0.07 dex (Kewley and Ellison 2008). Nevertheless, the absolute calibration of the diagnostic depends on the reference T_e measurements. If the metallicity range used to calibrate the SLD is not well-matched to the sample, the absolute values of O/H derived may be systematically offset from the true metallicity. When comparing Pilyugin and Grebel (2016)-derived O abundances of individual M31 H II regions, Bosomworth et al. (2025) found

uncertainties of 0.01 - 0.02 dex (see also Chapters 2 and 4 with more information on observations in Section 1.6.1). This highlights the efficiency of the Pilyugin and Grebel (2016) SLDs at investigating O abundance variations within M31 H II regions.

1.5.6 Effect of Metallicity on CO Conversion Factors

Now that we have introduced the concept of metallicity in detail, we revisit the relationship between CO conversion factors and metallicity introduced in Section 1.1.5. At high metallicities, more C and O is available to form CO (Maloney and Black 1988; Israel 1997) so $L_{\rm CO}$ and $M_{\rm CO}$ should be higher. As 30-50% of metals are predicted to deplete into dust grains (Savage and Sembach 1996; Draine et al. 2007), $M_{\rm dust}$ should also increase with metallicity. Dust shields H_2 and CO molecules from being destroyed by UV radiation, also suggesting $L_{\rm CO}$ and $M_{\rm mol}$ should increase with metallicity and $M_{\rm dust}$.

Based on Equation 1.7, $\alpha_{\rm CO}$ will be lower with increasing metallicity if $L_{\rm CO}$ increases more significantly than $M_{\rm mol}$. On the other hand, if $M_{\rm mol}$ increases faster, $\alpha_{\rm CO}$ will increase with metallicity. Measurements of $\alpha_{\rm CO}$ and $X_{\rm CO}$ from $M_{\rm dust}$ require an assumption for $R_{\rm g/d}$, with the MW value ($R_{\rm g/d}\approx$136) often being used. However, $R_{\rm g/d}$ may vary with metallicity (e.g., Israel 1997; Sandstrom et al. 2013). This suggests that $\alpha_{\rm CO}$ decreases with metallicity only if $\alpha'_{\rm CO}$ (equation 1.8) is constant, decreasing, or increasing less significantly than $R_{\rm g/d}$ is decreasing as a function of metallicity.

The gas fundamental metallicity relation (gas-FMR) states that for fixed M_*, O/H is inversely related to $M_{\rm mol}$ (Bothwell et al. 2013) for secularly evolving, star-forming galaxies. Thus, the gas-FMR predicts decreasing $\alpha_{\rm CO}$ with metallicity, but the effects of $M_{\rm dust}$ and $R_{\rm g/d}$ are not considered. This leads to assuming a linear correction to $\alpha_{\rm CO}$ with GCR based on the radial metallicity gradient (see Section 1.5.2). As $\alpha'_{\rm CO}$ depends only on $M_{\rm dust}$ and $L_{\rm CO}$, its dependence on metallicity can be inferred directly from observations of dust and CO from GMCs, and the metallicities of associated H II regions. Initial results of this test for M31 have implied a constant $\alpha'_{\rm CO}$ with metallicities of 8.45 $\lesssim$ O/H $\lesssim$ 8.65, so a linear correction to $\alpha'_{\rm CO}$ with GCR would be incorrect for this galaxy (Bosomworth et al. 2025).

1.6 Observational Techniques

The work presented in this thesis provides a multi-wavelength perspective of cloud-scale star formation, enabling us to probe the wide range of topics covered in this introduction section so far, all within M31. The observational techniques utilised are optical spectroscopy for Chapters 2 and 4 and mm observations for Chapter 3. In this subsection, we will cover the observational methods used to produce the results presented in this thesis.

1.6.1 Optical Spectroscopy

The optical spectra used to classify H II regions and calculate chemical abundances in Chapters 2 and 4 were obtained using the MMT 6.5-m diameter telescope, a joint operation of the Smithsonian Institution and the University of Arizona. The MMT observatory (MMTO) is located on the summit of Mt. Hopkins, Arizona at 2616-m elevation which reduces atmospheric effects. The original MMT telescope was comissioned in 1979 and had an effective apeture of 4.5-m from six 1.8-m primary mirrors. In 1998 – 2000, the telescope underwent a major upgrade, replacing the six primary mirrors with the current 6.5-m primary mirror (Williams et al. 2016). This doubled the telescope sensitivity and increased its angular field of view (FOV) to 1 deg. Figure 1.14 shows an image of the MMT observatory, highlighting its cubic shape which accommodates its altitude-azimuth (alt-az) mount[1].

Optical telescopes such as the MMT are often Cassegrain telescopes. Figure 1.15 shows a schematic diagram of a Cassegrain telescope. As shown by the direction of the arrows, light enters the telescope and is first reflected by a concave primary mirror. It is then reflected again by a convex secondary mirror, back to the plane of the primary mirror where it exits through a hole. To reduce the optical effects of temperature variations, the MMT primary mirror is made from borosilicate glass, which has a coefficient of thermal expansion that is a factor of three lower than that of normal glass. Its thin reflective surface is made of Al. The MMT primary mirror is considered a very "fast" mirror with a short focal ratio of f/1.25, meaning its focal length is 1.25 times the mirror diameter. This results in a compact design with a wide FOV, as well as faster imaging (Fabricant et al. 2005). This makes the MMT an excellent telescope for wide-field, multi-object surveys. The secondary mirror is interchangeable meaning a range of cameras and spectrographs can be used. The desired instrument is placed at the focal plane.

[1] https://www.mmto.org/

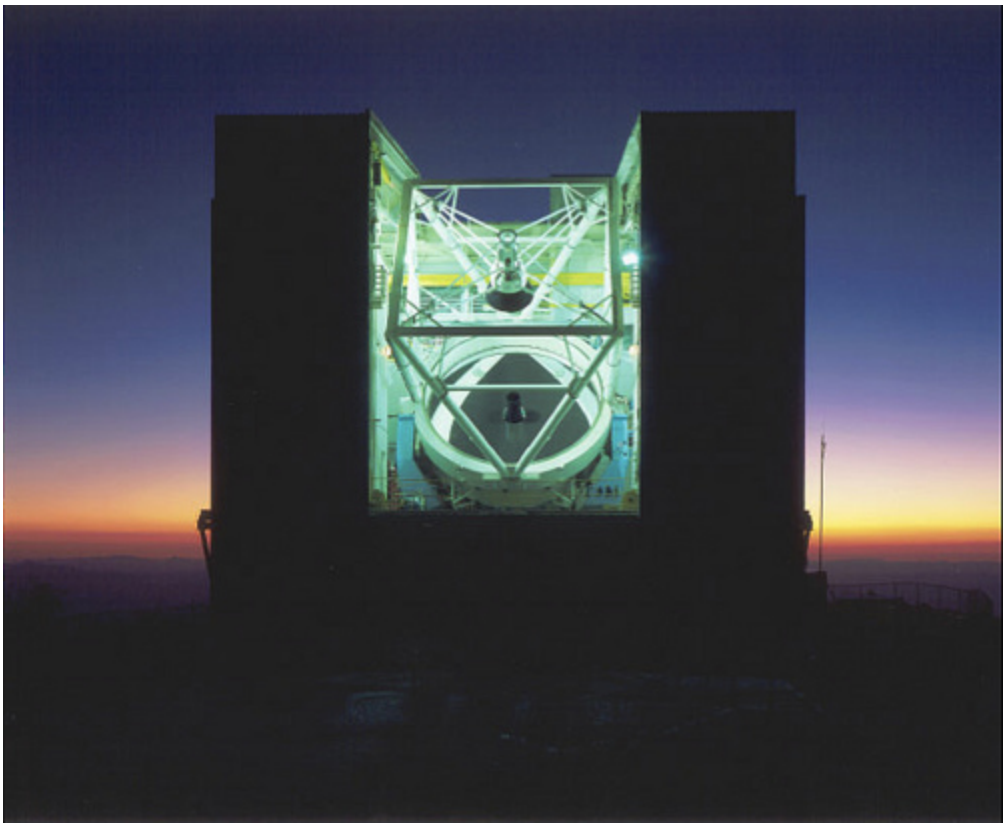

FIGURE 1.14: MMTO on the summit of Mt Hopkins; shutters on the front and top of the telescope are open to enable observations. Photo by Howard Lester.

The MMT survey presented in this thesis utilised the Hectospec spectrograph (Fabricant et al. 2005). Spectrographs measure light intensity at varying wavelengths and produce a spectrum. Hectospec is fed by 300 optical fibres, which can be used to observe 300 positions simultaneously, making it ideal for multi-object spectroscopy. Each 300-fibre observation includes all necessary exposures required for data reduction. Along with science exposures we obtained biases, dome and twilight flats, and comparison lamp exposures. The 270-groove mm^{-1} grating used yields a spectral resolution of 6.2 Å, spans the wavelength range of approximately 3500 to 10 000 Å. Within this range we obtained emission lines necessary to measure A_V and O/H and N/H from SLDs (see Sections 1.1.4 and 1.5.5). Figure 1.16 shows a top view of the fibre positioner.

The Hectospec reduction pipeline (Hsred v2.0) was used to reduce our spectra. From the set of relevant exposures (science exposures, biases, dome and twilight flats, comparison lamp exposures), the key reduction steps performed by Hsred are as follows (Fabricant et al. 2005):

- **Bias and Flat-field Correction -** Bias frames and twilight sky flats are applied to remove instrumental signatures and pixel-to-pixel sensitivity variations.

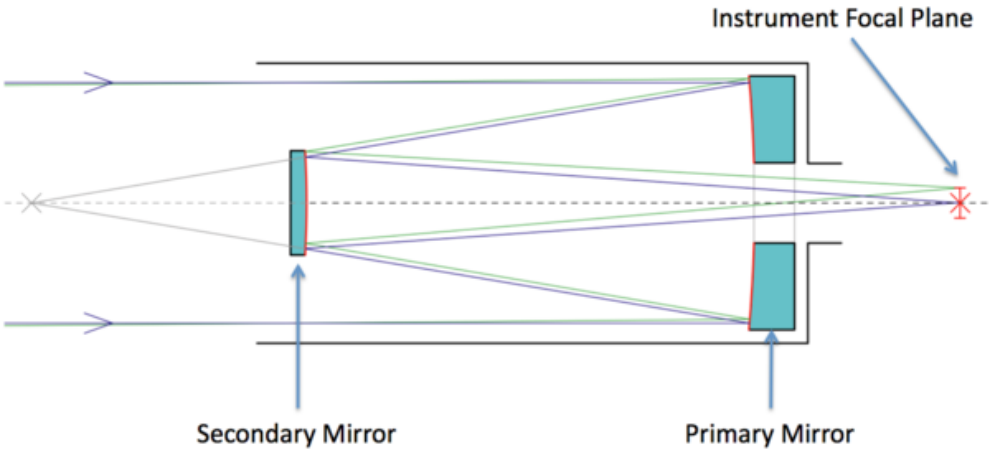

FIGURE 1.15: Schematic of a typical Cassegrain telescope. Arrows show the direction of light which enters the telescope from the left. Light is then reflected by the primary and secondary mirrors and finally exits through the hole in the primary mirror. Credit: MMTO[1]

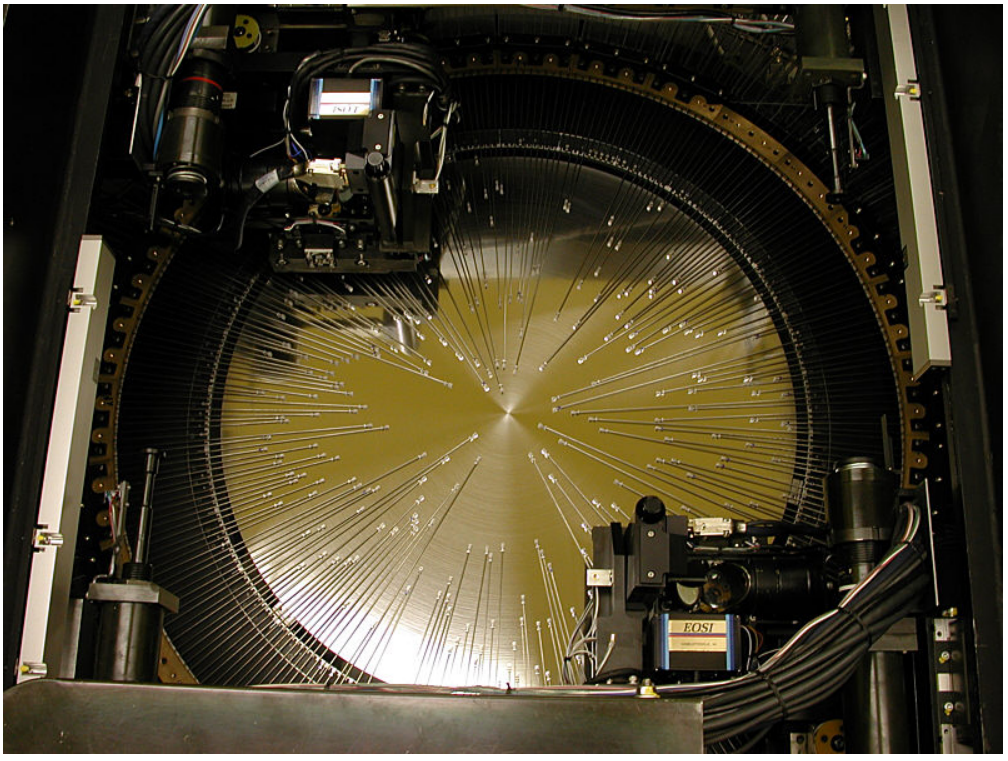

FIGURE 1.16: Top view of Hectospec's fibre positioner. Credit: Fabricant et al. (2005).

- **Wavelength Calibration -** Comparison lamp exposures with emission lines of known wavelengths are used to linearise the wavelength scale of the science spectra.
- **Sky Subtraction -** Offset sky exposures are subtracted to remove contamination from the Earth's atmosphere.

- **Combining Multiple Exposures -** Multiple observations of identical positions taken on the same night are combined to improve S/N.

Observations also need to be flux calibrated, which can be implemented in Hsred. However, due to the lack of known flux-calibration sources in our field of view, this was done manually using a standard star spectrum as described in Chapter 2. We also correct our spectra for visual extinction (see Section 1.1.4) in Chapter 2 by applying a reddening correction, assuming $H_\alpha/H\beta = 2.86$ and Case B recombination. The observed $H\alpha/H\beta$ ratio for each spectrum captures the total extinction along the line of sight, which includes both foreground MW extinction and internal extinction in M31. Since the foreground MW extinction is small ($E_{B-V} \approx 0.062$; Schlegel et al. 1998), the extinction correction primarily accounts for internal extinction within M31.

1.6.2 Submillimetre Interferometry

Interferometers combine the signals of multiple antennas to form interference patterns and can achieve higher spatial resolutions than single-dish telescopes. For a single-dish telescope, higher resolution can be achieved by increasing the size of the telescope's primary mirror. However, even the largest mirrors cannot match the resolution achieved by interferometers. Angular resolution, θ, is determined by equation 1.20,

$$\theta \approx \frac{\lambda}{D} \tag{1.20}$$

where D is the telescope's diameter (e.g., Monnier and Allen 2013). This means that interferometry is especially valuable at radio wavelengths. The longer wavelengths of radio observations compared to optical by a factor of ≈1000 result in the resolution of a radio telescope being ≈1000 times worse than that of an optical telescope of the same diameter. The effective diameter of an interferometer is determined by the baselines, B (the separations between the individual antennas), which can be made much larger than an individual telescope dish. The angular resolution of an interferometer is determined by equation 1.20, where B replaces D.

The long baselines in interferometry mean that higher resolutions can be achieved than are possible with a single dish. Longer baselines are sensitive to smaller angular scales, making interferometry ideal for resolving finer structures than possible with a single dish telescope, whilst spatial filtering removes extended structures from images. This is a result of the Fourier

transform relationship between the interference pattern and sky brightness distribution. The interference pattern produced is based on the relative arrival times of light to pairs of antennas, and produces a Fourier transform of the brightness distribution known as the complex visibilities $V(u, v)$, where (u, v) gives the projected separation of the antennas to the north and west (e.g., Lindroos et al. 2015). In a cross-correlation interferometer such as the SMA, each pair of antennas measures the phase and amplitude of a Fourier component, which are combined to construct the image (Keto 1997).

At radio, mm and sub-mm wavelengths, interferometers are strongly affected by atmospheric emission, receiver noise and the limited collecting area per antenna, all of which can significantly limit the achievable sensitivity (e.g., Thompson et al. 2017). Very long baseline interferometry (VLBI) demonstrates the trade-off between resolution and sensitivity in interferometry. By combining antennas separated by hundreds to thousands of km, VLBI can achieve angular resolutions down to microarcseconds (e.g., the Event Horizon Telescope; EHT; Event Horizon Telescope Collaboration et al. 2019). However, widely separated antennae cannot recover emission on large angular scales. Whilst longer baselines yield higher resolution, sensitivity is maximised by increasing collecting area with shorter baselines.

The millimetre and sub-mm wavelengths span 0.3 mm to a few millimetres, probing the cold ISM. Since mm wavelengths are affected by atmospheric absorption from water vapour in the Earth's atmosphere, telescopes are usually located at high altitudes or are space-based. For the work presented in Chapter 3, mm observations were obtained with the SMA located on Maunakea, Hawaii, at an elevation of 4090-m. The SMA consists of eight 6-m antennas operating in the frequency range 180 GHz to 420 GHz. This range probes the thermal dust continuum and rotational transitions of molecules such as CO(1-0) and CO(2-1). The eight SMA antennas are shown in Figure 1.17. The dishes may be arranged into different configurations, from sub-compact to extended, to achieve the desired resolution and sky coverage.

1.7 Thesis Motivation and Structure

In summary, the overall aim of this thesis project is to "zoom-in" on star formation, using both optical spectroscopy and millimetre interferometry, which together form a direct test of the metallicity dependence of $\alpha'_{\rm CO}$. We take advantage of our nearest large spiral galaxy neighbour,

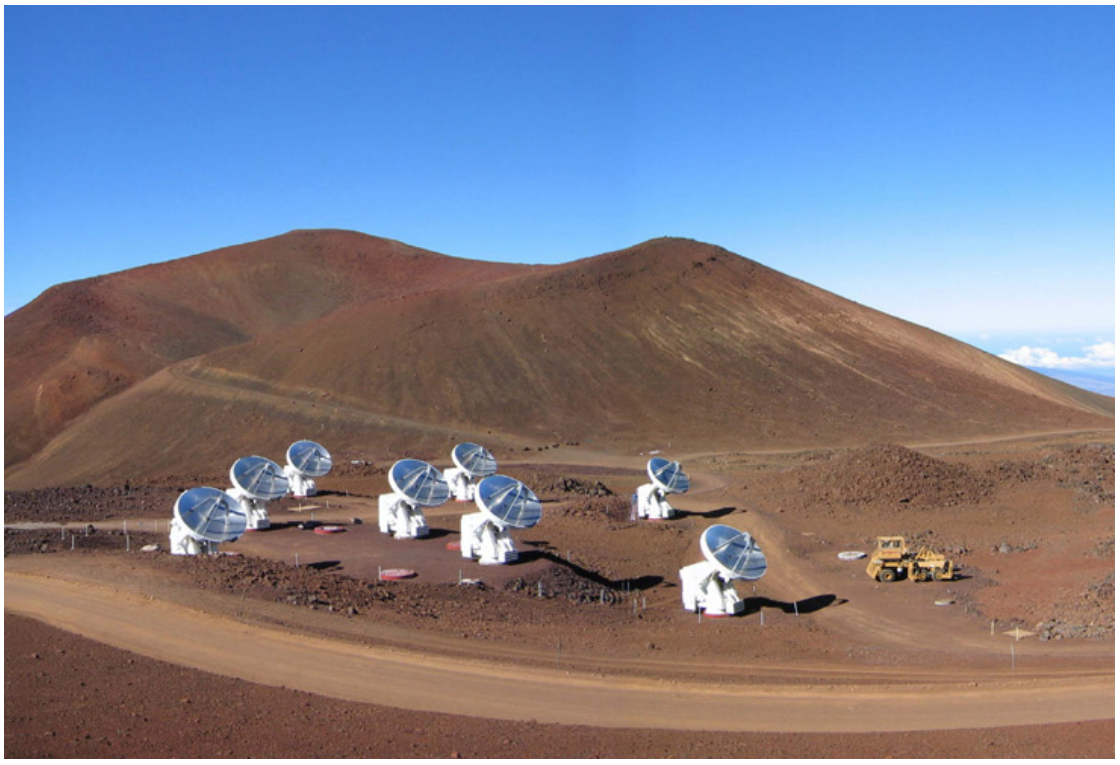

FIGURE 1.17: The eight 6m antennas of the SMA, acting together as a single telescope. Photo by Jonathan Weintroub.

M31, and the observational capabilities of the SMA and MMT. The science results of this thesis are presented in the following three chapters, as summarised here.

Chapter 2 investigates elemental abundance variations in H II regions across the disc of M31. This chapter is based on Bosomworth et al. (2025), published in MNRAS. We utilised strong line diagnostics to calculate both 12 + log(O/H) and 12 + log(N/H) of individual H II regions from MMT/Hectospec optical spectra. Observational details and the method to classify sources as H II regions or otherwise are discussed briefly. Results include the first direct test of the metallicity dependence of $\alpha'_{\rm CO}$, with values corresponding to M31 GMCs reported by Viaene et al. (2021).

In Chapter 3, we present results from the full sample of SMA dust emission detections associated with M31 GMCs, expanding on the results from the first two observing runs published by Forbrich et al. (2020) and Viaene et al. (2021). We outline the updated method of using velocity-integrated line emission to measure $L_{\rm CO}$ and to refine the final dust core sample used to calculate $\alpha'_{\rm CO}$. We extend the virial analysis of GMCs and ^{13}CO clumps presented in Lada et al. (2024) to our sample of dust cores. We also update the test of the metallicity dependence of $\alpha'_{\rm CO}$ with an increased sample size. This chapter is also in preparation as stand-alone journal article.

Chapter 4 revisits optical spectroscopy of H II regions to analyse log(N/O) variations across the disc of M31 from the same sample as Chapter 2. This chapter is also in preparation as a stand-alone journal article which is a follow-up to Bosomworth et al. (2025). Finally, in Chapter 5 we summarise the key results of this thesis, and in Chapter 6 we report the planned follow-up to this research.

Chapter 2

Cloud-scale Elemental Abundance Variations and the CO-to-dust Mass Conversion Factor in M31

2.1 Introduction

H II regions are clouds of gas that have been photoionised by nearby massive stars, the OB stars, often located near the edges of GMCs. OB stars have short lifetimes of $\lesssim$ 10 Myr, therefore, the elemental abundances of H II regions can be used to trace recent star formation and thus the latest stages of a galaxy's chemical evolution. Elemental abundance ratios such as O and N to hydrogen (H) i.e. O/H and N/H[1] (e.g., Pilyugin et al. 2010; Sánchez-Menguiano. et al. 2016), as well as N/O[2] (e.g., Belfiore et al. 2017), when traced across an entire galaxy, can be used to investigate its star formation history. Both star formation and the chemical history of galaxies are critical to our understanding of galaxy formation and evolution (Henry and Worthey 1999).

Stars form from the ISM, and nucleosynthesis gives rise to an increasing abundance of heavier elements (e.g., O and N) which are returned to the ISM upon the deaths of the stars and through stellar winds during the stellar evolution process. In disc galaxies, the resulting trend

[1] $12 + \log(\mathrm{O/H})$ and $12 + \log(\mathrm{N/H})$
[2] $\log(\mathrm{N/O})$

is predominantly a linear, radial decline in H II region metallicity because of the higher star-formation rates in the inner galaxy (Tinsley 1980). Accretion of external low-metallicity gas dilutes these products of nucleosynthesis and thus also affects the composition of the ISM.

Early on, measurements of gas-phase metallicity gradients helped build analytic models of the chemical evolution for galaxies (Matteucci et al. 1989). These gradients have also been compared with chemodynamical simulations of galaxies (e.g., Vincenzo and Kobayashi 2020). This topic has recently been summarised in the review papers by Kewley et al. (2019) and Maiolino and Mannucci (2019). Once this radial gradient is removed from the data and only residual metallicity, Δ(O/H), differences remain, the presence of higher-order differences within the ISM can be explored (e.g., Ho et al. 2017; 2018; Kreckel et al. 2019; Williams et al. 2022).

More recently, the focus has shifted from galactic-scale trends to local variations driven by mixing of the ISM. For example, Kreckel et al. (2020) identified a high level of chemical homogeneity over large (kpc) spatial scales, demonstrating that efficient mixing within the ISM on these scales is a common feature in their sample of spiral galaxies. On smaller scales, local enrichment of the ISM can occur due to nearby star formation (e.g. Ho et al. 2017; Groves et al. 2023). N-body/hydrodynamical simulations of disc galaxies by Khoperskov et al. (2023) involving multiple spiral arms, a radial metallicity gradient and local enhancement in the presence of radial migration of gas, predict azimuthal scatter in gas-phase metallicity at a given galactocentric radius of up to ≈ 0.05 dex associated with the spiral structure.

O and N abundances are used as proxies to trace gas-phase chemical abundances of H II regions throughout galaxies (e.g., Pilyugin et al. 2010; 2016). O, produced by massive stars, has a high relative abundance and therefore produces strong optical emission lines, making it the easiest proxy to measure. In stellar nucleosynthesis, N is produced from the CNO cycle. In the primary process, the seed C is produced in the same production, site e.g., massive (4–8 $M_{\odot}$) AGB and rotating stars (see footnote 4 in Kobayashi et al. 2023). In Galactic chemical evolution models (Kobayashi et al. 2020 and references therein), N enrichment from AGB stars appears at higher metallicities of the ISM than that from massive stars ($\approx$ 10 – 90 $M_{\odot}$) due to their lifetimes being longer (the N enrichment is not secondary but just delayed), In the secondary process, N is produced from the CNO already present in the progenitor star, and thus the N yield depends on the metallicity of the star (Clayton 1983; Arnett and Chevalier 1996). The secondary N increases also for metal-rich SNe, which also appear at high metallicities of the ISM. Because of the combination of secondary N and delayed primary N from AGB stars, the N/O ratio is roughly

proportional to the initial metallicity of the star-forming gas (see Vincenzo and Kobayashi 2018). Note that, confusingly, the observed N increase at high metallicity is often called "secondary N", but is caused by both the primary process in AGB stars and the secondary process in massive stars.

Observational studies show that there is a gradual, curved transition between primary and secondary N production in an N/O − O/H diagram (e.g., Lequeux et al. 1979; Izotov and Thuan 1999; Nicholls et al. 2017). The recent Simba-C model (Hough et al. 2023) reproduces the concentration of low-N/O values which have been observed in MaNGA (Mapping Nearby Galaxies at Apache Point Observatory) galaxies (Belfiore et al. 2017) for the same stellar mass range. However, although SIMBA-C shows a rise in N/O with increasing O/H, it does not reproduce the steepening at high-metallicities as shown in the trend derived from observational studies by Nicholls et al. (2017). Vincenzo and Kobayashi (2018) report that their simulation is able to reproduce the trend in N/O − O/H at high metallicities if they include failed SNe.

M31 is our most nearby large spiral galaxy ($\approx$ 780 pc; Stanek and Garnavich 1998). It has a prominent, star-forming ring at a galactocentric radius of approximately 10 kpc, seen in infrared (e.g., Habing et al. 1984; Gordon et al. 2006) and Hα (e.g., Arp 1964; Devereux et al. 1994) images. The star-forming ring, known as the RoF, has been shown to split near the position of M32 (Gordon et al. 2006), displaying a second, fainter ring at $\approx$ 14 kpc galactocentric radius (Haas et al. 1998). In this chapter, we report sub-cloud–scale ($\approx$ 5 pc) metallicity measurements toward individual H II regions in M31. We then perform further analysis with a focus on metallicity differences as a function of spatial separation between H II regions. Using MMT/Hectospec (Fabricant et al. 2005), we conduct a multi-object spectroscopic survey of hundreds of candidate H II regions in M31. We use line ratio measurements to both classify sources as H II regions (distinguishing them from planetary nebulae) and calculate their metallicities with strong line diagnostics. A range of metallicities and complex trends have been found in the past for some of the same sources by Sanders et al. (2012, hereafter S12).

The most relevant work to this study, given the identical instrumentation used, is the optical spectroscopic survey of M31 conducted by S12. Also using Hectospec data, they identified PNe and H II regions in M31 and calculated O and N abundances for these sources from emission line ratios. For PNe, the temperature-sensitive auroral line [O III] λ4363 was used to calculate direct O abundances. In H II regions, this line is too weak to be detected, and so various strong-line diagnostics were used. These are indirect methods of measuring chemical abundances derived

from the relations between ratios of strong emission lines and directly measured metallicities from observations (e.g., Zaritsky et al. 1994; Pilyugin et al. 2010; Marino et al. 2013) or photoionisation models (e.g., Kewley and Dopita 2002) or even a combined calibration approach (e.g., Pettini and Pagel 2004). S12 utilised five different O abundance diagnostics and metallicities were calculated for sample sizes of 48 - 192 H II regions depending the on frequencies of line detections. Radial abundance gradients calculated by S12 are in agreement with previous works using the same methods but also depend on the strong-line diagnostic used. For all diagnostics used, S12 found significant intrinsic scatter. Using their preferred strong-line method for H II regions (O3N2 from Nagao et al. 2006), they found that 33% of neighboring (within 0.5 kpc) pairs of H II regions vary by > 0.3 dex.

PNe observations can also be used to trace galaxy formation and chemical evolution, and this has been done previously for M31 (e.g., S12; Bhattacharya et al. 2022; Arnaboldi et al. 2022; Kobayashi et al. 2023). Compared to H II regions which reflect recent star formation, PNe abundances reflect the older ISM as they are ionised by red-giant stars at the end of their lifetimes. Temperature-sensitive auroral lines such as [O II]λ4363, [O II]λ7325 and [SIII]λ6312 are typically stronger in PNe than in H II regions and thus are detected more often. From the ratios of strong lines in the spectra to the corresponding auroral lines, the electron temperature (T_e) can be measured. This allows for PNe metallicities to be calculated by "direct" methods (e.g., Peimbert 1967; Osterbrock 1989; Bresolin et al. 2010; Bhattacharya et al. 2022). Direct abundance measurements require both the [O III]λ4363 and [O II]$\lambda\lambda$7320, 7330 auroral line doublet for the calculation of T_e. However, T_e-studies often lack temperature information for the O^+ zone because of the lack of [O II]$\lambda\lambda$7320, 7330 detection, which then is inferred from a close proxy temperature such as T_e(N II) or an empirical relation linking T_e(O III) to T_e(O II). Therefore, these T_e-based metallicities are rendered "semi-direct".

By calculating direct oxygen and argon abundances for > 200 PNe, Bhattacharya et al. (2022) compared the abundance gradients of PNe in the thin and thick discs of M31 and provided evidence that these are chemically distinct. For the thin disc, a significant negative O abundance gradient was found of similar magnitude to those found for M31 H II regions. In comparison, the thicker disc was found to have a slightly positive radial abundance gradient. One explanation offered was that the thin disc formed following a wet-merger event (a major merger of mass ratio 1:5 occurring $\approx 2.5 - 4.5$ Gyr ago; Bhattacharya et al. 2019); a collision between two gas-rich galaxies, where metal-poor gas was brought in by the satellite galaxy during the merger, causing

a burst of star formation. Simultaneously, the thicker disc was "radially homogenized" due to this wet-merger event (Bhattacharya et al. 2022).

The SFR of a galaxy depends on the mass of molecular gas ($M_{\rm mol}$) available in the ISM, and thus the mass of GMCs is crucial to investigating galaxy evolution. From the mass-metallicity relation (MZR; Lequeux et al. 1979), we know that gas-phase oxygen abundance increases with a galaxy's total stellar mass M_*. Mannucci et al. (2010) studied the relationship between O/H, M_* and SFR, which defines the FMR. Scaling relations have also been found to display secondary dependencies at (redshift) z = 0; the most relevant for this study is the gas-FMR (Bothwell et al. 2016) where at a fixed M_*, O/H is inversely related to $M_{\rm mol}$. By studying $M_{\rm mol}$ and metallicities of the same GMCs, we can begin to investigate these scaling relations.

The primary constituent of GMCs, H_2, is not observable in emission in M31 and therefore $M_{\rm mol}$ is often measured indirectly using the second most abundant emitter, CO. To convert this to $M_{\rm mol}$, the conversion factor between CO luminosity and $M_{\rm mol}$ ($\alpha_{\rm CO}$) is required. $\alpha_{\rm CO}$ is predicted to depend on metallicity; UV radiation destroys molecules depending on the amount of extinction. UV photons destroy both H_2 and CO molecules, however, H_2 can self-shield much more effectively (e.g., Draine and Bertoldi 1996; Lee et al. 1996). Thus, the CO-to-H_2 ratio is predicted to decrease at lower metallicities where UV can penetrate deeper into the clouds (e.g., Pelupessy and Papadopoulos 2009, Shetty et al. 2011). However, to calculate $\alpha_{\rm CO}$ from $M_{\rm dust}$, we must assume a value for the gas-to-dust ratio. To avoid this, Forbrich et al. (2020) derived the conversion factor for CO luminosity to dust mass ($M_{\rm dust}$), $\alpha'_{^{12}\rm CO}$, which does not depend on this assumption and can be measured more directly. Viaene et al. (2021) report $\alpha'_{\rm CO}$ for ^{12}CO and ^{13}CO towards 20 GMCs in M31, some of which we obtained metallicities for associated H II regions, allowing us to directly investigate the dependence of $\alpha'_{\rm CO}$ on metallicity.

This chapter is structured as follows. In Section 2.2 we describe our observations and how these were reduced. In Section 2.3 we discuss our methodology including emission line flux measurements, extinction correction, source classification and metallicity/abundance measurements. Our results, including radial metallicity gradients and two-point correlation functions of metallicity, are presented in Section 2.4. We present our summary in Section 2.5.

2.2 Observations and Data Reduction

2.2.1 Source Selection

Our targets were primarily selected from a catalog of candidate H II regions, Azimlu et al. (2011), many of which are associated with one of the 326 known GMAs in M31 from Kirk et al. (2015). Some additional sources from a Very Large Array (VLA) survey (Toomey et al. in prep.) were also observed. GMAs for which we have α_{CO} measurements from SMA data (Viaene et al. 2021; Forbrich et al. 2020) were of the highest priority for observation so that the effect of metallicity on GMC properties can be investigated. Selecting our targets in this way also increases the probability that we observe H II regions with measurable emission lines.

2.2.2 Observations

Observations were performed using the Hectospec spectrometer (Fabricant et al. 2005) at the MMT telescope located in Arizona, USA, using the 270 gpm (groove per millimetre) grating covering the wavelength range $\approx$3700 – 9150Å with a 6.2 Å resolution. Within this wavelength range we have access to multiple strong emission lines: Hα, Hβ, [O II]λ3727, [O III]$\lambda\lambda(4959, 5007)$, [N II]$\lambda\lambda(6548, 6584)$ and [S II]$\lambda\lambda(6717, 6731)$. Observations were taken during two separate observing runs; the first in October 2020 and the second in November and December of 2021. Hectospec has 300 fibres with an on-sky fibre radius of 1.5" (corresponding to $\approx$ 5 pc at the distance of M31), and the entire field-of-view is $\approx$ 1 deg in diameter. This was ideal for our purposes as we aimed to obtain a large sample of H II regions. For each pointing, these fibres are allocated as follows: on-sky fibres for sky-subtraction (a total of 35 across all runs) (see section 2.2.3), 12 – 24 pointing fibres (located at the outer edge of the spectrograph), with the rest allocated to science targets.

We have high-quality spectra for 294 H II regions in M31, and $\approx$ 300 other sources including 44 PNe. The locations of the H II regions are shown in Figure 2.1 and were distinguished from PNe as described in Section 2.3.3. Our target selection process enabled us to observe the entire disc at the galactocentric radis range $\approx$ 4 – 21 kpc. Unsurprisingly, we find that the majority of H II regions in M31 lie within the inner "Ring of Fire" (RoF) at a radius of 10 kpc, or the outer RoF at a radius of 14 kpc (Haas et al. 1998; Gordon et al. 2006), where the majority of star formation

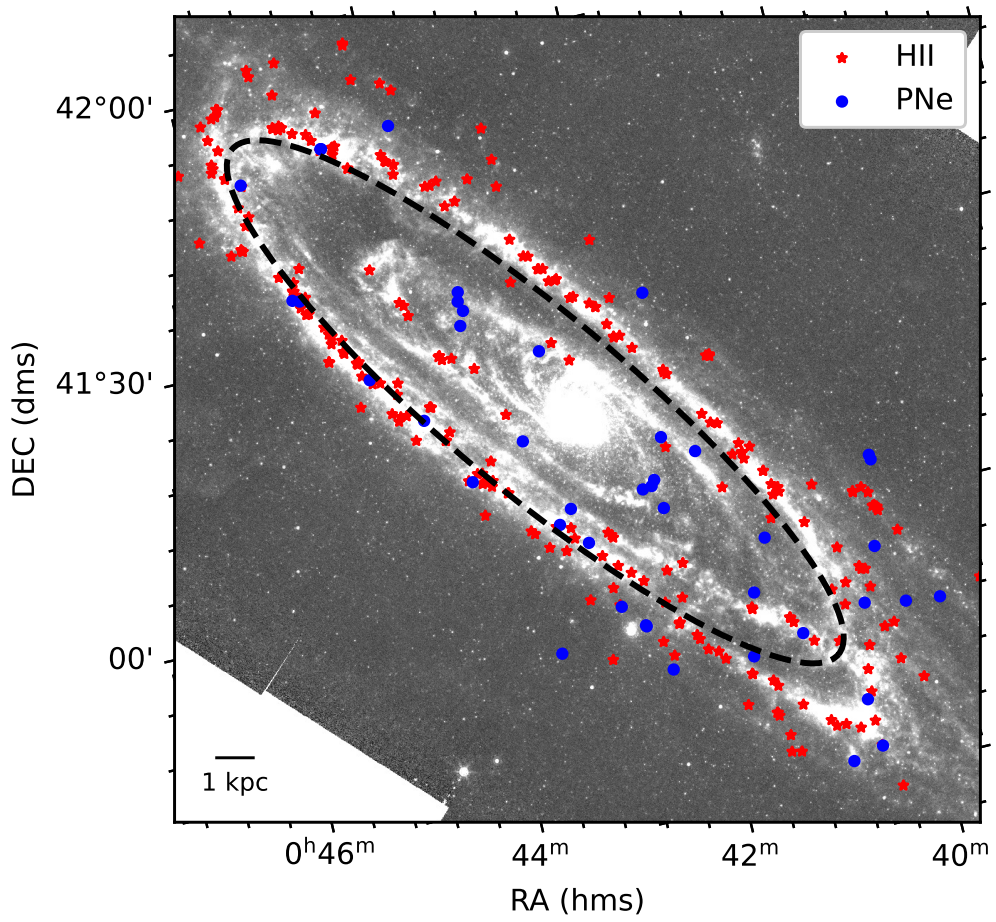

FIGURE 2.1: H II regions (red) and PNe (blue) are shown on the Spitzer MIPS 24-micron image (Gordon et al. 2006). Axes display the RA and DEC (J2000). We display the main RoF as defined by Gordon et al. (2006) as a black dashed line. The 1-kpc scalebar represents this distance on-sky at the distance of M31 (780 kpc; Stanek and Garnavich 1998). These are the targets for which we obtained high-quality Hectospec spectra and were able to classify the emission type using the emission line ratios.

occurs in M31 (Lewis et al. 2015). In Figure 2.1, we show the inner RoF as defined by Gordon et al. (2006); a circle of $\approx$ 10 kpc radius, offset from the galaxy centre by (5.5′, 3.0′).

The majority of our targets were observed multiple times, thus allowing us to confirm measurements from multiple spectra. Also, many of Kirk et al.'s GMAs have multiple associated H II regions in our source sample. As most H II regions are much larger than 5 pc (e.g., the Azimlu et al. 2011 sources have diameters up to $\approx$ 190 pc), we primarily observe portions of H II regions. Following Sanders et al. (2012), we assume that any inhomogeneities within individual H II regions are small and random and the region observed is representative of the entire H II region within given uncertainties.

2.2.3 Data Reduction

The observations were reduced using the Interactive Data Language (IDL) based Hectospec reduction pipeline 'Hsred 2.0'[3]. The steps performed are as follows: The frames were first debiased and flat fielded. Separate exposures were compared to identify and remove cosmic rays through interpolation. Individual spectra were then extracted, wavelength calibrated and combined. A number of fibres in each pointing were assigned to blank areas of sky within the focal plane: these are combined and used to perform sky subtraction on the target spectra. This sky subtraction method has already been compared to the use of different sky spectra (from areas of the sky ranging from local to distant) in S12 and only small differences were found in emission line ratios (mean difference of ≈ 0.01 dex) if different sky spectra were used for data reduction.

We applied a flux correction model to all spectra. There was a lack of known flux-calibration sources in our field of view, therefore, we use calibration information obtained from a 2019 observation of the flux standard Feige 34. This calibration is a per wavelength bin correction from 2019 with an identical wavelength axis to our spectra. A typical target airmass of 1.3 was assumed, consistent with S12. The flux calibration model is identical to that used by S12. For matching sources, we compared our emission line fluxes after flux calibration, but without extinction correction, with their Table 2. We found excellent agreement between the emission line fluxes.

Candidate Contribution

The Hectospec observations and raw data reduction with HSRED 2.0 were carried out by members of the collaboration prior to the start of this project. All subsequent stages of data preparation (applying the flux and extinction corrections) and scientific analysis were performed by the candidate.

2.3 Methodology and Data Analysis

In this section we describe our methodology. Emission line fluxes were measured with the intention of using the emission line ratios to classify sources, perform extinction correction, and calculate metallicities.

[3]https://www.mmto.org/hsred-reduction-pipeline/

2.3.1 Emission Line Fluxes

For emission line flux measurements, we utilised the Python package Specutils (Earl et al. 2024), applying a method similar to that of S12. Due to uncertainty in the flux calibration, we did not compute absolute line fluxes. Following Sanders et al. (2012) and others, we report line fluxes after renormalising the spectra to Hβ = 100, a dimensionless value representing a relative intensity scale, which is standard practice in spectroscopy when absolute flux calibration is uncertain (e.g., Liu et al. 2004; Zurita and Bresolin 2012). We extracted line profiles of width 60 Å (centred on the midpoint of the line) and subtracted a linear continuum (fit to the two 20 Å ranges on both sides of the line profile). We then fit Gaussians to the continuum-subtracted line profiles for the following lines: Hα, [O II]λ3727, [O III]$\lambda\lambda(4959, 5007)$, [N II]$\lambda\lambda(6548, 6584)$ and [S II]$\lambda\lambda(6717, 6731)$, and measured line fluxes by integrating over the Gaussian fit. See Appendix A for representative examples. We then found line fluxes compatible within the uncertainties with those of S12 for any matching source. In cases where lines are within 60 Å of one another (Hα and [N II]$\lambda\lambda(6548, 6584)$ and [S II]$\lambda\lambda(6717, 6731)$), we used a multiple Gaussian fit with one peak centred on each emission line in the range. Continuum subtraction was done still assuming a linear continuum; the corresponding extracted spectrum contains the required lines with an extension of 20 Å on both sides.

For each individual target, lines for the same transition were Doppler-shifted due to the blueshift of M31 as a whole and the rotation of the galaxy. We identified an initial velocity guess for each spectrum using the CO velocity field from Nieten et al. (2006), to identify the midpoint of each emission line. In the rare cases that no CO velocity was available within 10 pixels of the observation coordinates, the median CO velocity of the entire field, -267 km s^{-1}, was used as an initial guess. This method provided accurate enough wavelengts so that the exact line midpoints could be determined via a Gaussian fit.

The S/N of each line flux measurement was calculated based on the ratio of the flux value to the rms of the continuum-subtracted noise of 20 Å width on either side of the emission line. This flux/rms ratio was introduced only to define a S/N > 5 detection limit (chosen based on visual inspection) for lines, to ensure we are considering only emission lines that are clearly above any noise. These S/N values were not used to compute line flux uncertainties, which were measured from the standard deviation of repeat observations. Extinction-corrected emission line fluxes were used for metallicity calculation after the initial ratio of Hα/Hβ was calculated (see section 2.3.2). The extinction-corrected line flux ratios for our final sample of H II regions for which we

calculate corresponding abundances (see Section 2.3.4) are reported in Table 2.1. No correction was made for underlying stellar absorption as we estimate that this will have a very minimal effect on Balmer line fluxes. A test was already conducted on MMT spectra of H II regions in M31 by S12. Models from Starburst99 (Leitherer et al. 1999) were subtracted from underlying continua for both a low-and high-metallicity H II region. S12 found that the ratio of Hγ/Hβ changes by 1% at the most from uncorrected ratios. Additionally, they compared the Hα equivalent widths with the extinction measurements (A_V) and found no significant correlation. This indicates that Balmer absorption does not significantly affect measured line ratios for our H II region sample.

While the overall error budget for the emission line flux measurements can be difficult to ascertain, our repeat observations of the same targets provide us with the dispersion of multiple independent measurements for the majority of sources. In the cases in which we have only one observation of a source, the mean percentage uncertainty of this emission line (from sources that do have multiple corresponding spectra) is reported. We introduce a lower bound of 0.1 to uncertainties to reflect unquantifiable systematic uncertainties including uncertainties in the flux calibration, data reduction process, and continuum and Gaussian fitting to line profiles. When comparing line flux ratios from within the same spectrum, many of these systematic uncertainties cancel out. The minimum uncertainty of 0.1 represents a lower limit to the systematic uncertainty in line flux ratios (relative to Hβ = 100). We compared these to the flux uncertainties derived via error propagation from pipeline-produced sigma (per-wavelength bin uncertainty) spectra, and from those based on line S/N, and found in both cases that the latter errors are significantly smaller than those derived from averaging individual runs.

2.3.2 Extinction Correction

Interstellar extinction varies significantly with the line of sight and is dependent on wavelength. Dust attenuation affects key observable properties of star formation in galaxies, including emission line fluxes. To account for any discrepancies between the emission line fluxes of separate H II regions due to dust attenuation, we applied the optical/near-infrared (NIR) extinction curve from Cardelli et al. (1989) with $R_V = 3.1$, where R_V is the ratio of total to selective extinction (A_V/E_{B-V}). Since H II regions are primarily ionised by photons of energy > 13.6 eV which are usually not reabsorbed, case B recombination is assumed along with electron density and temperature typical of H II regions (10^4 cm^{-2} and 10^3 K, respectively). An intrinsic Balmer line ratio of Hα/Hβ = 2.86 is expected (Osterbrock and Ferland 2006). We calculated a visual

TABLE 2.1: Emission line flux ratios, (normalised to a dimensionless intensity relative to Hβ = 100) for M31 H II regions.

ID	RA, Dec. (J2000)	[O II] λ 3727	[O III] λ 4959	[O III] λ 5007	[N II] λ 6548	Hα λ 6563	[N II] λ 6584	[S II] λ 6717	[S II] λ 6731
1	0:39:13.01, 40:41:44.88	322 ± 26	26 ± 2	67 ± 5	19 ± 1	291 ± 1	68 ± 3	24 ± 1	19 ± 1
2	0:39:14.70, 40:48:33.12	460 ± 110	26 ± 4	75 ± 35	21 ± 4	290 ± 1	65 ± 5	32 ± 2	20 ± 2
3	0:39:16.50, 40:41:04.92	370 ± 7	54 ± 1	160 ± 3	19 ± 1	290 ± 0	56 ± 3	22 ± 1	16 ± 1
4	0:39:55.39, 40:55:49.18	258 ± 40	14 ± 1	43 ± 2	33 ± 1	293 ± 0	100 ± 3	27 ± 1	19 ± 1
5	0:40:00.60, 40:39:12.60	358 ± 19	11 ± 3	32 ± 4	41 ± 2	298 ± 1	125 ± 4	26 ± 4	18 ± 2
6	0:40:03.89, 40:58:27.12	360 ± 48	41 ± 3	127 ± 7	41 ± 1	285 ± 0	119 ± 4	62 ± 1	43 ± 4
7	0:40:04.01, 40:58:53.39	239 ± 2	42 ± 0	125 ± 2	19 ± 1	285 ± 0	55 ± 3	19 ± 0	13 ± 0
8	0:40:04.30, 40:58:45.84	407 ± 87	63 ± 1	184 ± 12	39 ± 3	285 ± 0	109 ± 3	49 ± 2	35 ± 1
9	0:40:05.30, 40:59:07.44	381 ± 90	56 ± 5	165 ± 11	38 ± 2	285 ± 0	101 ± 1	53 ± 1	36 ± 2
10	0:40:06.36, 40:59:04.05	185 ± 26	72 ± 2	197 ± 5	21 ± 1	285 ± 1	56 ± 3	27 ± 1	19 ± 1

The full table of 294 sources is available from Bosomworth et al.'s supplementary material; we only show a portion here for 10 sources. Uncertainties are estimated from the standard deviation of ratios obtained from repeat observations of the same source, when available (see text), with a lower bound of 0.1.

extinction (A_V) for each source following the method of Momcheva et al. (2013). Our extinction measurements were found to be consistent with those of S12 for the 20 sources we have in common. Our A_V values ranged from 0 to 4.7 with a median of 1.1. Individual A_V for our sample H II regions are reported in Table 2.2.

Figure 2.2 displays the H II region positions coloured by their corresponding extinctions. We find that the majority of A_V lie within the range $0 < A_V < 3$. The background image, the Spitzer MIPS 24-micron image (Gordon et al. 2006), highlights the dust distribution of M31. As expected the majority of dust is contained within the RoF. The lowest extinctions are mainly located in the outer galaxy, outside of the RoF, showing that our extinctions are consistent with the dust distribution within the galaxy. We note that there is also a range of A_V of $0 - 4.7$ for H II regions within the RoF.

2.3.3 Classification

Strong emission lines are a characteristic of ionised nebulae, of which H II regions and PNe are two main types. Both display the same emission lines but can be distinguished from their line ratios using a BPT diagram (Baldwin et al. 1981). The line intensity ratios of H II regions and PNe are different due to their primary excitation mechanisms; H II regions have massive OB stars at their centres, whereas PNe have much hotter low-/intermediate-mass central stars. Though these can also often be distinguished by their optical morphologies, classification from emission line ratios allows us to identify even those very compact H II regions that may be mistaken for PNe. We apply the classification of Kniazev et al. (2008) using the emission line flux ratios [O III]/Hβ (O3) and [N II]/Hα (N2). The positions of our sources on the diagram of O3 vs N2 are shown in Figure 2.3. Although we ultimately classified our sources using the Kniazev et al. (2008) classification, multiple classification dividers exist in the literature (e.g. Kewley et al. 2001; Kauffmann et al. 2003; Stasińska et al. 2008), indicating that there is an uncertainty in H II region classification when a source lies close to the defined boundary. Finally, we remove another 15 sources from our H II region sample which have previously been classified as supernova remnants (SNR) or symbiotic stars. In Figure 2.3, the typical uncertainty was calculated from the mean standard deviation of repeat observations of the N2 and O3 emission line ratios.

We note that the number of sources that we can classify from our entire dataset from the BPT diagram as shown in Figure 2.3 is larger than the number of sources for which we can calculate O

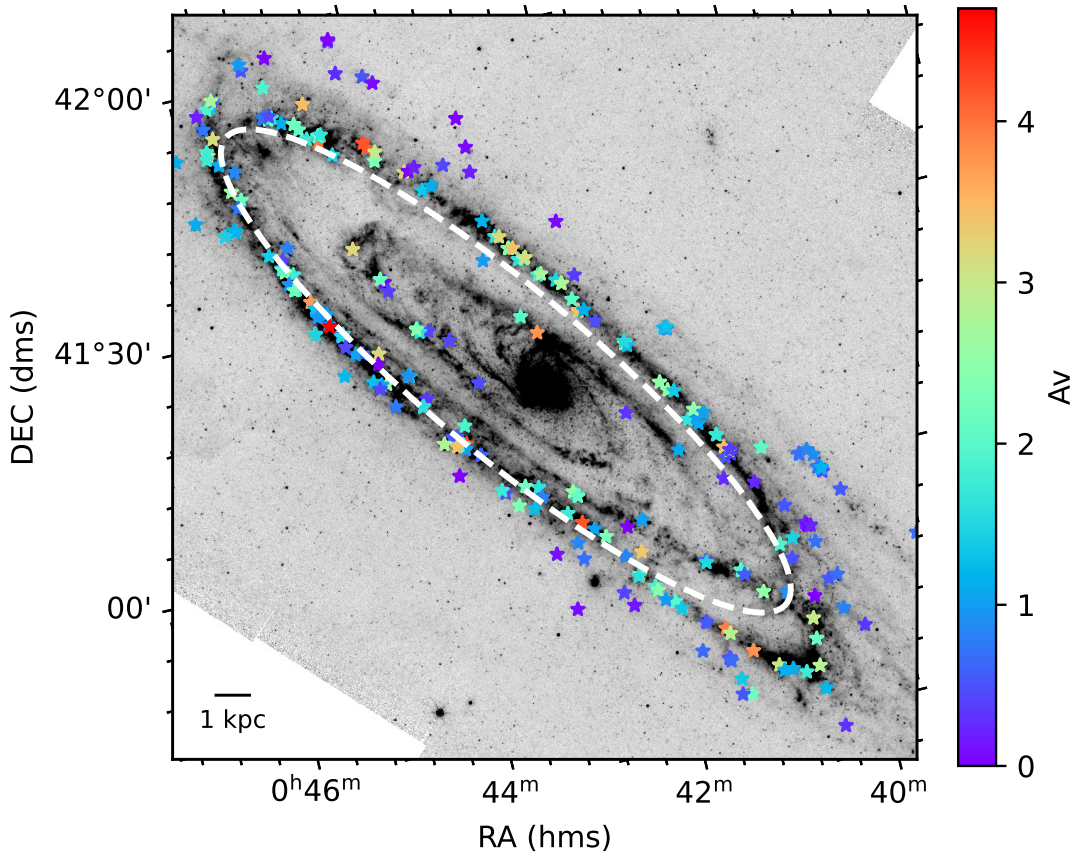

FIGURE 2.2: H II regions from our sample overplotted onto the *Spitzer* MIPS 24-micron image (Gordon et al. 2006). Symbols are colored according to A_V. As in Figure 2.1, we show the RoF fit from Gordon et al. (2006), in this case as a white dashed line. Axes display the RA and DEC (J2000). The 1 kpc scalebar represents this distance on-sky at the distance of M31 (780 kpc; Stanek and Garnavich 1998).

and N abundances (See section 2.3.4). The reason for this is that the BPT diagram requires only the lines Hα, Hβ and the stronger lines of the [O III] and [N II] doublets ([O III] λ5007 and [N II] λ6584), therefore, we only require these lines to have S/N > 5. By implementing a minimum S/N for these four lines only, we obtain 416 H II regions. In Figure 2.3 we include only those sources which have a S/N > 5 for all the lines required to calculate abundance as described in Section 2.3.4. Therefore, we include 309 H II regions (15 of which are removed from the final sample, as previously mentioned, due to being previously classified as SNR or symbiotic stars) and 44 PNe.

2.3.4 Strong-line Diagnostics

The use of strong-line diagnostics for our metallicity calculations allows us to probe a sample of H II regions covering the entire galactic disc. In comparison, we have access to the

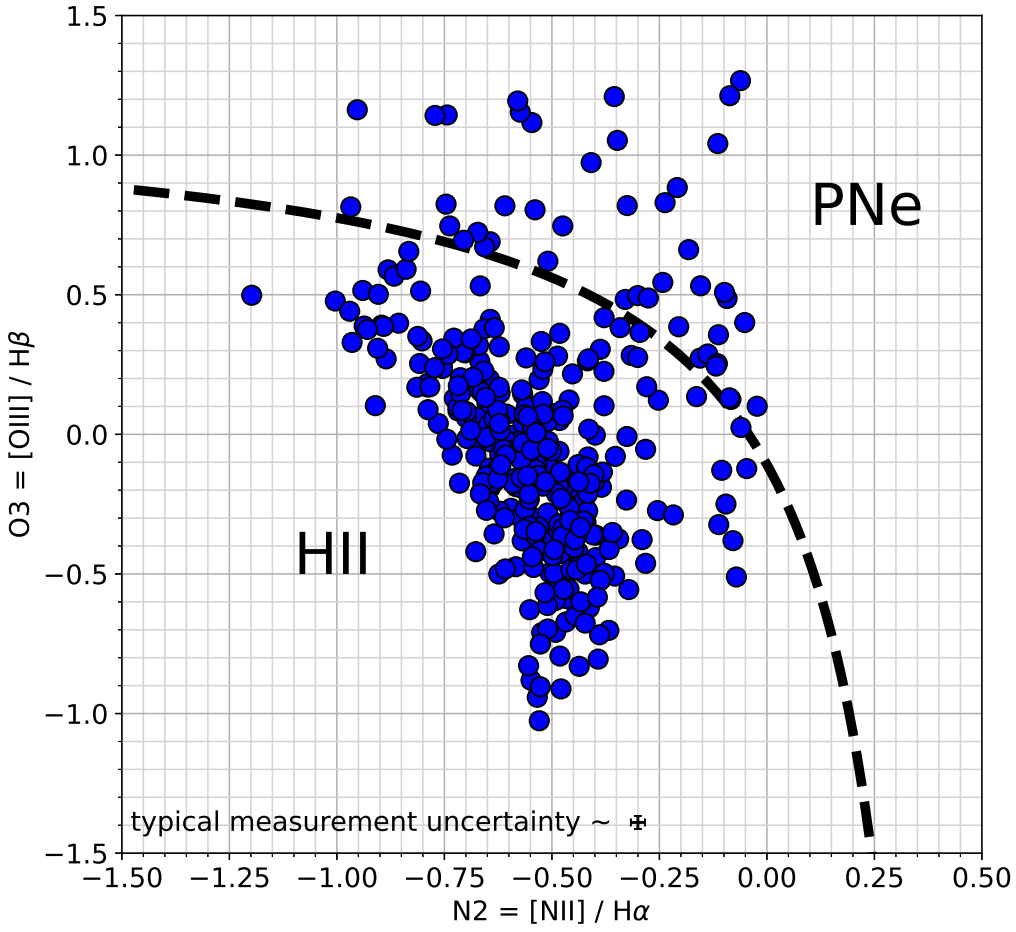

FIGURE 2.3: BPT diagram (Baldwin et al. 1981) used to distinguish H II regions and PNe from our optical spectra. The classification divider of Kniazev et al. (2008) is shown. The typical uncertainty is derived from the mean standard deviation of repeated observations of the same sources.

temperature-sensitive auroral line, [O III]λ4363, for just 4 H II regions. Various methods for calculating gas-phase metallicities and abundances (mainly O and N) from strong emission lines exist in the literature, derived for various combinations of emission line ratios. Calibrations can be either empirical or theoretical (see Section 4 of Kewley and Ellison 2008 for a full review of the topic). Empirical calibrations are derived from the relationship between T_e-based abundances and strong-line ratios (e.g., Pettini and Pagel 2004), whereas theoretical calibrations are derived from the relationship between strong-line ratios and a photoionisation model (sometimes combined with T_e-based abundances (e.g., Kewley and Dopita 2002; Kobulnicky and Kewley 2004). Metallicities are then often plotted with respect to their galactocentric radii so that a

radial gradient can be calculated. S12 applied five different diagnostics for O abundance to their sample of H II regions in M31: Zaritsky et al. (1994); Kewley and Dopita (2002); Pilyugin and Thuan (2005) and two from Nagao et al. (2006) utilising different calibrating emission line ratios. Their results show that the diagnostic chosen affects the metallicities calculated, along with the metallicity gradient. The uncertainty in absolute metallicity (O/H) can be up to 0.6 dex depending on the strong-line diagnostic used (Kewley and Ellison 2008).

It is for these reasons that we carefully consider our choice of strong-line diagnostic. In recent works, the strong-line abundance diagnostics of Pilyugin and Grebel (2016) (hereafter PG16) have been increasingly popular for the purpose of calculating metallicities of individual H II regions (e.g., Kreckel et al. 2019; Kreckel et al. 2020; Williams et al. 2022) due to the strong agreement (within ≈ 0.1 dex) with direct, T_e based Oxygen abundances (see Ho 2019). We note that a requirement of the calibration sample for PG16 is that their T_e-based metallicity must be in agreement with their C-calibration estimate within 0.1 dex (see their Section 2). This could suggest that the 0.1 dex arises by construction and does not reflect the true accuracy of the diagnostics for H II regions with different properties to their calibration sample. We also note that since we are observing fractions of H II regions within the beam size, we are sensitive to internal ionisation parameter fluctuations within H II regions (Jin et al. 2023). The calibration of PG16 provides us with two diagnostics for O abundance (R and S-calibration) and one N abundance diagnostic (R-calibration). The following emission line ratios are utilised in the PG16 calibrations:

$$N_2 = ([\text{N II}]\lambda6548 + [\text{N II}]\lambda6584)/\text{H}\beta$$
$$R_2 = ([\text{O II}]\lambda3727 + [\text{O II}]\lambda3729)/\text{H}\beta$$
$$R_3 = ([\text{O III}]\lambda4959 + [\text{O III}]\lambda5007)/\text{H}\beta$$
$$S_2 = ([\text{S II}]\lambda6717 + [\text{S II}]\lambda6731)/\text{H}\beta.$$

The spectral resolution of our data is not sufficient to resolve the [O II] doublet, so these lines are blended in our data. We obtain a single line flux for [O II] from a line of rest wavelength 3727 Å which is the sum of both lines. The R-calibration utilises the line ratios N_2, R_2 and R_3 whereas the S-calibration utilises the ratios N_2, S_2 and R_3, making these calibrations three-dimensional (3D). The high dimensionality of these diagnostics makes them less sensitive to the ionisation parameter than 1D and 2D diagnostics. We calculate both O and N abundances using the PG16 method, using N as our secondary tracer to further confirm any trends. Many

strong-line diagnostics, including PG16, separate H II regions into upper (high-metallicity) and lower (low-metallicity) branches and calibrate these separately, distinguished by the N_2 line ratio. All of our H II regions lie on the upper branch.

As previously discussed, the diagnostic chosen affects the metallicities calculated. S12 have already compared four different Oxygen abundance diagnostics to their sample of H II regions in M31. To directly compare the metallicities calculated for any matching source in our sample, we apply the O abundance diagnostic of Zaritsky et al. (1994) (hereafter Z94) also used in S12. Z94 is another empirical calibration, based on the strong-line ratio R_{23} = ([O II]λ3727 + [O III]$\lambda\lambda(4959, 5007)$)/H$\beta$ (Pagel et al. 1979). The Z94 method was chosen because it was derived from a similar dataset to ours; observations of individual H II regions in spiral galaxies, including MMT observations. The Z94 calibration is only calibrated for high-metallicity (12 + log(O/H) > 8.4 dex) H II regions, which include almost our entire sample if metallicities are calculated via the Z94 method. For the H II regions that are present in both our and the S12 samples, we find that Z94-calculated metallicities are in agreement within their respective uncertainties. The Z94 diagnostic is more sensitive to ionisation parameter fluctuations than the PG16 diagnostics as it only depends on one emission line ratio, and thus we use the PG16-derived metallicities in future discussion. O and N abundances calculated using different calibrations for individual H II regions in our sample are reported in Table 2.2

We estimate the uncertainties of the abundances for each diagnostic measured, again using the standard deviation of repeat observations of the same source, reflecting the total empirical error budget. Where a source has just one corresponding observation, to calculate the uncertainties reported in Table 2.2, the mean percentage uncertainty was calculated from sources with multiple observations, and this percentage was converted to absolute uncertainties for the single-observation sources. Additionally, we introduce a lower bound of 0.01 to the uncertainties, again to reflect unquantifiable systematic uncertainties. The standard deviation probes the error budget accounting for differences in atmospheric conditions between observations and slight differences between the individual Hectospec optical fibres. Uncertainties in absolute abundance due to the chosen metallicity diagnostic may be as large as 0.7 dex (Kewley and Ellison 2008) (although empirical calibrations produce O abundances that are in better agreement with directly-measured abundances), however, we are interested in metallicity differences between individual H II regions more than the absolute metallicities. Work analysing the reliability of relative H II region O abundances have shown that these are statistically robust between different calibrations (e.g., Ho et al. 2017). Finally, we note that selection effects may occur due to emission line detection;

any spectrum without all of the required lines detected at sufficient S/N could not be included in analysis. However, since we are analysing strong emission lines, this likely has little affect on the resulting trends.

2.4 Results and Discussion

We derived the radial O and N abundance gradients across M31 for H II regions using the strong-line methods Z94 and PG16 as outlined in Section 2.3.4. The Galactocentric radius of each H II region was calculated following Haud (1981). We assume the galactic centre of M31 and the position angle (PA) to be:

$$\alpha_0 = 00^{\mathrm{h}}42^{\mathrm{s}}44^{\mathrm{s}}.52 \ \ \text{(J2000)}$$
$$\delta_0 = +41^{\circ}16'08''.69 \ \ \text{(J2000)}$$
$$\mathrm{PA} = 37.7^{\circ}$$

(Haud 1981) and the angle of inclination to be $i = 12.5^{\circ}$ (Simien et al. 1979). We note that these deprojected distances from the Galactic centre of M31 rely on the assumption that all positions are within the same plane, and so some separations may be under- or over-estimated.

The following sub-sections are structured as follows. First, we present results for the radial O and N abundance gradients in M31. Then, we subtract the radial trends from our data to analyse reduced and enhanced abundances (compared to the radial average) and search for azimuthal trends around the RoF or variations with spiral arm structure. We look at the two-point correlation function of metallicity as a function of source separation and compare to other galaxies from Kreckel et al. (2020) and Williams et al. (2022). Finally, we analyse the relationship between H II region metallicities and the conversion factor for ^{12}CO luminosity to dust mass (M_{dust}), $\alpha'_{^{12}\mathrm{CO}}$.

2.4.1 Radial Abundance Gradients

Figure 2.4 shows H II region metallicities as a function of GCR. We show the typical uncertainty of a given measurement as the mean standard deviation of repeat observations of the same sources. We then calculate the radial metallicity (O/H) gradient of our sample of 294 H II regions for each calibration, calculated from bootstrap resampling of least-squares fitting, where the average

TABLE 2.2: Chemical abundances of M31 H II regions.

ID	R.A., Dec. (J2000)	R [a] (kpc)	Av[b] (mag)	(O/H)* *R*-cal[c]	(O/H)* *S*-cal[d]	(O/H)* Z94[e]	(N/H)* *R*-cal[f]
1	0:39:13.01, 40:41:44.88	16.07	1.00 ± 0.13	8.42 ± 0.02	8.50 ± 0.01	8.89 ± 0.03	7.34 ± 0.05
2	0:39:14.70, 40:48:33.12	18.33	0.66 ± 0.15	8.36 ± 0.05	8.47 ± 0.03	8.71 ± 0.18	7.16 ± 0.15
3	0:39:16.50, 40:41:04.92	15.44	0.08 ± 0.04	8.39 ± 0.02	8.47 ± 0.01	8.69 ± 0.01	7.26 ± 0.03
4	0:39:55.39, 40:55:49.18	15.56	0.54 ± 0.01	8.55 ± 0.01	8.61 ± 0.01	9.01 ± 0.05	7.67 ± 0.05
5	0:40:00.60, 40:39:12.60	11.00	0.33 ± 0.08	8.57 ± 0.01	8.67 ± 0.01	8.90 ± 0.03	7.64 ± 0.04
6	0:40:03.89, 40:58:27.12	15.51	0.40 ± 0.15	8.62 ± 0.01	8.58 ± 0.02	8.75 ± 0.05	7.75 ± 0.04
7	0:40:04.01, 40:58:53.40	15.69	1.16 ± 0.01	8.44 ± 0.01	8.49 ± 0.01	8.90 ± 0.01	7.42 ± 0.03
8	0:40:04.30, 40:58:45.84	15.59	0.88 ± 0.08	8.61 ± 0.02	8.58 ± 0.01	8.60 ± 0.12	7.69 ± 0.09
9	0:40:05.30, 40:59:07.44	15.61	0.68 ± 0.14	8.59 ± 0.02	8.55 ± 0.01	8.66 ± 0.11	7.67 ± 0.11
10	0:40:06.36, 40:59:04.05	15.43	0.75 ± 0.13	8.50 ± 0.02	8.45 ± 0.01	8.84 ± 0.03	7.61 ± 0.05

[a]Source galactocentric radius, calculated as described in Section 2.4. [b]Extinction calculated as described in Section 2.3.2. [c]Oxygen abundance calculated using the PG16 *R*-calibration. [d]Oxygen abundance calculated using the PG16 *S*-calibration. [e]Oxygen abundance calculated using the Z94 calibration. [f]Nitrogen abundance calculated using the PG16 *R*-calibration. *(O/H) = 12 + log(O/H) and (N/H) = 12 + log(N/H).

The full table of 294 sources is available from Bosomworth et al.'s supplementary material; we only show a portion here for 10 sources. Uncertainties are estimated from the standard deviation of abundances obtained from repeat observations of the same source, when available (see text), with a lower bound of 0.01.

y-distance between the data points and the best-fit line is minimised. Gradient uncertainties correspond to the standard deviation of the individual bootstrap gradient calculations.

For the PG16 calibrations (top panel of Figure 2.4) we find metallicity (O/H) radial gradients of -0.0129 ± 0.0020 dex kpc^{-1} (R-calibration) and -0.0097 ± 0.0014 dex kpc^{-1} (S-calibration), which are in agreement within 2σ. Both gradients are in agreement within 1σ with those that S12 obtained using the diagnostics of Kewley and Dopita (2002) and Nagao et al. (2006). The S-calibration result is also consistent with the S12 result using the Pilyugin and Thuan (2005) diagnostic within 1σ. Thus, despite small differences between gradients calculated using different calibrations, the PG16-derived gradients are consistent (within $\lesssim 3\sigma$) with those of other diagnostics. Separating the galaxy separately into two halves down the minor axis, we calculated radial gradients (S-calibration) for the two halves of the galaxy, obtaining -0.0103 ± 0.0022 dex kpc^{-1} for PA < 180 deg and -0.0066 ± 0.0024 dex kpc^{-1} for PA > 180 deg. These are both consistent with the radial gradient of the full sample from the S-calibration and with one another within 1σ uncertainties.

The metallicity (O/H) gradient we calculate from the Z94 diagnostic as shown in Figure 2.4 (bottom panel) is -0.0201 ± 0.0028 dex kpc^{-1}. This result is in agreement within 1σ with the radial metallicity gradient calculated by Sanders et al. (2012) also using Z94-derived abundances (-0.0208 ± 0.0048 dex kpc^{-1}) and that calculated by Z94 (-0.020 ± 0.007 dex kpc^{-1}). It is also consistent within 1σ with the Zurita and Bresolin (2012) T_e-derived gradient of -0.028 ± 0.014 dex kpc^{-1} (with PG16 gradients being in agreement within 2σ with Zurita and Bresolin 2012). The more direct method produces a somewhat steeper gradient than strong-line diagnostics, albeit with a larger uncertainty, therefore results are still in agreement within 1-2σ. The radial metallicity gradients in our work calculated from the Z94 and the PG16 R-calibration agree within 2σ (Z94 and PG16 S-calibration agree within 3σ). Therefore, the radial metallicity gradient of M31 varies only slightly depending on the strong-line diagnostic used. The Z94-based gradient has remained unchanged over several decades, despite improvements in data quality and increased sample size, indicating that this result/calibration is consistent. However, strong-line diagnostics are constantly being re-evaluated based on T_e-metallicity datasets and improved photoionisation models. Therefore, defining the most accurate metallicity gradient for M31 remains an active research area.

Wenger et al. (2019) built on previous Milky Way (MW) H II region studies (e.g., Balser et al. 2011), finding an O abundance gradient of -0.052 ± 0.004 dex kpc^{-1} from T_e line measurements.

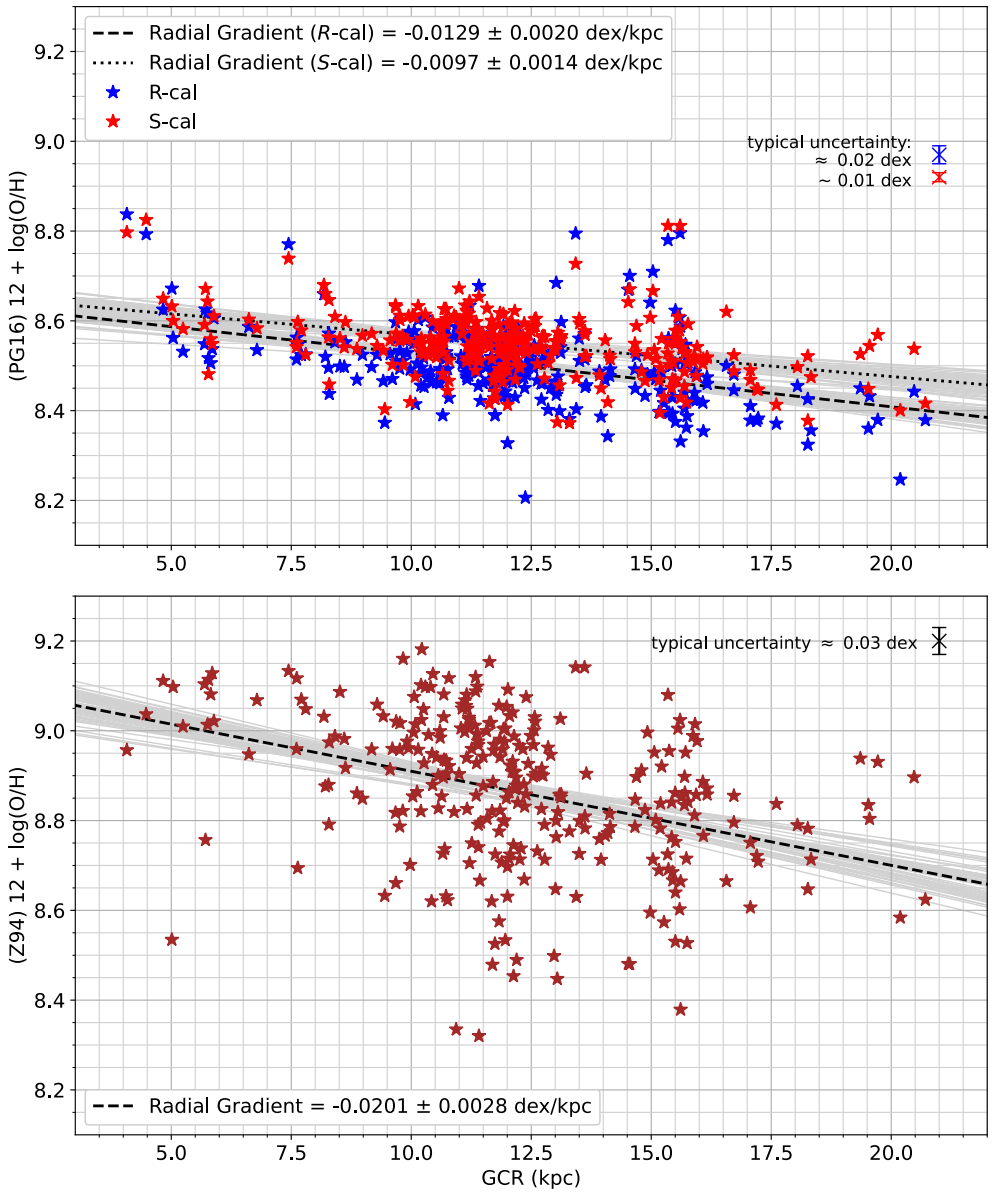

FIGURE 2.4: Oxygen abundance, 12 + log(O/H), of H II regions in M31 from the *top* PG16 *R*- and *S*-calibrations and the *bottom* Z94 diagnostic as a function of galactocentric radius.

A radial O abundance gradient of -0.041 ± 0.006 dex kpc^{-1} was calculated by Esteban and García-Rojas (2018). Compared to the O abundance gradients calculated in this work from PG16 diagnostics (which is in agreement within 0.1 dex with direct, T_e-based metallicity measurements; Ho 2019), the radial gradient of the MW is $\approx 4-6$ times steeper than that of M31. Kreckel et al. (2019) found O/H gradients for their sample of 8 spiral galaxies, also derived from PG16 *S*-calibration abundances, ranging from -0.0199 to -0.1586 dex kpc^{-1} (excluding one galaxy which produced a positive gradient). Therefore, the O abundance gradient of M31 is shallow compared to those of these spiral galaxies.

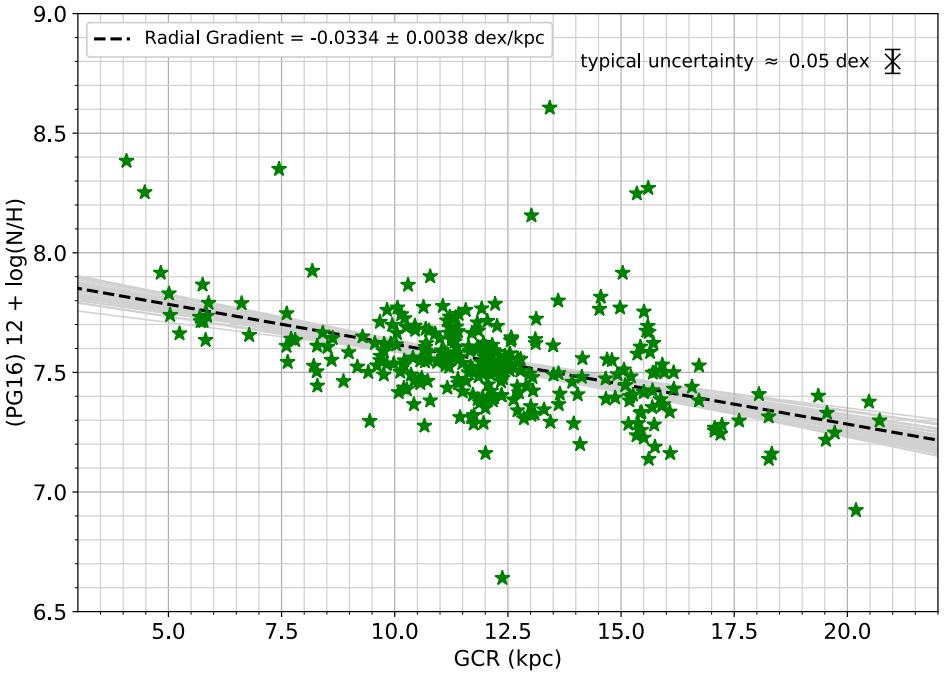

FIGURE 2.5: Nitrogen abundance, 12 + log(N/H), of H II regions in M31 from the PG16 *R*-calibration as a function of galactocentric radius.

Again from bootstrap resampling, we calculate an N abundance gradient of -0.0334 ± 0.0038 dex kpc^{-1} from 294 H II regions using the *R*-calibration of PG16. We display this result in Figure 2.5. The N abundance gradient is significantly larger than the O abundance gradient, by a factor of $\approx 1.7-3.4$ depending on the choice of strong-line diagnostic. This is consistent with simulations from Vincenzo and Kobayashi (2018) who found increasing N/O with O/H in spatially resolved star-forming disc galaxies, and a resulting negative radial N/O abundance gradient.

The N abundance gradient calculated in this work is consistent with that from S12 (-0.0303 ± 0.0049) which uses the strong-line diagnostic of Pilyugin et al. (2010), an older version of the N abundance diagnostic from PG16. For the MW, Esteban and García-Rojas (2018) found N abundance gradients ranging from -0.047 to -0.050 ± 0.008 dex kpc^{-1} from direct H II region abundances of 13 sources. This is steeper than the N abundance gradient found in this work for M31, by a factor of $\approx 1.4-1.5$. As found for the O abundance profile, there is statistically significant scatter around the best-fitting N abundance profile, thus providing further evidence that there are abundance variations beyond the radial relation. Figures 2.4 and 2.5 show that H II regions at a similar galactocentric radius can have very different metallicities, as also shown in S12 in their Figures 8 and 14.

Although our abundance gradients are in agreement with those of previous work, Figures 2.4 and 2.5 show that there is significant (greater than the typical uncertainty) scatter around the best-fitting relation at all galactocentric radii. The majority of M31 H II regions are located at radii of $\approx$ 12 and 15 kpc. These correspond to the approximate locations of the main RoF and its outer component (Lewis et al. 2015). If the metallicity variations throughout M31 could be fully explained by just the radial profile, we would expect these sources all to have a similar metallicity. However, in Figure 2.4 (top panel) we see O abundances ranging from $\approx$ 8.35 to 8.75 (excluding two outliers), from PG16 *S*-calibration-based abundances, for sources within the RoF ($\approx 10 - 16$ kpc). The metallicity range covered by RoF H II regions is even larger for the Z94 diagnostic ($\approx 8.4 - 9.2$) though this is partially due to the inherent uncertainty of the diagnostic. S12 found no dependence of metallicity or gradient on the surface brightness of H II regions for their similar sample.

Our final H II region sample requires all emission lines required for the strong line calibrations (see Section 2.3.4) to have S/N > 5, producing a sample size of 294. We can extend our sample size by assuming a 3:1 ratio for the strong to weak lines in the [O III] and [N II] doublets (Storey and Zeippen 2000). We investigated this following the method outlined in Kreckel et al. (2020): we measure only the lines [O III]λ5007 and [N II]λ6584, the stronger lines in each doublet, and divide these line fluxes by 3 to obtain the line fluxes of [O III]λ4859 and [N II]λ6548. Therefore, the condition that the weaker lines of the doublet must have S/N > 5 for the abundances to be recorded can be eliminated, increasing the number of H II regions to 322 . This is lower than the 416 classified H II regions (see Section 2.3.3) because both of the lines in the [S II] doublet are still required to have S/N > 5. Calculating the radial metallicity gradients for the extended sample, we obtain gradients consistent within 1σ to the previously reported gradients in this section, for all abundance diagnostics and tracers. Ultimately, the 3:1 ratio assumption does not significantly increase our sample size and leads to no change to our results. Therefore, we use our sample of 294 H II regions, measuring both lines in the [O III] and [N II] doublets, for all further analyses.

2.4.2 Non-radial Trends

We next subtract the *S*-calibration radial-profile from individual H II region O abundances, so that only residual metallicities remain. We chose to use the *S*-calibration abundances for this purpose because the [S II] lines are less affected by extinction than the [O II] line (see Fig. 3

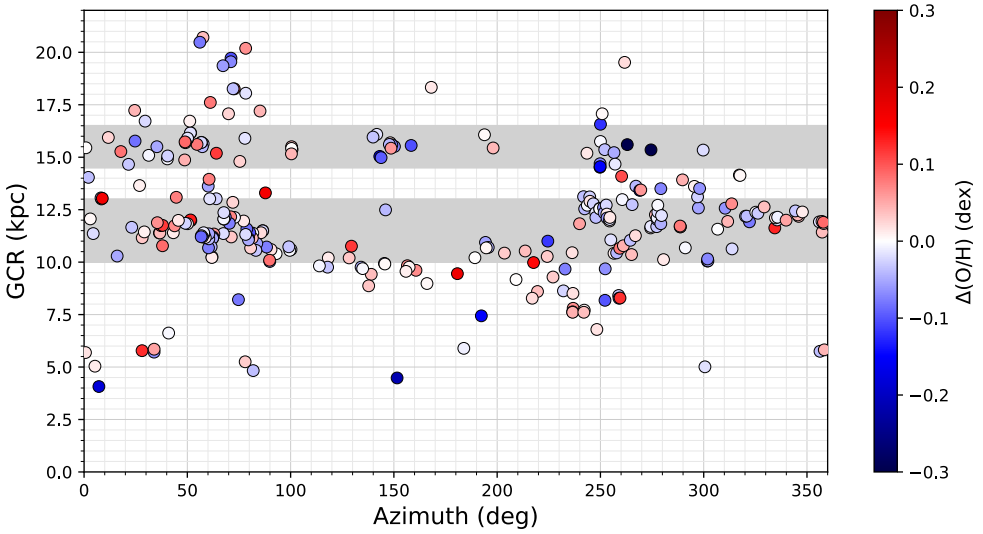

FIGURE 2.6: Galactocentric radius (GCR kpc) vs azimuthal angle for H II regions in M31, where the azimuthal angle is deprojected with 0° corresponding to the northern major axis and increasing clockwise. Points are coloured by their corresponding radial-fit subtracted Oxygen abundance, $\Delta(\mathrm{O/H})$, from the PG16 *S*-calibration. The approximate positions and widths of the RoF components, based on where the majority of our sources lie, are shown by the grey-shaded regions.

from Cardelli et al. 1989), decreasing the inherent uncertainty. This is also identical to the calibration used in other works investigating H II region metallicity scatter across galaxy discs (e.g., Kreckel et al. 2019), enabling us to make direct comparisons without the uncertainty due to using different calibrations. This enables us to investigate any second-order trends such as azimuthal effects and variations corresponding to galactic features such as spiral arms and the RoF. In Figure 2.6 we show the source GCR vs deprojected azimuthal angle (in the clockwise direction with 0° corresponding to the major axis of M31 in the northern direction) of H II regions, with data points coloured according to their Δ(O/H) from the PG16 *S*-calibration. From this plot we find little evidence of systematic metallicity trends in the azimuthal direction, but rather that the scatter (standard deviation 0.06 dex) around the best-fitting relation occurs across the entire galaxy. This is true even for sources at a similar galactocentric radius, as shown for the sources located within the RoF at radii of $\approx 10 - 13$ kpc as well as its outer component at radii of $\approx 14.5 - 16.5$ kpc, highlighted on Figure 2.6.

Previous studies have shown that small but statistically significant scatter around the radial profile typically occurs distributed across the galaxy (Kreckel et al. 2019; Grasha et al. 2022). Alongside this, studies have shown hints of distinct azimuthal variations in the form of enhanced abundances along spiral arms (e.g., Kreckel et al. 2019; Grasha et al. 2022), although statistical

tests failed to quantify a systematic correlation due to the large scatters present across the entire galaxies. On the other hand, Ho et al. (2017) found a statistical difference (≈ 0.2 dex) between spiral-arm and inter-arm regions, finding that 76% of H II regions within the main spiral are above the radial profile whilst only 19% of inter-arm regions are. We note that in these spiral galaxies, the majority of H II regions are located within the spiral arms, however, in M31 the majority are located in the RoF. For H II regions located in the RoF, we see an approximately equal number of reduced abundance H II regions as we do enhanced abundance H II regions, as expected due to the nature of the best-fit profile. This scatter could reflect that the ISM is not fully mixed on small scales, possibly due to recent localised enrichment from star formation or SNe.

A strong positive correlation between Δ(O/H) and ionisation parameter hints that local enrichment is linked to differences in the local physical conditions (Grasha et al. 2022). Along with evidence that H II regions with enhanced abundances have high ionisation parameters, Hα luminosity, younger star clusters, and high CO luminosity in the associated molecular clouds (Kreckel et al. 2019), this suggests that local enrichment has occurred due to recent star formation. Kreckel et al. (2019) also see a correlation between reduced abundance H II regions and an increased Hα velocity dispersion, which indicates the dynamical state of the ionised gas. This indicates that large-scale mixing may have taken place, introducing pristine material from outside the galaxy.

We suggest that a similar explanation may be relevant to M31. In Figures 2.7 and 2.8 we show the mean and standard deviation of Δ(O/H) in bins of varying of galactocentric radius. Figure 2.7 uses bins of equal radial widths (3 kpc) that overlap by 50% of the bin size. For Figure 2.8 we use bins containing approximately equal numbers of sources, N, where N = 34 or 35. In both figures we see that the standard deviation (i.e., the scatter of Δ(O/H)) is in the range $\approx 0.03 - 0.10$ dex and that approximately 30% of H II regions have $|\Delta(\mathrm{O/H})| > 1\sigma$ and 20% of those outliers have $|\Delta(\mathrm{O/H})| > 2\sigma$. The greatest scatter occurs at GCR $\approx$ 15 kpc which corresponds to the outer RoF (the corresponding sources are shown as pink upside-down triangles); this is also where we see the most enhanced abundance H II regions. In comparison, the main RoF at radii of $\approx 10 - 13$ kpc is where we see the least scatter, suggesting that this material is more well-mixed than in the outer RoF component. However, as we see both enhanced and reduced abundances of $|\Delta(\mathrm{O/H})| > 1\sigma$ distributed across the entire disc, general systematic trends have not been identified. We note that we make no statement on the exact location and size of the RoF, and our approximation is based on the distribution of our H II region sample.

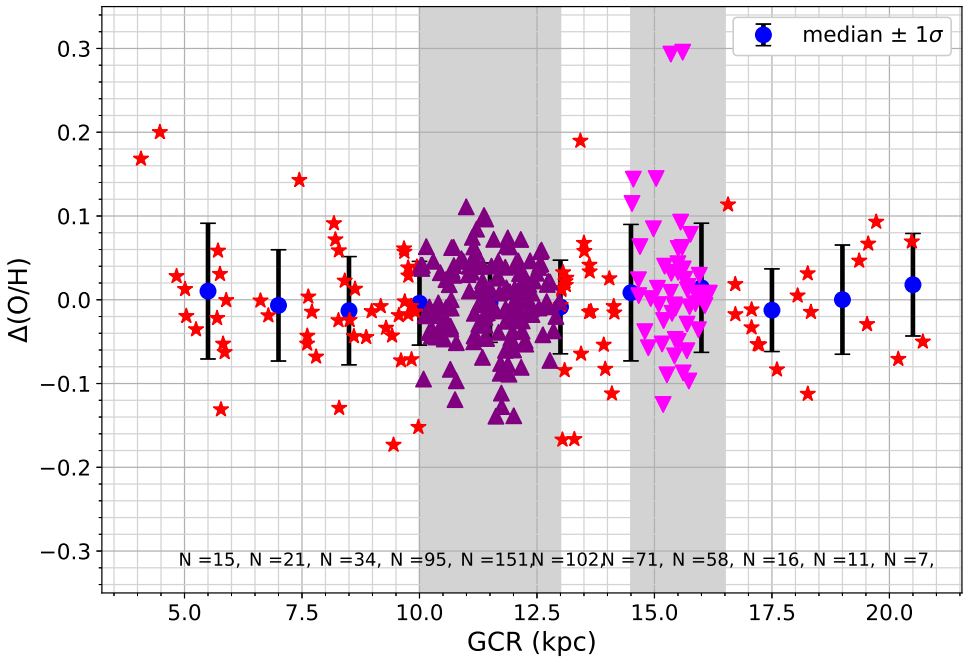

FIGURE 2.7: Δ(O/H) (PG16 *S*-calibration) as a function of galactocentric radius, with individual H II regions shown in red and the means ofbins of equal radial size (3 kpc) shown as blue circles. Bins are separated by 1.5 kpc and overlap by 50%. Sources located within the main RoF at radii of ≈ 10 – 13 kpc are shown in dark purple and sources located within the outer RoF component at radii of ≈ 14.5 – 16.5 kpc are shown in pink. In grey we show the approximate positions and widths of the RoF components, based on where the majority of our sources lie. The black bars show the standard deviation of the sources in each bin, which have N number of sources.

The presence of enhanced abundance H II regions indicates that material has likely been enriched due to recent star formation and SNe. Simulations indicate that kpc-scale mixing can take 100 - 350 Myr (Roy and Kunth 1995; de Avillez and Low 2002). Simulations performed by de Avillez and Low (2002) indicate a mixing timescale of ≈ 350 Myr for the Galactic SN rate. More recent simulations of higher resolution by Emerick et al. (2018) show that cold gas can become well-mixed on ≈ 50 Myr timescales, with metal mixing occurring more rapidly in hotter phases before cooling. H II regions trace metal enrichment from massive stars with lifetimes of $\lesssim$ 10 Myr, therefore, there may be some SN-enriched material in M31 that is not yet fully mixed, causing inhomogenities in the ISM to remain.

A possible explanation for the lower-metallicity gas is that it may have been brought into M31 from outside of the galaxy, resulting in reduced abundance H II regions. A possible source of this lower-metallicity gas is a recent collision with M32 which models predict occurred

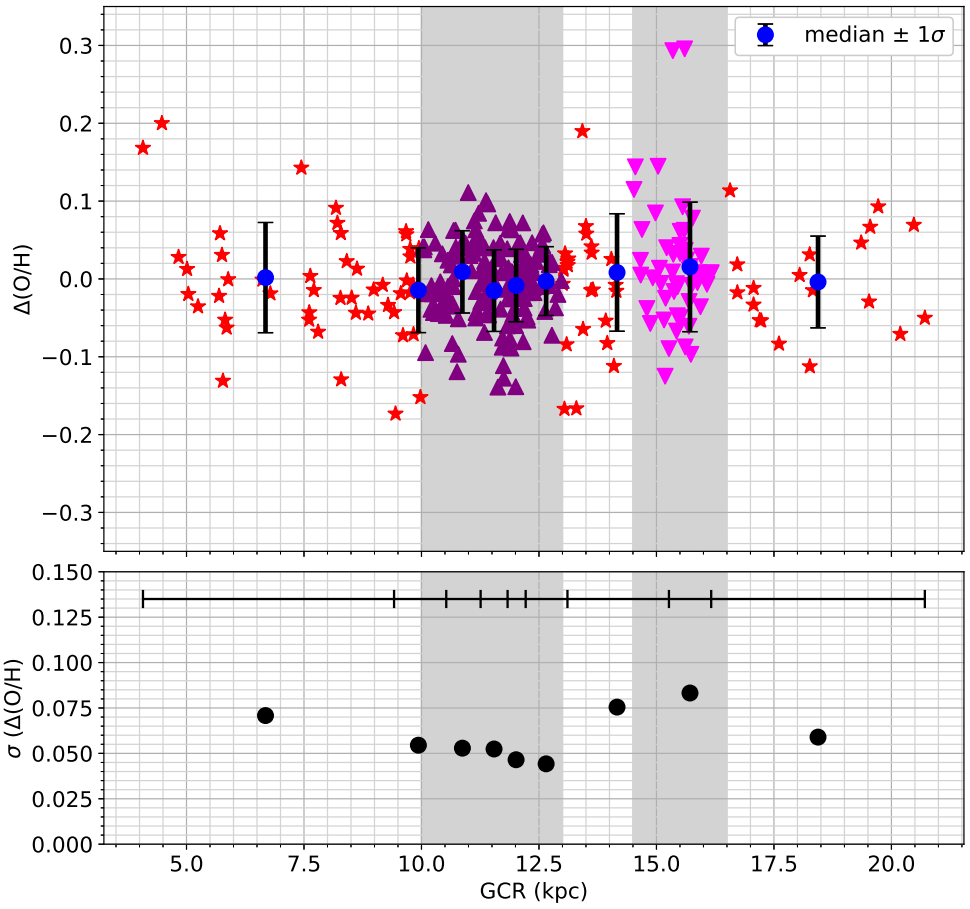

FIGURE 2.8: *Top* As in Figure 2.7 but for bins of approximately equal number of sources (N = 34 or 35). Sources located within the RoF at radii of ≈ 10 – 13 kpc are shown in dark purple and sources located within the outer RoF component at radii of ≈ 14.5 – 16.5 kpc are shown in pink. The grey regions represent approximate RoF positions, as in Figure 2.7. Vertical black bars show the standard deviation of the sources in each bin. *Bottom* Standard deviation as a function of radius. The black bars show the radial range covered by each bin, relevant to both panels.

≈ 200 – 800 Myr ago (Block et al. 2006; Davidge et al. 2012; Dierickx et al. 2014). Lower-metallicity (in comparison to the metallicity of gas in M31) gas may have been stripped from M32 and not yet fully mixed into M31, especially if the collision occurred closer to ≈ 200 Myr ago. Most 1σ outliers are located within the RoF, which is believed to have formed during the collision with M32 (Braun 1991). The differences in the standard deviations of the residual scatter are also displayed in Figure 2.8. The global scatter over all values of GCR is ≈ 0.06 dex. However, we see in Figure 2.8 that the standard deviation can be as low as < 0.04 dex

within the main/inner RoF, suggesting that this material is well mixed. On the contrary, the standard deviation scatter is as high as > 0.09 dex for the outer RoF. In Figures 2.7 and 2.8 we see increased scatter in Δ(O/H) at GCR ≈ 15 kpc, suggesting that the material in the outer RoF is less well-mixed than that in the inner RoF. For comparison, Kreckel et al. (2019) found global scatters of 0.03 – 0.05 dex for their galaxies.

2.4.3 Two-point Correlation Function of Metallicity

Following the method of Kreckel et al. (2020), we calculate the two-point correlation function of residual metallicity within increasing H II region separation (up to 10 kpc) after the radial trend has been subtracted (Figure 2.9) using their equation 5. As was also done in their work, we also compute a randomised sample by randomly shuffling the metallicities (PG16 *S*-calibration) amongst our H II region positions. We calculate the correlation function via bootstrap resampling and taking the average and standard deviation over 100 iterations. From this we investigate the separation between H II regions within which we no longer see the same degree of homogeneity above that expected from the randomised sample.

Our two-point correlation function is shown in Figure 2.9. We show, for both the *R*-calibration and the *S*-calibration, that the correlation falls below 0.5 (the 50% correlation scale) at ≈ 0.6 kpc separation and below 0.3 at ≈ 1.2 kpc separation. This is significantly different to the randomised sample for which the correlation falls below 0.5 at ≈ 0.3 kpc separation and below 0.3 at ≈ 0.6 kpc separation. From this we conclude that there is a correlation of H II region metallicities for nearby sources above what we would see if the scatter around the radial gradient was completely random. The two-point correlation functions of the 19 PHANGS-MUSE (Physics at High Angular Resolution in Nearby Galaxies - The Multi Unit Spectroscopic Explorer) spiral galaxies are reported in Williams et al. (2022). The 50% correlation scales found range from 0.19 - 1.08 kpc apart from one galaxy which reaches 0.5 correlation at 4.12 kpc. This suggests that M31 is quite well-correlated on small scales which is similar in general to these galaxies, when comparisons are made using the same strong-line diagnostic (PG16 *S*-calibration). The models of de Avillez and Low (2002) predict that mixing slows down exponentially with separation, which is a possible explanation as to why galaxies are typically found to be less well-mixed on kpc scales than on sub-kpc scales.

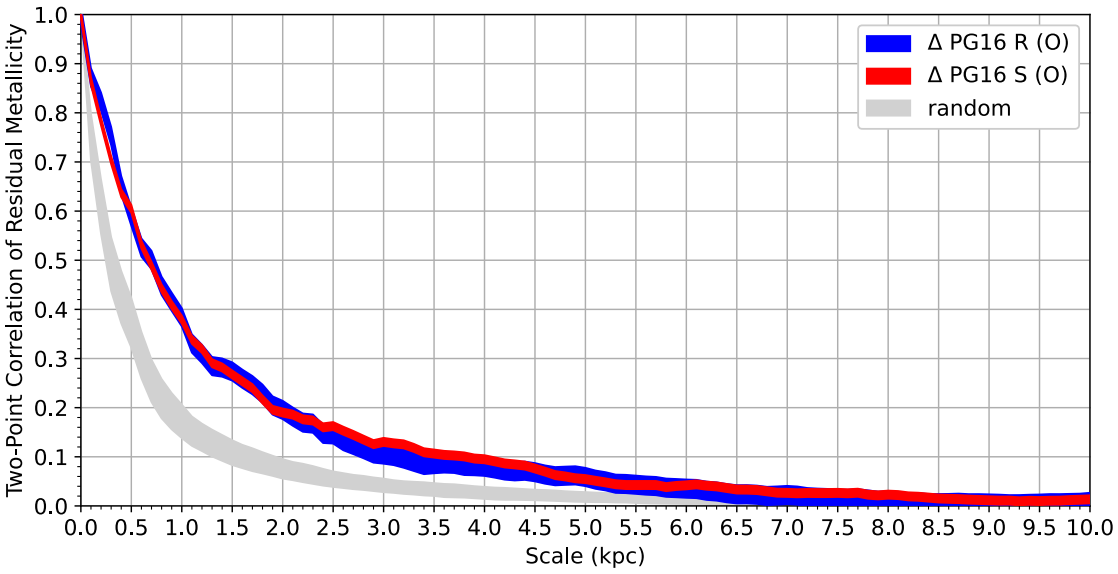

FIGURE 2.9: Two-point correlation function of residual H II region metallicity within a given spatial scale up to 10 kpc for the PG16 strong-line diagnostics. In grey, we show the two-point correlation function if the metallicities are randomised, i.e. if metallicity and position within the galaxy are uncorrelated.

2.4.4 Metallicity Dependence of $\alpha'_{^{12}\mathrm{CO}}$

Many of our optical spectra supplement SMA observations for which we have dust continuum emission measurements of individual GMCs (see Viaene et al. 2021). This gives us the opportunity to directly study any apparent metallicity dependence of $\alpha'_{^{12}\mathrm{CO}}$, the ratio of dust mass and CO luminosity. Both the dust mass and the CO luminosity are likely to vary with metallicity, which could either exacerbate or mitigate ensuing changes of the ratio. What we compare here are Viaene et al.'s $\alpha'_{^{12}\mathrm{CO}}$ measurements of individual clouds and the metallicities of associated H II regions obtained in this study. We plot the resulting relationship between H II region oxygen abundances (from the *S*-calibration of PG16) and GMC $\alpha'_{^{12}\mathrm{CO}}$ (as defined in Viaene et al. 2021) in Figure 2.10. The majority of the sample displays an approximately constant $\alpha'_{^{12}\mathrm{CO}} \approx (0.0605 \pm 0.009)\ \mathrm{M}_\odot(\mathrm{K\,km\,s^{-1}\,pc^2})^{-1}$ across the metallicity range probed; however, the lowest-metallicity data point exhibits elevated $\alpha'_{^{12}\mathrm{CO}}$ than that of other sources by more than 1σ. Thus, while there is little evidence for a strong metallicity dependence of $\alpha'_{^{12}\mathrm{CO}}$ in this work, the two lowest-metallicity outliers may be tentative evidence for increasing $\alpha'_{^{12}\mathrm{CO}}$ at lower metallicities. This finding is consistent with the prediction from Bolatto et al. (2013) that a significant change in $\alpha(\mathrm{CO})$ is generally only expected for low metallicities, i.e. $12 + \log(\mathrm{O/H}) < 8.4$ dex. A larger sample size probing $12 + \log(\mathrm{O/H}) < 8.5$ dex is required to confirm the trend. At higher metallicities, variations in H II region metallicity and GMC $\alpha'_{^{12}\mathrm{CO}}$ may largely cancel.

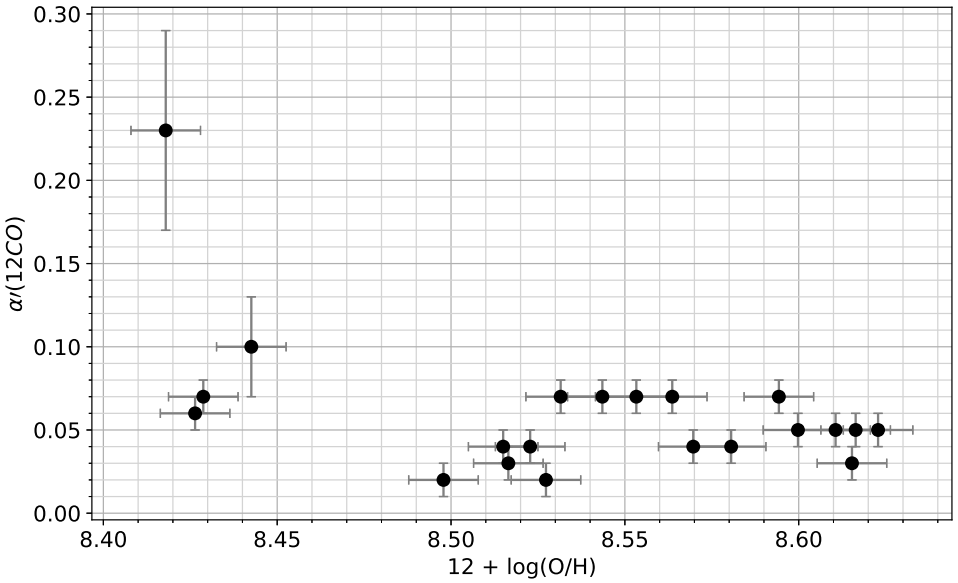

FIGURE 2.10: Variation of the CO-to-dust-mass conversion factor, $\alpha'_{^{12}\mathrm{CO}}$, with metallicity (O) for H II regions with SMA detections reported by Viaene et al. (2021). Some GMCs have multiple associated H II regions. Uncertainties in the *S*-calibration-calculated metallicities are the same as for Figure 2.4. $\alpha'_{^{12}\mathrm{CO}}$ and uncertainties are taken from Viaene et al. (2021).

We note again that $\alpha'_{^{12}\mathrm{CO}}$ does not take into account the gas-to-dust ratio, which is also predicted to depend on metallicity.

2.5 Summary

From our optical spectroscopic survey of M31 we have identified and calculated O and N abundances for 294 H II regions from their emission line ratios. From our analysis, we conclude the following:

1. We find an oxygen (O) abundance gradient of -0.0113 ± 0.0016 dex kpc^{-1} by taking the mean of the gradients calculated using the PG16 *R*-calibration and *S*-calibration. We explored the use of the R_{23} diagnostic of Z94, finding that the radial metallicity gradient agrees within 2σ with those from the PG16 calibrations. Weak auroral lines are necessary to calculate a more precise, direct gradient, but these are only detected in four of our sources with a S/N > 3.

2. M31 has a relatively shallow O abundance gradient compared to those of other spiral galaxies, e.g., those from Kreckel et al. (2019). In comparison to the Milky Way it is shallower by a factor of $\approx 4-6$ depending on the choice of methodology.

3. We find a nitrogen (N) abundance gradient of -0.0334 ± 0.0038 dex kpc^{-1} from the PG16 *R*-calibration, in agreement within the uncertainty with that from S12 calculated for M31 using the diagnostic from Pilyugin et al. (2010).

4. The N abundance gradient of M31 is $\approx 1.7-3.4$ (depending on the chosen calibration) times steeper than the O abundance gradient, indicating that the N/O ratio is higher towards the centre. This is consistent with cosmological simulations (Vincenzo and Kobayashi 2018) which show a negative N/O radial gradient.

5. Around our *S*-calibration O radial best-fitting relation we measure a standard deviation (in scatter) of ≈ 0.06 dex, exceeding the mean inherent measurement uncertainty of ≈ 0.01 dex. After subtracting the radial fit from the metallicities to get residual metallicities, $\Delta(\mathrm{O/H})$, we see significant outliers that exceed this scatter by up to 5σ. This confirms conclusions from previous works (e.g., S12, Kreckel et al. 2020) that a radial gradient is not sufficient to describe metallicity variations between H II regions in spiral galaxies.

6. The presence of both enhanced- and reduced-metallicity H II regions (compared to the radial profile) throughout the disc may reflect local variations in enrichment, and incomplete mixing of metals. Possibly, external gas of lower relative metallicity has been brought into the galaxy from outside. This may have occurred during a collision between M31 and M32 occurring 200 - 800 Myrs ago. previous work suggests that enhanced-metallicity (compared to the radial gradient) H II regions may indicate local ISM enrichment by recent star-formation and SNe (Ho et al. 2017).

7. From the two-point correlation function, we see that metallicities are well-correlated (compared to the random sample) at sub-kpc scales. There is evidence of an exponential decrease in the speed of mixing (i.e. de Avillez and Low 2002) with increasing spatial separation so it is expected that kpc-scale inhomogenities will be present for longer periods of time. Additionally, inefficient mixing on larger scales could suggest that not all material brought in by a putative collision is mixed yet and causes reduced abundance H II regions in our sample.

8. We study the variations of $\alpha'_{^{12}\mathrm{CO}}$ using an SMA survey of the associated GMCs (Viaene et al. 2021) with O abundance. Across a relatively large range of metallicities, we find little evidence for a significant dependence of $\alpha'_{^{12}\mathrm{CO}}$ on O abundance at $12 + \log(\mathrm{O/H}) > 8.5$ for H II regions associated with GMCs observed by the SMA. However, the lowest-metallicity ($12+\log(\mathrm{O/H}) \approx 8.42$) data point in Figure 2.10 has a high $\alpha'_{^{12}\mathrm{CO}}$ value, which is significant by $> 1\sigma$.

9. Future work will aim to obtain $\alpha'_{^{12}\mathrm{CO}}$ measurements for more GMCs in M31 for which we also have H II region abundances, so that the correlation between the two factors can be investigated further. We will also investigate the chemical abundance throughout the M31 disc further through analysis of N/O.

Chapter 3

Resolved Dust Emission and CO Isotopologues in Giant Molecular Clouds of the Andromeda Galaxy

3.1 Introduction

GMCs are the main sites of star formation. The physical conditions within GMCs determine the SFR, the primary metric for studies of galaxy (e.g., Saintonge and Catinella 2022) and cosmic evolution (e.g., Madau and Dickinson 2014; Tacconi et al. 2020). Molecular gas provides the fuel for star formation. H makes up $\approx$ 75% of the total gas mass of the cold ISM, and within GMCs, H is mainly molecular (H_2). Additionally, GMCs are composed of approximately 24% atomic He and 1% interstellar dust by mass (Saintonge and Catinella 2022). Both H_2 and He are difficult to detect at the cold temperatures typical of GMCs; therefore, we rely on rarer molecules to detect and probe the molecular gas. In particular, CO is primarily used in extragalactic studies (see, e.g., Bolatto et al. 2013 for a review) because it emits the strongest molecular emission lines in cold GMCs. However, CO only accounts for $\approx$ 0.03% of GMC mass (e.g., Heyer and Dame 2015), is optically thick in dense cloud regions due to its high opacity and depletes onto dust grains. As a result, CO traces the diffuse GMC envelopes and does not reflect the denser regions of the cloud. Dense gas is key to understanding global SFE and the SFR (Gao and Solomon 2004; Lada et al. 2010; Lada et al. 2012), and so it is vital to investigate alternative tracers that better probe the physical properties of clouds.

Observations of dust extinction in MW GMCs have provided detailed information on cloud structure as well as the first robust measurements of GMC masses (e.g., Lada et al. 1994; Alves et al. 2001; Goodman et al. 2009; Lada et al. 2010). Dust is $\approx 30\times$ more abundant than CO in GMCs, and since molecules such as H_2 and CO form on the surfaces of dust grains (e.g., Wakelam et al. 2017), it is well mixed with molecular gas. At mm wavelengths, we can probe thermal dust continuum emission, which traces H_2 gas mass and column density more accurately than CO due to its lower optical depth (e.g., Scoville et al. 2016; 2017). Although dust extinction measurements are independent of dust temperature ($T_{\rm dust}$), dust emission depends on $T_{\rm dust}$ and opacity (κ_ν). However, unlike molecular excitation lines, dust emission does not depend on excitation conditions.

To fully understand the star formation processes and conditions in a galaxy, we need to probe GMCs across the entire disc of the galaxy. This is difficult in the MW because of distance measurement uncertainties and line-of-sight dust extinction, particularly for clouds located near the center of the galaxy. GMCs within an external galaxy are approximately the same distance from us, and therefore we can obtain a large sample of measurements at a consistent resolution. As the most easily observable tracer, CO is primarily used to trace molecular gas in extragalactic GMCs. The first spatially resolved CO detections of extragalactic GMCs were made in the Andromeda Galaxy (Vogel et al. 1987; Lada et al. 1988). More recently, observations of extragalactic GMCs in CO on $\approx$ 100 pc scales (e.g., PHANGS-ALMA; Leroy et al. 2021) and resolved observations on $\approx$ 10 pc scales (e.g., Colombo et al. 2014; Faesi et al. 2018) have become routine.

Herschel studies reveal the spatial distribution of GMAs in M31, traced by dust emission at $\approx$ 93 pc spatial resolution (Fritz et al. 2012; Kirk et al. 2015). These GMAs have sizes of $\approx 80 - 300$ pc, and thus typically encompass associations of multiple unresolved GMCs. Generally, GMCs have sizes of $\approx 20 - 100$ pc, which means that individual GMCs are not resolved by *Herschel*. Extragalactic studies of resolved GMCs are predominantly limited to CO due to the high sensitivity required to detect and resolve dust emission from extragalactic GMCs. This is particularly challenging at mm/sub-mm wavelengths where thermal dust emission is faint. At mid-IR and far-IR wavelengths the dust emission is brighter, but the necessary angular resolution to resolve individual clouds would require prohibitively large telescope apertures, making these observations extremely costly. The southern-hemisphere based Atacama Large Millimeter Array (ALMA) cannot observe M31 due to its location in the northern-hemisphere sky; however, the recent wideband sensitivity upgrade of the SMA (Grimes et al. 2016) has

enabled the first resolved dust emission detections of GMCs in an external spiral galaxy, M31, at $\lesssim$ 15 pc scale (Forbrich et al. 2020; Viaene et al. 2021).

To detect resolved dust continuum from individual GMCs in M31, long exposure times were required. Therefore, observing the entire galaxy would be extremely difficult, and as a result, a sample of targets was selected from the HELGA dust continuum survey of *Herschel*-identified GMAs (Kirk et al. 2015). The aforementioned SMA survey obtained simultaneous dust emission and three CO isotopologues: ^{12}CO(2−1), ^{13}CO(2−1), and C^{18}O(2−1), with identical calibration, (u, v) coverage, and thus spatial scale (see Forbrich et al. 2020; Viaene et al. 2021; Lada et al. 2024). Since M31 GMCs have an approximately uniform distance from us ($\approx$ 780 kpc; Stanek and Garnavich 1998), this dust survey has the advantage of eliminating significant uncertainties in distance measurements present in MW studies.

Two previous papers report 32 dust continuum detections (10 resolved) associated with M31 GMCs from the analysis of the first two observing runs of an SMA large survey (Forbrich et al. 2020; Viaene et al. 2021). In this paper, we present an updated analysis of the now completed survey after four observing runs, increasing the sample size to 71 dust continuum detections (26 resolved). The sensitivity of these observations enabled resolved dust emission detections on scales of $\approx$ 15 pc. Since the sensitivity to dust in these observations is not sufficient to trace entire GMCs, individual dust detections are hereafter referred to as "dust cores" (following Viaene et al. 2021). The sensitivity achieved in ^{12}CO enables measurement of the full ^{12}CO(2-1) emitting area of each GMC (Viaene et al. 2021), allowing us to identify the dust emission associated with these clouds.

From CO and dust emission in the same clouds, we can directly calculate $\alpha'_{\rm CO}$, the ratio between dust mass ($M_{\rm dust}$) and CO luminosity ($L_{\rm CO}$). This ratio is related to the CO-to-H_2 conversion factor, $\alpha_{\rm CO}$ (the ratio between molecular gas mass, $M_{\rm mol}$, and $L_{\rm CO}$) through the gas-to-dust ratio ($R_{\rm g/d}$). Therefore, calculating $\alpha_{\rm CO}$ requires an assumption of $R_{\rm g/d}$, for which the typical MW ratio is $R_{\rm g/d} \approx 136$ (including a factor of 1.36 to account for He; Draine et al. 2007). However, chemical evolution models (e.g., Mattsson and Andersen 2012; Hirashita and Harada 2017) and observations (e.g., Sandstrom et al. 2013; Giannetti et al. 2017) have shown that $R_{\rm g/d}$ can vary with dust grain size and metallicity. By measuring $\alpha'_{^{12}\rm CO}$ and $\alpha'_{^{13}\rm CO}$ independently of $R_{\rm g/d}$, we exploit the full capability of dust as a molecular gas tracer and gain insight into the ISM conditions of star formation directly from these observations. Moreover, by deriving $\alpha'_{\rm CO}$

for both the ^{12}CO and the rarer CO isotopologue ^{13}CO in the same sources, we can compare molecular gas components with different opacities.

The combination of CO and dust continuum emission observations with identical astrometry enables the calculation of both the luminous and virial masses of these dust cores. Lada et al. (2024) evaluate the Larson paradigm, which states that GMCs are in dynamical equilibrium with gravity, for a sample of 117 GMCs in M31. Using data from the same SMA survey described in this work and employing ^{12}CO(2 − 1) to trace cloud boundaries, Lada et al. found that this paradigm does not hold for most M31 GMCs. In contrast, for the denser regions of GMCs traced by ^{13}CO emission in these observations, the majority were found to be gravitationally selfbound. These ^{13}CO detections are referred to as 'clumps' because they, like dust, do not trace entire GMCs, and a single GMC can have multiple associated clumps. In this chapter, we assess the virial state of resolved dust cores, which are constrained to the denser regions of GMCs in our observations.

The accuracy of CO as a molecular gas tracer depends on correctly accounting for the effects of metallicity on CO abundance and conversion factors. CO conversion factors, $X_{\rm CO}$ and $\alpha_{\rm CO}$, are predicted to vary with metallicity (e.g., Leroy et al. 2011; Bolatto et al. 2013). At lower metallicities, less C and O are available, resulting in lower CO abundance (Maloney and Black 1988; Israel 1997). Therefore, $L_{\rm CO}$ per unit gas mass is predicted to decrease at lower metallicities. Furthermore, approximately 30 − 50% of metals are expected to deplete onto dust grains (Savage and Sembach 1996; Draine et al. 2007), so $M_{\rm dust}$ and dust opacity should also increase with metallicity. Dust extinction shields H_2 and CO molecules from photodissociation by UV radiation.

Therefore, more effective dust shielding at higher metallicities allows CO to trace a larger fraction of the molecular gas (e.g., Glover et al. 2010, 2012). The metallicity dependence of $\alpha'_{\rm CO}$ provides insight into the relative effects of metallicity on $M_{\rm dust}$ and $L_{\rm CO}$, and how this in turn could affect $\alpha_{\rm CO}$ if $R_{\rm g/d}$ is assumed to be constant. In Bosomworth et al. (2025), an approximately constant $\alpha'_{^{12}\rm CO}$ was found across the metallicity range 12 + log(O/H) = 8.4–8.7. A possible explanation for this behavior is that the simultaneous effects on $M_{\rm dust}$ and $L_{\rm CO}$ may cancel out at these metallicities. By comparing our $\alpha'_{^{12}\rm CO}$ values from the updated dust core sample with gas-phase oxygen abundance measurements (O/H) of individual H II regions associated with a subset of these GMCs, we update the result presented in Bosomworth et al. (2025). This allows us to further constrain the metallicity dependence of $\alpha'_{\rm CO}$.

This chapter is structured as follows. In Section 3.2, we describe our SMA observations and the selection of our target sources. In Section 3.3, we outline our methodology and data analysis procedures. In Section 3.4, we present the results of our analyses, including $L_{\mathrm{CO}(2-1)}$ for both ^{12}CO and ^{13}CO, along with the corresponding measurements of M_{dust} and α'_{CO}. Additionally, we perform a virial analysis of the dust cores and investigate the metallicity dependence of $\alpha'_{^{12}\mathrm{CO}}$. Finally, in Section 3.5, we present our summary and conclusions.

3.2 Observations

Observations were obtained from an SMA large program targeting individual resolved GMCs in M31. This survey used the SMA in the subcompact configuration, which achieved a synthesized beam size of $4\farcs5 \times 3\farcs8$ ($\approx$ 15 pc). Occasionally, one or two antennas were out of service due to technical issues, which increased the typical beam size to $\approx 8'' \times 5''$ ($\approx$ 30 $\times$19 pc), still sufficient to resolve individual GMCs. At a frequency of 230-GHz (1.3 mm), the bandwidth was 32 GHz for the first two observing runs and was subsequently increased to 48 GHz for the final two runs. Within this frequency range, we have access to thermal dust continuum emission and the ^{12}CO$(2-1)$, ^{13}CO$(2-1)$, and C^{18}O$(2-1)$ molecular lines. Analysis and results from the first two observing runs are presented by Forbrich et al. (2020) and Viaene et al. (2021).

As the entire galaxy could not be observed within a reasonable time frame (this would require 10000 pointings and 60000 hours of observing time), targets were selected from the HELGA dust continuum survey of *Herschel*-identified GMAs (Kirk et al. 2015). The targets were chosen to cover a representative range of *Herschel* fluxes and physical cloud properties present throughout the M31 disc. Toward the beginning of the survey, it was found that the likelihood of detecting dust continuum emission on $\approx$ 15 pc scales was not strongly correlated with *Herschel* flux on $\approx$ 100 pc scales, nor was it dependent on position within the disc (Forbrich et al. 2020). The spatial distribution of the SMA-observed GMAs across M31 are displayed in Figure 3.1, overlaid on the Spitzer MIPS Infrared 24 microns image (Gordon et al. 2006). These observations produced dust detections from GMCs distributed across the disc of M31, spanning a wide range of galactocentric radii and *Herschel* fluxes.

Data were collected from 100 pointings toward 80 targets over four fall seasons from 2019 to 2022. Each source was observed for $\approx$ 6 hours, and the target sensitivity of 0.20 mJy beam^{-1} to dust continuum was consistently achieved. The typical root-mean-squared (rms) values reached for the

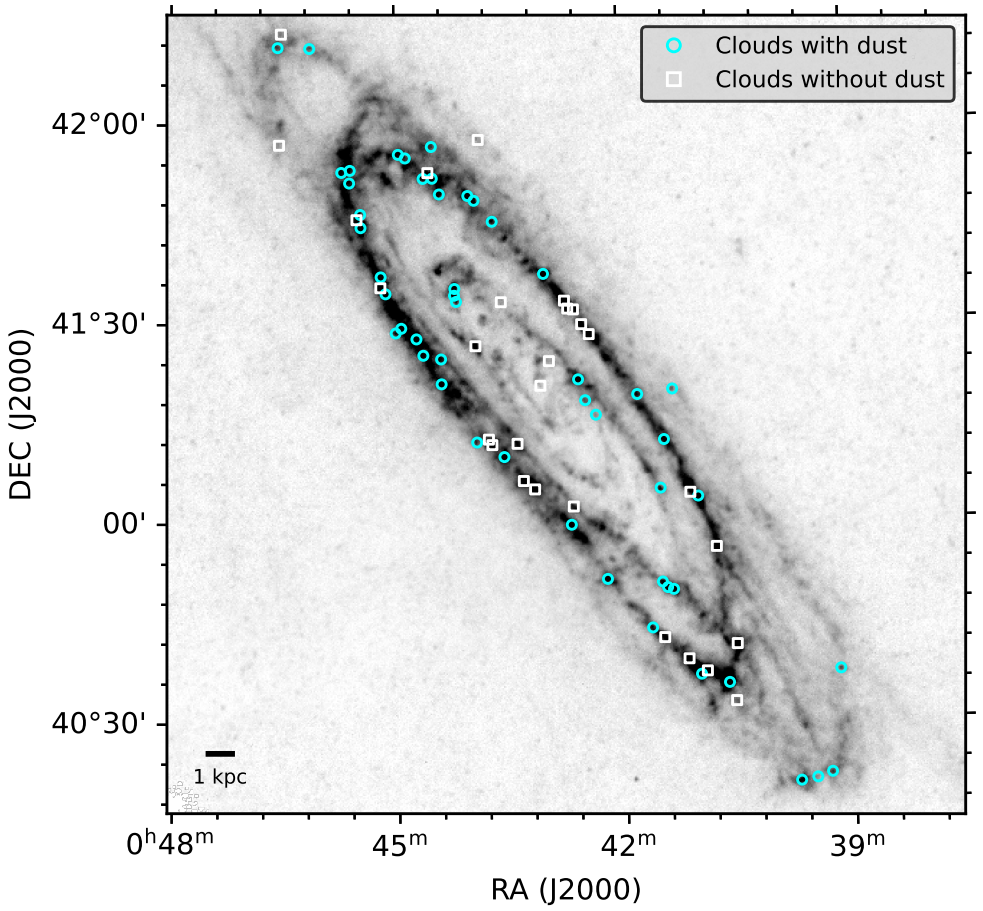

FIGURE 3.1: Locations of SMA-observed GMAs (Kirk et al. 2015) over-plotted onto the *Herschel* Spectral and Photometric Imaging Receiver (SPIRE) 500-micron image (Fritz et al. 2012), with GMAs for which we obtained dust detections displayed as open circles, and GMAs observed but with no dust detections displays as filled circles. The 1 kpc scalebar assumes the distance to M31 to be 780 kpc; (Stanek and Garnavich 1998).

^{12}CO(2−1) and ^{13}CO(2−1) molecular lines respectively are 0.86 Jy beam^{-1} and 0.23 Jy beam^{-1} (0.06 K and 0.04 K), per $\approx \Delta$ 1 km s^{-1} channel. We obtained dust continuum detections associated with GMCs for 51 of the targeted GMAs. A typical resolution of $\approx$ 15 pc was achieved. Two receivers were used, RxA and RxB, tuned to local oscillator frequencies of 225.55 GHz and 233.55 GHz, respectively. This provided a CO spectral sampling of 140.0 kHz per channel, and initially a continuous bandwidth between 213.55 and 245.55 GHz. Subsequently, the coverage was extended to between 209.5 GHz and 249.5 GHz, with an overlap of 8 GHz.

These data were obtained in the form of spectral cubes. Channels containing ^{12}CO(2 − 1) and ^{13}CO(2−1) emission were extracted and analysed separately using the Millimeter Interferometer Reduction Interactive Data Language (MIR IDL) software for the SMA. Emission lines from other molecular and recombination transitions that fall within the bandpass (e.g., $H_2CO(3-2)$ and H30α) are extremely weak and do not contribute to continuum contamination. Continuum images

were computed from the average of the line-free channels. For ^{12}CO(2 − 1) and ^{13}CO(2 − 1), data cubes containing the velocity information were produced, from which integrated-intensity (moment 0) maps were created by summing over a velocity interval determined by the CO line profiles. CO line fluxes and luminosities (and their respective uncertainties) are calculated as described in Section 3.3.2. The data reduction steps as detailed in Forbrich et al. (2020) are as follows:

- **Primary phase and amplitude gain calibration -** Corrects observations for artefacts due to the instrument and variations in atmospheric conditions by observations of bright calibrator sources.
- **Absolute flux calibration -** Calibrates the flux scale using observations of sources with known fluxes.
- **Passband calibration -** Corrects transmission as a function of frequency channel using observations of a bright point source, removing variations in the instrumental response between individual channels to ensure a flat bandpass across the bandwidth.
- **Raw data smoothing and editing -** Prepares data for imaging by removing statistical noise and outliers.

Raw spectra were binned to a velocity resolution of 1.3 km s^{-1}. Additional spectral flagging, inversion (smoothing to 1.5 km s^{-1}), and CLEANing were performed in Miriad[1]. Quasars were used as bright calibrator sources, and the flux calibration sources were Neptune and Uranus. Data are in the form of spectral cubes, and the CO-contaminated channels were extracted and analysed using the MIR IDL software for the SMA. Raw spectra were binned to a velocity resolution of 1.3 km s^{-1}. Additional spectral flagging, and CLEANing were performed in Miriad. Integrated intensity (moment 0) maps were created for both ^{12}CO(2 − 1) and ^{13}CO(2 − 1) for all sources.

Candidate Contribution

The SMA observations, raw data reduction with Miriad and MIR-IDL, and computation of the CO moment 0 maps were all carried out by members of the collaboration before the start of this project. A pipeline to calculate $M_{\rm dust}$ and moment 0 map-based $L_{\rm CO}$ was created by members of the collaboration and applied to the full SMA sample by the candidate. The line-profile-derived $L_{\rm CO}$ measurements, and further scientific analysis was performed by the candidate.

[1] cfa.harvard.edu/sma/miriad/

3.3 Methodology

In this section, we outline the extraction of thermal dust emission detections from continuum images and refine the final sample for further analysis. The sample presented here includes those previously reported in Viaene et al. (2021), along with new observations and updated measurements obtained using the methodology outlined below. We make use of both dust continuum images and CO moment 0 maps to ensure that our detected dust continuum cores are associated with GMCs. In addition, CO velocity information is used to extract spectral line profiles for $L_{\rm CO}$ measurements. For the analysis of GMCs and ^{13}CO clumps, as defined by their CO emission contours from this same dataset, we refer to Lada et al. (2024).

3.3.1 Dust Core Extraction

To identify and extract individual GMCs and dust cores from each observation, we define contours based on the map rms, σ. The rms of the moment 0 map reflects the noise of the velocity integrated map, measured from the corners of the image where emission is weakest. The high sensitivity achieved in the ^{12}CO(2 – 1) data means that the 3σ contours typically trace the entire CO-emitting area of each GMC (Viaene et al. 2021). The ^{12}CO(2 – 1) emission is therefore not limited by sensitivity, but by the extent of the CO emission from a cloud. A watershed segmentation was used to identify and extract individual dust cores from each observation, which places markers at all pixels with values $< 1\sigma$. These correspond to the local minima, from which the algorithm 'floods' the image, until it reaches pixels with values $\geq 3\sigma$. This results in isolated 3σ contours corresponding to separate dust cores.

Because the dust continuum images and CO moment 0 maps have identical astrometry, we no longer depend on the global image statistics to identify dust continuum emission. Instead, we perform a targeted search within the GMC boundaries. We employ a 2.5σ detection threshold, lower than the 3σ threshold used by Forbrich et al. (2020) and Viaene et al. (2021). A 2.5σ threshold improves the sensitivity to dust emission compared to previous analyses and introduces only minimal contamination from unrelated foreground or background sources. Applying this criterion to the entire survey, including the observations previously analysed by Forbrich et al. (2020) and Viaene et al. (2021), more than doubles the size of the previous sample.

At the achieved sensitivity, dust emission and ^{13}CO do not trace the entire extent of each GMC, and we find that a single GMC can have multiple associated dust cores and ^{13}CO clumps. Dust

continuum emission at the 2.5σ level was detected in 35 targeted GMAs, associated with 57 separate GMCs. Compared to the previous sample from Viaene et al. (2021), the complete sample of dust cores has increased from 32 to 71, and the number of resolved cores has increased from 10 to 26.

We define a resolved dust core as one which has a 2.5σ contour at least 20% larger than the synthesised beam and analyse these separately from the unresolved sources. This allows us to evaluate the extent to which measurements may be affected by differences in the beam-filling factors of CO and dust. Finally, pixels outside the half-power primary beam (of radius $r = 27.5''$, or ≈100 pc) are removed, except for one source (K098Bd1; see Figure B.1) where we find a resolved dust detection associated with a GMC whose dust and CO contours both partially overlap the edge of the half-power primary beam.

3.3.2 CO Luminosity Measurements

To calculate the CO luminous mass, $M_{\rm lum}$, we use CO line profiles extracted from the same regions of each GMC as the dust emission. We extract line profiles for ^{12}CO(2 − 1) and ^{13}CO(2 − 1) Over a 100 km s^{-1}-wide band, centred on the line peak, and computed within the boundaries of each individual dust core. In the case of resolved dust cores, we extract the mean line profile of all pixels within the 2.5σ dust core boundary. For unresolved dust cores, we follow the same method but instead extract the line profile of the peak pixel within each contour. The line profiles are well resolved in velocity, and their line widths are comparable to those of MW GMCs (e.g., ≈ 4 − 6 km s^{-1}; Rice et al. 2016), except for source K008, which contains two dust cores with extracted ^{12}CO line widths of ≈ 18 and ≈ 31 km s^{-1}. The CO intensity, $I_{\rm CO}$, of each dust core is measured by integrating under a Gaussian fit to the line profile. We then calculate $L_{\rm CO}$ following Equation 3.1,

$$L_{\rm CO} = I_{\rm CO} \times A_{\rm source}, \tag{3.1}$$

where $A_{\rm source}$ is in pixels and corresponds to the 2.5σ contour area for spatially resolved sources, and the beam area for unresolved sources.

Previous $L_{\rm CO}$ measurements reported by Forbrich et al. (2020) and Viaene et al. (2021) were derived from moment 0 maps. Unlike the dust emission, our ^{12}CO(2 − 1) observations are not

limited by sensitivity, and the emission is detected in all moment 0 images. Given the strength of the ^{12}CO(2 − 1) emission, regions of images that are free of ^{12}CO emission are much less common than for dust and ^{13}CO emission. Note that fainter (<3σ) ^{12}CO emission is present over the majority of each image, whilst bright ($\geq 3\sigma$) ^{12}CO emission is confined to GMCs. This makes an accurate determination of the ^{12}CO image rms difficult. The updated method used in this work improves the uncertainty estimate of $I_{\rm CO}$, which is calculated following:

$$\delta I_{\rm CO} = \sigma_{\rm channel}\, \Delta v \sqrt{N_{channel}} \tag{3.2}$$

where $\sigma_{\rm channel}$ is the rms noise per channel calculated from two 20 km s^{-1} ranges on both sides of the CO line profile, Δv is the channel width (1.3 km s^{-1}) and N is the number of channels summed over the line. This ratio is multiplied by the dust core area (resolved sources) or the beam area (unresolved sources) to calculate the uncertainty in $L_{\rm CO}$. The images' rms is still used to define the 3σ contours for CO emission.

The final sample of dust cores can be further refined based on their respective CO line profiles. The presence of multiple peaks within a line profile indicates that there are multiple sources along the line of sight contributing to the emission in the moment 0 maps and dust continuum image. In these cases, we cannot determine the fraction of dust emission corresponding to each source, and therefore the measured dust properties may not reflect those of an individual GMC. For this reason, we define a subsample of dust cores with approximately single-Gaussian ^{12}CO and ^{13}CO line profiles (hereafter referred to as '1G,' following the terminology of Lada et al. 2024). Although an estimate of $\alpha'_{^{12}\rm CO}$ for these dust cores could be made, this introduces additional uncertainties due to the unknown dust emission fraction corresponding to each CO velocity component. This criterion also excludes 12 dust cores for which the ^{13}CO peak is not present in the spectrum. As ^{13}CO is expected to spatially align with the dust emission (see Section 3.4.1 and Forbrich et al. 2020; Viaene et al. 2021), this further refines our sample to the highest-quality data to ensure reliable measurements. The 1G sample excludes 26 sources (5 resolved) from the full sample, including 15 from the Viaene et al. (2021) sample.

Compared to the previous sample from Viaene et al. (2021), our final sample of dust cores with 1G CO line profiles in both ^{12}CO and ^{13}CO has increased from 32 to 46 and the number of resolved cores has increased from 10 to 21. The 1G source requirement eliminated 25 sources (4 resolved), including 15 from the Viaene et al. (2021) sample. The removal of the multi-component

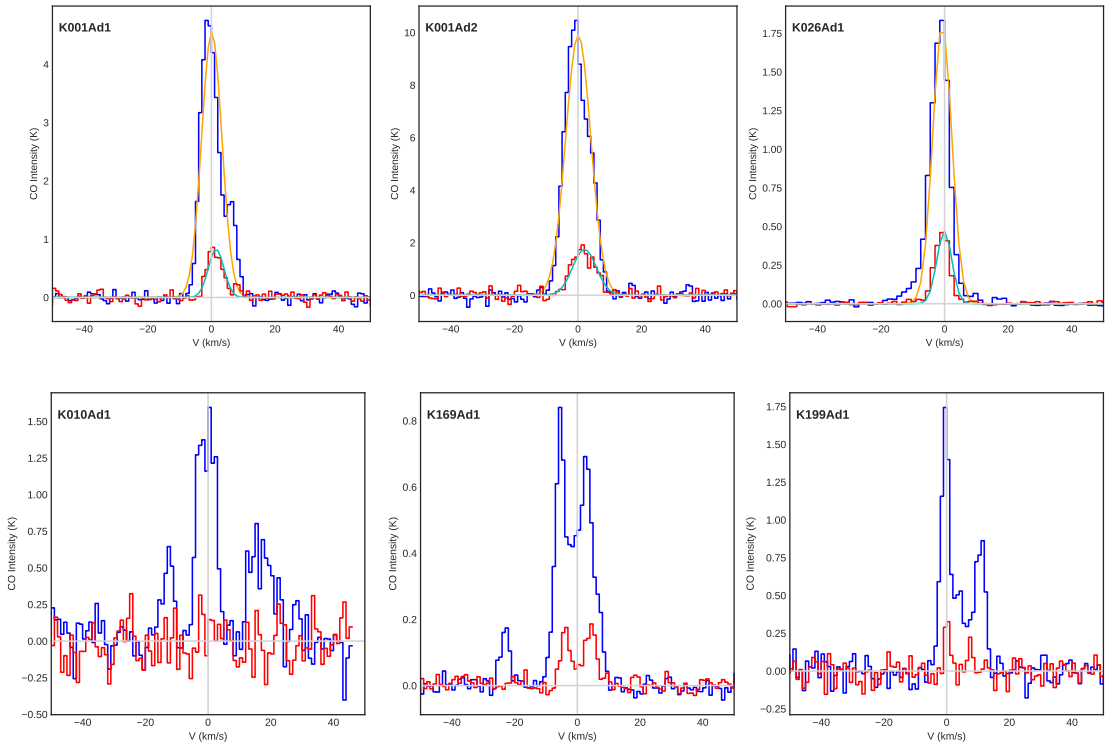

FIGURE 3.2: CO(2 – 1) line profiles for six individual dust cores. The top panels show three dust cores from the 1G sample, while the bottom panels show three dust cores with multiple-component CO line profiles. Both ^{12}CO and ^{13}CO spectral lines are displayed with the corresponding Gaussian fits.

and weak ^{13}CO dust cores has little effect on our scientific conclusions; including these only introduces additional noise and scatter about the mean $\alpha'_{^{12}\mathrm{CO}}$ in Section 3.4.3. Additionally, dust cores with no/ weak ^{13}CO cannot be used to calculate M_{vir} for Section 3.4.4 due to the lack of a ^{13}CO velocity dispersion measurement.

In Figure 3.2, we show CO line profiles for 1) three dust cores from our 1G sample and 2) three dust cores with multiple-component line profiles. We display both ^{12}CO and ^{13}CO line profiles with corresponding Gaussian fits for the 1G sources, from which the CO intensity was measured. The line profiles for the entire dust core sample are displayed in Figure B.1, along with the corresponding dust continuum images.

Whether a source was classified as 1G was determined by individual inspection of each dust core's ^{12}CO and ^{13}CO line profile. We note that there are some uncertainties from line blending or optical depth effects that may lead to an imperfect Gaussian in some sources. Minor deviations from a perfect Gaussian shape were allowed if the secondary peak was judged to be small and unlikely to have a significant contribution to the dust emission. Lada et al. (2024) calculated

formal uncertainties in velocity dispersions and integrated intensities for CO line profiles extracted from this same survey, corresponding to entire GMCs rather than dust cores, as is done in this work. For ^{12}CO, the uncertainties in measurements of line dispersion and intensity are 3% and 8%, respectively. For ^{13}CO, uncertainties of 4% and 15% were found. These relatively small uncertainties highlight the high quality of these spectra. Therefore, we conclude that the uncertainties in these Gaussian fits are likely similar.

3.3.3 Dust Mass Measurements

To calculate the dust mass of an individual core, $M_{\rm dust}$, we use the modified blackbody emission model from Hildebrand (1983):

$$M_{\rm dust} = \frac{S_\nu D^2}{\kappa_\nu B_\nu(T_{\rm dust})}. \tag{3.3}$$

Here, $D = 780$ kpc (Stanek and Garnavich 1998), and S_ν is the continuum flux density measured within the 2.5σ contour, in units of Jy beam^{-1}, and $B_\nu(T)$ is the emission spectrum of a blackbody as a function of frequency. We adopt a dust opacity of $\kappa_\nu = 0.0425$ m^2 kg^{-1} from the THEMIS dust model (Jones et al. 2017) at 230-GHz, which has been calibrated using *Planck* data and the MW dust constraints of Ysard et al. (2015). This dust model has previously been shown to perform well in radiative transfer modeling of M31 by Viaene et al. (2017). Finally, we assume a dust temperature of $T_{\rm dust} = 18$ K, the median value derived for 2015's GMAs.

To measure $M_{\rm dust}$ from our continuum images, we must first calculate S_ν for each dust core. For spatially resolved sources, we calculate the average flux from all pixels within each 2.5σ contour and multiply this value by the source area (in pixels) to obtain S_ν. For unresolved sources, we use the peak pixel flux and multiply this by the beam area (in pixels).

There is a possible uncertainty associated with the assumption of a constant dust temperature; therefore, the magnitude of this effect was previously assessed by Viaene et al. (2021). By assuming constant dust temperatures of $T_{\rm dust} = 15$ K and $T_{\rm dust} = 25$ K (the range of dust temperatures found for GMAs studied by Kirk et al. 2015) in the dust mass calculations, Viaene et al. (2021) found that a ±5 K variation in dust temperature does not significantly affect the calculated values of $\alpha'_{\rm CO}$ (see Figure 4 of Viaene et al. 2021).

In Equation 3.3, $M_{\rm dust} \propto D^2$, and so the assumption that all GMCs in M31 are at a constant distance from us introduces uncertainties. However, the variation in the relative distances to M31 GMCs is much smaller than the mean line-of-sight distance to M31. For a cloud at galactocentric radius (r), the maximum offset from the assumed distance is $\Delta d = r \sin i$, where i is the inclination angle of M31 (77°; Walterbos and Kennicutt 1987). The largest value of r in our sample is $\approx r = 16$ kpc (GMA K291). This yields a maximum possible offset of $\Delta d = 15.6$ kpc, an uncertainty in D of 2%. This corresponds to a maximum uncertainty of 4% in M_{dust}. We therefore conclude that distance variations between sources do not significantly affect our estimates of $M_{\rm dust}$.

3.4 Results and Discussion

The following section presents the results of our analysis of the dust core sample. After applying the aforementioned methodology to this sample of 71 dust cores, we obtained the size, continuum flux, and $L_{\rm CO}$ of each individual detection. We first combine $M_{\rm dust}$ with the corresponding CO(2-1) emission to measure $\alpha'_{\rm CO}$ (i.e., $M_{\rm dust}/L_{\rm CO}$) for both ^{12}CO and ^{13}CO of all the dust cores. For spatially resolved dust cores, we perform a virial analysis to determine whether these are self-bound by gravity and approximately satisfy the virial theorem. Finally, we compare our results to the H II region metallicities from Bosomworth et al. (2025) to update the direct test of the metallicity dependence of $\alpha'_{\rm CO}$.

3.4.1 Dust Continuum Images and CO Line Profiles

Dust continuum images of the 51 observed GMAs containing one or more dust cores, along with the CO line profiles of any associated dust cores are displayed in Appendix B, with an example provided in Figure 3.3. CO contours in Figure 3.3 are from the CO(2-1) moment 0 maps, which have identical astrometry and (u, v) coverage to the continuum images, allowing us to directly compare their spatial extent.

In all maps, the ^{12}CO emission is more spatially extended than the ^{13}CO emission, which is in turn more extended than the continuum emission. This indicates that, at the sensitivity of our observations, we detect ^{13}CO and dust continuum emission from the higher column density regions of GMCs, while ^{12}CO traces the entire extent of the molecular cloud. NOEMA images presented by Forbrich et al. (2023) show that the dust continuum emission in these observations

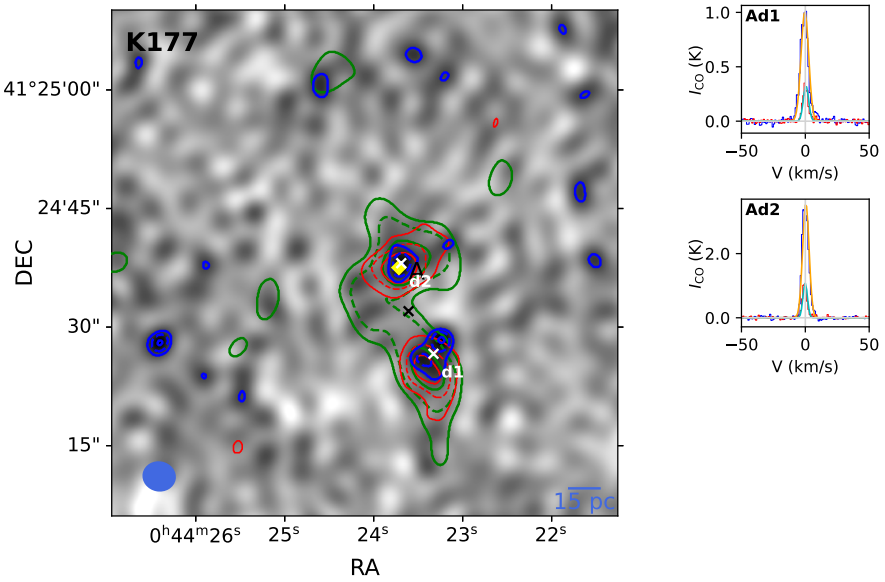

FIGURE 3.3: *Left,* SMA maps of dust continuum emission of individual Kirk et al. (2015) GMAs in M31, for fields which contain one or more dust cores. Blue contours display dust continuum emission at 2.5σ, 3.5σ and 4.5σ, where σ is the continuum image background rms, the values given in Table 3.1. Green contours display ^{12}CO at 3, 6, 12, 24 and 48σ. Red contours display ^{13}CO at 3, 6 and 10σ. The corresponding centre of mass (by area) of individual GMCs as traced by ^{12}CO at 3σ are marked by black 'x's', and by white 'x's' for individual dust cores as traced by dust continuum at 2.5σ. *Right,* Corresponding CO line profiles extracted from within individual dust cores, for both ^{12}CO and ^{13}CO. We mark any H II regions, identified from optical spectroscopy (Bosomworth et al. 2025), which are associated with GMCs containing a 1G dust core as yellow diamonds (see Section 3.4.5). Gaussian fits to line profiles are displayed for the 1G sample. The complete figure set (51 images) is presented in Appendix B.

is spatially similar to the HCN and HCO$^+$ emission, both of which have high dipole moments compared to CO and are assumed to trace dense gas (i.e. $n(\mathrm{H_2}) \gtrsim 10^4$ cm^{-3}), indicating that we are probing similarly dense material at the available sensitivity.

3.4.2 Dust Core Properties

The left panel of Figure 3.4 displays the dust mass distribution for the entire sample of 71 dust cores, and the right panel shows the dust mass distribution for the 47 1G dust cores only, with the numbers of spatially resolved and unresolved cores displayed separately. These include dust cores previously reported by Viaene et al. (2021), but with updated dust masses calculated using the 2.5σ detection threshold, as described in Section 3.3.3. Resolved dust cores lie primarily in the dust mass range of $M_{\mathrm{dust}} \approx 200 - 700$ M$_\odot$. The multi-component (hereafter 'multi-G') sample contains only five resolved sources. By comparing the two histograms in Figure 3.4, we conclude that the majority of the non-1G sources are unresolved and have $M_{\mathrm{dust}} \lesssim 200$ M$_\odot$. The

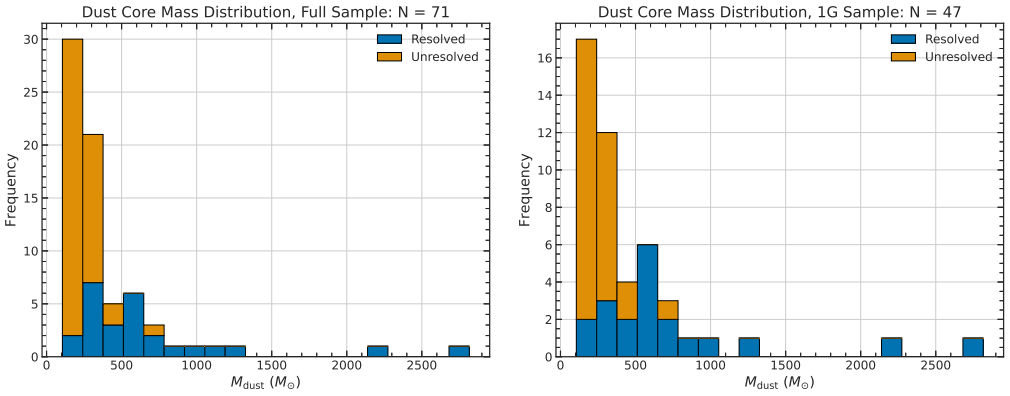

FIGURE 3.4: Histogram of dust masses for *left,* our full sample of dust cores, of which 26 are spatially resolved and 45 unresolved and *right,* our 1G sample of dust cores, of which 20 are spatially resolved and 27 unresolved.

remaining dust cores in our sample are resolved, and three have $M_{\rm dust} > 1000$ M$_\odot$. From lowest to highest mass, these are identified as K026Ad1, K191Ad1, and K213Ad1.

We present the properties of individual dust cores from our final sample in Table 3.1, derived as described above. Dust core nomenclature is, firstly, based on the corresponding Kirk et al. (2015) GMA name. Within a given GMA, each GMC is labelled alphabetically as A, B, C, etc., from highest to lowest CO mass. Finally, we label each individual dust core within each GMC as d1, d2, etc., in order of highest to lowest $M_{\rm dust}$. The deconvolved radii of our resolved dust cores range from $\approx$ 10 to 23 pc, while the deconvolved radii of the 3σ ^{12}CO contours range from $\approx$ 26 to 61 pc, confirming that we do not trace the entire GMCs with dust emission.

Despite the identical astrometry, the peaks of CO and dust emission do not always spatially align. One possible explanation, proposed by Viaene et al. (2021), is that the dust peaks may correspond to hotter dust heated by ongoing star formation at the edges of GMCs, and are therefore spatially separated from the cold gas. The possibility that continuum emission originates from an associated H II region and is contaminated by free-free emission has already been investigated by Forbrich et al. (2023), who found that at 230-GHz, free-free emission contributes only 6 – 23% of the continuum flux of clouds with VLA-detected H II regions.

The relative sensitivity of our observations to different tracers is crucial for understanding the structure of molecular gas in GMCs. Since the CO and continuum observations were obtained simultaneously with the same calibration, imaging, and astrometry, experimental offsets are eliminated. From the areas of the 2.5σ contours for dust emission and the 3σ contours for CO, we find that dust traces 10 – 60% of the area traced by ^{12}CO, and 35 – 80% of the area

TABLE 3.1: Dust core properties.

Source	RA, Dec.[a]	Radius (deconv.)	S_ν	rms	Beam Size	$M_{\rm dust}$	$I_{^{12}\rm CO}$	$I_{^{13}\rm CO}$
	J2000	pc	mJy	mJy beam^{-1}	a × b (arcsec^2)	$M_\odot$	K km s^{-1}	K km s^{-1}
K001Ad1	00:39:10.2, +40:37:22.2	7.5	0.9 ± 0.2	0.2	4.4 × 3.4	280 ± 66	28.5 ± 0.2	4.0 ± 0.2
K001Ad2	00:39:09.8, +40:37:16.8	4.8	0.6 ± 0.2	0.2	4.4 × 3.4	207 ± 66	34.9 ± 0.3	5.8 ± 0.2
K008Ad1	00:42:27.2, +41:18:18.8	7.2	0.5 ± 0.1	0.1	4.1 × 3.6	170 ± 40	8.7 ± 0.5	0.2 ± 0.1
K008Ad2	00:42:28.8, +41:18:22.3	4.3	0.3 ± 0.1	0.1	4.1 × 3.6	115 ± 40	30.5 ± 0.3	0.2 ± 0.1
K010Ad1	00:42:34.5, +41:21:09.0	4.6	0.5 ± 0.1	0.1	3.9 × 3.4	158 ± 45	4.1 ± 0.3	0.2 ± 0.1
K026Ad1*	00:41:29.7, +41:04:56.2	20.8	4.0 ± 0.4	0.2	4.5 × 4.0	1315 ± 125	13.5 ± 0.1	2.8 ± 0.1
K029Ad1	00:42:20.5, +41:16:02.5	5.1	0.5 ± 0.2	0.2	4.1 × 3.5	177 ± 51	16.4 ± 0.6	0.8 ± 0.2
K060Ad1	00:41:00.1, +40:36:59.2	5.4	0.6 ± 0.2	0.2	4.2 × 3.5	183 ± 60	7.7 ± 0.2	1.4 ± 0.2
K060Ad2	00:40:59.5, +40:36:45.5	4.6	0.5 ± 0.2	0.2	4.2 × 3.5	154 ± 60	1.4 ± 0.2	0.2 ± 0.1
K063Ad1*	00:40:40.1, +40:35:40.5	14.1	1.0 ± 0.2	0.1	3.8 × 3.5	325 ± 54	6.7 ± 0.1	0.9 ± 0.1
K063Ad2	00:40:39.2, +40:35:38.9	4.6	0.4 ± 0.1	0.1	3.8 × 3.5	118 ± 32	8.0 ± 0.2	1.0 ± 0.2
K063Ad3	00:40:39.0, +40:35:31.0	4.7	0.3 ± 0.1	0.1	3.8 × 3.5	105 ± 32	12.2 ± 0.3	1.7 ± 0.2
K067Ad1*	00:41:38.1, +40:43:56.6	10.1	0.7 ± 0.2	0.2	4.2 × 3.7	213 ± 60	11.0 ± 0.1	2.2 ± 0.1
K071Ad1*	00:41:00.8, +41:03:59.4	12.6	1.9 ± 0.3	0.2	4.0 × 3.6	627 ± 115	11.3 ± 0.2	2.4 ± 0.1
K071Ad2	00:41:00.8, +41:03:36.4	4.3	0.8 ± 0.2	0.2	4.0 × 3.6	267 ± 78	23.7 ± 1.3	3.1 ± 0.2
K078Bd1*	00:41:28.0, +41:12:06.9	10.1	0.8 ± 0.2	0.2	4.0 × 3.4	248 ± 71	4.4 ± 0.2	0.4 ± 0.1
K081Ad1	00:41:47.4, +41:18:55.2	6.9	0.7 ± 0.2	0.2	4.0 × 3.5	232 ± 66	18.5 ± 0.3	3.7 ± 0.2

Table 3.1 (continued)

Source	RA, Dec.	Radius (deconv.)	S_ν	rms	Beam Size	$M_{\rm dust}$	$I_{^{12}\rm CO}$	$I_{^{13}\rm CO}$
	J2000	pc	mJy	mJy beam^{-1}	a × b (arcsec^2)	$M_\odot$	K km s^{-1}	K km s^{-1}
K092Ad1*	00:41:22.1, +40:49:52.2	18.0	1.6 ± 0.2	0.2	6.9 × 5.0	522 ± 76	5.4 ± 0.1	1.4 ± 0.1
K093Ad1*	00:41:25.7, +40:49:55.9	11.7	1.3 ± 0.3	0.2	4.2 × 3.6	427 ± 96	9.2 ± 0.1	2.2 ± 0.4
K094Ad1	00:41:29.2, +40:50:49.6	6.3	0.5 ± 0.2	0.2	4.2 × 3.3	166 ± 56	19.9 ± 0.2	3.5 ± 0.1
K098Ad1	00:43:02.8, +41:37:21.5	5.0	0.7 ± 0.2	0.2	4.0 × 3.6	223 ± 80	19.0 ± 0.3	2.5 ± 0.2
K098Bd1*	00:42:59.5, +41:37:07.3	13.4	2.3 ± 0.4	0.2	4.0 × 3.6	746 ± 125	27.4 ± 0.2	5.3 ± 0.2
K119Bd1*	00:43:34.4, +41:09:43.9	18.4	3.1 ± 0.3	0.2	3.9 × 3.5	1002 ± 97	8.0 ± 0.1	1.7 ± 0.1
K120Ad1*	00:43:55.1, +41:12:06.5	10.2	0.9 ± 0.2	0.2	4.0 × 3.4	280 ± 73	5.0 ± 0.1	1.1 ± 0.1
K121Dd1	00:42:43.3, +40:59:40.5	5.2	0.4 ± 0.1	0.1	3.6 × 3.2	127 ± 38	1.1 ± 0.2	0.3 ± 0.1
K134Ad1	00:44:23.0, +41:49:18.0	8.2	0.9 ± 0.3	0.3	5.5 × 4.7	299 ± 92	8.6 ± 0.2	1.7 ± 0.1
K134Ad2	00:44:23.8, +41:49:28.5	5.6	0.8 ± 0.3	0.3	5.5 × 4.7	250 ± 92	6.0 ± 0.1	0.7 ± 0.1
K136Ad1*	00:44:29.6, +41:51:43.8	21.7	3.3 ± 0.3	0.2	4.4 × 3.9	1086 ± 97	10.3 ± 0.4	2.3 ± 0.1
K136Ad2	00:44:31.3, +41:51:53.1	4.3	0.5 ± 0.1	0.2	4.4 × 3.9	173 ± 42	8.6 ± 0.3	1.6 ± 0.1
K138Ad1*	00:44:36.9, +41:51:42.6	13.5	2.0 ± 0.2	0.1	3.5 × 3.3	641 ± 69	20.0 ± 0.1	4.0 ± 0.1
K142Ad1	00:44:57.8, +41:55:24.4	8.6	0.8 ± 0.2	0.2	8.1 × 5.0	259 ± 79	0.6 ± 0.1	0.1 ± 0.1
K142Ad2	00:44:56.9, +41:55:20.6	6.6	0.8 ± 0.2	0.2	8.1 × 5.0	246 ± 79	0.6 ± 0.1	0.1 ± 0.1
K143Ad1	00:44:51.2, +41:54:38.7	4.8	0.7 ± 0.2	0.2	4.0 × 3.5	231 ± 67	9.9 ± 0.2	0.9 ± 0.2
K149Ad1	00:45:36.6, +41:51:05.1	8.5	0.6 ± 0.2	0.2	3.9 × 3.5	178 ± 57	11.1 ± 0.2	2.0 ± 0.1

Table 3.1 (continued)

Source	RA, Dec.	Radius (deconv.)	S_ν	rms	Beam Size	$M_{\rm dust}$	$I_{^{12}\rm CO}$	$I_{^{13}\rm CO}$
	J2000	pc	mJy	mJy beam^{-1}	a × b (arcsec^2)	$M_\odot$	K km s^{-1}	K km s^{-1}
K151Ad1	00:45:27.0, +41:44:26.8	7.6	0.6 ± 0.2	0.2	8.1 × 5.0	200 ± 68	8.4 ± 0.1	0.7 ± 0.1
K153Ad1	00:45:27.5, +41:46:25.8	8.8	0.8 ± 0.2	0.2	8.0 × 4.9	253 ± 66	11.9 ± 0.1	1.4 ± 0.1
K153Ad2	00:45:27.7, +41:46:38.9	5.3	0.6 ± 0.2	0.2	8.0 × 4.9	182 ± 66	9.2 ± 0.1	1.0 ± 0.1
K154Ad1*	00:45:36.0, +41:53:00.4	13.4	1.1 ± 0.2	0.1	4.0 × 3.7	347 ± 67	5.1 ± 0.1	0.8 ± 0.1
K157Ad1*	00:45:43.7, +41:52:43.9	7.5	0.9 ± 0.2	0.2	4.2 × 3.7	280 ± 58	11.7 ± 0.4	1.9 ± 0.1
K157Bd1	00:45:41.8, +41:52:45.3	11.1	1.0 ± 0.2	0.2	4.2 × 3.7	321 ± 74	6.9 ± 0.2	0.2 ± 0.1
K157Bd2	00:45:44.8, +41:52:40.8	4.9	0.6 ± 0.2	0.2	4.2 × 3.7	202 ± 58	7.6 ± 0.1	1.1 ± 0.1
K160Ad1	00:45:07.7, +41:34:20.7	10.8	1.0 ± 0.2	0.2	8.1 × 5.0	324 ± 61	6.1 ± 0.1	1.0 ± 0.2
K160Bd1	00:45:09.2, +41:34:33.1	6.5	0.7 ± 0.2	0.2	8.1 × 5.0	229 ± 61	4.0 ± 0.3	0.5 ± 0.1
K160Cd1	00:45:08.6, +41:34:52.8	14.6	1.2 ± 0.2	0.2	8.1 × 5.0	389 ± 61	5.2 ± 0.6	0.6 ± 0.1
K162Ad1*	00:45:11.5, +41:36:58.0	14.3	1.4 ± 0.2	0.2	5.2 × 4.3	463 ± 77	23.1 ± 0.5	3.6 ± 0.6
K162Ad2	00:45:10.8, +41:37:08.0	6.7	0.6 ± 0.2	0.2	5.2 × 4.3	208 ± 58	16.6 ± 0.2	2.3 ± 0.4
K169Ad1*	00:44:38.2, +41:25:10.9	13.6	1.3 ± 0.2	0.1	3.6 × 3.3	434 ± 65	8.8 ± 0.2	1.7 ± 0.1
K170Ad1*	00:44:42.5, +41:27:36.8	15.2	1.7 ± 0.3	0.1	3.5 × 3.2	562 ± 84	15.2 ± 0.3	2.9 ± 0.1
K171Ad1	00:44:55.7, +41:29:14.7	7.4	0.8 ± 0.2	0.2	4.0 × 3.6	252 ± 69	15.5 ± 0.3	3.7 ± 0.2
K174Ad1	00:44:24.2, +41:21:04.8	7.5	0.9 ± 0.2	0.2	3.9 × 3.5	289 ± 56	6.7 ± 0.4	1.2 ± 0.1
K174Cd1	00:44:23.8, +41:20:29.2	4.8	0.7 ± 0.2	0.2	3.9 × 3.5	212 ± 56	4.0 ± 0.2	0.2 ± 0.1

Table 3.1 (continued)

Source	RA, Dec.	Radius (deconv.)	S_ν	rms	Beam Size	$M_{\rm dust}$	$I_{^{12}\rm CO}$	$I_{^{13}\rm CO}$
	J2000	pc	mJy	mJy beam^{-1}	a × b (arcsec^2)	$M_\odot$	K km s^{-1}	K km s^{-1}
K176Ad1*	00:45:00.2, +41:28:32.5	19.3	1.9 ± 0.3	0.2	8.1 × 5.0	624 ± 94	10.4 ± 0.1	1.8 ± 0.3
K177Ad1*	00:44:25.0, +41:24:47.9	9.8	0.4 ± 0.1	0.1	3.8 × 3.4	141 ± 35	7.5 ± 0.1	1.7 ± 0.1
K177Ad2	00:44:24.1, +41:24:42.8	7.2	0.4 ± 0.1	0.1	3.8 × 3.4	134 ± 29	18.5 ± 0.1	3.9 ± 0.1
K190Ad1*	00:44:30.3, +41:56:29.6	15.0	1.8 ± 0.2	0.2	4.9 × 4.2	598 ± 68	4.6 ± 0.1	0.4 ± 0.1
K191Ad1*	00:44:01.5, +41:49:11.2	16.0	6.9 ± 0.8	0.4	4.2 × 3.3	2270 ± 254	34.9 ± 0.4	6.6 ± 1.1
K192Ad1	00:43:55.9, +41:48:22.5	4.9	1.3 ± 0.4	0.3	4.0 × 3.7	411 ± 120	20.0 ± 0.3	4.8 ± 0.3
K199Ad1	00:43:42.0, +41:45:14.7	7.0	0.7 ± 0.2	0.2	4.0 × 3.6	233 ± 61	4.8 ± 0.4	0.5 ± 0.1
K213Ad1*	00:42:13.9, +40:51:17.2	22.9	8.6 ± 0.8	0.3	4.3 × 3.7	2816 ± 252	18.5 ± 0.1	3.3 ± 0.1
K238Cd1	00:44:10.8, +41:35:08.4	5.7	0.7 ± 0.2	0.2	7.8 × 4.9	217 ± 79	4.3 ± 0.2	0.4 ± 0.1
K239Ad1*	00:44:12.0, +41:34:11.5	15.8	1.1 ± 0.2	0.2	7.8 × 4.9	368 ± 80	1.5 ± 0.1	0.2 ± 0.1
K239Ad2	00:44:12.5, +41:34:07.3	3.4	0.7 ± 0.2	0.2	7.8 × 4.9	215 ± 70	10.6 ± 0.1	1.5 ± 0.2
K240Ad1	00:44:11.8, +41:33:07.4	4.8	0.7 ± 0.2	0.2	4.0 × 3.5	241 ± 72	7.0 ± 0.2	1.0 ± 0.1
K240Bd1	00:44:12.7, +41:33:13.8	4.9	0.7 ± 0.2	0.2	4.0 × 3.5	233 ± 72	7.7 ± 0.2	0.6 ± 0.2
K270Ad1*	00:39:18.4, +40:21:53.1	18.4	2.4 ± 0.2	0.1	3.5 × 3.2	787 ± 72	7.9 ± 0.1	1.2 ± 0.1
K270Ad2	00:39:19.3, +40:22:00.8	4.6	0.3 ± 0.1	0.1	3.5 × 3.2	109 ± 29	10.9 ± 0.1	1.5 ± 0.1
K273Bd1*	00:39:43.2, +40:20:43.0	11.1	0.9 ± 0.2	0.2	4.0 × 3.5	295 ± 73	0.8 ± 0.2	0.1 ± 0.1
K275Bd1	00:39:30.3, +40:21:09.8	5.4	0.8 ± 0.2	0.2	4.2 × 3.4	266 ± 68	9.5 ± 0.2	1.4 ± 0.1

Table 3.1 (continued)

Source	RA, Dec.	Radius (deconv.)	S_ν	rms	Beam Size	$M_{\rm dust}$	$I_{^{12}\rm CO}$	$I_{^{13}\rm CO}$
	J2000	pc	mJy	mJy beam^{-1}	a × b (arcsec^2)	$M_\odot$	K km s^{-1}	K km s^{-1}
K291Ad1	00:46:33.3, +42:11:31.5	9.5	1.1 ± 0.2	0.2	4.4 × 3.8	358 ± 66	5.4 ± 0.1	0.6 ± 0.1
K297Ad1	00:46:07.9, +42:11:26.0	15.0	2.1 ± 0.2	0.2	7.8 × 5.0	675 ± 62	12.6 ± 0.1	1.8 ± 0.1
K301Ad1*	00:41:19.3, +41:19:47.8	15.4	2.3 ± 0.2	0.1	3.5 × 3.2	755 ± 77	22.1 ± 0.1	4.2 ± 0.1

Notes. * Resolved dust cores.

[a] Right Ascention (RA) and Declination (Dec.) list the coordinates of the centre of mass of each dust core.

traced by ^{13}CO emission at the sensitivity achieved. We note that these ratios depend on the depth of the observations, so deeper observations would increase the areas traced by ^{13}CO and dust emission. Nevertheless, they demonstrate that, in this study, ^{13}CO and dust emission trace denser gas compared to ^{12}CO. The filamentary nature of molecular clouds implies that at these smaller scales we are probing higher column densities (Dame and Lada 2023). Furthermore, dust and ^{13}CO emission from this SMA survey is cospatial with HCN from NOEMA (Forbrich et al. 2023), further indicating that dust emission is tracing high-volume-density gas, compared to the more diffuse gas traced by ^{12}CO.

HCN is an assumed dense molecular gas tracer, tracing H_2 densities of $\gtrsim 3\times10^4$ cm^{-3}, compared to CO, which traces densities of $\gtrsim 300$ cm^{-3} (Gao and Solomon 2004). However, recent studies suggest that HCN can also be detected at lower densities (Pety et al. 2017; Dame and Lada 2023). Forbrich et al. (2023) found that the dust emission from the SMA discussed in this work and the HCN emission from NOEMA observations of a subset of the six M31 GMCs, are strongly spatially coincident, suggesting that both surveys independently trace the high-column-density gas of those GMCs, reflecting the limited sensitivity. Our observations are therefore consistent with the idea that, at the sensitivity achieved in this study, dust can trace dense molecular gas in GMCs, which is closely related to the SFR (e.g., Lada et al. 2010, 2012).

3.4.3 CO Conversion Factors

To convert from CO luminosity to molecular gas mass, we require a conversion factor, typically defined as $\alpha_{\rm CO} = M_{\rm mol}/L_{\rm CO}$, where $M_{\rm mol}$ is the molecular gas mass of the cloud. Knowledge of the CO conversion factor is critical when dust emission is not detected and only CO is available, such as in distant extragalactic sources. Here, we use dust emission to calibrate $\alpha_{\rm CO}$. From our observations of dust and CO emission, we can directly measure the dust mass-to-light ratio, $\alpha'_{\rm CO}$. With an assumed $R_{\rm g/d}$, $\alpha'_{\rm CO}$ can then be converted to $\alpha_{\rm CO}$ by $\alpha_{\rm CO} = \alpha'_{\rm CO} \times R_{\rm g/d}$.

For M31 GMCs, we calculate $\alpha'_{\rm CO}$ for both ^{12}CO(2 − 1) and ^{13}CO(2 − 1), denoted as $\alpha'_{^{12}\rm CO}$ and $\alpha'_{^{13}\rm CO}$, respectively. Since in all cases both values correspond to identical spatial areas, this provides insight into the differences between the two isotopologues as molecular gas tracers. Because ^{12}CO is the most easily observable and often the only tracer available for distant GMCs, calculating $\alpha'_{^{13}\rm CO}$ for the same sources allows us to assess potential optical depth effects in ^{12}CO by checking the consistency of the derived cloud dust masses.

We compute $\alpha'_{\rm CO}$ for the 1G dust core sample only, as for CO line profiles with multiple peaks, it is difficult to determine whether the dust emission originates from the GMC or from unrelated structures along the line of sight. Individual dust core $\alpha'_{^{12}\rm CO}$ are displayed in Figure 3.5 and reported in Table 3.2. A minimum uncertainty of 0.01 is adopted. The weighted mean $\alpha'_{^{12}\rm CO}$ for spatially resolved dust cores is $0.070 \pm 0.031\ M_\odot\ (\mathrm{K\,km\,s^{-1}\,pc^2})^{-1}$, which is in excellent agreement with the previous measurement of $0.064 \pm 0.029\ M_\odot\ (\mathrm{K\,km\,s^{-1}\,pc^2})^{-1}$ from Viaene et al. (2021). The mean $\alpha'_{^{12}\rm CO}$ of resolved and unresolved dust cores considered separately, shown in Figure 3.5, are consistent within 1σ. However, for unresolved dust cores, the source size cannot be reliably determined, introducing additional uncertainty in the corresponding measurements. The uncertainties reported in the mean $\alpha'_{\rm CO}$ represent the standard deviation of the individual dust core measurements and are similar in magnitude to those found by Viaene et al. (2021).

Although no explicit $\alpha'_{^{12}\rm CO}$ value has been calculated for MW GMCs, one can estimate it from the Bolatto et al. (2013) $\alpha_{\rm CO}$ for ^{12}CO$(1-0)$, assuming a gas-to-dust ratio of $R_{\rm g/d} \approx 136$ and an intensity ratio of $I_{\rm CO}(1-0)/I_{\rm CO}(2-1) = 0.7$. This yields a MW $\alpha'_{^{12}\rm CO} \approx 0.045\ M_\odot\ (\mathrm{K\,km\,s^{-1}\,pc^2})^{-1} \pm 0.3$ dex. $\alpha'_{^{12}\rm CO}$ calculated here for M31 agrees within 1σ, with a smaller relative uncertainty compared to the MW estimate.

TABLE 3.2: α'_{CO} of individual 1G dust cores from both $L_{^{12}CO(2-1)}$ and $L_{^{13}CO(2-1)}$.

Source	$\alpha'_{^{12}CO(2-1)}$ $M_\odot$ (K km s^{-1} pc^2)$^{-1}$	$\alpha'_{^{13}CO(2-1)}$ $M_\odot$ (K km s^{-1} pc^2)$^{-1}$
K001Ad1	0.04 ± 0.01	0.30 ± 0.07
K001Ad2	0.03 ± 0.01	0.15 ± 0.05
K026Ad1*	0.07 ± 0.01	0.34 ± 0.03
K063Ad1*	0.08 ± 0.01	0.56 ± 0.12
K063Ad3	0.04 ± 0.01	0.29 ± 0.10
K067Ad1*	0.06 ± 0.02	0.29 ± 0.08
K071Ad1*	0.11 ± 0.02	0.52 ± 0.10
K071Ad2	0.05 ± 0.01	0.38 ± 0.11
K081Ad1	0.06 ± 0.02	0.29 ± 0.09
K092Ad1*	0.09 ± 0.01	0.36 ± 0.05
K093Ad1*	0.10 ± 0.02	0.43 ± 0.12
K094Ad1	0.04 ± 0.01	0.21 ± 0.07
K098Bd1*	0.05 ± 0.01	0.24 ± 0.04
K098Ad1	0.05 ± 0.02	0.40 ± 0.15
K119Bd1*	0.12 ± 0.01	0.54 ± 0.05
K120Ad1*	0.16 ± 0.04	0.76 ± 0.21
K134Ad1	0.05 ± 0.02	0.26 ± 0.08
K134Ad2	0.06 ± 0.02	0.52 ± 0.20
K136Ad2	0.07 ± 0.02	0.39 ± 0.10
K138Ad1*	0.05 ± 0.01	0.27 ± 0.03
K149Ad1	0.07 ± 0.02	0.41 ± 0.13
K151Ad1	0.04 ± 0.01	0.44 ± 0.16
K153Ad1	0.03 ± 0.01	0.29 ± 0.08
K153Ad2	0.03 ± 0.01	0.29 ± 0.11
K154Ad1*	0.12 ± 0.02	0.74 ± 0.15
K157Bd2	0.11 ± 0.03	0.76 ± 0.24
K160Cd1	0.07 ± 0.02	0.60 ± 0.20
K162Ad1*	0.03 ± 0.01	0.19 ± 0.04
K162Ad2	0.04 ± 0.01	0.26 ± 0.08
K170Ad1*	0.05 ± 0.01	0.26 ± 0.04

Table 3.2 (continued)

Source	$\alpha'_{^{12}\mathrm{CO}}$ $M_\odot$ (K km s^{-1} pc^2)$^{-1}$	$\alpha'_{^{13}\mathrm{CO}}$ $M_\odot$ (K km s^{-1} pc^2)$^{-1}$
K171Ad1	0.07 ± 0.02	0.30 ± 0.08
K176Ad1*	0.05 ± 0.01	0.28 ± 0.06
K177Ad1*	0.06 ± 0.02	0.27 ± 0.07
K177Ad2	0.03 ± 0.01	0.17 ± 0.04
K190Ad1*	0.18 ± 0.02	1.84 ± 0.28
K191Ad1*	0.08 ± 0.01	0.42 ± 0.08
K192Ad1	0.09 ± 0.03	0.37 ± 0.11
K213Ad1*	0.09 ± 0.01	0.51 ± 0.05
K239Ad2	0.03 ± 0.01	0.23 ± 0.09
K240Bd1	0.14 ± 0.04	1.63 ± 0.62
K240Ad1	0.16 ± 0.05	1.05 ± 0.34
K270Ad1*	0.09 ± 0.01	0.59 ± 0.06
K270Ad2	0.06 ± 0.02	0.42 ± 0.12
K275Bd1	0.12 ± 0.03	0.79 ± 0.21
K291Ad1	0.25 ± 0.05	2.20 ± 0.56
K297Ad1	0.08 ± 0.01	0.58 ± 0.06
K301Ad1*	0.05 ± 0.00	0.24 ± 0.03

Notes. * Resolved dust cores.

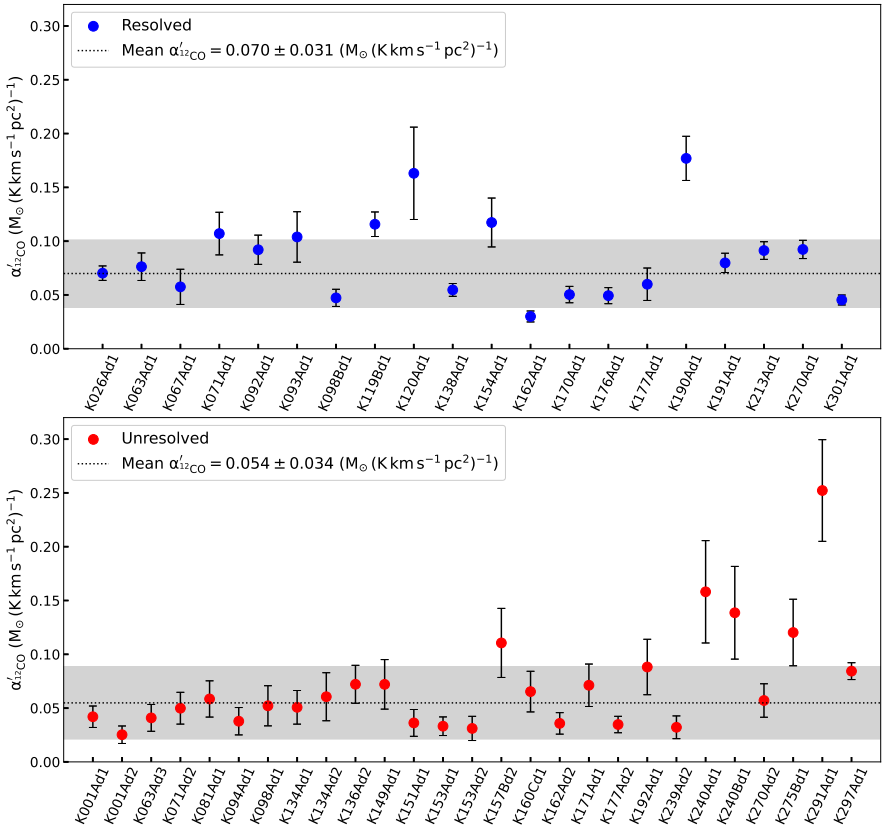

FIGURE 3.5: ^{12}CO conversion factors, $\alpha'_{^{12}CO}$, for individual 1G dust cores for: *top,* spatially resolved sources and *bottom,* unresolved sources. We display the mean $\alpha'_{^{12}CO}$ calculated for resolved and unresolved sources as a dotted line, with the 1σ standard deviation represented by the shaded region.

As done for $\alpha'_{^{12}CO}$, individual $\alpha'_{^{13}CO}$ of 1G dust cores in M31 are displayed in Figure 3.6 and reported in Table 3.2. The mean $\alpha'_{^{13}CO}$ of resolved sources is 0.37 ± 0.20 $M_\odot$ (K km s^{-1} pc^2)$^{-1}$, which is in excellent agreement with the previous mean of 0.36 ± 0.15 $M_\odot$ (K km s^{-1} pc^2)$^{-1}$ reported by Viaene et al. (2021). We see that the mean $\alpha'_{^{13}CO}$ for resolved and unresolved dust cores are again in agreement within 1σ.

In this study, we calculate α'_{CO} from dust core emission rather than from the entire GMC. The differences between the factors derived from dust cores within the same GMC are smaller than the overall standard deviation, indicating that these measurements are representative of the entire GMCs within the uncertainties. However, because the ^{12}CO emission is more extended than the dust emission, α'_{CO} when computed over the entire GMC will be low. Therefore, our α'_{CO} measurements reflect the dense regions of GMCs.

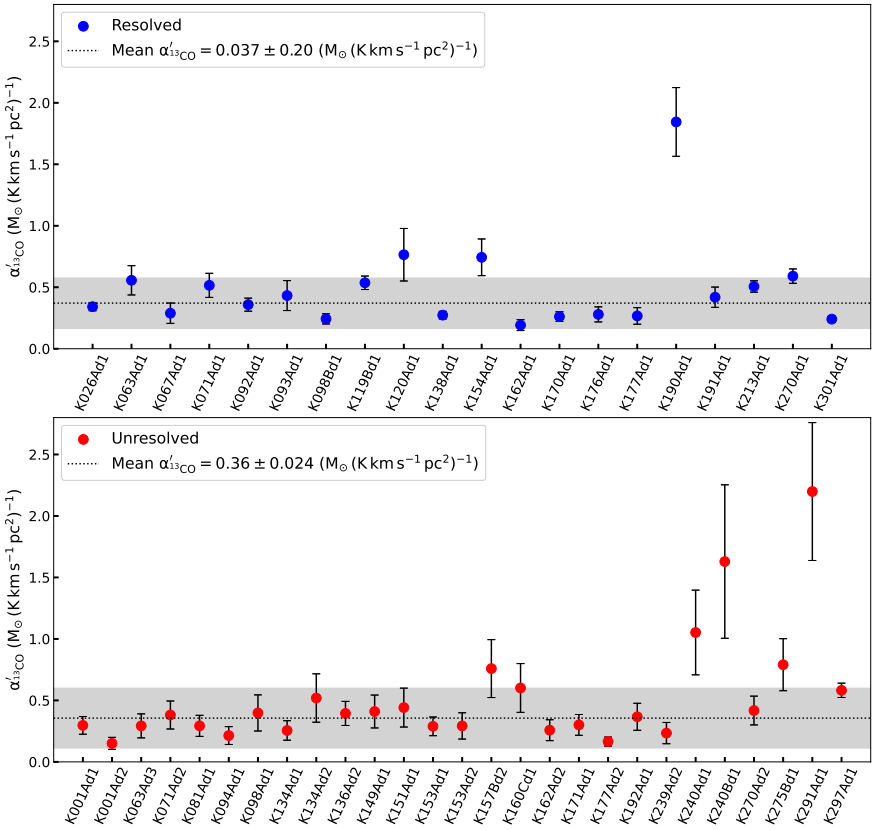

FIGURE 3.6: ^{13}CO conversion factors, $\alpha'_{^{13}CO(2-1)}$, of individual 1G dust clouds for: *top,* spatially resolved sources and *bottom,* unresolved sources. As in Figure 3.5, we display the mean $\alpha'_{^{13}CO}$ calculated for resolved and unresolved sources as a dotted line, with the 1σ standard deviation represented by the shaded region.

We investigated internal variations in α'_{CO} by examining the best-resolved dust cores on a pixel-by-pixel basis; however, because the beam size is much larger than a pixel, measurements are not independent. This analysis revealed only marginal ($\approx 4\sigma$) differences in α'_{CO} between pixels separated by more than one beam, and at smaller scales the likelihood of temperature variations further increases. Therefore, we find little evidence for significant α'_{CO} variation within a dust core.

Lada et al. (2024) found that M31 GMCs belong to one of two classes: dense and diffuse. Dense GMCs are identified by their strong ^{13}CO$(2-1)$ emission lines. We further expect that all 1G dust cores are associated with dense GMCs, as all display measurable ^{13}CO$(2-1)$ emission.

In dust cores K071Ad1, K119Bd1, K120Ad1, K154Ad1, and K190Ad1, the dust emission peak lies near the edge of the GMC, where CO emission is weaker. Consequently, values of $L_{^{12}CO}$

and sometimes $L_{^{13}\mathrm{CO}}$ are lower than at the cloud centre, where the peak CO emission occurs. As a result, the ratio of $M_{\mathrm{dust}}/L_{\mathrm{CO}}$ is biased high. This may be due to variations in T_{dust} within the GMC. For source K190Ad1 to yield $\alpha'_{^{12}\mathrm{CO}} = 0.07\ \mathrm{M}_{\odot}\ (\mathrm{K\,km\,s^{-1}\,pc^2})^{-1}$, a T_{dust} of 38 K would be required. The other aforementioned outliers would require 25 K $\lesssim T_{\mathrm{dust}} \lesssim$ 36 K. In Orion, T_{dust} derived from continuum emission is typically 20 – 30 K (e.g., Bouvier et al. 2021), but can be as high as $T_{\mathrm{dust}} \lesssim 50$ K in warmer regions (Shirley et al. 2005). In M17, T_{dust} ranges from $\approx 10-100$ K (Dupac et al. 2002). These measurements are obtained on much smaller scales than those used in this work (< 0.1 pc). Therefore, while a T_{dust} of 38 K can occur in a region heated by a nearby H II region, this is unlikely on 15 pc scales. On larger scales, *Herschel* observations indicate a T_{dust} range of 15 – 20 K for M31 GMAs (Kirk et al. 2015). Thus, variations in $\alpha'_{^{12}\mathrm{CO}}$ between clouds may reflect T_{dust} differences, it is also possible that some dust continuum emission is not physically associated with the GMC.

3.4.4 Virial Analysis

Next, we performed a virial analysis of the resolved 1G dust cores in our sample to investigate the influence of gravity and turbulence on cloud dynamics. We include only 1G resolved sources in this analysis, as source radii and ^{13}CO(2 – 1) linewidths are required to calculate the virial mass (M_{vir}) following Equation 3.4. Lada et al. (2024) showed that, while most M31 GMCs are unbound, the strongest ^{13}CO emission arises from bound GMCs. As discussed in Section 3.4.2, dust traces the densest regions within these GMCs, therefore providing additional insight into the physical conditions that govern star formation.

The virial theorem states that for a self-gravitating GMC, the kinetic energy (KE) is twice the absolute value of its gravitational potential energy (GPE). This implies that the internal KE from turbulence is balanced by self-gravity. Assuming a stratified cloud with an internal density gradient of $\rho(r) \propto r^{-1}$ (Solomon et al. 1987), M_{vir} is then given by

$$M_{\mathrm{vir}} = \frac{4.5 R \sigma^2}{G}, \tag{3.4}$$

where σ is the velocity dispersion in km s^{-1} and R is the effective radius in pc.

For a virialized cloud, the virial parameter,

$$\alpha_{\mathrm{vir}} = \frac{2\ \mathrm{KE}}{\mathrm{GPE}}, \tag{3.5}$$

is equal to 1. The virial nature of a system can be inferred from the relationship between $M_{\rm vir}$ and $M_{\rm lum}$, where a one-to-one scaling relation is expected for virialized clouds. Larson (1981) derived the following relation between velocity dispersion and mass;

$$\sigma \propto M^{0.20}, \tag{3.6}$$

with an rms deviation of 0.12 dex. Lada et al. (2024) found an almost identical relation for M31 GMCs using the same observations discussed here. For a virialized system, $M_{\rm vir} = M_{\rm lum}^{1.0}$ is expected (e.g., Lada et al. 2024).

The virial mass of each dust core is derived using its ^{13}CO linewidth for velocity dispersion, as this is more suitable than the ^{12}CO linewidth for this purpose, because dust and ^{13}CO are better spatially matched in our observations (see Section 3.4.1). $M_{\rm lum}$ is calculated following Equation 3.7 using the $\alpha'_{^{12}\rm CO}$ derived for each individual dust core and assuming $R_{\rm g/d} = 136$,

$$M_{\rm lum} = R_{\rm g/d} \times \alpha'_{^{12}\rm CO} \times L_{^{12}\rm CO} \tag{3.7}$$

where both $\alpha'_{^{12}\rm CO}$ and $L_{^{12}\rm CO}$ are measured within the dust core area. This yields the dust-based gas mass of the dust core. Because both $\alpha'_{\rm CO}$ and $L_{\rm CO}$ are evaluated for each individual dust core, and this calculation is mathematically equivalent to $M_{\rm lum} = 136 \times M_{\rm dust}$. Consequently, identical results are obtained when using $\alpha'_{^{12}\rm CO}$ for either ^{12}CO or ^{13}CO.

Figure 3.7 displays the relationship between $M_{\rm vir}$ and $M_{\rm lum}$ for our 20 resolved 1G dust cores. The majority (80%) of dust cores are found to be gravitationally bound and approximately virialized. Although four dust cores lie within the unbound area of Figure 3.7, they all lie within approximately 1σ of the bound line and are therefore likely also bound. We note that the use of ^{13}CO linewidths for σ provides upper limits for the $M_{\rm vir}$ of these dust cores, and ideally, C^{18}O linewidths would be used, as this tracer has a lower optical depth.

Lada et al. (2024) present a virial analysis of M31 GMCs traced by ^{12}CO and ^{13}CO from the same dataset. When $M_{\rm vir}$ and $M_{\rm lum}$ are calculated for entire GMCs as traced by ^{12}CO at 3σ, only 43% of the clouds are gravitationally bound. However, when masses are computed within the ^{13}CO-emitting 'clumps' (traced by ^{12}CO at 3σ) 94% of these are bound and approximately virialized Lada et al. (2024). The results found here are consistent with those of Lada et al. (2024): when considering the entire cloud, M31 GMCs appear largely unbound, but the masses

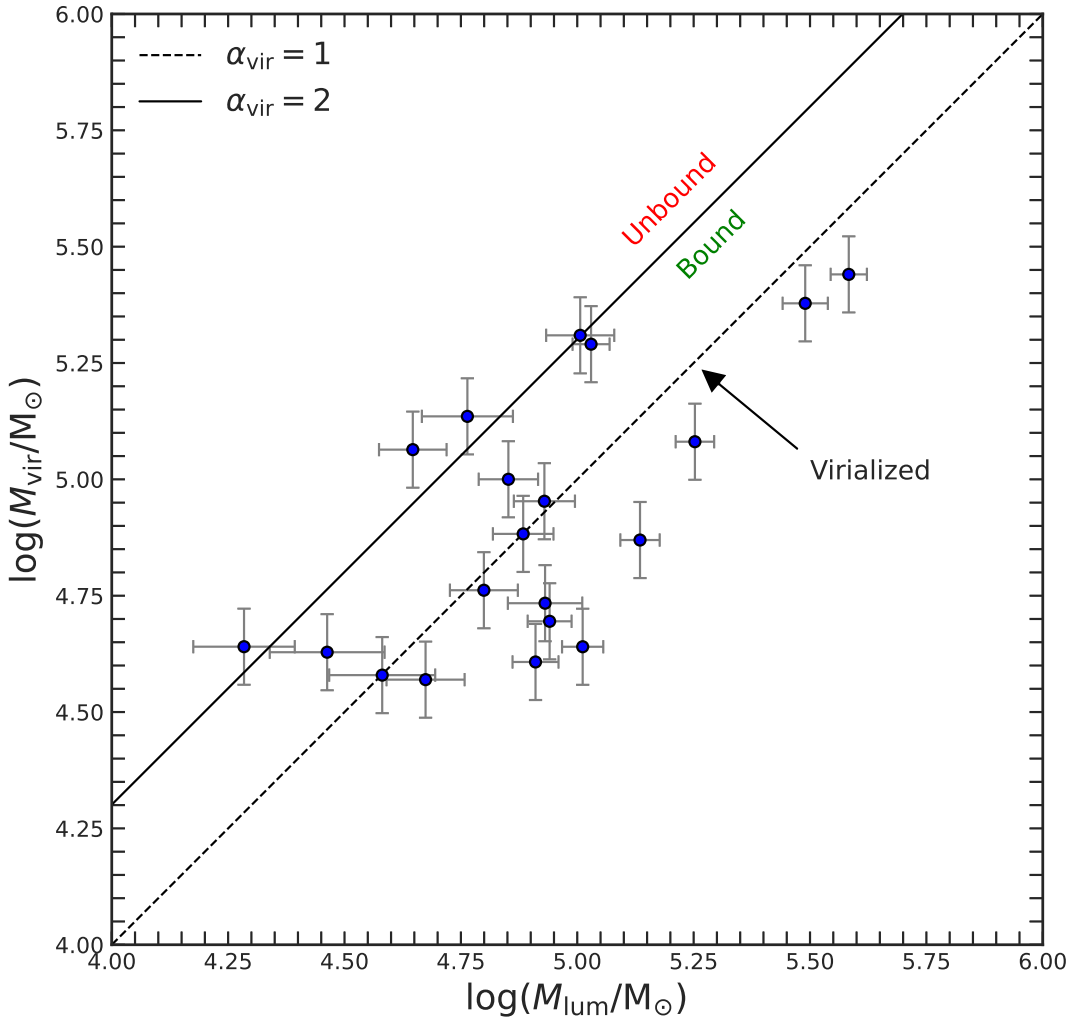

FIGURE 3.7: Comparison between the virial mass (M_{vir}) and the dust-based gas mass (M_{lum}), both from within the 2.5σ dust continuum contour, for individual spatially resolved dust cores in our sample. The solid line shows the boundary separating gravitationally bound (|GPE| > KE) cores from unbound (i.e., |GPE| < KE) cores. The dashed line represents the virial condition, when M_{vir} = M_{lum} (i.e., |GPE| = 2KE).

of the denser regions traced by dust and ^{13}CO are themselves bound and close to being in virial equilibrium and are contained within bound GMCs. This is also similar to the results from Evans et al. (2021) for MW GMCs, where 70 – 80% of GMCs were found to be unbound, but 60% of the ^{13}CO clouds were bound. Both Lada et al. (2024) and Evans et al. (2021) found that the bound fraction of GMCs increases with cloud mass.

3.4.5 Metallicity Dependence of $\alpha'_{\rm CO}$

As introduced in Section 3.1, we update the result presented in Bosomworth et al. (2025), investigating the metallicity dependence of $\alpha'_{\rm CO}$. This SMA sample contains 30 1G dust cores associated with the same GMCs as 30 H II regions from Bosomworth et al. (2025). We note that the dust cores and H II regions are not necessarily spatially coincident. H II region metallicities were calculated from MMT/Hectospec optical spectroscopy. The primary metallicity trend found in spiral galaxies such as M31 is a negative linear correlation with Galactocentric radius, as expected for spiral galaxies (e.g., Tinsley 1980; Kewley et al. 2019; Maiolino and Mannucci 2019). $\alpha_{\rm CO}$ is predicted to be higher at low metallicities (Bolatto et al. 2013), and for α'CO if $R_{\rm g/d}$ is constant. Therefore, $\alpha_{\rm CO}$ may also be assumed to vary linearly with Galactocentric radius.

First, both dust and CO are more abundant in higher metallicity environments. Second, the dust mass and CO luminosity are each expected to vary independently with metallicity. Dust plays a crucial role in shielding CO from destruction by UV photons; therefore, at lower metallicities, a greater fraction of CO is destroyed by UV radiation (Bolatto et al. 2013). These combined effects may either exacerbate or mitigate variations in the ratio of $M_{\rm dust}$-to-$L_{\rm CO}$.

We display the updated relationship between $\alpha'_{\rm CO}$ and O/H in Figure 3.8. Across the metallicity range $8.40 \lesssim 12 + \log({\rm O/H}) \lesssim 8.65$, we find that $\alpha'_{^{12}{\rm CO}}$ remains approximately constant with a mean of $0.062 \pm 0.029\ M_\odot\ ({\rm K\ km\ s^{-1}\ pc^2})^{-1}$, consistent within 2σ for most data points. The majority of sources in this sample have metallicities of $12 + \log({\rm O/H}) > 8.5$, and a significant dependence of $\alpha_{\rm CO}$ on metallicity is primarily expected at $12 + \log({\rm O/H}) < 8.4$. In Figure 3.8, one dust core at $12 + \log({\rm O/H}) \approx 8.42$ exhibits a significantly (1σ) higher $\alpha'_{^{12}{\rm CO}}$ relative to the mean, suggesting that a larger sample at lower metallicities is required to determine whether a trend in $\alpha'_{\rm CO}$ exists.

Our results are consistent with a constant $\alpha_{\rm CO}$ if the MW value of $R_{\rm g/d} \approx 136$ is assumed. This contrasts with theoretical predictions that $\alpha_{\rm CO}$ is negatively correlated with metallicity. By probing the metallicity range $12 + \log({\rm O/H}) < 8.5$ with a sufficiently large sample size, we can better constrain the metallicity dependence of $\alpha'_{^{12}{\rm CO}}$ in M31 and similar galaxies. Alternatively, it may be that $R_{\rm g/d}$ varies with metallicity.

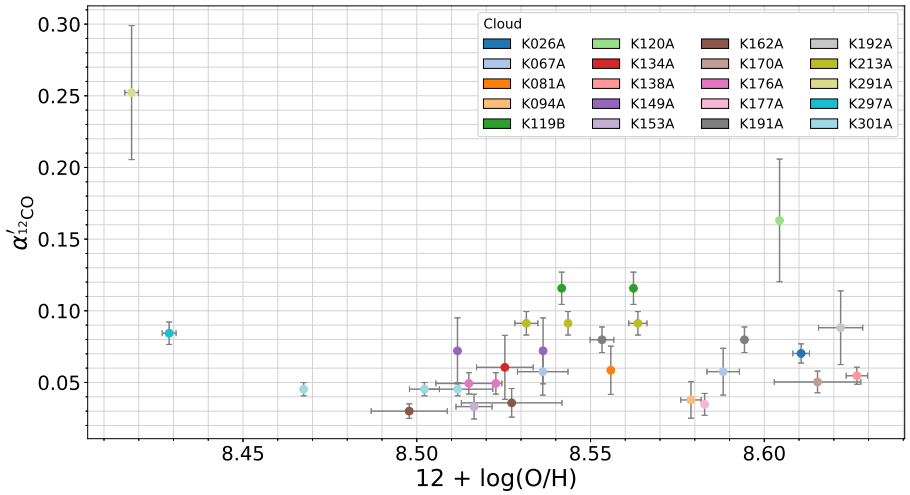

FIGURE 3.8: Variation of the CO-to-dust-mass conversion factor, $\alpha'_{^{12}CO}$, with metallicity (oxygen abundance) for SMA dust detections in this work, which have at least one associated H II region identified from optical spectroscopy Bosomworth et al. (2025). Some GMAs have multiple H II regions, so the data points are coloured according to the associated GMA/GMC.

3.5 Summary and Conclusions

The recent upgrade to the SMA wideband receiver has enabled the first spatially resolved dust continuum detections of individual GMCs in M31. Earlier studies by Forbrich et al. (2020) and Viaene et al. (2021) showed that using SMA observations of simultaneous CO(2–1) and 230-GHz continuum emission at $\approx$ 15 pc resolution, it is possible to derive the dust mass-to-light conversion factor (α'_{CO}) for 32 dust cores associated with M31 GMCs (10 spatially resolved). Analysis from the initial two observing runs of the SMA survey revealed that α'_{CO} for M31 GMCs is approximately constant and similar to that of the MW when $R_{g/d} = 136$ is assumed. In this paper, we analyse the now-completed SMA survey, consisting of four observing runs targeting 80 *Herschel*-identified GMAs. We increased the sample to 71 dust continuum detections (26 resolved) associated with 56 GMCs. We identified a subsample of 47 '1G' dust cores with CO line profiles well represented by a single Gaussian (20 resolved). We calculated α'_{CO} for both $^{12}CO(2-1)$ and $^{13}CO(2-1)$ for the 1G sample, then assessed whether the resolved 1G dust cores are gravitationally bound and/or virialzied. Finally, we updated the test of the metallicity dependence of α'_{CO} using H II region metallicities presented in Bosomworth et al. (2025).

- We re-analysed the entire dataset using a dust emission detection threshold of 2.5σ and limited the final sample to detections associated with GMCs defined by $^{12}CO(2-1)$ emission, identifying new detections in the original two observing runs as well as in the

new observations. The defined '1G' subsample consists of sources with single-component line profiles in both ^{12}CO(2 − 1) and ^{13}CO(2 − 1), thus eliminating confusion due to overlapping emission.

- We calculated the CO-to-dust mass conversion factor, $\alpha'_{\rm CO}$, for 47 1G dust cores. The mean values derived from the sample of 20 resolved sources are $\langle \alpha'_{^{12}{\rm CO}(2-1)} \rangle = 0.070 \pm 0.031\ M_\odot\ ({\rm K\,km\,s^{-1}\,pc^2})^{-1}$ and $\langle \alpha'_{^{13}{\rm CO}(2-1)} \rangle = 0.37 \pm 0.20\ M_\odot\ ({\rm K\,km\,s^{-1}\,pc^2})^{-1}$. These factors are in excellent agreement with those previously reported by Forbrich et al. (2020) and Viaene et al. (2021).

- Assuming a MW value of $R_{\rm g/d} = 136$, the corresponding CO-to-molecular mass conversion factor is $\langle \alpha_{^{12}{\rm CO}(2-1)} \rangle_{\rm M31} = 9.52 \pm 4.22\ M_\odot\ ({\rm K\,km\,s^{-1}\,pc^2})^{-1}$. The corresponding MW $\langle \alpha_{^{12}{\rm CO}(2-1)} \rangle_{\rm MW} = 6.1\ M_\odot\ ({\rm K\,km\,s^{-1}\,pc^2})^{-1}$, derived from the Bolatto et al. (2013) value for CO(1–0). $\langle \alpha_{^{12}{\rm CO}(2-1)} \rangle_{\rm M31}$ agrees with that of the MW within the 1σ uncertainties. Our uncertainty estimate is comparable to that recommended by Bolatto et al. (2013) for the MW but has a smaller relative uncertainty and is statistically derived.

- We found that 80% of the dust cores are gravitationally bound (i.e., GPE < KE). Moreover, all sources lie within 1σ of the gravitationally bound condition. This is consistent with the findings of Lada et al. (2024), who reported that M31 GMCs are largely unbound, but that dense gas regions (identified from ^{13}CO emission) are contained within bound GMCs. Our results therefore suggest that the dust cores are located within these bound GMCs.

- Finally, we updated 2025's test of $\alpha'_{\rm CO}$ variations with metallicity (O/H). We found no evidence of a $\alpha'_{^{12}{\rm CO}}$ dependence on metallicity across the metallicity range $8.50 \lesssim 12 + \log({\rm O/H}) \lesssim 8.65$. However, the presence of one dust core of metallicity ${\rm O/H} \approx 8.42$ with an elevated $\alpha'_{^{12}{\rm CO}}$ may be tentative evidence that at lower metallicities, $\alpha'_{\rm CO}$ is higher. Further studies probing the range ${\rm O/H} \leq 8.40$ are required to confirm this trend.

Chapter 4

Variation of the Nitrogen-to-Oxygen ratio in H II Regions Across the Disc of M31

4.1 Introduction

H II regions are made up of gas ionised by young, massive (OB) stars. Therefore, through their chemical abundances we trace the latest stage of star formation within a galaxy. Common tracers of gas-phase metallicity in H II regions include O and N and their relative ratios, typically expressed as 12 + log(O/H), 12 + log(N/H) and log(N/O)[1] (e.g., Peimbert and Costero 1969a;b; Vila-Costas and Edmunds 1993). Chemical abundances of H II regions are crucial to our understanding of chemical enrichment processes in star-forming galaxies (see reviews by Tinsley 1980; Matteucci 2021, and references therein).

Most of the elements heavier than helium (He), known as 'metals' in astronomy, are produced in stars and returned to the ISM upon the stars' deaths and during stellar evolution via e.g. stellar winds. Subsequent generations of stars then form from this enriched material (Burbidge et al. 1957). Abundance ratios of elements formed during nucleosynthesis in different mass stars can provide further insight into SFHs and galaxy chemical enrichment, in particular by comparing observations (e.g. Vargas et al. 2014; Li et al. 2016) with simulations (e.g. Tinsley 1979; Thomas et al. 2005; Kobayashi et al. 2020). The ratio of N to O is a useful probe of the relative

[1] O/H, N/H and N/O

contributions of massive and intermediate mass stars to ISM enrichment (e.g., Chiappini et al. 2003; Vincenzo and Kobayashi 2018).

ionised gas emits optical emission lines that enable us to calculate chemical abundances. Gas-phase abundances can be directly measured from electron temperature (T_e)-sensitive auroral lines (e.g., Peimbert and Costero 1969b; Garnett 1992; Osterbrock and Ferland 2006) or indirectly using strong-line calibrations when auroral lines are not detected (e.g., Pagel et al. 1979; Pilyugin 2001; Kewley and Dopita 2002; Pettini and Pagel 2004). Strong-line calibrations are especially useful for extragalactic and high metallicity H II regions for which auroral lines are generally weak. Many strong-line calibrations have been derived for various ratios of strong emission lines, from empirical (e.g., Zaritsky et al. 1994; Marino et al. 2013; Pilyugin and Thuan 2005, 2010) or theoretical (e.g. Kewley and Dopita 2002; Kobulnicky and Kewley 2004) calibrations. Absolute metallicities can vary as much as 0.7 dex depending on the choice of strong-line diagnostic (see review by Kewley and Ellison 2008) and this can also affect the radial gradient value (e.g., Sanders et al. 2012). Pilyugin and Grebel (2016, hereafter PG16) developed 3-dimensional (3D) calibrations for calculating O/H, N/H and N/O. 3D calibrations depend on a combination of three different emission line ratios, reducing dependence on the ionisation parameter compared to calibrations of lower dimensionalities, which can introduce scatter in measurements (Pilyugin 2001; Kewley and Dopita 2002). N and O abundances calculated from these diagnostics have good agreement (within ≈0.1 dex) with direct measurements (Ho 2019).

While Fe is most commonly used as a proxy for stellar metallicities, O is the preferred tracer of gas-phase metallicity because it is the third most abundant element in the ISM after H and He. Synthesised during the α-process in massive ($> 8\ M_\odot$) stars, O is returned to the ISM through CCSNe on timescales of ≈10 Myr. O is also produced along with N and C in the CNO cycle. N production has two main nucleosynthetic origins. Primary N is ejected into the ISM by CCSNe and therefore enrichment occurs on timescales similar to O nucleosynthesis. Massive AGB stars ($M = 4 - 8\ M_\odot$) also produce primary N, enriching the ISM over a longer timescale (Kobayashi et al. 2011). Secondary N is formed in the CNO cycle from CNO already present in the parent star from previous generations of star formation and therefore increases with the initial stellar metallicity (Matteucci 1986; Vila-Costas and Edmunds 1993; Vincenzo et al. 2016). Additionally, in higher-metallicity H II regions, enhanced N abundance partially arises from primary N produced in massive AGB stars (Kobayashi et al. 2011, 2023). AGB stars have lifetimes longer than those of massive stars, delaying their enrichment compared to massive stars. Therefore, at high metallicity, N increases with metallicity due to both secondary

and delayed (from AGB stars) primary N. Secondary N has been shown to dominate when the star has O/H > 0.25 $(O/H)_{\odot}$ (Nicholls et al. 2017).

Scaling diagrams showing abundance ratios (e.g. N/O) as a function of metallicity provide insight into how stars of different masses contribute to a galaxy's chemical enrichment. Vila-Costas and Edmunds (1992) showed that scaling diagrams of $N/O - O/H$ can be explained by primary and secondary nucleosynthesis productions of N, and Nicholls et al. (2017) produced a general relation from MW stellar and nebular abundances across a wide metallicity range. The N/O ratio at a given metallicity can vary significantly depending on the star-formation conditions. At low metallicities, N/O is constant with increasing O/H, since most primary N is produced in massive stars over similar timescales to O. The onset of secondary and delayed primary N is dependent on the SFH of a galaxy, so the metallicity at which N/O increases with O/H will vary between galaxies and the $N/O - O/H$ function is unlikely to be the same for all galaxies (Nicholls et al. 2017).

The relation of Nicholls et al. (2017) can be used to compare with data from other galaxies. The simulation of Vincenzo and Kobayashi (2018) takes into account the different nucleosynthesis productions of O and N from stellar sources. For their sample of 33 galaxies, their results clearly show an increase of N/O with O/H at high O/H, in agreement with the MW (Nicholls et al. 2017). This means that N/O can vary radially in spiral galaxies, where the SFE can be higher by up to a factor of 10 in a galaxy centre compared to its outskirts (Leroy et al. 2008), with N displaying a steeper gradient than O (e.g., Rolleston et al. 2000; Berg et al. 2020).

The simulations of Vincenzo and Kobayashi (2018) which show that more massive galaxies exhibit higher N/O ratios, and that N/O decreases with increasing redshift, driven by the mass-metallicity relation. This is the result of the secondary behaviour (including secondary N and delayed primary N from AGB stars) in N production, where N abundance increases over time more than O abundance. The average $N/O - O/H$ srelation produced displays a steeper trend at high metallicities in galaxies that have highly concentrated SFHs at earlier times (Vincenzo and Kobayashi 2018).

M31 is the nearest large spiral galaxy to the MW and provides an external view of galaxy-wide elemental abundance variations on scales comparable to MW studies (e.g., Sanders et al. 2012; Bosomworth et al. 2025, hereafter Paper I). The disc of M31 has a ≈ 2.4 times larger scale length and ≈ 2 times more massive than the MW disc (Yin et al. 2009). From chemical evolution

models, the thick disc of M31 is predicted to have been produced by a more intense and shorter duration starburst than that of the MW (Kobayashi et al. 2023).

In Paper I, we classified and calculated O/H and N/H of 284 individual H II regions in M31 using optical emission lines. Relatively shallow (compared to those of other spiral galaxies) O/H and N/H radial gradients of -0.0113 ± 0.0016 dex kpc^{-1} and -0.0303 ± 0.0049 dex kpc^{-1} were calculated, respectively. The N/H gradient is $\approx 2.7\times$ steeper than the O/H gradient, indicating that N/O is also higher towards the galaxy centre, in agreement with cosmological simulations of resolved galaxies at kpc scales (Vincenzo and Kobayashi 2018).

In this work, we expand the chemical abundance analysis of Paper I to investigate the N/O ratios of H II regions in detail and compare them to simulations and observations of other spiral galaxies. This study will provide insight into the relative contributions of stars of different masses to the chemical enrichment history of M31. This chapter is structured as follows. In Section 4.2 we describe our methodology for calculating the N/O abundance ratios of individual H II regions. The results and discussion are presented in Section 4.3. Finally, in Section 4.4 we present our summary and conclusions.

4.2 Methodology

In Paper I we measured emission line fluxes from Gaussian fits centred on their respective velocity-shifted wavelengths. For details of the identification of the emission lines we refer to Paper I. From these, we corrected for extinction using the curve of Cardelli et al. (1989) assuming $R_V = 3.1$, Hα/H$\beta = 2.86$ (Osterbrock and Ferland 2006) and case B recombination (e.g., Peimbert et al. 2017). We then identified individual H II regions using a BPT diagram (Baldwin et al. 1981) of [O III]λ5007/Hβ against [N II]λ6584/Hα and assuming the relation of Kniazev et al. (2008). Finally, we calculated abundances the from strong-line diagnostics for the 294 H II regions for which we detected all of the emission lines required at S/N > 5. Details on the observational and target selection methodology is provided in Chapter 2 Section 2.2.

The O/H values reported in Paper I were calculated using the strong-line calibrations of Zaritsky et al. (1994, hereafter Z94) and the R and S-calibrations of PG16, while the N/H values were calculated using the PG16 R-calibration. The PG16 calibrations are 3D, reducing the effect of

the ionisation parameter, and each requires three of the following emission line ratios:

$$N_2 = ([\text{N II}]\lambda6548 + [\text{N II}]\lambda6584)/\text{H}\beta$$
$$R_2 = ([\text{O II}]\lambda3727 + [\text{O II}]\lambda3729)/\text{H}\beta$$
$$R_3 = ([\text{O III}]\lambda4959 + [\text{O III}]\lambda5007)/\text{H}\beta$$
$$S_2 = ([\text{S II}]\lambda6717 + [\text{S II}]\lambda6731)/\text{H}\beta,$$

where the R-calibration (R-cal) requires N_2, R_2 and R_3 and the S-calibration (S-cal) requires N_2, R_3 and S_2. For O/H, PG16 derived both R-cal and S-cal. For N/H, only an R-cal is available. The Z94 calibration for O/H uses the R_{23} line ratio, defined as

$$R_{23} = ([\text{O II}]\lambda3727 + [\text{O III}]\lambda4959 + [\text{O III}]\lambda5007)/\text{H}\beta.$$

In this work, we subsequently calculate N/O following $\text{N/O} = \text{N/H} - \text{O/H}$[2] using the three O/H diagnostics outlined above. We also calculate N/O from the R-cal based N/O diagnostic of PG16 (see their equation 13). We list N/O calculated by the four different methods for individual sources in Table 4.1. Uncertainties in individual measurements are derived by taking the standard deviation of measurements obtained from multiple spectra of the same source, as described in Paper I.

4.3 Results and Discussion

4.3.1 Nitrogen vs Oxygen Abundance

In Paper I, the N/H radial gradient in M31 was found to be $\approx 2.7\times$ steeper than its O/H gradient. In Figure 4.1 we show the correlation between O/H and N/H for our H II region sample. Following Paper I, individual uncertainties are calculated from the standard deviation of repeated measurements of the same source, which provides an estimate of the statistical component of the empirical error budget, but does not capture systematic uncertainties inherent to the abundance diagnostic. As a result, the true total error in absolute abundance measurements is larger.

We estimated the uncertainties on the linear relations using bootstrap resampling. Linear fits were obtained with SciPy's `odr` (orthogonal distance regression) function, which minimizes the

[2]Based on log10 notations, simplified here as previously defined.

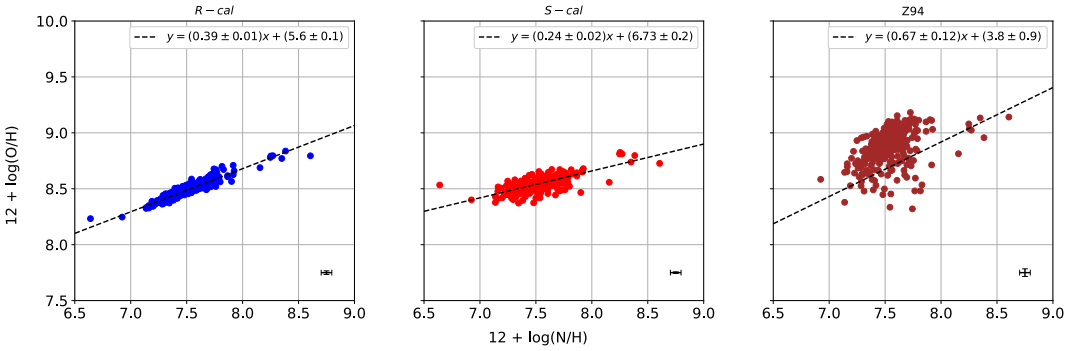

FIGURE 4.1: Oxygen vs nitrogen abundance of M31 H II regions calculated using, from *left* to *right*, the PG16 *R*-cal, PG16 *S*-cal, and the Z94 calibration. Linear fits to the data are shown. The typical uncertainty of the individual data points is displayed in the bottom-right corner of each panel.

TABLE 4.1: N/O of M31 H II regions from our final sample.

ID	RA	DEC	R[a] (kpc)	(N/O)*R*-cal[b]	(N/O) *S*-cal[c]	(N/O) Z94[d]	(N/O) PG16[e]
1	0:39:13.01	40:41:44.88	16.07	-1.08 ± 0.06	-1.17 ± 0.06	-1.55 ± 0.08	-0.99 ± 0.10
2	0:39:14.70	40:48:33.12	18.33	-1.20 ± 0.16	-1.32 ± 0.15	-1.55 ± 0.23	-1.22 ± 0.09
3	0:39:16.50	40:41:04.92	15.44	-1.13 ± 0.04	-1.21 ± 0.03	-1.43 ± 0.03	-1.15 ± 0.01
4	0:39:55.39	40:55:49.18	15.56	-0.88 ± 0.05	-0.94 ± 0.05	-1.33 ± 0.07	-0.89 ± 0.05
5	0:40:00.60	40:39:12.60	11.00	-0.92 ± 0.04	-1.03 ± 0.04	-1.26 ± 0.05	-0.94 ± 0.02
6	0:40:03.89	40:58:27.12	15.51	-0.87 ± 0.04	-0.82 ± 0.04	-1.00 ± 0.06	-0.95 ± 0.03
7	0:40:04.01	40:58:53.39	15.69	-1.02 ± 0.04	-1.06 ± 0.04	-1.47 ± 0.03	-1.02 ± 0.01
8	0:40:04.30	40:58:45.84	15.59	-0.91 ± 0.10	-0.89 ± 0.09	-0.91 ± 0.15	-1.01 ± 0.07
9	0:40:05.30	40:59:07.44	15.61	-0.92 ± 0.11	-0.88 ± 0.11	-1.00 ± 0.16	-1.00 ± 0.08
10	0:40:06.36	40:59:04.05	15.43	-0.89 ± 0.05	-0.84 ± 0.04	-1.23 ± 0.06	-0.87 ± 0.07

Notes. Uncertainties are estimated from the standard deviation of repeat observations when available (see text), with a lower bound of 0.01 dex.
[a] Source galactocentric radius, deprojected. [b] N/O calculated using N/H and O/H from PG16 (*R*-cal). [c] N/O calculated using N/H from PG16 (*R*-cal) and O/H from PG16 (*S*-cal). [d] N/O calculated using N/H from PG16 (R-cal) and O/H from Z94. [e] N/O calculated following Equation 13 of PG16. Our final sample includes 294 sources, and we show only a portion of the full table here for 10 sources.

perpendicular distances from the data points to the fitted line. We drew a different random sample of 150 sources for 100 bootstrap iterations and computed linear fits. The mean and standard deviation were then calculated for the slope and intercepts of the fits, and their associated uncertainties. The fit gradients shown in the left and centre panels of Figure 4.1, using O/H from *R*-cal and *S*-cal respectively, have an $\approx 5\sigma$ difference, indicating that the trend between O/H and N/H is dependent on the strong-line calibration used. Both calibrations display a positive linear trend with N/H increasing more rapidly than O/H. The increased scatter around the trend using *S*-cal measurements of O/H is likely inherent to the calibration. The reduced scatter around the trend seen when O/H and N/H are both calculated using *R*-cal is expected by construction, because both are derived using the same emission lines.

The slope of the best-fit linear relation between O/H and N/H derived using the Z94 calibration for O/H is 0.67 ± 0.12. The broader dispersion of O/H arises because Z94 yields systematically higher metallicities for metal-rich H II regions relative to direct abundances and PG16. As a result, the $\mathrm{O/H} - \mathrm{N/H}$ gradient is naturally steepened when comparing N/H from PG16 and O/H from Z94. As mentioned previously, PG16 calibrations are entirely empirical and in good agreement with direct abundance measurements. The Z94 diagnostic is also calibrated on T_e-based measurements, mixing empirical and theoretical studies. By deriving both O/H and N/H using the same calibration, this ensures that trends reflect real chemical behaviour rather than differences between calibration methods.

In Paper I, the uncertainties of O/H for individual H II regions were found to be $\approx 0.01 - 0.02$ dex for the PG16 calibrations. The uncertainties of N/H were $\approx$ 0.05 dex. PG16 calculated a relative uncertainty of 0.1 dex between the strong line calibration abundances and the directly calculated abundances of and N in their sample. They find no systematic offset between the PG16 calibrations and T_e-based values, and state that any potential systematic uncertainty is determined by the validity of the T_e based metallicity scale for H II regions. Differences between individual H II region abundances (derived using different calibrations) in our sample are significantly smaller.

Also, in Paper I we investigated the scatter of the radial-fit subtracted abundances, finding no secondary galaxy-scale trends beyond the radial gradient. However, a scatter (standard deviation) of $0.06 - 0.07$ dex was found around the O/H radial gradient, and of 0.18 dex around the N/H radial gradient. In the case of both O/H and N/H, this scatter is significantly larger than the

uncertainty of individual H II region abundances by a factor of $3-6$, indicating that this scatter is real in all cases.

Figure 4.2 displays the relationship between O/H and N/H of individual H II regions once the radial fit-predicted abundances (see Section 4.3.2) have been subtracted. In general, the trends displayed again indicate that N/H increases faster than O/H, and the slopes are identical to those of Figure 4.1 within uncertainties therefore this trend is not a result of the radial gradient alone. The steeper slope displayed when Z94 abundances of O/H are used is the same as that in Figure 4.1 within the uncertainties and is again affected by overestimations and increased noise in O/H from the Z94 calibration. Surprisingly, even when excluding the radial relationship from abundance values, the dynamic range probed is $\approx -0.3-0.5$ dex for O/H and $\approx -1-1.1$ dex for N/H, indicating that much of the dynamic range observed is not due to the radial metallicity gradient.

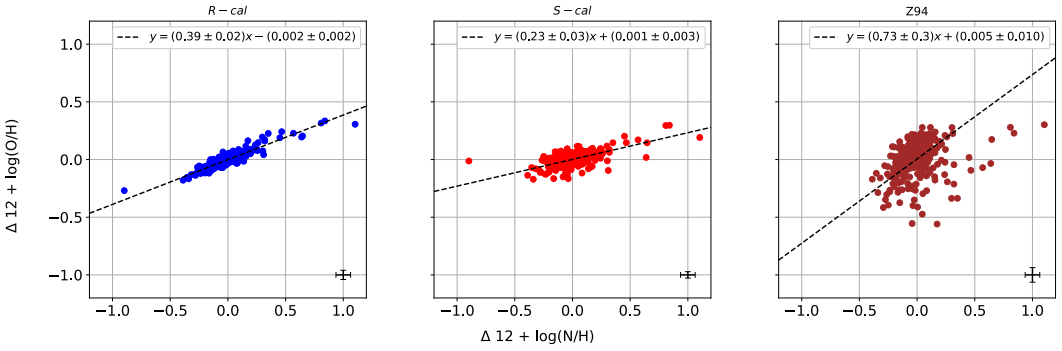

FIGURE 4.2: Radial gradient subtracted oxygen vs nitrogen abundance of M 31 H II regions with abundances calculated using, from *left* to *right*, the PG16 *R*-cal, PG16 *S*-cal, and the Z94 calibration. Linear fits to the data are shown. The typical uncertainty of the individual data points is displayed in the bottom-right corner of each panel.

4.3.2 log(N/O) Gradients

As previously mentioned, we can further investigate the relative N and O abundances of individual H II regions using the radial gradient of N/O. Using N/O abundance ratios calculated following the methodology outlined in Section 4.2, we compute the radial gradients using four different N/O calculations. In Figure 4.3 we show the variations of N/O with GCR. We again fit straight lines using bootstrap resampling and give the mean and standard deviations of the gradient and the intercept. We find that the gradients and intercepts of all three PG16 methods agree within 1σ. This indicates no statistically significant difference between the choices of PG16 calibration.

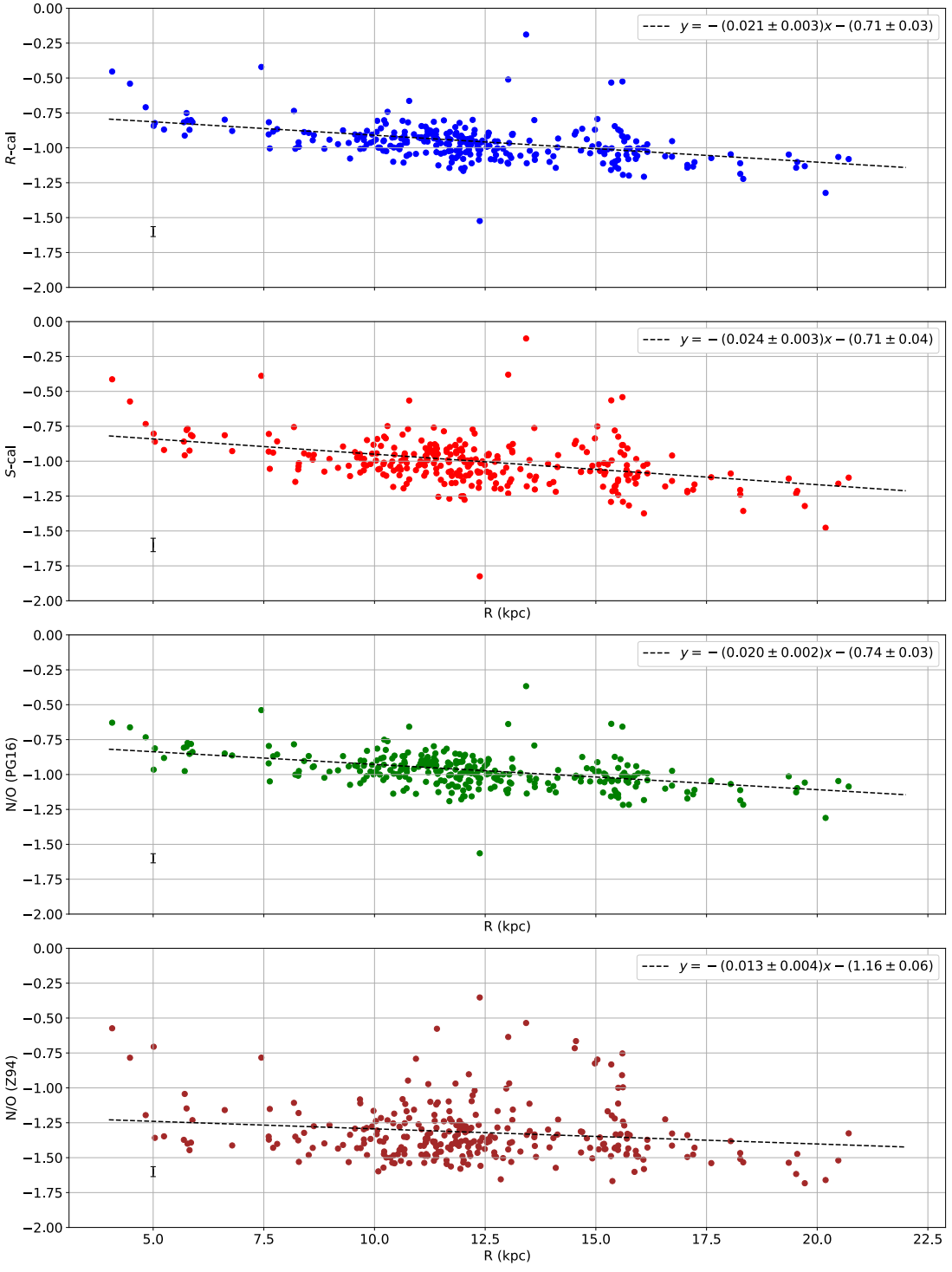

FIGURE 4.3: Variations of N/O with galactocentric radius for M 31 H II regions with abundances calculated using four different methods (three from Pilyugin and Grebel 2016 and one from Zaritsky et al. 1994). Linear fits to the data are shown. The typical uncertainty of the individual data points is displayed in the bottom-left corner of each panel.

For the Z94 calibration, we see a shallower gradient, but one in agreement with those of the other methods within 2σ. The intercept is significantly lower due to the steeper O/H gradient and higher metallicities of Z94-derived abundances identified in Paper I. Croxall et al. (2016) found the Pilyugin and Grebel (2016) *S*-cal and *R*-cal reproduced the directly calculated gradient and the level of scatter within 1σ compared to their T_e-based metallicity measurements of M 101 H II regions. This suggests that the abundances produced by the PG16 diagnostics reflect the true abundance gradients and scatter within the uncertainties. The overestimated O/H measurements from Z94 lead to underestimated N/O compared to PG16.

Abundance ratios of N/O calculated from N/H − O/H have measurement uncertainties of ≈ 0.04 − 0.05 dex, depending on the O/H calibration. Using the PG16 N/O calibration, the measurement uncertainties are ≈ 0.03 dex. The standard deviation (scatter) around the radial fit is ≈ 0.10 − 0.15 fit for the three methods of calculating N/O involving PG16 calibrations. The scatter of N/O around the radial fit exceeds the measurement uncertainties by up to 3σ, so we see real variations beyond the radial gradient of N/O as well as O/H.

One factor that can introduce scatter in abundances from strong-line diagnostics is internal temperature variations in H II regions (Peimbert 1967; Garnett 1992; Rubin et al. 2003). Croxall et al. (2016) found a similar scatter of ≈ 0.074 edex around the radial fits of both O/H and N/O for M 101. N/O is relatively insensitive to temperature variations, due to the similar excitation conditions of N and O (Pagel et al. 1979), suggesting that O/H is also not significantly impacted by internal temperature variations. Increased scatter of N/O compared to O/H could be the product of secondary N production in M 31, while variations of local enrichment due to nearby star formation (Kreckel et al. 2019; Bosomworth et al. 2025) could enhance the N/O ratio locally. However, N/H measurements also have higher inherent uncertainties due to the relative weakness of the N emission lines compared to the O lines in H II region spectra. This is likely to introduce larger scatter around our N/O fits compared to O/H fits.

4.3.3 log(N/O)-log(O/H) Scaling Diagrams

Chemical abundance scaling diagrams provide insight into the relative contributions of primary and secondary N and therefore the relative contribution of stars of different masses. In Figure 4.4 we show the variations of N/O with increasing metallicity (O/H) of individual M31 H II regions in M31. We display separately the O/H from the three calibrations outlined in Section 4.2. In each plot, we show the relationships of both N/O calculated from N/H - O/H using the

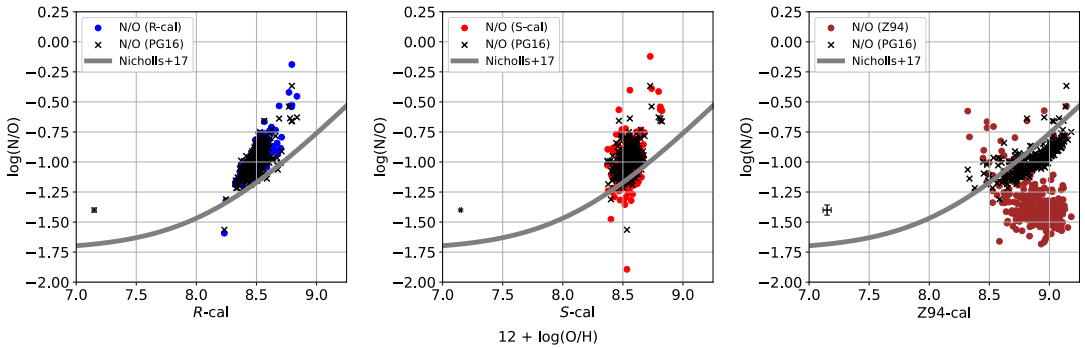

FIGURE 4.4: Variations of N/O with O/H of M 31 H II regions with O/H abundances calculated using two different strong-line calibrations from Pilyugin and Grebel (2016) and one from Zaritsky et al. (1994). On all plots, we display in black N/O from the PG16 calibration of N/O. We show the relation of Nicholls et al. (2017) as a grey solid line. The typical uncertainty of the individual data points is displayed in the bottom-left corner of each panel (see text).

respective O/H calibration, and the N/O calibration of PG16. We compare our measurements to the Nicholls et al. (2017) relation, which applies to MW nebular abundances, but has been shown to provide a satisfactory description of extragalactic nebular abundance behaviour (see Nicholls et al. 2017 Figure 4).

We see that, for our H II region sample, N/O increases with O/H. This trend is displayed at high metallicities where secondary N behavior dominates. This suggests our H II region sample probes the metallicity range where N/O increases linearly with O/H in M31.

The PG16 N/O calibration reduces the scatter of measurements around their mean fit in all cases. Comparing PG16 N/O with Z94 O/H, the trend is flattened, as a result of the wider range of metallicities arising from the Z94 calibration. The negative slope seen for the Z94 O/H when used to calculate N/O is unexpected and likely reflects limitations of the Z94 calibration. Z94 is calibrated for H II regions with $12 + \log(\mathrm{O/H}) \gtrsim 8.4$, and so its reliability decreases as metallicities approach or fall below this threshold. Z94 also overestimates O/H at higher metallicity compared to PG16 and T_e-derived values. T_e-based measurements are predicted to underestimate O/H at $12 + \log(\mathrm{O/H}) \gtrsim 8.6$ due to temperature fluctuations (e.g., Stasińska 1978; 2005; Kewley and Ellison 2008). We note that, because the PG16 calibrations are entirely empirical, these metallicity values are likely to be influenced by these same effects, suggesting caution when interpreting trends for $12 + \log(\mathrm{O/H}) \gtrsim 8.6$.

In Figure 4.4, the values of O/H for M 31 H II regions are offset by $\approx +0.2$ dex from the Nicholls et al. (2017) relation for both PG16 calibrations. Also, at $\approx \mathrm{O/H} \gtrsim 8.6$ we see a steeper rise in N/O for M31. The Nicholls et al. (2017) calibration sample itself shows that at higher

metallicity, points tend to lie preferentially above the mean relation, as shown in their Figure. 5. The Simba-C model (Hough et al. 2023) also shows a rise in N/O with increasing O/H but does not reproduce the steepening at high metallicities as derived by Nicholls et al. (2017) from observations. IFU studies using strong-line N/O diagnostics (e.g. Kojima et al. 2017) find a similar positive offset of $\approx 0.1 - 0.2$ dex using N/O calculated from strong-line diagnostics. This suggests that strong-line methods may systematically overestimate N/O relative to T_e-based abundances.

Differences in N/O relative to O/H in galaxies may be attributed to differing SFHs (e.g., Henry et al. 2000; Croxall et al. 2015). Vincenzo and Kobayashi (2018) found that N/O decreases with redshift, implying that N is produced over longer timescales than O. High N/O in H II regions also implies increased star formation at earlier times, leading to increased N production over time. This is in agreement with the chemical evolution model of Kobayashi et al. (2023), which suggests that the M31 disc was formed by a more intense initial starburst than the MW disc. We note that the results presented here are not conclusive evidence of a steeper N/O trend at high metallicities in M 31 relative to the MW. The findings of Zurita and Bresolin (2012) further support this caution, because, using T_e-based abundances over a similar metallicity range, no clear positive trend in N/O at high O/H was found in M 31. While these results reveal a well-defined positive $\mathrm{N/O} - \mathrm{O/H}$ trend characteristic of secondary nitrogen production, absolute N/O values and the steep trend at high metallicity are likely due to systematic uncertainties inherent to empirical strong-line diagnostics.

The presence of H II regions with enhanced N/O compared to other sources of similar metallicities suggests localised increased secondary N production. This may indicate a contribution of N from Wolf-Rayet (W-R) stars (e.g., Henry et al. 2000). Croxall et al. (2016) found that the presence of features typical of W-R stars in some of their sources does not, however, lead to trends of altered abundances in their $\mathrm{N/O} - \mathrm{O/H}$ diagram. On the other hand, López-Sánchez et al. (2007) found that N/O enrichment correlates with what is expected from W-R star ejecta. This finding is in agreement with the simulations of Vincenzo and Kobayashi (2018) for which, at $z = 0$, increased scatter of N/O is identified.

Using the *R*-cal method of PG16 for both N/O and O/H tightens any correlation, as identified in Section 4.3.1 for N/H and O/H. As a result, panel 1 of Figure 4.4 displays less scatter than panel 2. The positive trend is present also when we compare PG16 N/O with Z94 O/H. The PG16 N/O

diagnostic is constructed to increase with the N_2/R_2 line ratio (see their Fig. 6), and therefore a positive slope will naturally appear no matter the O/H calibration used.

To evaluate the magnitude of a possible pre-existing trend when the PG16 calibrations are used, we compute a test using abundances from randomised line ratios. The results of this test are presented in Appendix C. The positive slope of the $N/O - O/H$ relation for PG16 methods is significantly steeper in Figure 4.4 than for the random data, suggesting the steeper N/O slope seen for M31 is not entirely due to the calibration. Randomised data using the Z94 O/H diagnostic does not produce a statistically significant slope, indicating that independent and accurate methods are essential to robustly compare N/O with O/H, and this would ideally be done using direct abundance measurements.

4.3.4 Two-point Correlation Function of Residual N and N/O

In Paper I, we investigated the correlation of metallicity (O/H) as a function of H II region separation using a two-point correlation function. This technique was introduced by Kreckel et al. (2020), and we followed their methodology of first subtracting the radial-fit-predicted abundances from individual H II region abundances. In Paper I, the two-point correlation function of O/H was found to be significantly higher than that of the randomised sample until spatial scales of $\approx 3 - 5$ kpc, implying material is well-mixed on small scales. A possible explanation for this is that mixing slows down exponentially with spatial scale as predicted in simulations (de Avillez and Low 2002).

In this section we expand our analysis to both N/H and N/O and compare this with O/H as well as with results from a randomised sample. As described in Paper I, following Kreckel et al. (2020), a random sample was produced by assigning abundances from our sample to H II region positions at random. We display the two-point correlation functions of N/H and N/O in Figure 4.5.

For N/H, we find that the 50% correlation is reached at a separation of ≈ 0.6 kpc, and the 30% correlation at a separation of $\approx 1 - 1.5$ kpc. For N/O, the 50% and 30% correlation scales lie at $0.4 - 0.7$ kpc and $0.7 - 1.1$ kpc, respectively, depending on the method used to calculate N/O. N/H is more correlated than the randomised sample until a ≈ 2 kpc separation, while N/O remains above the randomised level only to $\approx$0.5 kpc. The 50% and 30% correlation scales for both N/H and N/O agree within 1σ with those of O/H, suggesting that approximately the

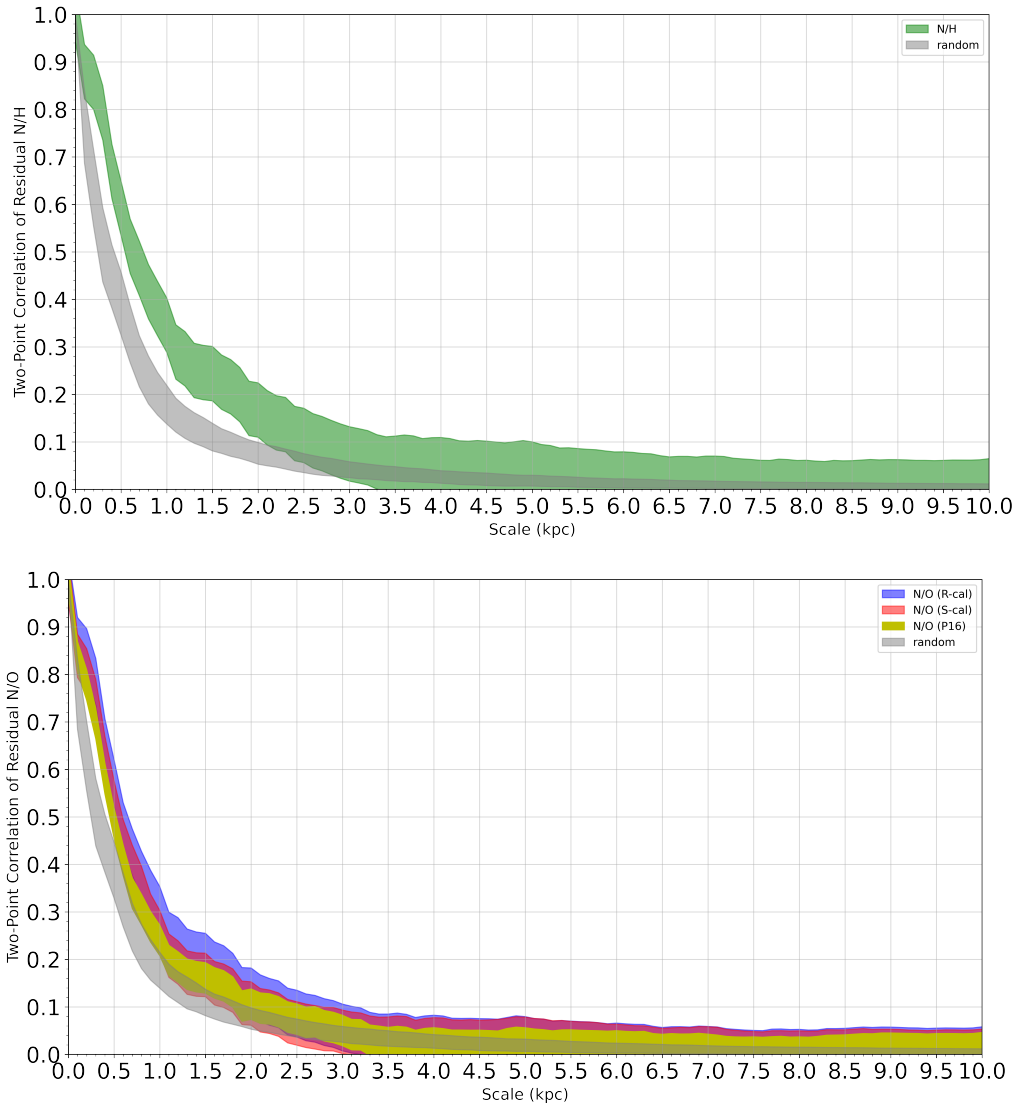

FIGURE 4.5: Two-point correlation function of residual abundances for N abundance from the PG16 *R*-cal (*top*), and N/O abundance from three PG16 methods outlined in Section 4.2 (*bottom*). For comparison, in each panel we also display the result from randomized abundances, which shows what the trend would be if the abundances and source position were uncorrelated.

same level of spatial variation is found using all three elemental abundance ratios. However, the separation at which the correlation function remains above the randomised sample is significantly different, and for O/H this occurs at $\approx$ 5.5 kpc, suggesting that O/H is more correlated over larger separations than both N/H and N/O.

However, because the typical uncertainties in N/H and N/O are comparable to the observed small-scale variations, while the O/H uncertainties are significantly smaller, the smaller difference between the real and randomised two-point correlation functions of N/H and N/O are likely due to higher measurement noise rather than a difference in the chemical distributions on these

small scales. Consequently, only O/H provides a small enough precision to identify small-scale abundance variations in this dataset.

4.4 Summary and Conclusions

Following Paper I, from multi-object spectroscopy we analyse the N/O (calculated from strong-line calibrations) variations of H II regions both across the disc of M31 and as a function of metallicity. From our analysis, we conclude the following:

- The gradient of $12 + \log(\mathrm{N/H})$ vs $12 + \log(\mathrm{O/H})$ is $\approx 2.3 \pm 0.2$ calculated from the mean of the PG16 *R* and *S* calibrations of O/H, consistent with the results from Paper I that N decreases with increasing GCR more severely than O, leading to higher N/O in the galaxy centre. This is in agreement with the cosmological simulations of Vincenzo and Kobayashi (2018). A positive trend is additionally seen in radial fit-subtracted abundances, implying this is not a result of radial metallicity gradients alone.

- We find a radial abundance gradient of N/O of $\approx 0.023 \pm 0.03$ dex kpc^{-1}, calculated from the mean fit of the three PG16 methods. If the Z94 O/H are used to calculate N/O, we find a shallower gradient but one in agreement within 2σ.

- We identify significant variations around the radial fit of N/O, as well as those previously identified for O/H and N/H (Paper I). For N/O, the scatter (standard deviation) is $\approx 0.10 - 0.15$ depending on the choice of PG16 method, up to 3σ above measurement uncertainties.

- We see a linear increase of N/O with O/H for M31 H II regions, steeper than that found for the MW (Nicholls et al. 2017). This is in agreement with simulations suggesting that N/O decreases with redshift (Vincenzo and Kobayashi 2018). A possible explanation is that the initial starburst that formed the disc of M31 was more intense and of a longer duration than that of the MW (Kobayashi et al. 2023), resulting in higher N/O over time.

- O/H from any of the PG16 calibrations is the best tracer of small-scale abundance variations within M31 based on our observations, as the N abundances have higher uncertainties. Therefore, O/H is best to reveal information on mixing efficiency at varying spatial scales.

Chapter 5

Conclusions

In this thesis, we presented an investigation into star formation on sub-cloud scales from observations of the Andromeda Galaxy. The overarching aim is to understand the initial conditions of star formation across an entire galaxy similar to the Milky Way. This was achieved by characterising dust and gas properties of giant molecular clouds, and the chemical properties of associated H II regions. In this section, we outline the key results of each chapter.

Chapter 2: Cloud-scale elemental abundance variations and the CO-to-dust-mass conversion factor in M31

Spiral galaxies generally display a negative radial trend in metallicity, a result of inside-out galaxy formation which results in a higher star formation rate towards the galaxy centre. However, significant scatter around this radial gradient suggests that the radial gradient alone does not describe the metallicity variation across the galaxy disc. In Chapter 2 we investigate metallicity variation across the disc of M31 from optical spectroscopy using the MMT/Hectospec. Optical emission line ratios are used to first distinguish between H II regions and planetary nebulae and subsequently measure the chemical abundances of oxygen and nitrogen. The focus of this study is H II regions, which reflect ongoing star formation. The radial gradient of oxygen abundance from M31 H II regions is relatively shallow in comparison to other spiral galaxies and is shallower than the Milky Way value by a factor of $\sim 4-6$. The nitrogen abundance gradient is steeper than that of oxygen abundance by a factor of $\sim 1.7-3.4$, additionally indicating that the nitrogen-to-oxygen ratio is higher towards the centre of the galaxy, a result which is consistent with cosmological simulations.

Significant scatter of up to 6σ standard deviation around the radial gradient is present throughout the disc. However, no large-scale azimuthal trends were identified. The two-point correlation function of metallicity indicates that values are well-correlated on sub-kpc scales, and less so on larger scales. This supports the prediction from simulations that mixing speed decreases exponentially, and therefore kpc-scale inhomogeneities are present for longer periods of time. Enrichment compared to the radial gradient is an indication towards locations of recent star formation and supernovae. On the other hand, reduced abundances may indicate the presence of pristine material brought into the galaxy from an external source. This is possible evidence of the M31-M32 collision predicted to have occured 200 - 800 Myr ago. Finally, the first results of a direct test of the metallicity dependence of the CO luminosity to dust mass ratio ($\alpha'_{^{12}\mathrm{CO}}$) in M31 indicate that $\alpha'_{^{12}\mathrm{CO}}$ may increase at lower metallicity. Additional Dust observations at lower metallicities are crucial to confirm this trend.

Chapter 3: Resolved Dust Emission and CO Isotopologues in Giant Molecular Clouds of the Andromeda Galaxy

The CO-to-H_2 conversion factor, α_{CO}, is essential for extragalactic observations. CO is by far the brightest emitter at radio wavelengths and so can be observed at great distances. Therefore, an accurate estimation of α_{CO} is required to accurately constrain H_2 properties of GMCs. To accurately constrain α_{CO}, we can use a tracer of optically thin material, such as thermal dust emission. However, as dust emission is less bright, observations of resolved GMCs are primarily limited to the Milky Way. However, the recent wideband receiver upgrade to the SMA has enabled the first resolved dust continuum detections from M31 GMCs. In Chapter 3, we analyse results from the now completed survey which obtained simultaneous dust continuum and CO isotopologues with identical astrometry.

A total of 46 dust continuum detections associated with GMCs were obtained, of which 21 are resolved. The sensitivity of observations to ^{12}CO was high enough to trace entire GMCs by 3σ contours. The CO-to-dust mass conversion factor, α'_{CO}, was obtained for all dust cores from $^{12}\mathrm{CO}(2-1)$ and $^{13}\mathrm{CO}(2-1)$ luminosities. α'_{CO} was found to be approximately constant across the sample, and in agreement with the Milky Way value within uncertainties. We conclude that the majority (74%) of dust detections are bound, consistent with the result previously found for ^{13}CO from the same survey. Results suggest that whilst M31 GMCs were previously found to be largely unbound, dense material is contained within bound substructures. Finally, from the updated sample of dust detections, $\alpha'_{^{12}\mathrm{CO}}$ was again found to be approximately constant with metallicity.

Chapter 4: Variation of the Nitrogen-to-Oxygen ratio in H II regions across the disc of M31
From the nitrogen-to-oxygen abundance ratio, log(N/O), information on the relative enrichment of the interstellar medium from stars of different masses can be inferred. Theoretical simulations suggest that log(N/O) is higher towards the centre in spiral galaxies, and radial abundance gradients derived in Chapter 2 are in agreement. A diagram of log(N/O) against 12 + log(O/H) provides information on the enrichment due to primary and secondary nitrogen nucleosynthesis with increasing metallicity. In Chapter 4, log(N/O) was calculated for our sample of 294 H II regions.

Firstly, we found that nitrogen and oxygen abundances increase linearly with one another, with nitrogen increasing more significantly. This is true also for N/O values excluding the radial best-fitting relation, indicating this is not entirely due to metallicity gradients. Significant scatter around the radial gradient is also present in N/O, alongside O/H and N/H. For the metallicity range probed, N/O generally increases with O/H, consistent with the onset of secondary nitrogen behaviour. At lower metallicities, when primary nitrogen dominates, N/O is constant with increasing O/H and the transition region between primary and secondary nitrogen is a non-linear curve. At high metallicities, N/O increases with O/H more rapidly than seen for the Milky Way. While this may support evidence that M31 formed from a more intense and rapid initial starburst than the Milky Way, systematic offsets due to strong-line calibrations cannot be ruled out. Finally, the best tracer of local abundance variation in M31 from our observations is O/H, due to higher measurement uncertainties from nitrogen-based abundance ratios.

Concluding Remarks
In conclusion, this thesis provides a comprehensive view of star formation across the disc of M31 from a multi-wavelength perspective. Optical spectroscopy of H II regions reveals significant deviations from radial-fit predicted metallicities, indicating local variations in chemical enrichment, and potentially reflecting recent ($\approx$ 200 Myr) interactions with satellite galaxies. From mm-wavelength observations of dust and CO$(2-1)$ emission, we build on previous work to further demonstrate that star formation takes place in dense, gravitationally bound, and approximately virialized structures within GMCs. Dust continuum emission traces the physical conditions of the dense gas from which stars form, enabling constraints on $\alpha_{\rm CO}$, a crucial parameter for accurately measuring molecular gas masses in extragalactic astronomy. Together,

these studies highlight that combining dust-calibrated $\alpha_{\rm CO}$ and H II region metallicities for the same clouds across a range of environments is essential to further advance understanding of if/how $\alpha_{\rm CO}$ varies between or within galaxies. In turn, this provides deeper insight into the initial conditions of star formation in spiral galaxies like M31 and the MW.

Chapter 6

Future Work

This thesis has opened up exciting further studies, in particular from improving observational capabilities enabling observations of resolved dust emission in M31. An advantage of simultaneous dust and molecular line information of the same sources, is that the CO velocities can provide structural information on the individual molecular clouds. This is particularly beneficial for a nearby and highly inclined spiral galaxy such as M31, which contains a range of velocities relative to the Milky Way. Therefore, we will combine single-dish data from the IRAM 30m telescope and the SMA interferometry survey presented in Chapter 3 of the same clouds. Single-dish data will provide the velocity information of larger structures, and allow us to assess how GMCs fit into more extended structures, whilst SMA observations can measure velocities of individual clouds and cloud substructure. Velocity information provides insight into the number clouds or sources positioned along the line of sight, using the line wavelengths we can disentangle individual clouds.

In Chapters 2 and 4 we calculated oxygen and nitrogen abundances from strong-line diagnostics. The nitrogen and oxygen abundances compared in Chapter 4 are not independently calculated and depend on the same strong-line ratios. Although we found that the trend displayed in the log(N/O) vs log(O/H) diagram is significantly steeper than that obtained using random line ratios, the best way to independently calculate nitrogen and oxygen abundance is from the corresponding auroral lines. Esteban et al. (2009), 2020 have published line-intensities of M31 H II regions on larger scales than our observations, but that include directly calculated abundances. We plan to measure PG16 abundances from these measurements to produce a comparison with the log(N/O)-log(O/H) diagram from our data.

Appendix A

Optical Emission Line Fits

In this Section we show the Gaussian fits to the emission line profiles for the strong lines measured in Chapter 2 to calculate O and N abundances. We show examples from two spectra of M31 H II regions in our sample in Figure A.1. One spectrum from the top 2 per cent highest signal-to-noise spectra in our sample, and one spectrum from the bottom 30 per cent lowest signal-tonoise spectra in our sample. The respective Gaussian fits to each line profile are additionally shown.

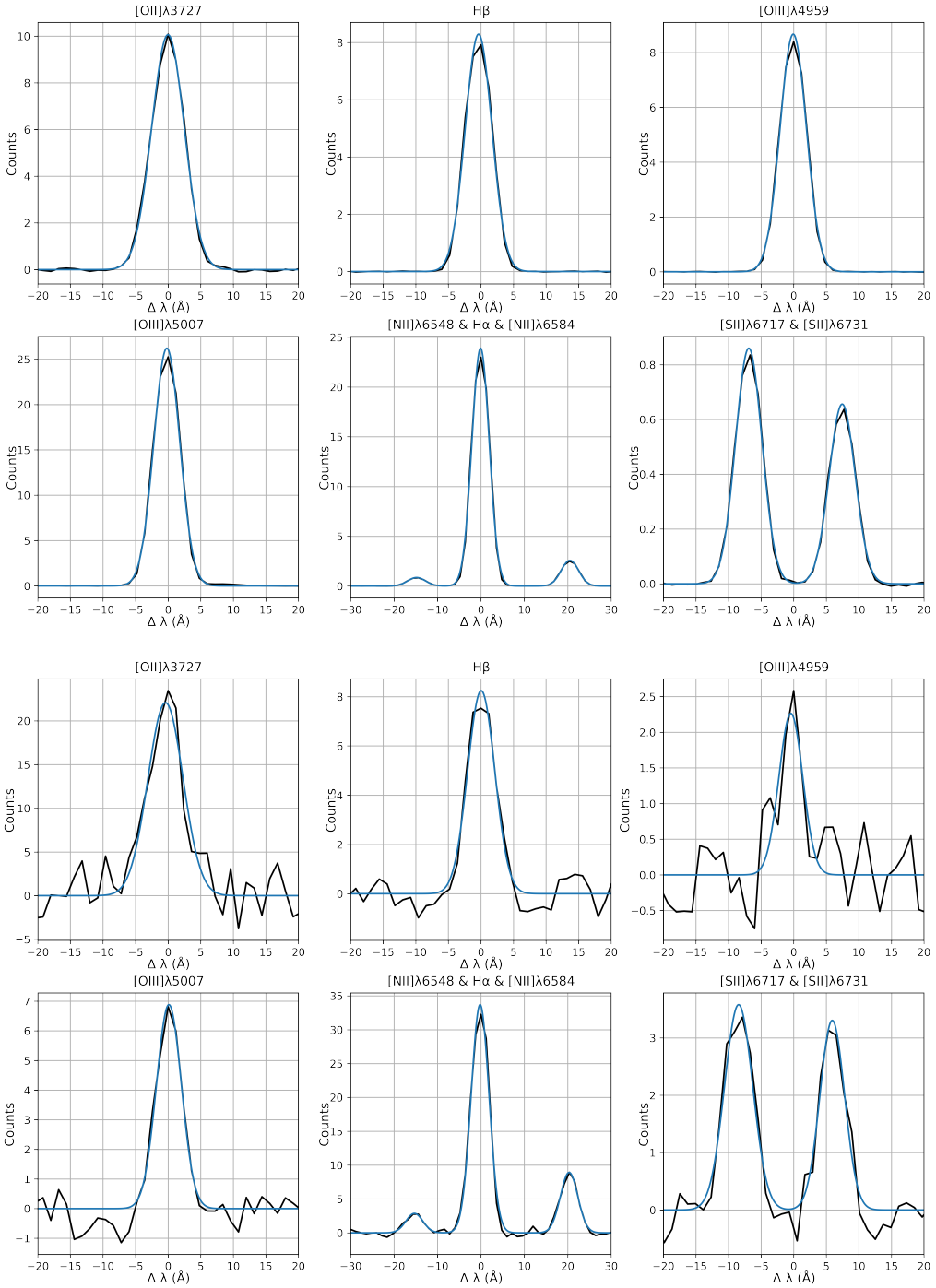

FIGURE A.1: Emission line profiles for the strong lines measured in two example spectra. *Top:* spectrum in the top 2 per cent signal-to-noise (row 7 from the Chapter 2 data tables). *Bottom:* spectrum in the bottom 30 per cent signal-to-noise (row 6 from the Chapter 2 data tables). On the x-axis, 0 represents the rest wavelength of the lines. In the case the line profile of Hα and the [N II] doublet, we centre the wavelength-axis on the midpoint of Hα. For the [S II] doublet, we centre the wavelength axis on the mid-point between the rest wavelengths of both lines.

Appendix B

SMA Dust Cores Complete Catalog

In this section, we present an atlas of all dust continuum emission maps and corresponding CO line profiles for all dust cores from the SMA survey utilised in Chapter 3.

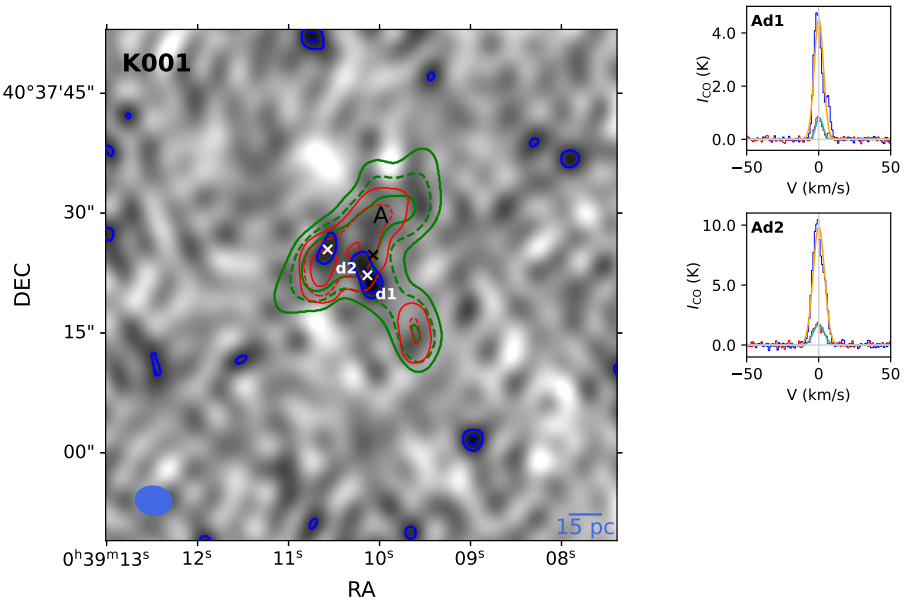

FIGURE B.1: *Left,* SMA maps of dust continuum of individual Kirk et al., (2015) GMAs in M31, for fields which contain one or more dust cores. The centres of mass (by area) of individual GMCs are marked by black 'x's', and by white 'x's' for individual dust cores. Contours are the same as for Figure 3. *Right,* Corresponding CO line profiles extracted from within individual dust cores, for both ^{12}CO and ^{13}CO. We mark any H II regions, identified from optical spectroscopy (Chapter 2), which are associated with GMCs containing a 1G dust core as yellow diamonds. Gaussian fits to line profiles are displayed for the 1G sample.

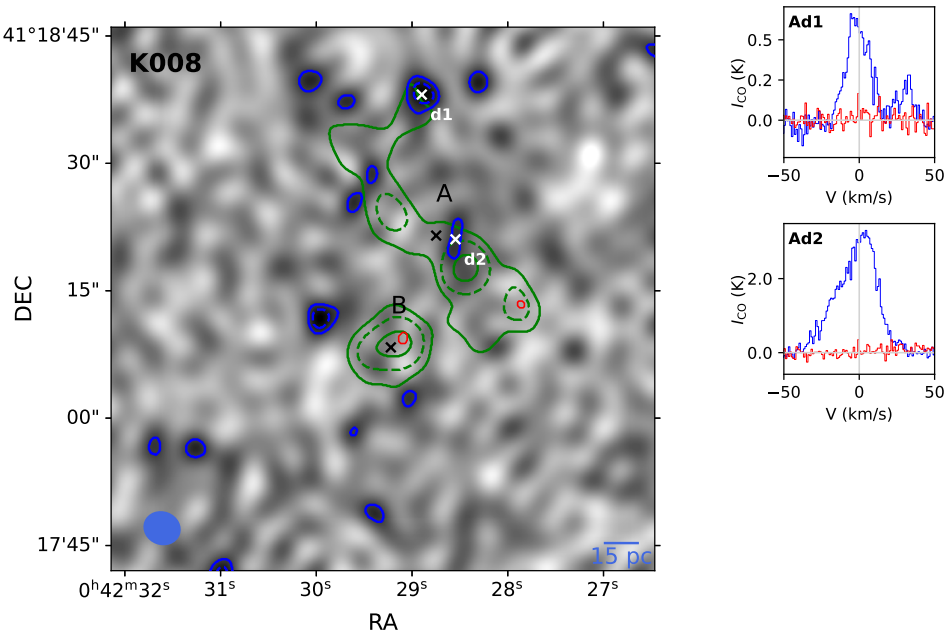

FIGURE B.1: (continued.)

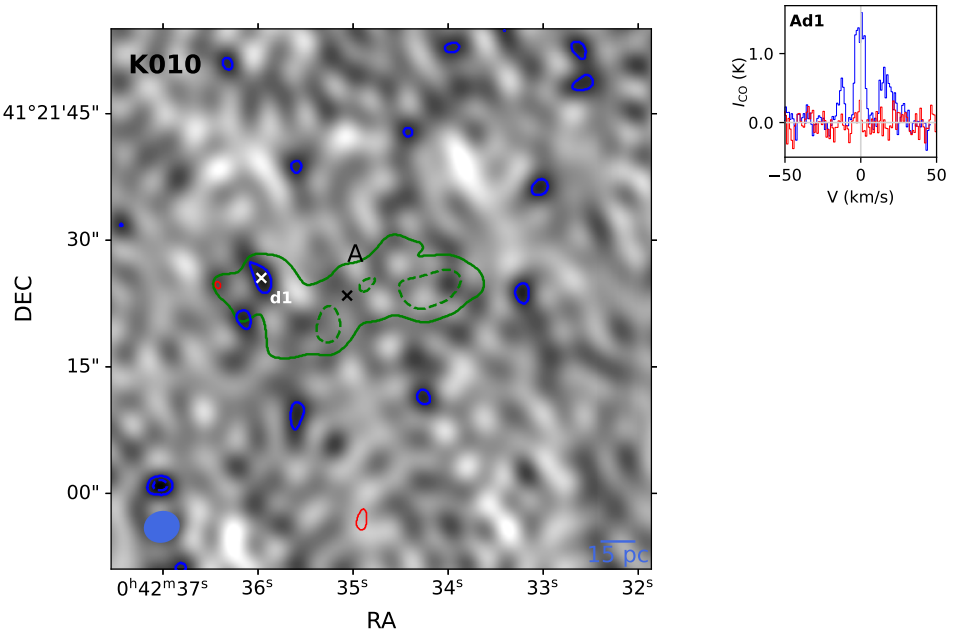

FIGURE B.1: (continued.)

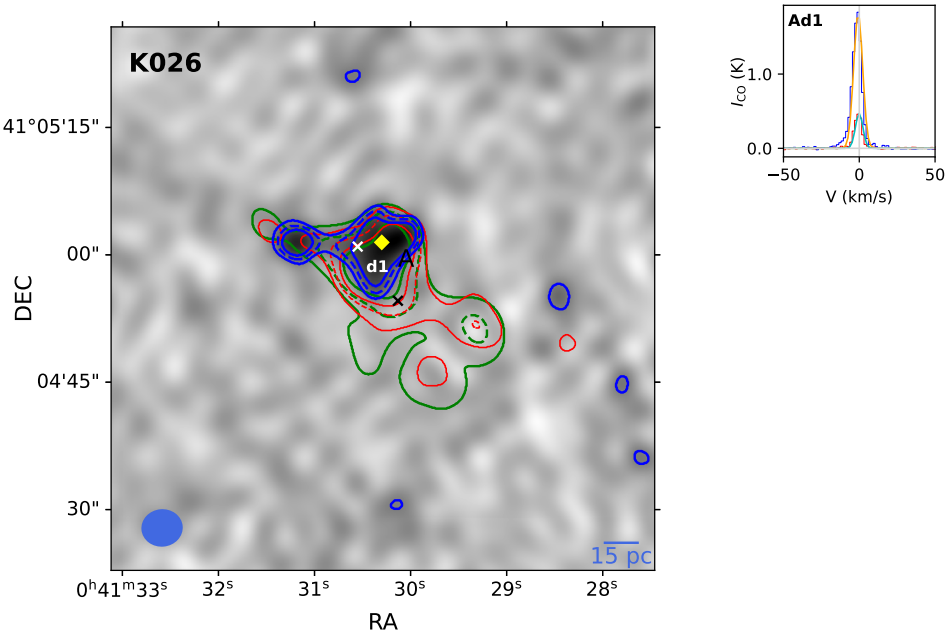

FIGURE B.1: (continued.)

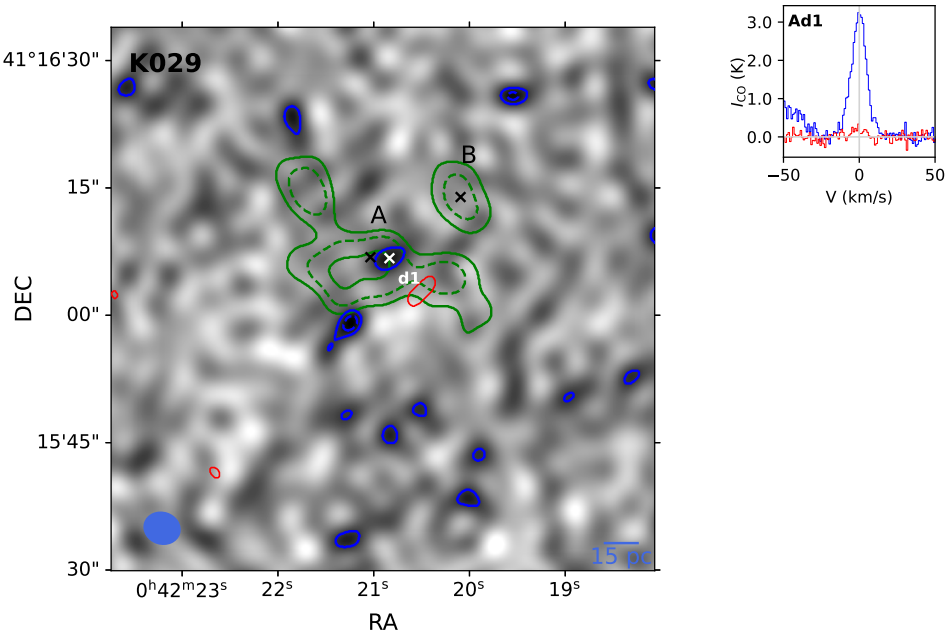

FIGURE B.1: (continued.)

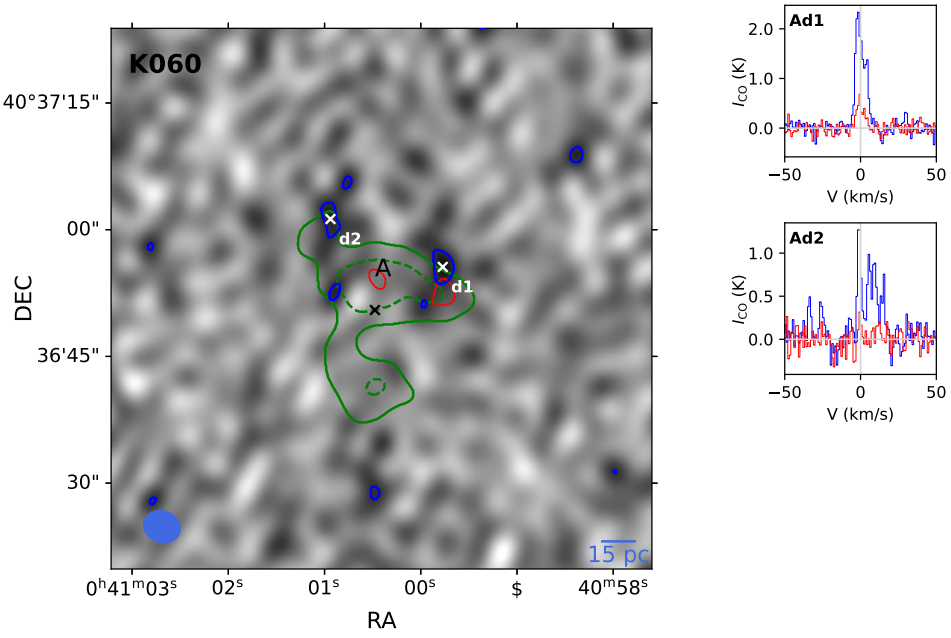

FIGURE B.1: (continued.)

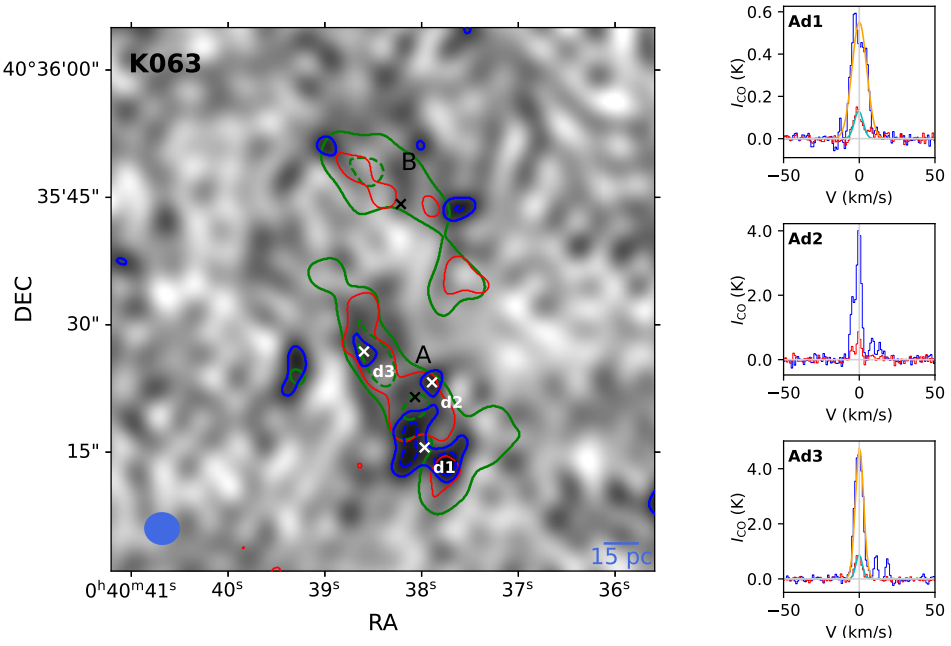

FIGURE B.1: (continued.)

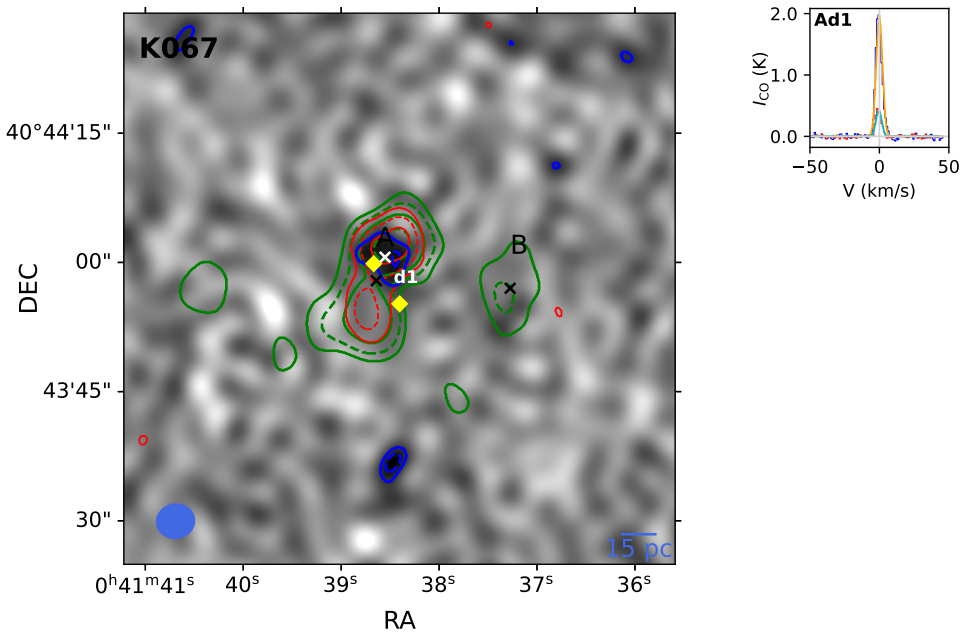

FIGURE B.1: (continued.)

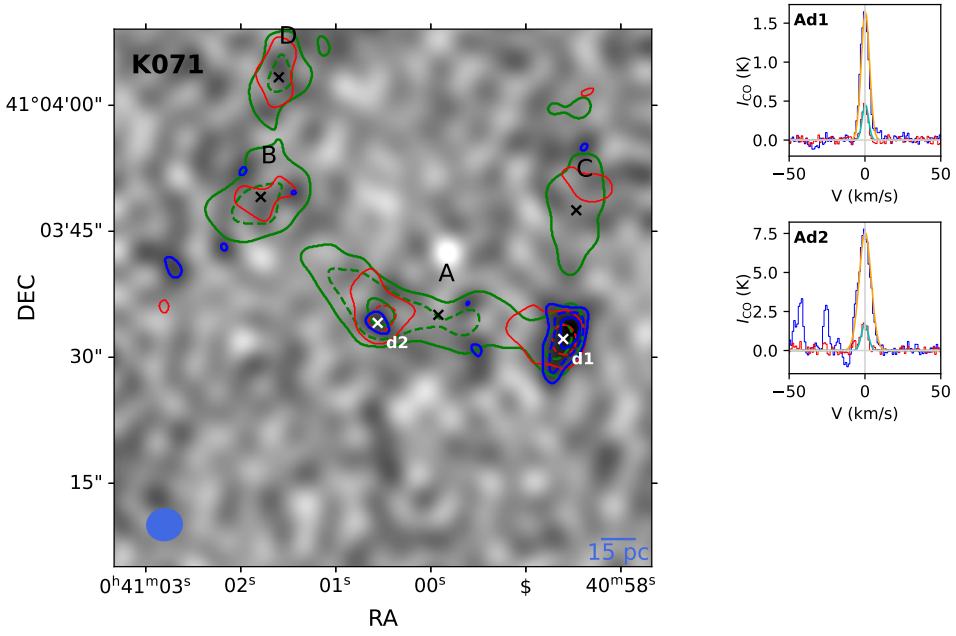

FIGURE B.1: (continued.)

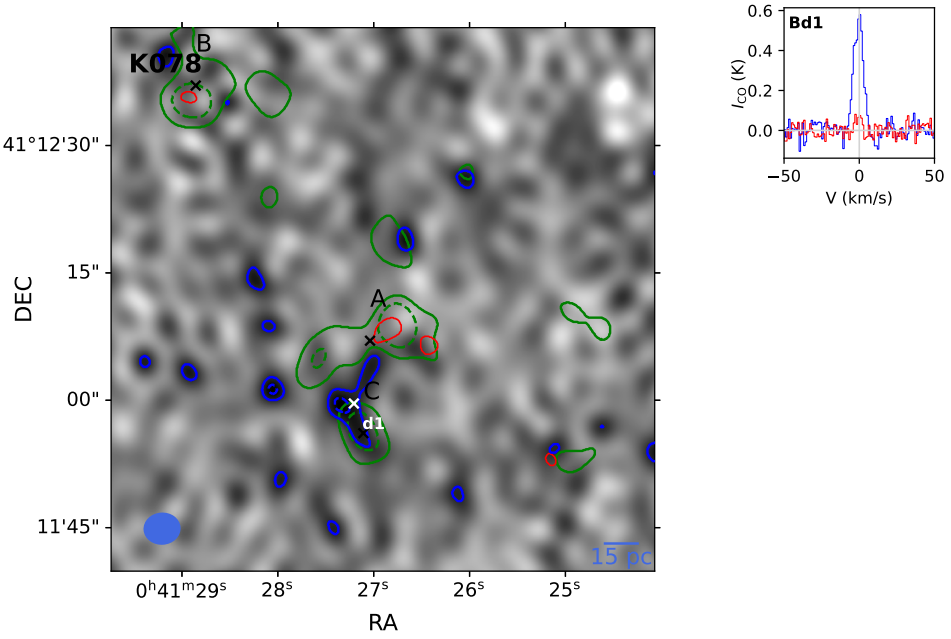

FIGURE B.1: (continued.)

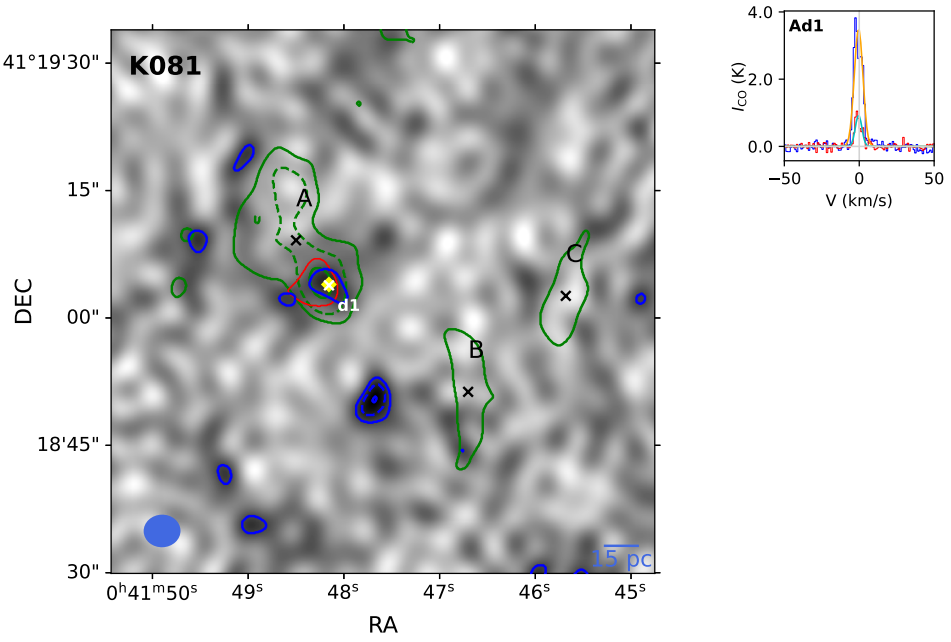

FIGURE B.1: (continued.)

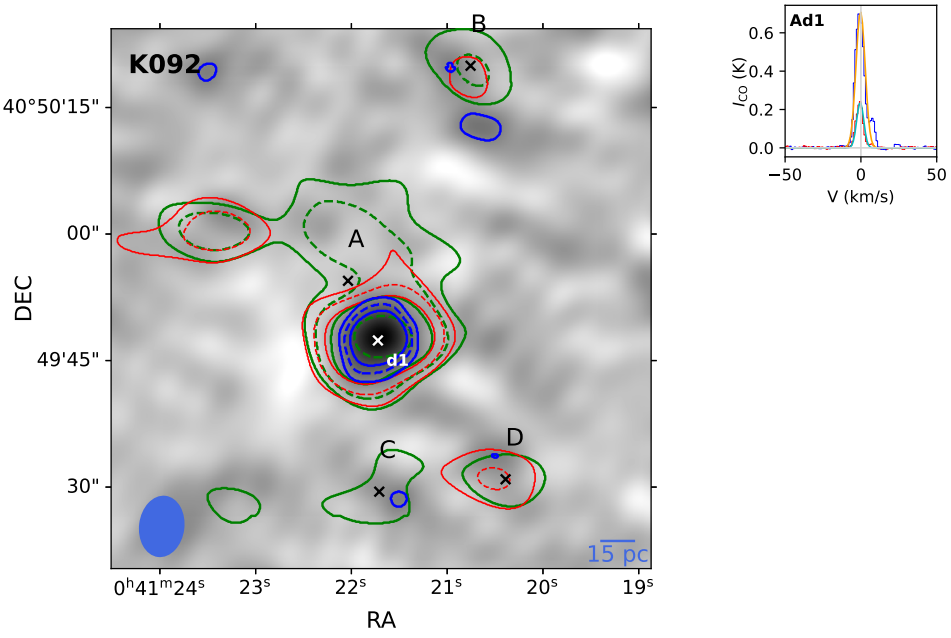

FIGURE B.1: (continued.)

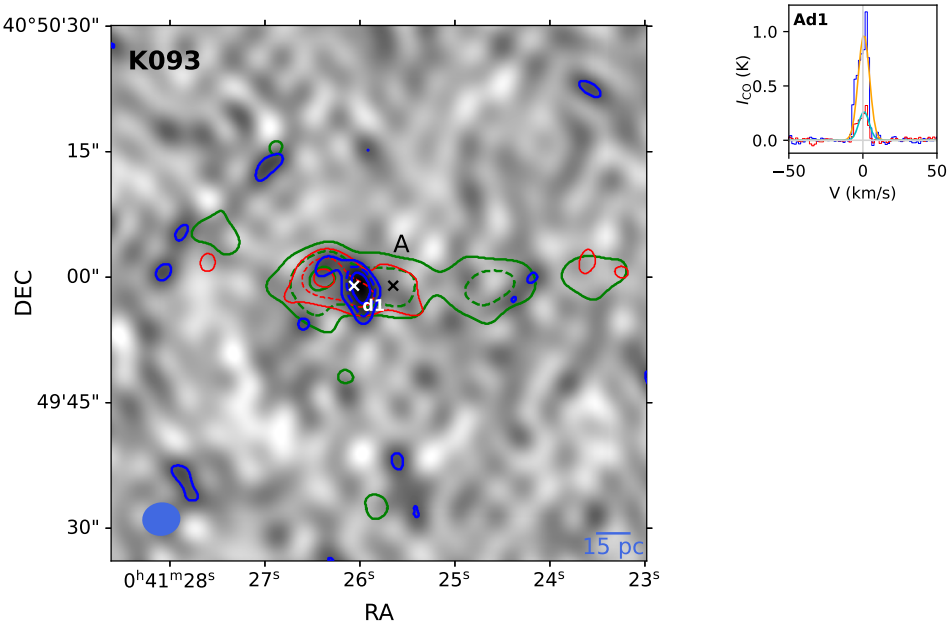

FIGURE B.1: (continued.)

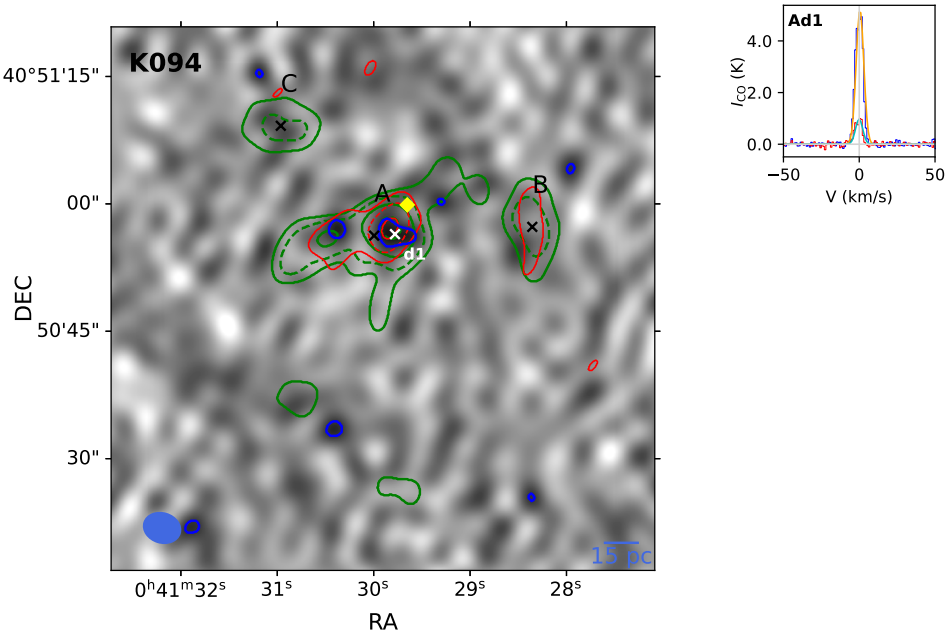

FIGURE B.1: (continued.)

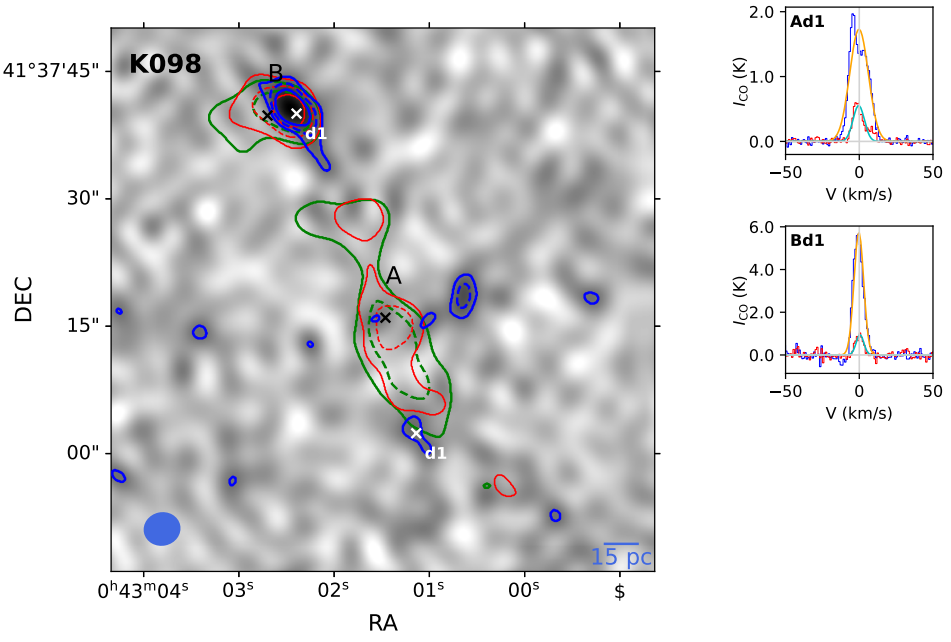

FIGURE B.1: (continued.)

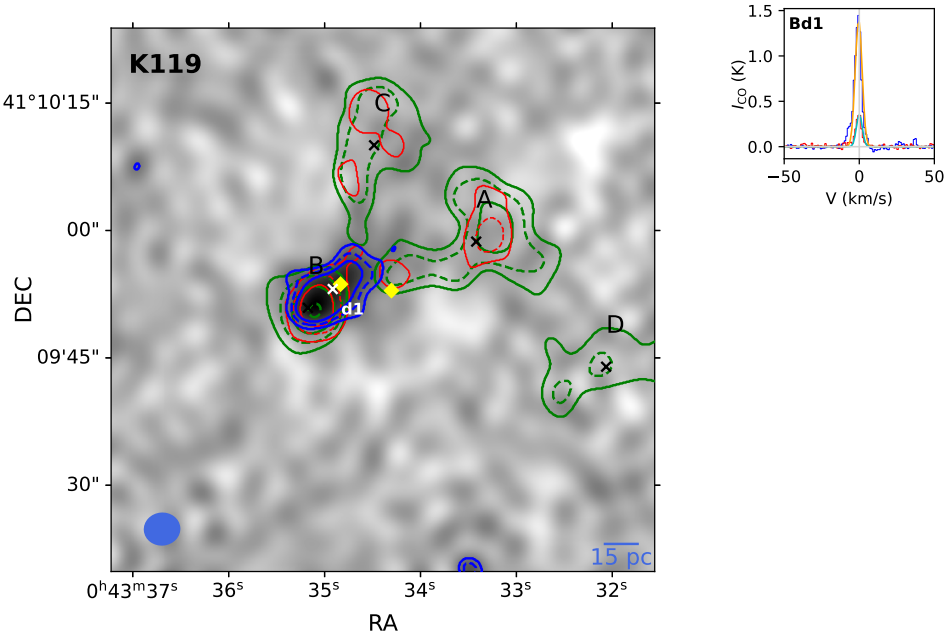

FIGURE B.1: (continued.)

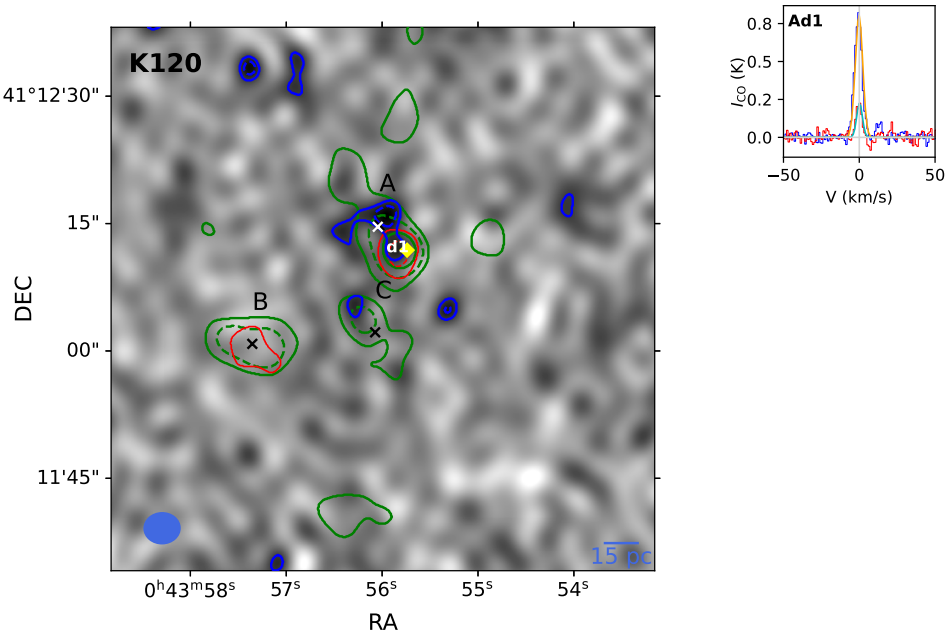

FIGURE B.1: (continued.)

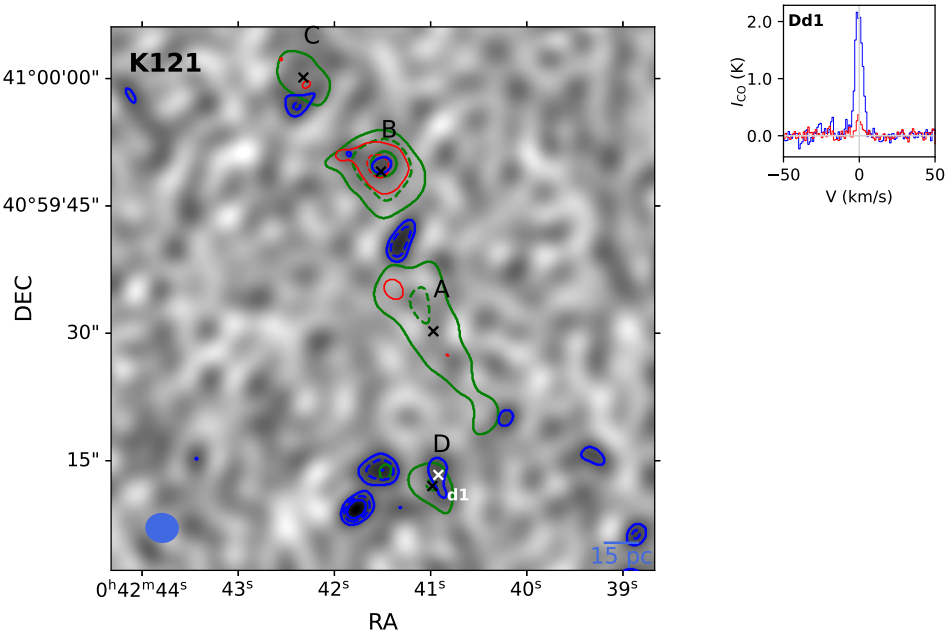

FIGURE B.1: (continued.)

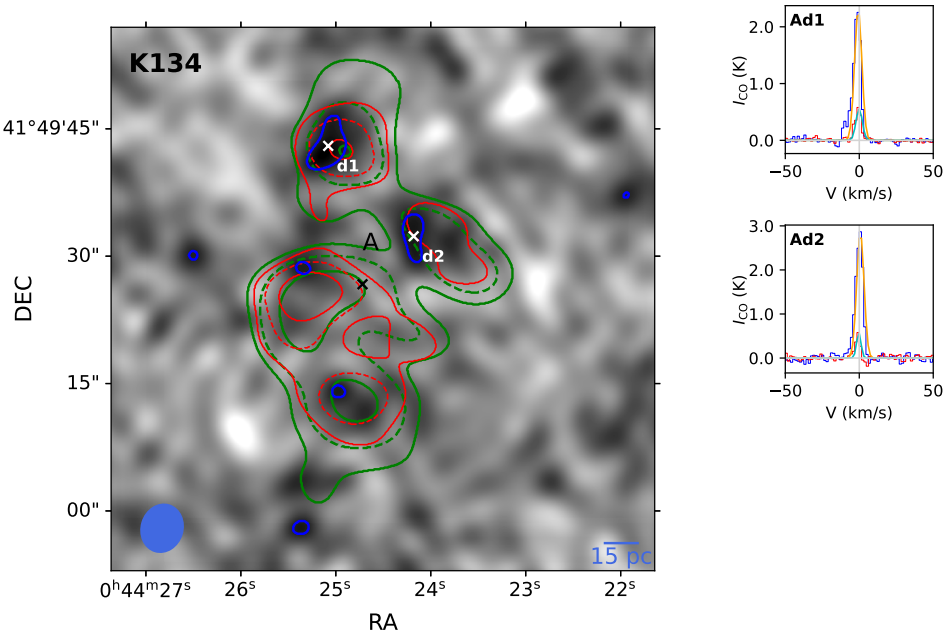

FIGURE B.1: (continued.)

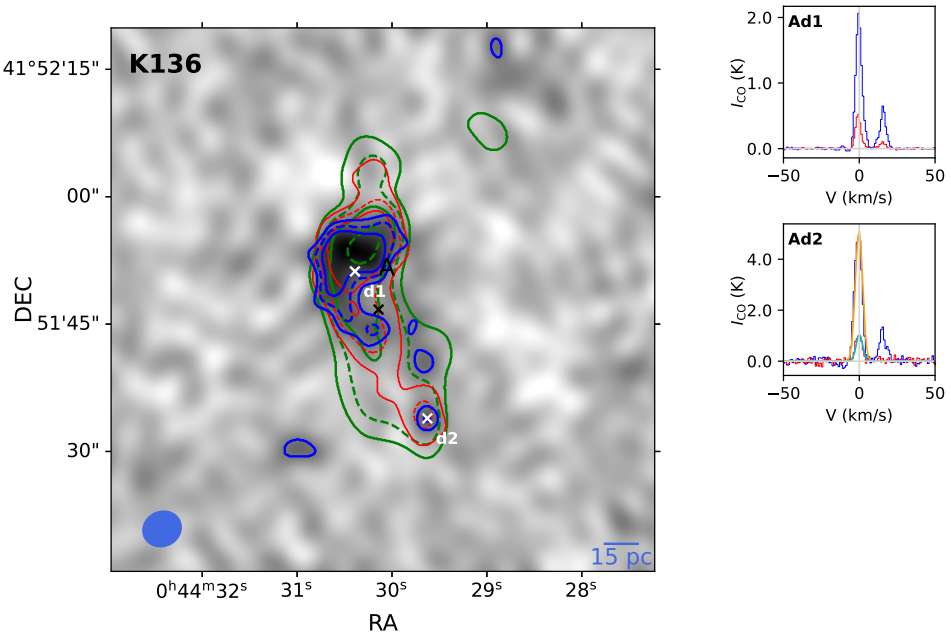

FIGURE B.1: (continued.)

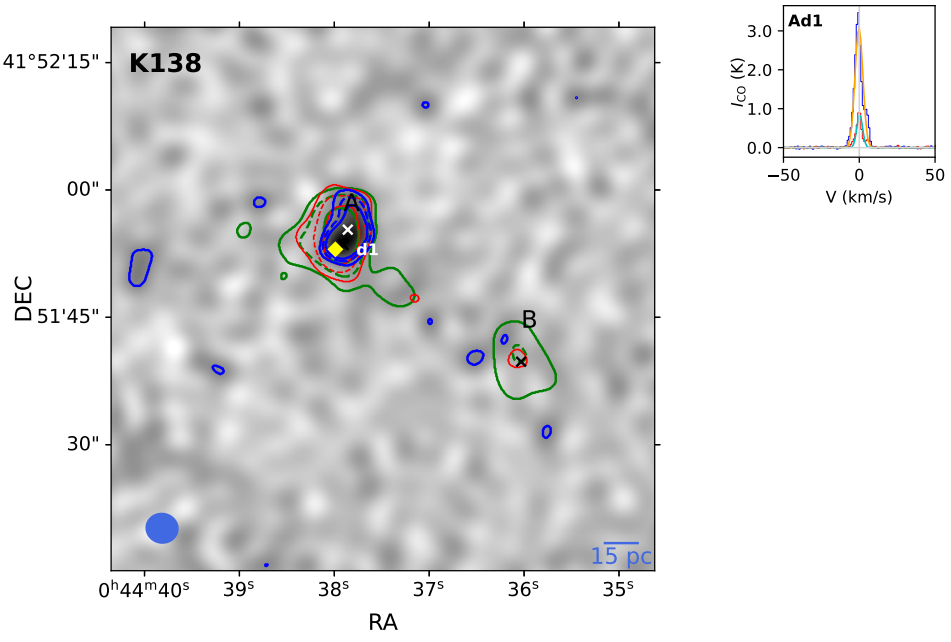

FIGURE B.1: (continued.)

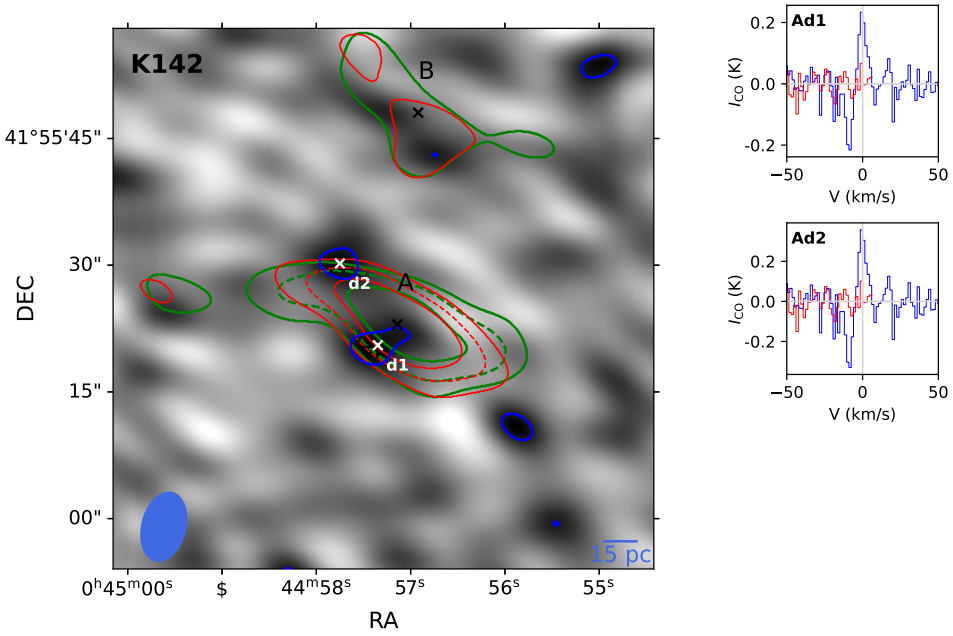

FIGURE B.1: (continued.)

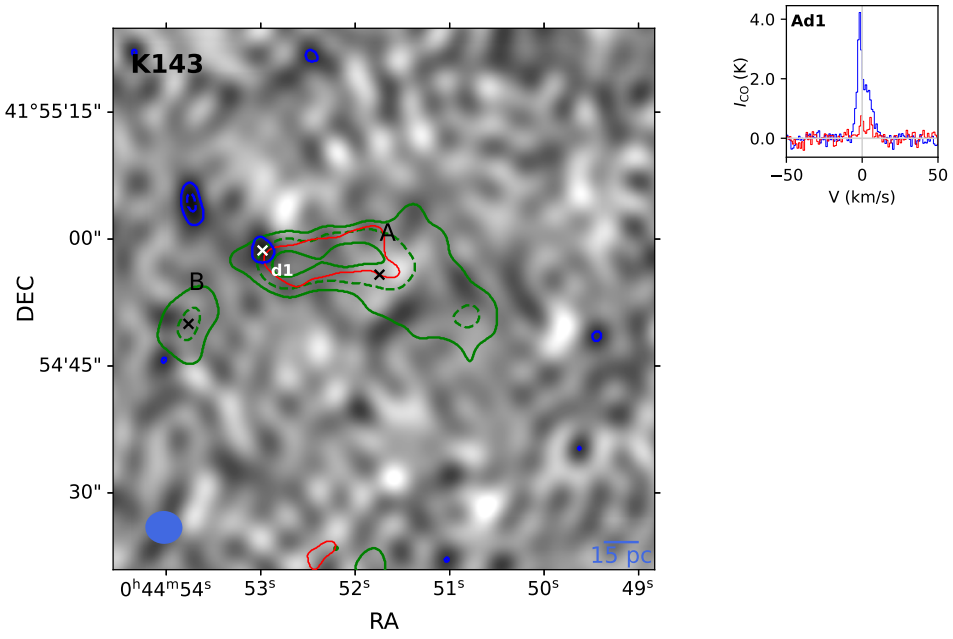

FIGURE B.1: (continued.)

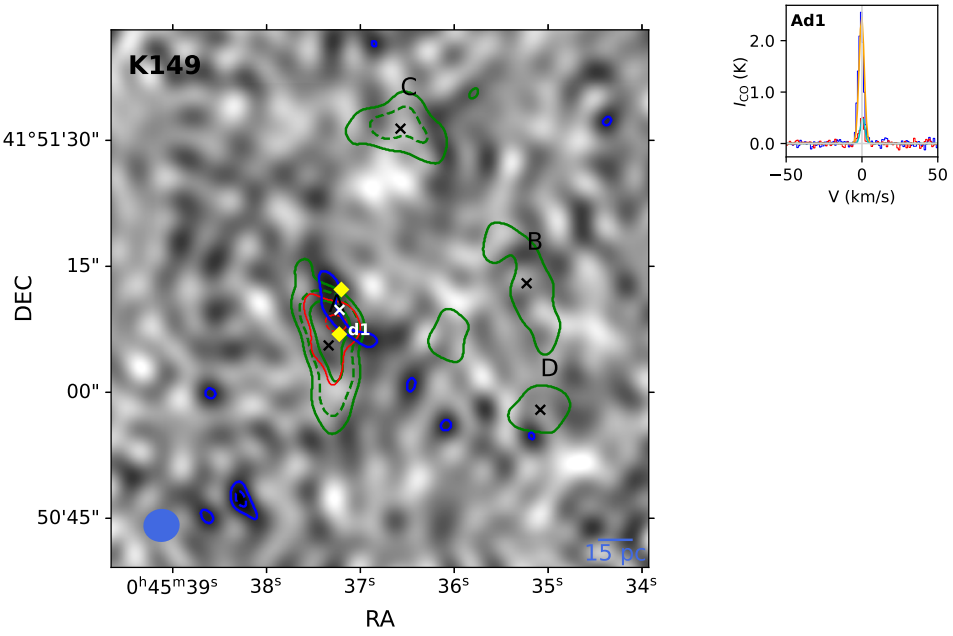

FIGURE B.1: (continued.)

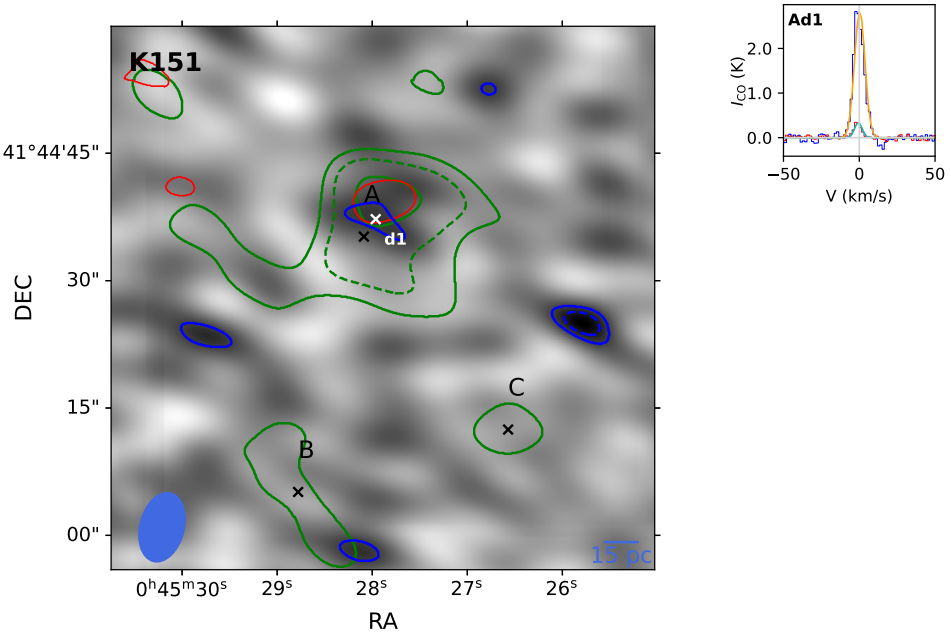

FIGURE B.1: (continued.)

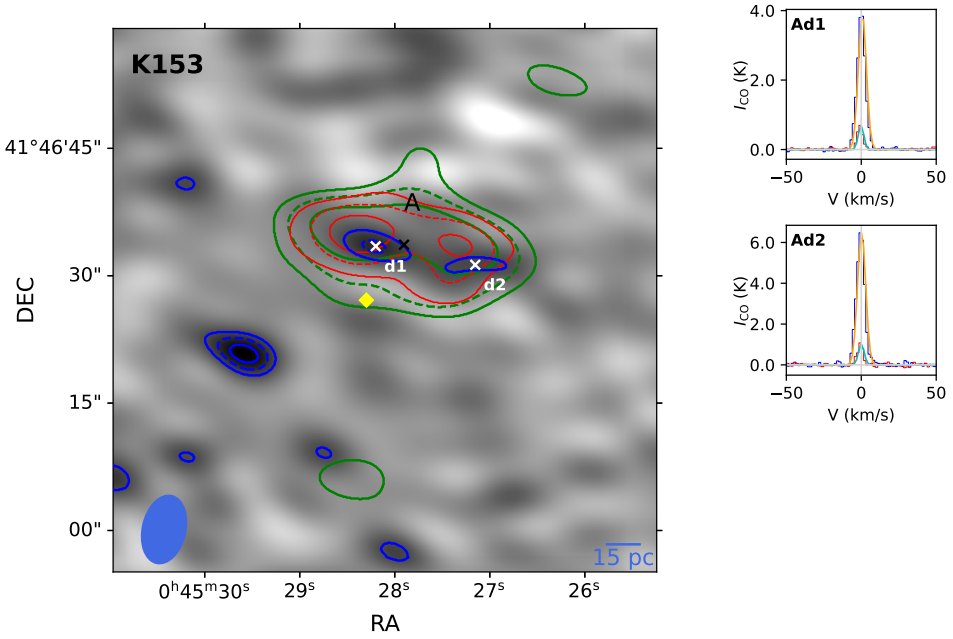

FIGURE B.1: (continued.)

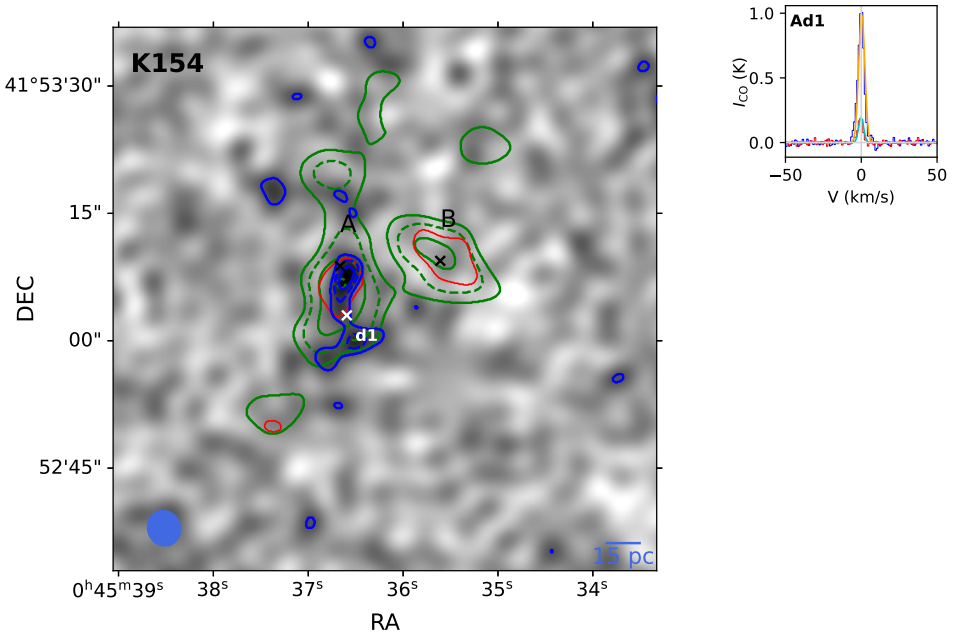

FIGURE B.1: (continued.)

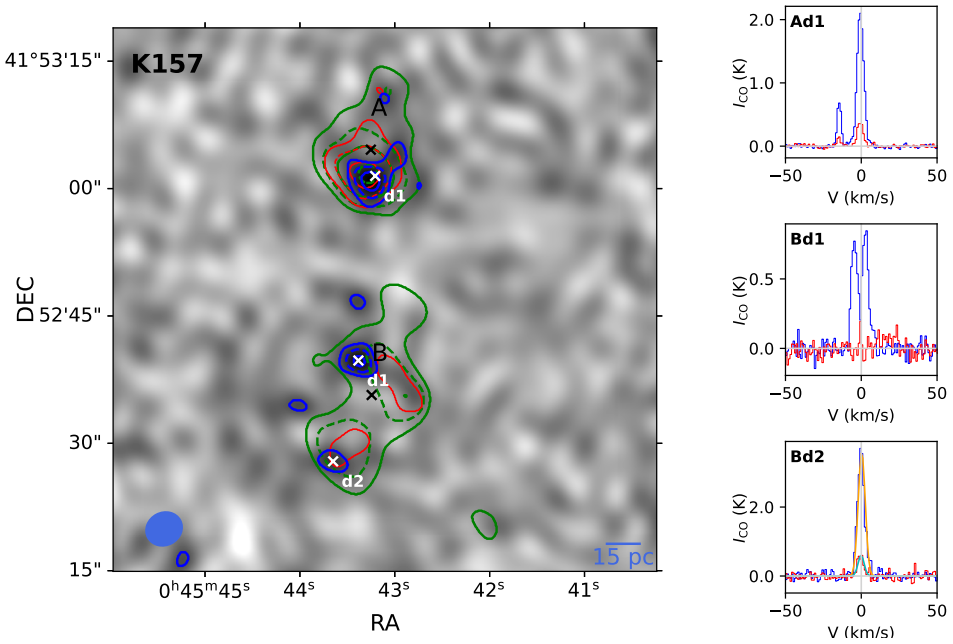

FIGURE B.1: (continued.)

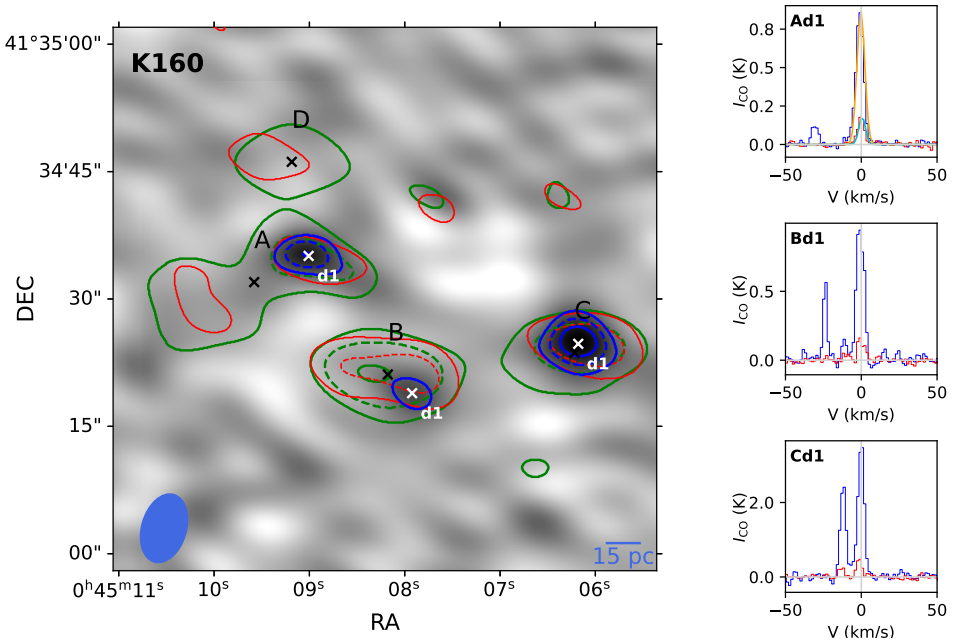

FIGURE B.1: (continued.)

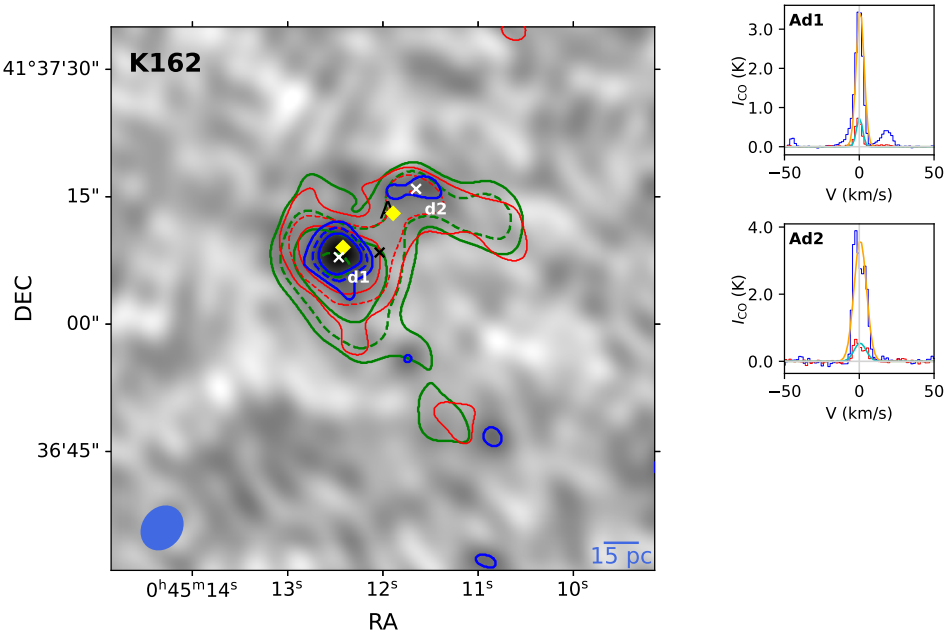

FIGURE B.1: (continued.)

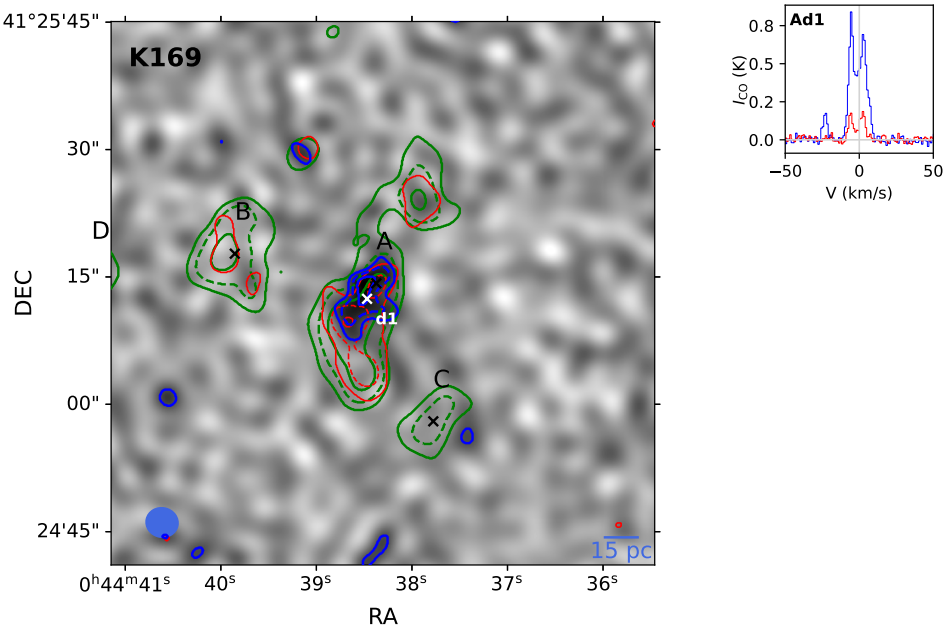

FIGURE B.1: (continued.)

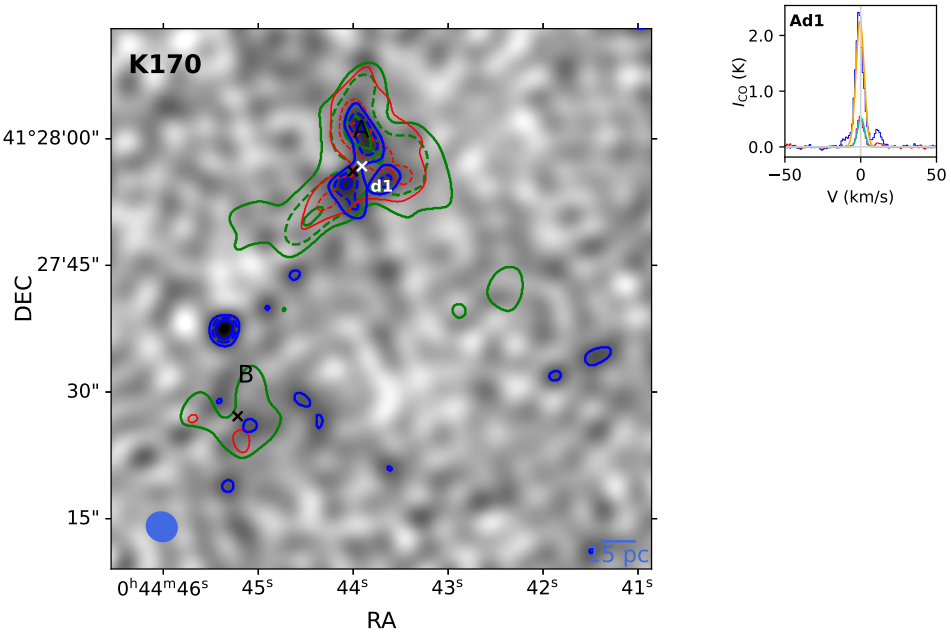

FIGURE B.1: (continued.)

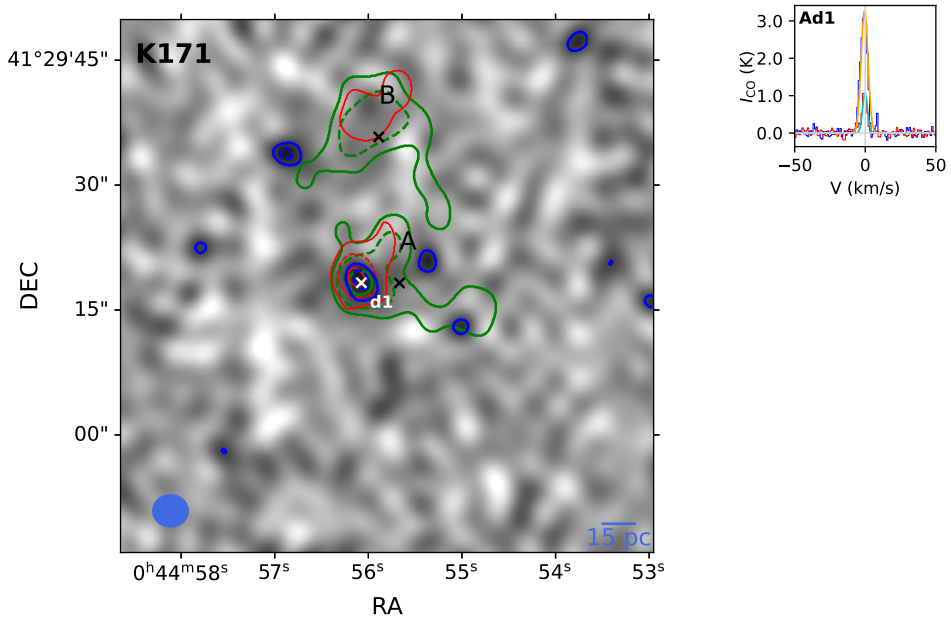

FIGURE B.1: (continued.)

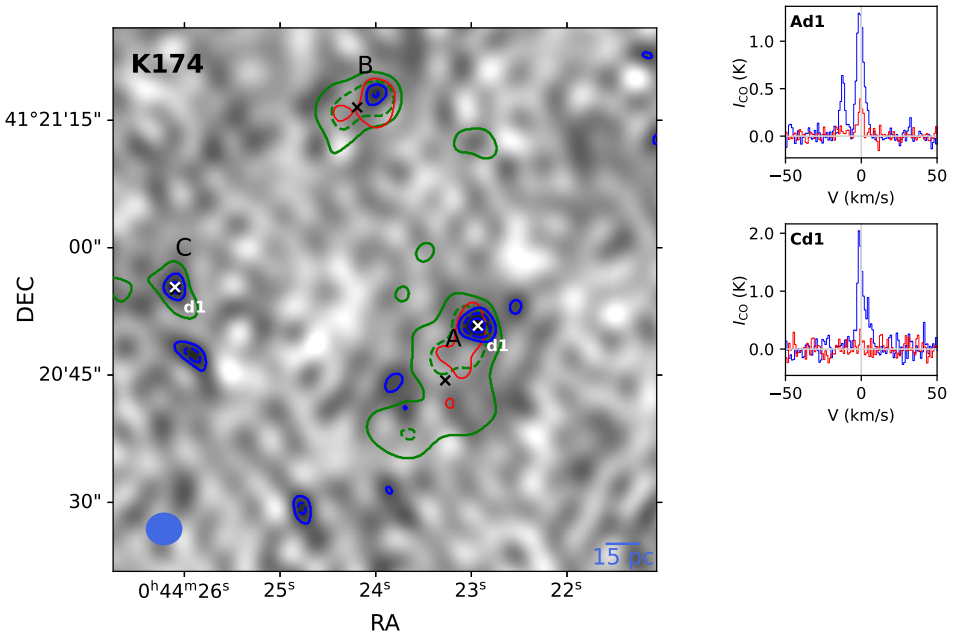

FIGURE B.1: (continued.)

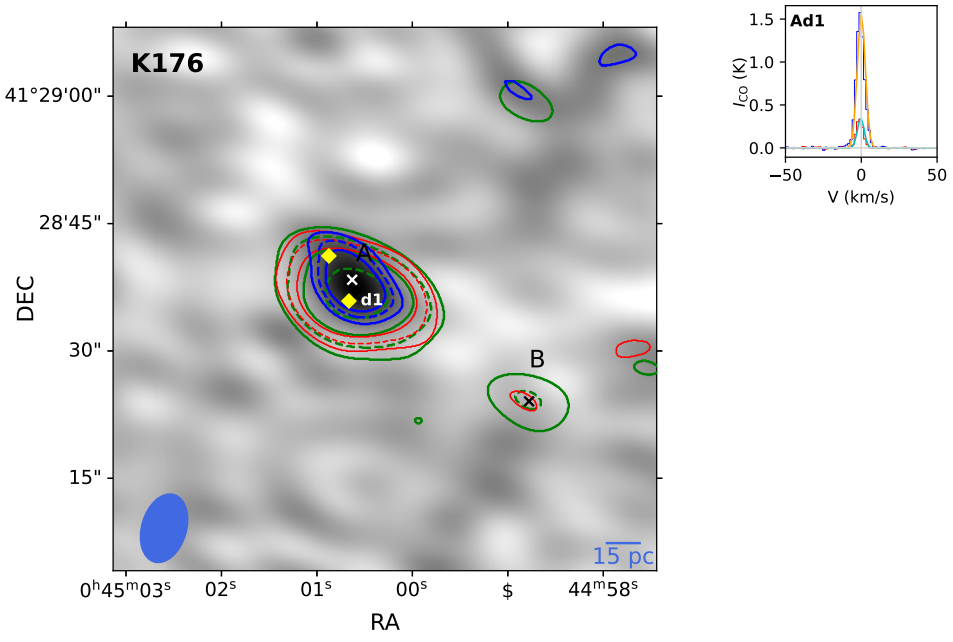

FIGURE B.1: (continued.)

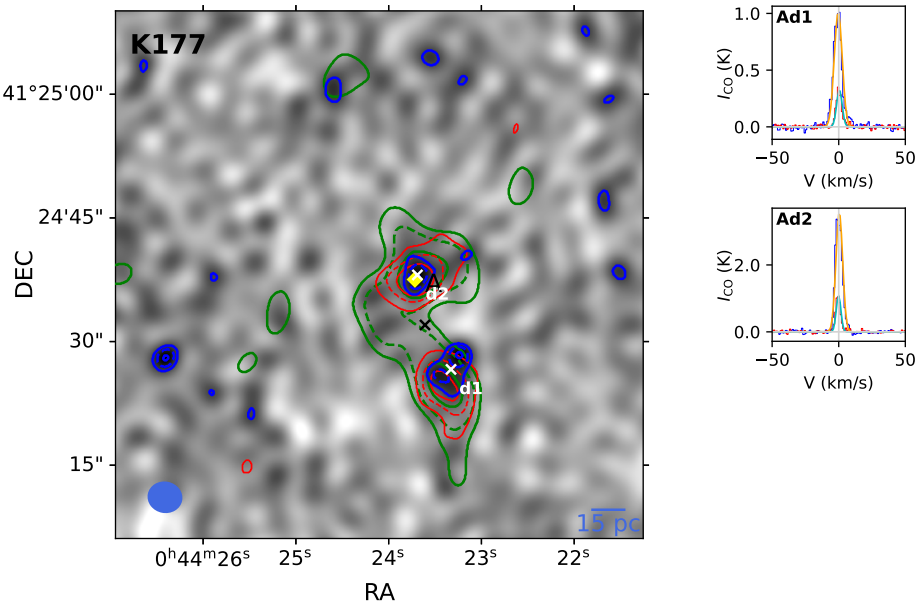

FIGURE B.1: (continued.)

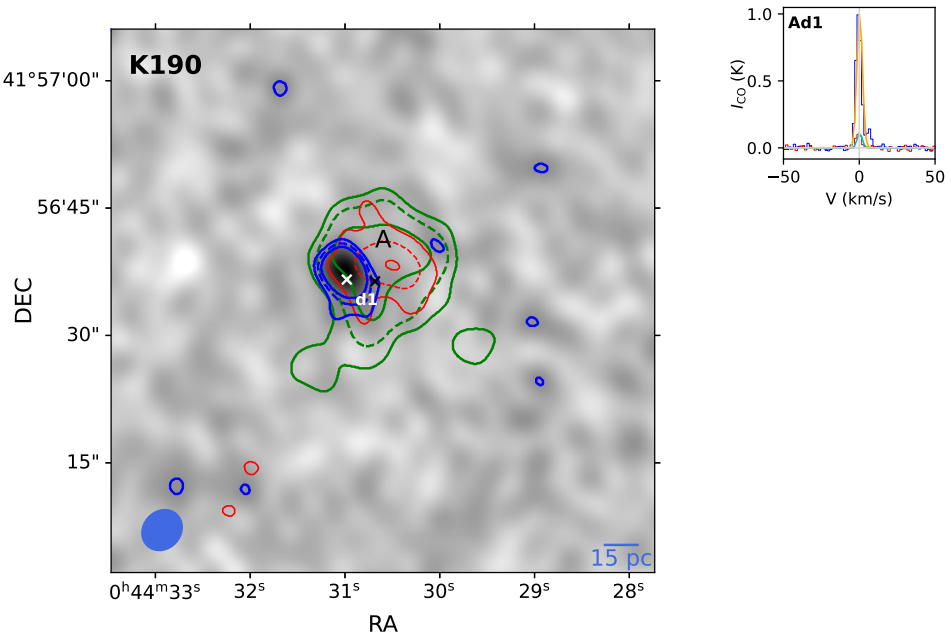

FIGURE B.1: (continued.)

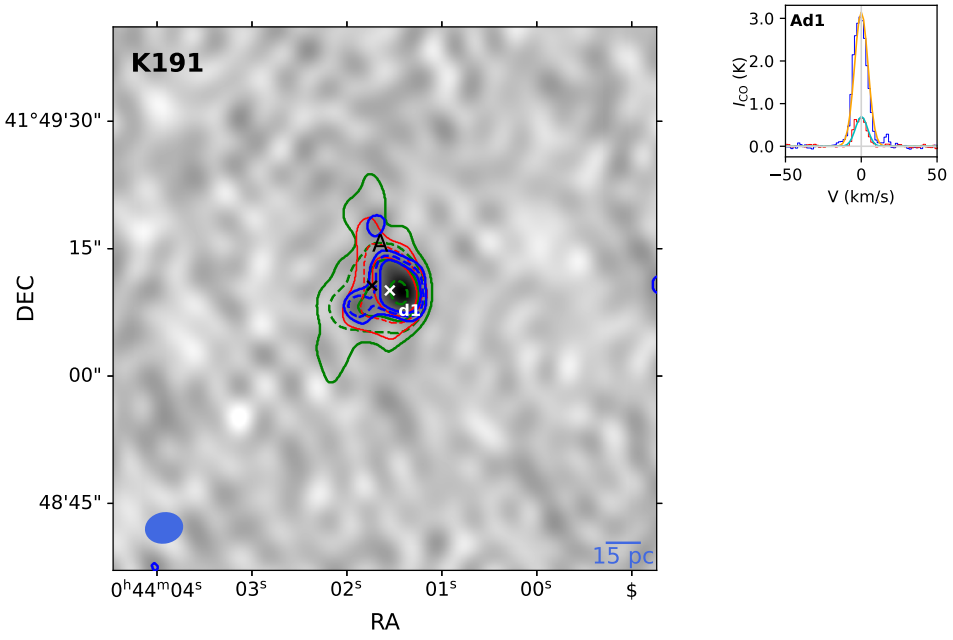

FIGURE B.1: (continued.)

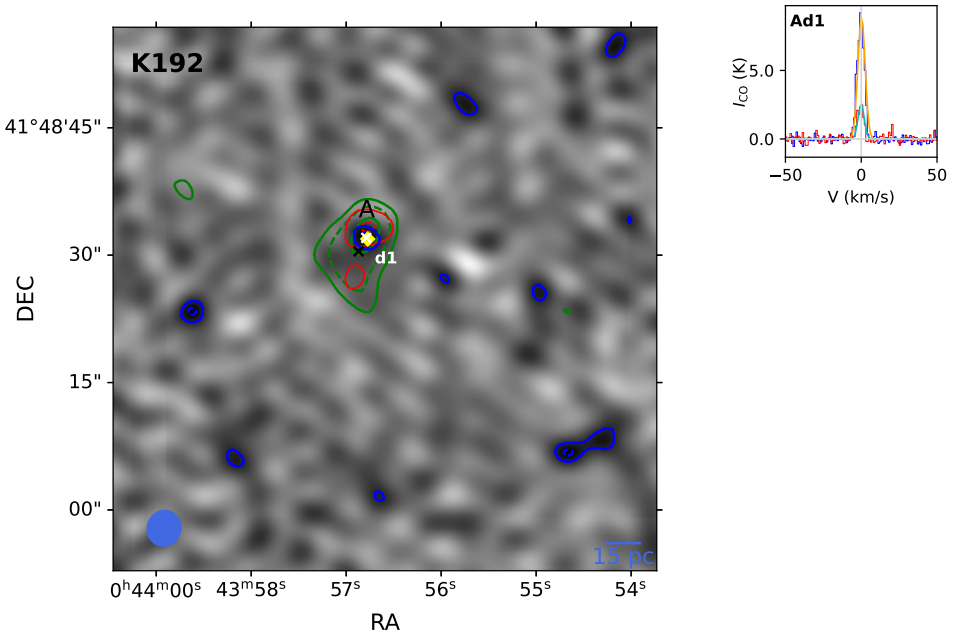

FIGURE B.1: (continued.)

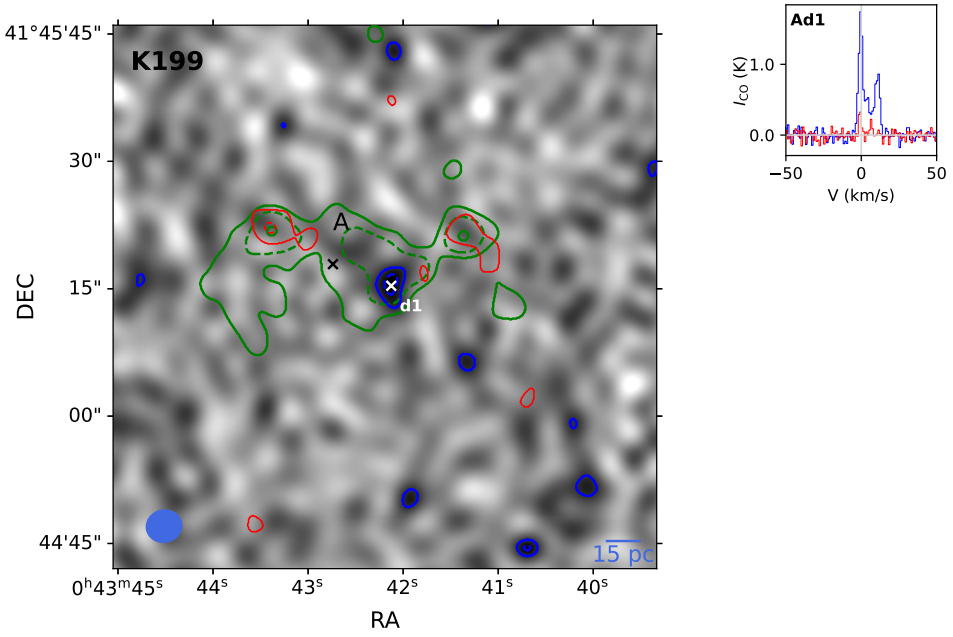

FIGURE B.1: (continued.)

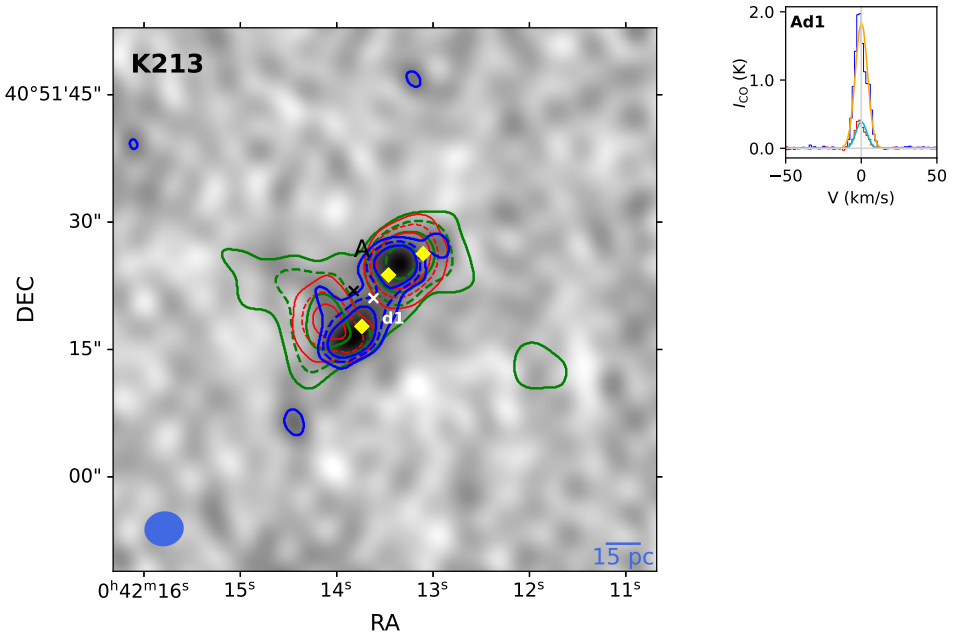

FIGURE B.1: (continued.)

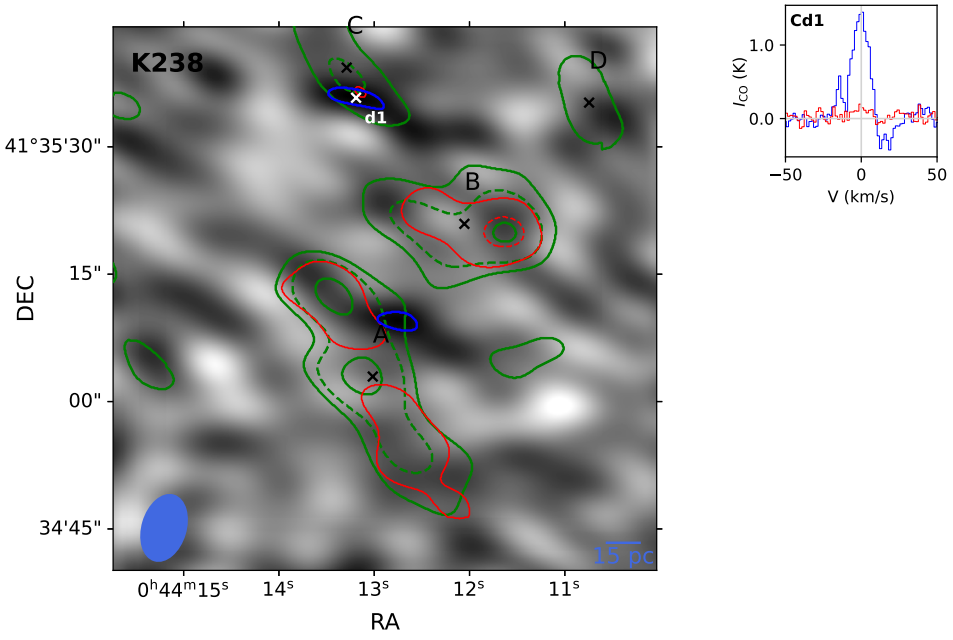

FIGURE B.1: (continued.)

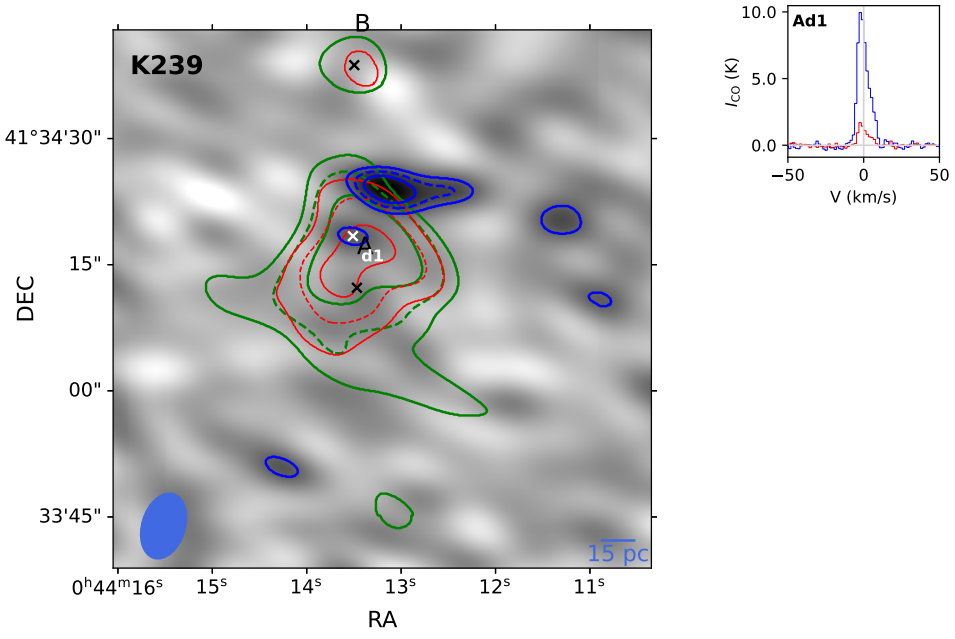

FIGURE B.1: (continued.)

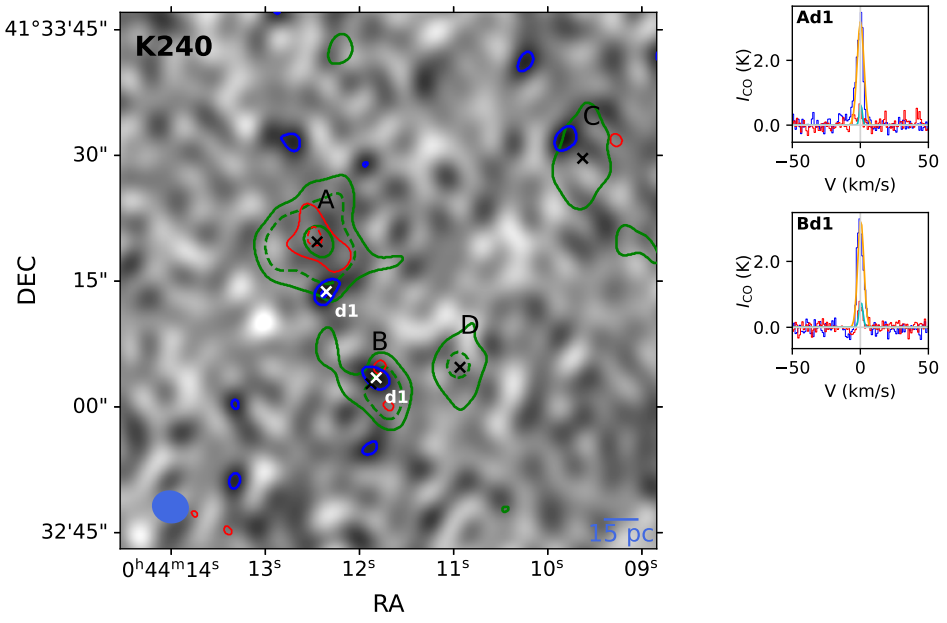

FIGURE B.1: (continued.)

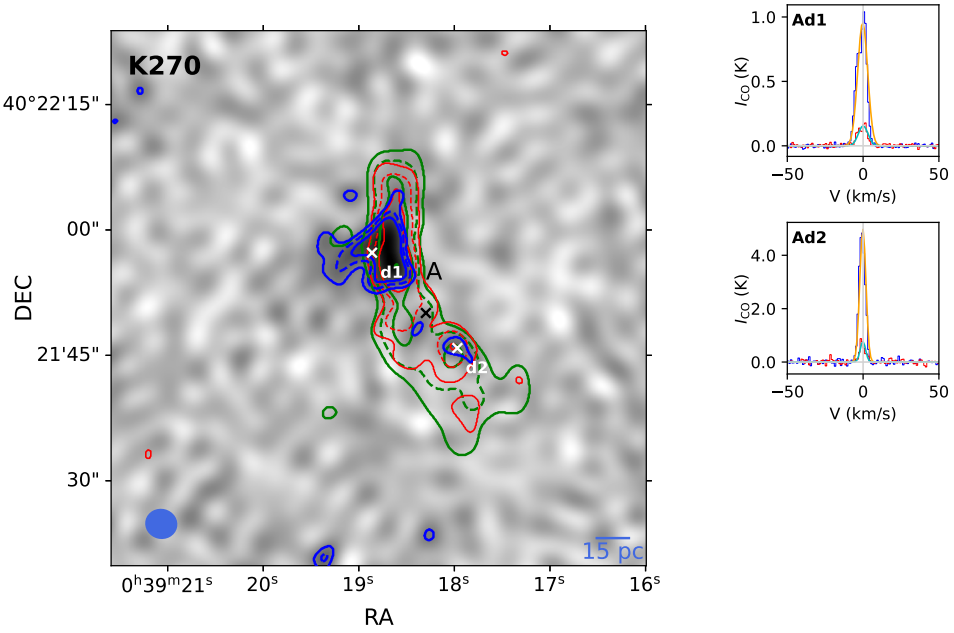

FIGURE B.1: (continued.)

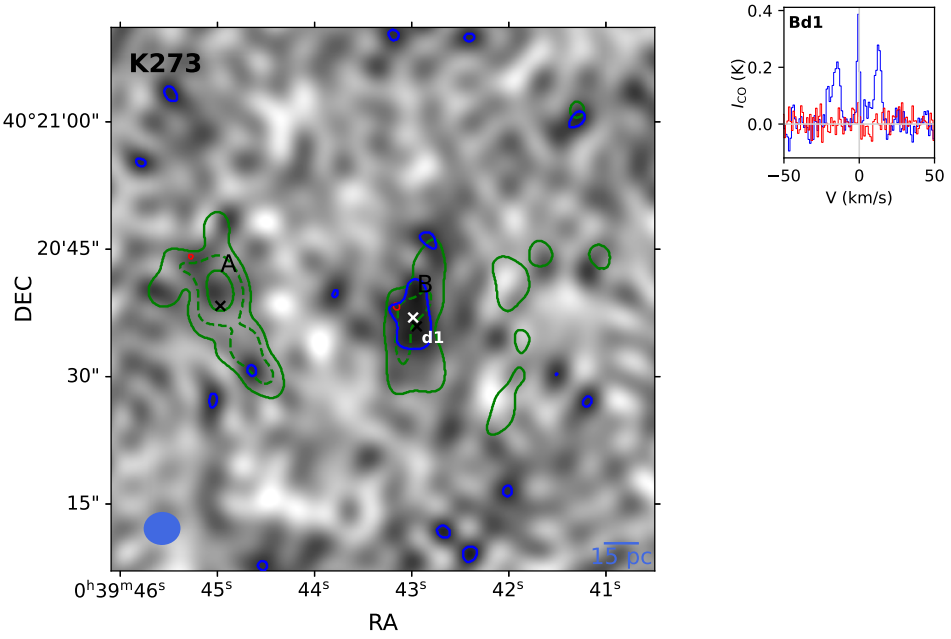

FIGURE B.1: (continued.)

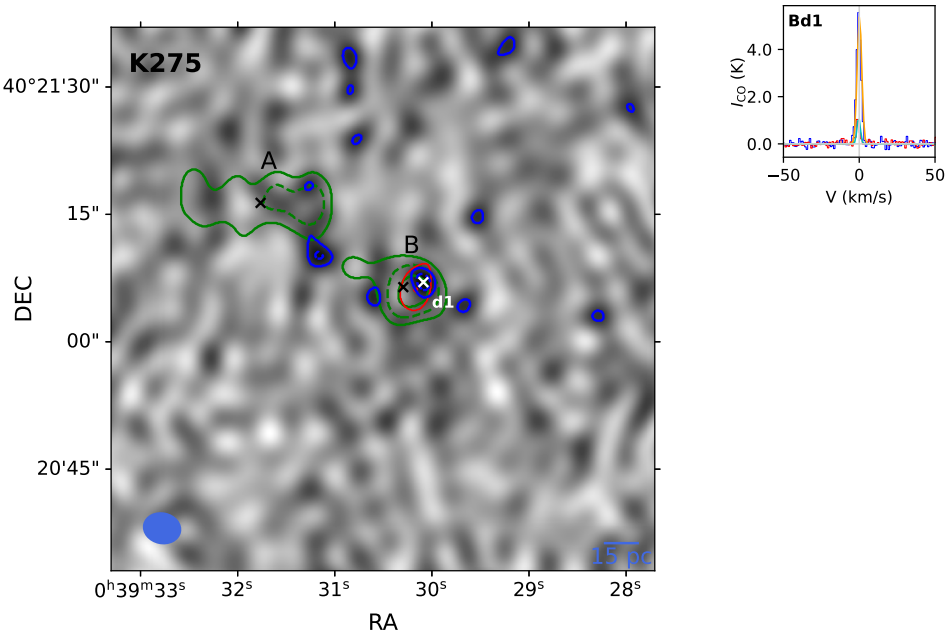

FIGURE B.1: (continued.)

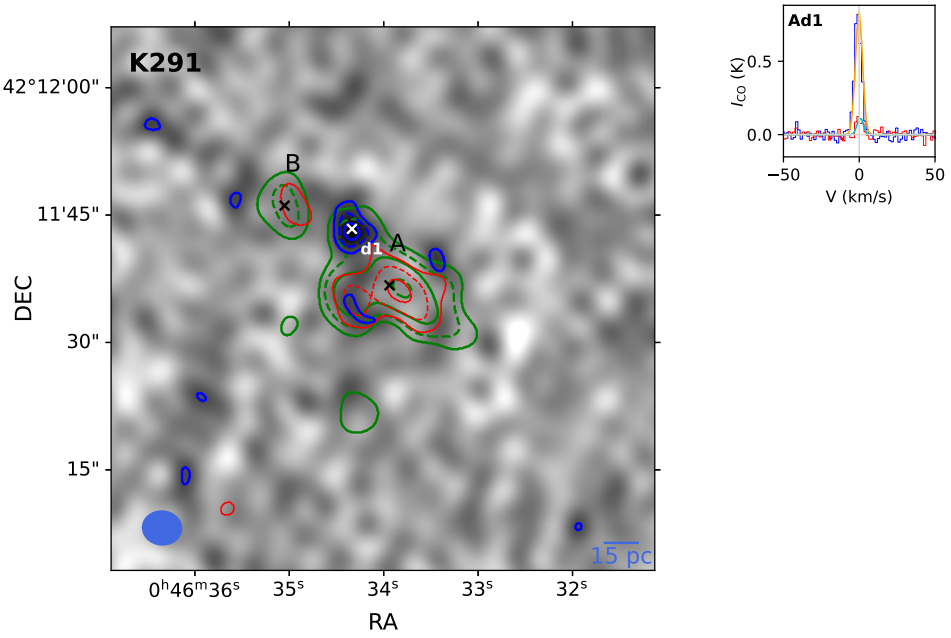

FIGURE B.1: (continued.)

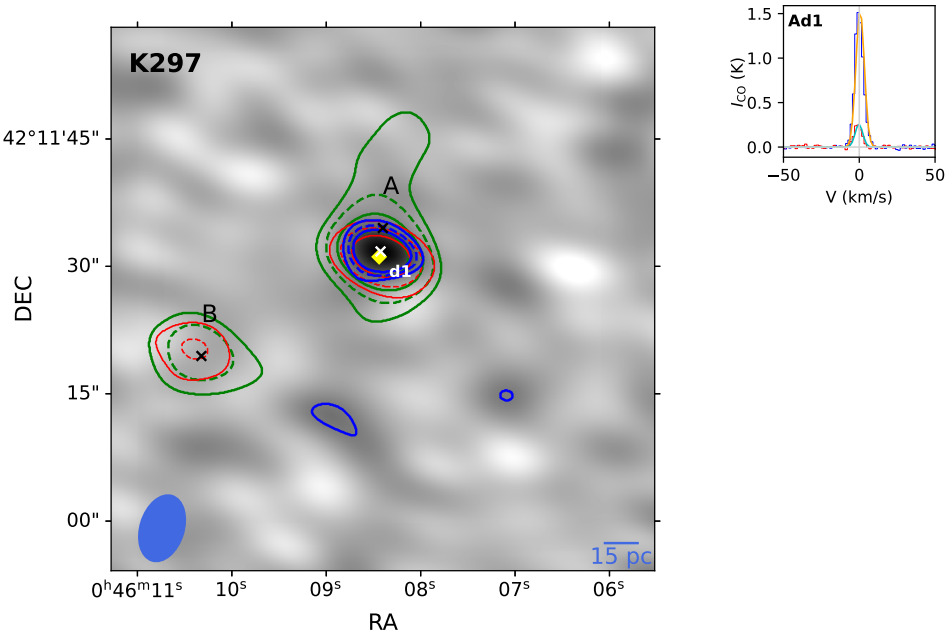

FIGURE B.1: (continued.)

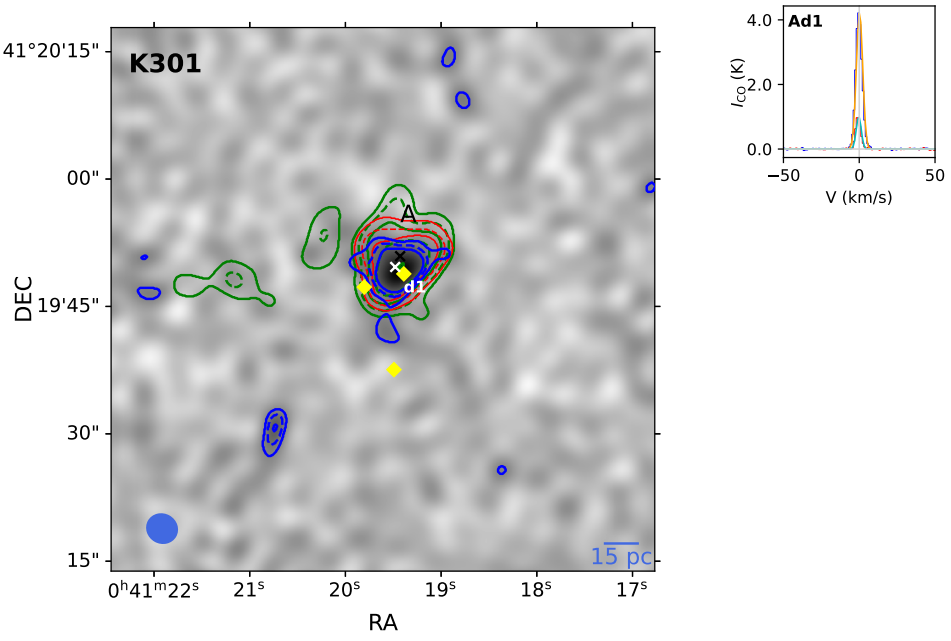

FIGURE B.1: (continued.)

Appendix C

N/O-O/H Relations From Random Line Ratios

The use of the same line ratios (especially N_2) in the calculation of N/O and O/H for the same diagram can lead to false tightening of correlations. In this section, we assign random emission line ratios (within the range of values found in our data) for our 294 H II regions, and thereafter produce N/O-O/H scaling diagrams to test the magnitude of the inherent correlations. We include the Z94 despite the possible discrepancy of up to 0.6 dex with directly calculated abundances (Kewley and Ellison 2008), to compare PG16 methods to N/O and O/H calculated independently.

From Figure C.1, we find that using the PG16 calibrations for both N/O and O/H on the same diagram indeed introduces a positive correlation even for a random sample. These slopes are

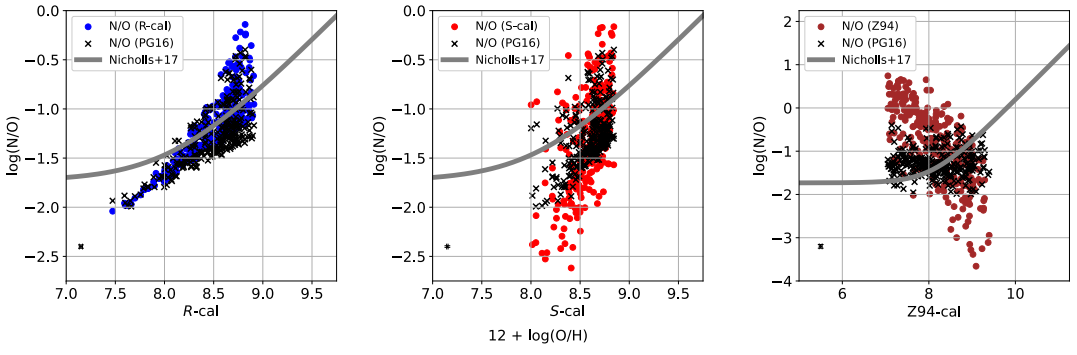

FIGURE C.1: N/O-O/H diagrams as displayed in Chapter 4 but using random emission line ratios assigned to our H II regions. On all plots, we display in black again the N/O values from the PG16 N/O calibration. We include the average MW relation from Nicholls et al. (2017) as a solid line. The typical uncertainties of the individual data points are displayed in the lower left, the same as for the diagrams in Chapter 4.

significantly flatter than found from real data in Chapter 4, suggesting the increase in N/O seen for M31 compared to the general MW relation is real. A negative trend is seen when Z94 O/H values are used for the same random sample, further indicating that this trend is inherent to the calibration.

Bibliography

Aller, 1942. The Spectra of the Emission Nebulosities in Messier 33. *ApJ*, 95:52.

Alloin, Collin-Souffrin, Joly, et al., 1979. Nitrogen and oxygen abundances in galaxies. *A&A*, 78:200.

Alves, Lada, and Lada, 2001. Internal structure of a cold dark molecular cloud inferred from the extinction of background starlight. *Nature*, 409:159.

Arnaboldi, Bhattacharya, Gerhard, et al., 2022. The survey of planetary nebulae in andromeda (m31). *Astronomy Astrophysics*, 666:a109. Https://www.aanda.org/articles/aa/pdf/2022/10/aa44258-22.pdf.

Arnett, 1973. Explosive Nucleosynthesis in Stars. *Annual Review of Astronomy and Astrophysics*, 11:73.

Arnett and Chevalier, 1996. Supernovae and nucleosynthesis: An investigation of the history of matter, from the big bang to the present. *Physics Today - PHYS TODAY*, 49.

Arp, 1964. Spiral Structure in M31. *ApJ*, 139:1045.

Azimlu, Marciniak, and Barmby, 2011. A new catalog of h ii regions in m31. *AJ*, 142:139.

Baldwin, Phillips, and Terlevich, 1981. Classification parameters for the emission-line spectra of extragalactic objects. *Publications of the Astronomical Society of the Pacific*, 93(551):5.

Balser, Rood, Bania, et al., 2011. Hii region metallicity distribution in the milky way disk. *The Astrophysical Journal*, 738(1):27.

Bekki, Couch, Drinkwater, et al., 2001. A New Formation Model for M32: A Threshed Early-Type Spiral Galaxy? *ApJ*, 557(1):L39.

Belfiore, Maiolino, Tremonti, et al., 2017. SDSS IV MaNGA - metallicity and nitrogen abundance gradients in local galaxies. *MNRAS*, 469(1):151.

Bendo, Baes, Bianchi, et al., 2015. The identification of dust heating mechanisms in nearby galaxies using Herschel 160/250 and 250/350 μm surface brightness ratios. *MNRAS*, 448(1):135.

Berg, Pogge, Skillman, et al., 2020. CHAOS IV: Gas-phase Abundance Trends from the First Four CHAOS Galaxies. *ApJ*, 893(2):96.

Bernard, Ferguson, Richardson, et al., 2015. The nature and origin of substructure in the outskirts of M31 - II. Detailed star formation histories. *MNRAS*, 446(3):2789.

Bertoldi and McKee, 1992. Pressure-confined Clumps in Magnetized Molecular Clouds. *ApJ*, 395:140.

Bhattacharya, Arnaboldi, Caldwell, et al., 2022. The survey of planetary nebulae in Andromeda (M31) - IV. Radial oxygen and argon abundance gradients of the thin and thicker disc. *MNRAS*, 517(2):2343.

Bhattacharya, Arnaboldi, Magda, Caldwell, Nelson, et al., 2019. The survey of planetary nebulae in andromeda (m 31) - ii. age–velocity dispersion relation in the disc from planetary nebulae. *AA*, 631:A56.

Bigiel, Leroy, Walter, et al., 2008. The Star Formation Law in Nearby Galaxies on Sub-Kpc Scales. *AJ*, 136(6):2846.

Birnboim and Dekel, 2003. Virial shocks in galactic haloes? *MNRAS*, 345(1):349.

Block, Bournaud, Combes, et al., 2006. An almost head-on collision as the origin of two off-centre rings in the Andromeda galaxy. *Nature*, 443(7113):832.

Bohr, 1913. I. on the constitution of atoms and molecules. *The London, Edinburgh, and Dublin Philosophical Magazine and Journal of Science*, 26(151):1.

Bolatto, Wolfire, and Leroy, 2013. The CO-to-H_2 Conversion Factor. *Annual Review of Astronomy and Astrophysics*, 51(1):207.

Bosomworth, Forbrich, Lada, et al., 2025. Cloud-scale elemental abundance variations and the CO-to-dust-mass conversion factor in M31. *MNRAS*, 536(4):3803.

Bothwell, Maiolino, Kennicutt, et al., 2013. A fundamental relation between the metallicity, gas content and stellar mass of local galaxies. *Monthly Notices of the Royal Astronomical Society*, 433(2):1425.

Bothwell, Maiolino, R., Cicone, C., et al., 2016. Galaxy metallicities depend primarily on stellar mass and molecular gas mass. *A&A*, 595:A48.

Bouvier, López-Sepulcre, Ceccarelli, et al., 2021. ORion Alma New GEneration Survey (ORANGES). I. Dust continuum and free-free emission of OMC-2/3 filament protostars. *A&A*, 653:A117.

Braun, 1991. The Distribution and Kinematics of Neutral Gas in M31. *ApJ*, 372:54.

Bregman, 1980. The galactic fountain of high-velocity clouds. *ApJ*, 236:577.

Bresolin, 2017. Metallicities in the Outer Regions of Spiral Galaxies. In Knapen, Lee, and Gil de Paz, editors, *Outskirts of Galaxies*, volume 434 of *Astrophysics and Space Science Library*, page 145.

Bresolin, Stasińska, Vílchez, et al., 2010. Planetary nebulae in M33: probes of asymptotic giant branch nucleosynthesis and interstellar medium abundances*. *Monthly Notices of the Royal Astronomical Society*, 404(4):1679.

Brocklehurst and Seaton, 1972. On the interpretation of radio recombination line observations. *MNRAS*, 157:179.

Burbidge, Burbidge, Fowler, et al., 1957. Synthesis of the Elements in Stars. *Reviews of Modern Physics*, 29(4):547.

Busso, Gallino, and Wasserburg, 1999. Nucleosynthesis in Asymptotic Giant Branch Stars: Relevance for Galactic Enrichment and Solar System Formation. *Annual Review of Astronomy and Astrophysics*, 37:239.

Cardelli, Clayton, and Mathis, 1989. The Relationship between Infrared, Optical, and Ultraviolet Extinction. *ApJ*, 345:245.

Carruthers, 1970. Rocket observation of interstellar molecular hydrogen. *Astrophysical Journal, vol. 161, p. L81*, 161:L81.

Chiappini, Matteucci, and Romano, 2001. Abundance gradients and the formation of the milky way. *The Astrophysical Journal*, 554(2):1044.

Chiappini, Romano, and Matteucci, 2003. Oxygen, carbon and nitrogen evolution in galaxies. *MNRAS*, 339(1):63.

Chisholm, Tremonti, and Leitherer, 2018. Metal-enriched galactic outflows shape the mass-metallicity relationship. *MNRAS*, 481(2):1690.

Choi, Guhathakurta, and Johnston, 2002. Tidal Interaction of M32 and NGC 205 with M31: Surface Photometry and Numerical Simulations. *AJ*, 124(1):310.

Clayton, 1983. *Principles of Stellar Evolution and Nucleosynthesis*. Astronomy / Astrophysics. University of Chicago Press.

Colombo, Hughes, Schinnerer, et al., 2014. The pdbi arcsecond whirlpool survey (paws): Environmental dependence of giant molecular cloud properties in m51*. *The Astrophysical Journal*, 784(1):3.

Condon, 1992. Radio emission from normal galaxies. *Annual Review of Astronomy and Astrophysics*, 30:575.

Cox, Jonsson, Somerville, et al., 2008. The effect of galaxy mass ratio on merger-driven starbursts. *MNRAS*, 384(1):386.

Croxall, Pogge, Berg, et al., 2015. Chaos. ii. gas-phase abundances in ngc 5194. *The Astrophysical Journal*, 808(1):42.

Croxall, Pogge, Berg, et al., 2016. CHAOS III: Gas-phase Abundances in NGC 5457. *ApJ*, 830(1):4.

Dalcanton, 2007. The Metallicity of Galaxy Disks: Infall versus Outflow. *ApJ*, 658(2):941.

Dalcanton, Fouesneau, Hogg, et al., 2015. The Panchromatic Hubble Andromeda Treasury. VIII. A Wide-area, High-resolution Map of Dust Extinction in M31. *ApJ*, 814(1):3.

Dame and Lada, 2023. A Complete HCN Survey of the Perseus Molecular Cloud. *ApJ*, 944(2):197.

Davidge, McConnachie, Fardal, et al., 2012. The recent stellar archeology of m31—the nearest red disk galaxy*. *The Astrophysical Journal*, 751(1):74.

de Avillez and Low, 2002. Mixing timescales in a supernova-driven interstellar medium. *The Astrophysical Journal*, 581(2):1047.

de Vaucouleurs, de Vaucouleurs, Corwin, et al., 1991. *Third Reference Catalogue of Bright Galaxies*.

Devereux, Price, Wells, et al., 1994. Two Views of the Andromeda Galaxy H(alpha) and Far Infrared. *AJ*, 108:1667.

Dierickx, Blecha, and Loeb, 2014. Signatures of the m31-m32 galactic collision. *The Astrophysical Journal*, 788(2):L38.

Dong, Li, Wang, et al., 2016. High-resolution mapping of dust via extinction in the M31 bulge. *MNRAS*, 459(2):2262.

Dopita, Kewley, Heisler, et al., 2000. A Theoretical Recalibration of the Extragalactic H II Region Sequence. *ApJ*, 542(1):224.

Dopita, Kewley, Sutherland, et al., 2016. Chemical abundances in high-redshift galaxies: a powerful new emission line diagnostic. , 361:61.

Draine, 2011. *Physics of the Interstellar and Intergalactic Medium*.

Draine and Bertoldi, 1996. Structure of Stationary Photodissociation Fronts. *ApJ*, 468:269.

Draine, Dale, Bendo, et al., 2007. Dust Masses, PAH Abundances, and Starlight Intensities in the SINGS Galaxy Sample. *ApJ*, 663(2):866.

D'Souza and Bell, 2018. The andromeda galaxy's most important merger about 2 billion years ago as m32's likely progenitor. *Nature Astronomy*, 2.

Dupac, Giard, Bernard, et al., 2002. Submillimeter dust emission of the M 17 complex measured with PRONAOS. *A&A*, 392:691.

Earl, Tollerud, O'Steen, et al., 2024. astropy/specutils: v1.16.0.

Ekström, Georgy, Eggenberger, et al., 2012. Grids of stellar models with rotation. I. Models from 0.8 to 120 $M_{\odot}$ at solar metallicity (Z = 0.014). *A&A*, 537:A146.

Emerick, Bryan, Mac Low, et al., 2018. Metal Mixing and Ejection in Dwarf Galaxies Are Dependent on Nucleosynthetic Source. *ApJ*, 869(2):94.

Esteban, Bresolin, García-Rojas, et al., 2020. Carbon, nitrogen, and oxygen abundance gradients in M101 and M31. *MNRAS*, 491(2):2137.

Esteban, Bresolin, Peimbert, et al., 2009. Keck HIRES Spectroscopy of Extragalactic H II Regions: C and O Abundances from Recombination Lines. *ApJ*, 700(1):654.

Esteban and García-Rojas, 2018. Revisiting the radial abundance gradients of nitrogen and oxygen of the Milky Way. *Monthly Notices of the Royal Astronomical Society*, 478(2):2315.

Evans, Heyer, Miville-Deschênes, et al., 2021. Which molecular cloud structures are bound? *The Astrophysical Journal*, 920(2):126.

Event Horizon Telescope Collaboration, Akiyama, Alberdi, et al., 2019. First M87 Event Horizon Telescope Results. I. The Shadow of the Supermassive Black Hole. *ApJ*, 875(1):L1.

Ewen and Purcell, 1951. Observation of a Line in the Galactic Radio Spectrum: Radiation from Galactic Hydrogen at 1,420 Mc./sec. *Nature*, 168(4270):356.

Fabricant, Fata, Roll, et al., 2005. Hectospec, the mmt's 300 optical fiber-fed spectrograph. *Publications of the Astronomical Society of the Pacific*, 117(838):1411.

Faesi, Lada, and Forbrich, 2018. The alma view of gmcs in ngc 300: Physical properties and scaling relations at 10 pc resolution. *The Astrophysical Journal*, 857(1):19.

Ferland, Korista, Verner, et al., 1998. CLOUDY 90: Numerical Simulation of Plasmas and Their Spectra. *PASP*, 110(749):761.

Forbrich, Lada, Pety, et al., 2023. Tracing dense gas in six resolved gmcs of the andromeda galaxy. *Monthly Notices of the Royal Astronomical Society*, 525(4):5565.

Forbrich, Lada, Viaene, et al., 2020. First resolved dust continuum measurements of individual giant molecular clouds in the andromeda galaxy. *ApJ*, 890:42.

Fraternali and Binney, 2008. Accretion of gas on to nearby spiral galaxies. *MNRAS*, 386(2):935.

Fritz, Gentile, G., Smith, M. W. L., et al., 2012. The herschel exploitation of local galaxy andromeda (helga) - i. global far-infrared and sub-mm morphology. *AA*, 546:A34.

Gao and Solomon, 2004. The Star Formation Rate and Dense Molecular Gas in Galaxies. *ApJ*, 606(1):271.

Garnett, 1992. Electron Temperature Variations and the Measurement of Nebular Abundances. *AJ*, 103:1330.

Genzel and Stutzki, 1989. The Orion molecular cloud and star-forming region. *Annual Review of Astronomy and Astrophysics*, 27:41.

Giannetti, Leurini, König, et al., 2017. Galactocentric variation of the gas-to-dust ratio and its relation with metallicity. *A&A*, 606:L12.

Glover and Clark, 2012. Approximations for modelling CO chemistry in giant molecular clouds: a comparison of approaches. *MNRAS*, 421(1):116.

Glover, Federrath, Mac Low, et al., 2010. Modelling CO formation in the turbulent interstellar medium. *MNRAS*, 404(1):2.

Goodman, Pineda, and Schnee, 2009. The "true" column density distribution in star-forming molecular clouds. *The Astrophysical Journal*, 692(1):91.

Gordon, Bailin, Engelbracht, et al., 2006. Spitzer MIPS Infrared Imaging of M31: Further Evidence for a Spiral-Ring Composite Structure. *ApJ*, 638(2):L87.

Gordon and Burton, 1976. Carbon monoxide in the Galaxy. I. The radial distribution of CO, H_2, and nucleons. *ApJ*, 208:346.

Grasha, Chen, Battisti, et al., 2022. Metallicity, Ionization Parameter, and Pressure Variations of H II Regions in the TYPHOON Spiral Galaxies: NGC 1566, NGC 2835, NGC 3521, NGC 5068, NGC 5236, and NGC 7793. *ApJ*, 929(2):118.

Griffin, Abergel, Abreu, et al., 2010. The Herschel-SPIRE instrument and its in-flight performance. *A&A*, 518:L3.

Grimes, Blundell, Paine, et al., 2016. Next generation receivers for the submillimeter array. In Holland and Zmuidzinas, editors, *Millimeter, Submillimeter, and Far-Infrared Detectors and Instrumentation for Astronomy VIII*, volume 9914, page 991424. International Society for Optics and Photonics, SPIE.

Groves, Kreckel, Santoro, et al., 2023. The PHANGS-MUSE nebular catalogue. *MNRAS*, 520(4):4902.

Haas, Lemke, Stickel, et al., 1998. Cold dust in the Andromeda Galaxy mapped by ISO. *A&A*, 338:L33.

Habart, Peeters, Berné, et al., 2024. PDRs4All. II. JWST's NIR and MIR imaging view of the Orion Nebula. *A&A*, 685:A73.

Habing, Miley, Young, et al., 1984. Infrared emission from M31. *ApJ*, 278:L59.

Haud, 1981. Gas Kinematics in M31. , 76(2):477.

Henry, Edmunds, and Köppen, 2000. On the Cosmic Origins of Carbon and Nitrogen. *ApJ*, 541(2):660.

Henry and Worthey, 1999. The distribution of heavy elements in spiral and elliptical galaxies. *Publications of the Astronomical Society of the Pacific*, 111(762):919.

Herwig, 2005. Evolution of Asymptotic Giant Branch Stars. *Annual Review of Astronomy and Astrophysics*, 43(1):435.

Heyer, Carpenter, and Snell, 2001. The Equilibrium State of Molecular Regions in the Outer Galaxy. *ApJ*, 551(2):852.

Heyer and Dame, 2015. Molecular clouds in the milky way. *Annual Review of Astronomy and Astrophysics*, 53(Volume 53, 2015):583.

Heyer, Krawczyk, Duval, et al., 2009. Re-Examining Larson's Scaling Relationships in Galactic Molecular Clouds. *ApJ*, 699(2):1092.

Hildebrand, 1983. The determination of cloud masses and dust characteristics from submillimetre thermal emission. , 24:267.

Hillebrandt and Niemeyer, 2000. Type IA Supernova Explosion Models. *Annual Review of Astronomy and Astrophysics*, 38:191.

Hillenbrand, Hoffer, and Herczeg, 2013. An enhanced spectroscopic census of the orion nebula cluster. *The Astronomical Journal*, 146(4):85.

Hirashita and Harada, 2017. Effects of dust evolution on the abundances of CO and H_2. *MNRAS*, 467(1):699.

Ho, 2019. A machine learning artificial neural network calibration of the strong-line oxygen abundance. *Monthly Notices of the Royal Astronomical Society*, 485(3):3569.

Ho, Meidt, Kudritzki, et al., 2018. Azimuthal variations of gas-phase oxygen abundance in NGC 2997. *A&A*, 618:A64.

Ho, Seibert, Meidt, et al., 2017. The chemical evolution carousel of spiral galaxies: Azimuthal variations of oxygen abundance in ngc1365. *The Astrophysical Journal*, 846(1):39.

Hodge, 1980. The dark nebulae of M 31. *AJ*, 85:376.

Hough, Rennehan, Kobayashi, et al., 2023. SIMBA-C: an updated chemical enrichment model for galactic chemical evolution in the SIMBA simulation. *MNRAS*, 525(1):1061.

Hubble, 1927. The classification of spiral nebulae. *The Observatory*, 50:276.

Hughes, Meidt, Colombo, et al., 2013. A comparative study of giant molecular clouds in m51, m33, and the large magellanic cloud. *The Astrophysical Journal*, 779(1):46.

Israel, 1997. H_2 and its relation to CO in the LMC and other magellanic irregular galaxies. *A&A*, 328:471.

Israelian, Ecuvillon, Rebolo, et al., 2004. Galactic evolution of nitrogen. *A&A*, 421:649.

Izotov and Thuan, 1999. Heavy-Element Abundances in Blue Compact Galaxies. *ApJ*, 511(2):639.

Jenkins, 2009. A Unified Representation of Gas-Phase Element Depletions in the Interstellar Medium. *ApJ*, 700(2):1299.

Jin, Sutherland, Kewley, et al., 2023. Spatially resolved temperature and density structures of nearby h ii regions. *The Astrophysical Journal*, 958(2):179.

Jones, Köhler, Ysard, et al., 2017. The global dust modelling framework THEMIS. *A&A*, 602:A46.

Karakas and Lattanzio, 2014. The dawes review 2: Nucleosynthesis and stellar yields of low- and intermediate-mass single stars. *Publications of the Astronomical Society of Australia*, 31:e030.

Kauffmann, Heckman, Tremonti, et al., 2003. The host galaxies of active galactic nuclei. *Monthly Notices of the Royal Astronomical Society*, 346(4):1055.

Kaufman, Bash, Kennicutt, et al., 1987. Giant H II Regions in M81. *ApJ*, 319:61.

Kennicutt, 1984. Structural properties of giant H II regions in nearby galaxies. *ApJ*, 287:116.

Kennicutt, Kobulnicky, and Pizagno, 1998. Measuring Metal Abundances of Distant Galaxies from Integrated Emission-Line Spectra. In *American Astronomical Society Meeting Abstracts*, volume 193 of *American Astronomical Society Meeting Abstracts*, page 70.08.

Kennicutt, Lee, Funes, et al., 2008. An Hα Imaging Survey of Galaxies in the Local 11 Mpc Volume. *ApJ*, 178(2):247.

Kepner, 1999. Inside-out galaxy formation. *The Astrophysical Journal*, 520(1):59.

Kereš, Katz, Weinberg, et al., 2005. How do galaxies get their gas? *MNRAS*, 363(1):2.

Keto, 1997. The Shapes of Cross-Correlation Interferometers. *ApJ*, 475(2):843.

Kewley and Dopita, 2002. Using strong lines to estimate abundances in extragalactic h ii regions and starburst galaxies. *The Astrophysical Journal Supplement Series*, 142(1):35.

Kewley, Dopita, Sutherland, et al., 2001. Theoretical modeling of starburst galaxies. *The Astrophysical Journal*, 556(1):121.

Kewley and Ellison, 2008. Metallicity calibrations and the mass-metallicity relation for star-forming galaxies. *The Astrophysical Journal*, 681(2):1183.

Kewley, Nicholls, and Sutherland, 2019. Understanding galaxy evolution through emission lines. *Annual Review of Astronomy and Astrophysics*, 57(1):511.

Khoperskov, Sivkova, Saburova, et al., 2023. ISM metallicity variations across spiral arms in disk galaxies. The impact of local enrichment and gas migration in the presence of a radial metallicity gradient. *A&A*, 671:A56.

Kirk, Gear, Fritz, et al., 2015. The Herschel Exploitation of Local Galaxy Andromeda (HELGA). VI. The Distribution and Properties of Molecular Cloud Associations in M31. *ApJ*, 798(1):58.

Klessen and Glover, 2016. Physical Processes in the Interstellar Medium. *Saas-Fee Advanced Course*, 43:85.

Kniazev, Pustilnik, and Zucker, 2008. Spectroscopy of two PN candidates in IC 10*. *Monthly Notices of the Royal Astronomical Society*, 384(3):1045.

Kobayashi, Bhattacharya, Arnaboldi, et al., 2023. On the α/Fe Bimodality of the M31 Disks. *ApJ*, 956(1):L14.

Kobayashi, Karakas, and Lugaro, 2020. The Origin of Elements from Carbon to Uranium. *ApJ*, 900(2):179.

Kobayashi, Karakas, and Umeda, 2011. The evolution of isotope ratios in the Milky Way Galaxy. *MNRAS*, 414(4):3231.

Kobulnicky and Kewley, 2004. Metallicities of 0.3<z<1.0 Galaxies in the GOODS-North Field. *ApJ*, 617(1):240.

Kormendy, Fisher, Cornell, et al., 2009. Structure and Formation of Elliptical and Spheroidal Galaxies. *ApJ*, 182(1):216.

Kreckel, Ho, Blanc, et al., 2019. Mapping Metallicity Variations across Nearby Galaxy Disks. *ApJ*, 887(1):80.

Kreckel, Ho, Blanc, et al., 2020. Measuring the mixing scale of the ISM within nearby spiral galaxies. *Monthly Notices of the Royal Astronomical Society*, 499(1):193.

Kudoh and Basu, 2003. Nonlinear Hydromagnetic Wave Support of a Stratified Molecular Cloud. *ApJ*, 595(2):842.

Lada, Forbrich, Lombardi, et al., 2012. Star Formation Rates in Molecular Clouds and the Nature of the Extragalactic Scaling Relations. *ApJ*, 745(2):190.

Lada, Forbrich, Petitpas, et al., 2024. The molecular clouds of m31. *The Astrophysical Journal*, 966(2):193.

Lada, Lada, Clemens, et al., 1994. Dust Extinction and Molecular Gas in the Dark Cloud IC 5146. *ApJ*, 429:694.

Lada, Lombardi, and Alves, 2010. On the star formation rates in molecular clouds. *The Astrophysical Journal*, 724(1):687.

Lada, Margulis, Sofue, et al., 1988. Observations of Molecular and Atomic Clouds in M31. *ApJ*, 328:143.

Langer, 2012. Presupernova Evolution of Massive Single and Binary Stars. *Annual Review of Astronomy and Astrophysics*, 50:107.

Larson, 1981. Turbulence and star formation in molecular clouds. *Monthly Notices of the Royal Astronomical Society*, 194(4):809.

Lee, Herbst, Pineau des Forets, et al., 1996. Photodissociation of H_2_ and CO and time dependent chemistry in inhomogeneous interstellar clouds. *A&A*, 311:690.

Lee, Hwang, and Lee, 2011. Hii region luminosity function of the interacting galaxy m51. *The Astrophysical Journal*, 735(2):75.

Leitherer, Schaerer, Goldader, et al., 1999. Starburst99: Synthesis models for galaxies with active star formation. *The Astrophysical Journal Supplement Series*, 123(1):3.

Lequeux, Peimbert, Rayo, et al., 1979. Chemical Composition and Evolution of Irregular and Blue Compact Galaxies. *A&A*, 80:155.

Leroy, Bolatto, Gordon, et al., 2011. The co-to-h2 conversion factor from infrared dust emission across the local group. *The Astrophysical Journal*, 737(1):12.

Leroy, Schinnerer, Hughes, et al., 2021. PHANGS-ALMA: Arcsecond CO(2-1) Imaging of Nearby Star-forming Galaxies. *ApJ*, 257(2):43.

Leroy, Walter, Brinks, et al., 2008. The star formation efficiency in nearby galaxies: Measuring where gas forms stars effectively. *The Astronomical Journal*, 136(6):2782.

Lewis, Dolphin, Dalcanton, et al., 2015. The Panchromatic Hubble Andromeda Treasury. XI. The Spatially Resolved Recent Star Formation History of M31. *ApJ*, 805(2):183.

Li and Bryan, 2020. Simple yet powerful: Hot galactic outflows driven by supernovae. *The Astrophysical Journal Letters*, 890(2):L30.

Li, Han, Xiang, et al., 2016. A method of measuring the [/fe] ratios from the spectra of the lamost survey. *Research in Astronomy and Astrophysics*, 16(7):010.

Lindroos, Knudsen, Vlemmings, et al., 2015. Stacking of large interferometric data sets in the image- and uv-domain - a comparative study. *MNRAS*, 446(4):3502.

Liu, Liu, Luo, et al., 2004. Chemical abundances of planetary nebulae from optical recombination lines – I. Observations and plasma diagnostics. *MNRAS*, 353(4):1231.

López-Sánchez, Esteban, García-Rojas, et al., 2007. The Localized Chemical Pollution in NGC 5253 Revisited: Results from Deep Echelle Spectrophotometry. *ApJ*, 656(1):168.

Madau and Dickinson, 2014. Cosmic star-formation history. *Annual Review of Astronomy and Astrophysics*, 52(Volume 52, 2014):415.

Maiolino and Mannucci, 2019. De re metallica: the cosmic chemical evolution of galaxies. *The Astronomy and Astrophysics Review*, 27(1):3. Https://link.springer.com/content/pdf/10.1007/s00159-018-0112-2.pdf.

Maloney, 1990. Are Molecular Clouds in Virial Equilibrium? *ApJ*, 348:L9.

Maloney and Black, 1988. I CO/N(H 2) Conversions and Molecular Gas Abundances in Spiral and Irregular Galaxies. *ApJ*, 325:389.

Mannucci, Cresci, Maiolino, et al., 2010. A fundamental relation between mass, star formation rate and metallicity in local and high-redshift galaxies. *MNRAS*, 408(4):2115.

Marino, Rosales-Ortega, Sánchez, et al., 2013. The O3N2 and N2 abundance indicators revisited: improved calibrations based on CALIFA and T_e-based literature data. *A&A*, 559:A114.

Massey, Olsen, Hodge, et al., 2006. A Survey of Local Group Galaxies Currently Forming Stars. I. UBVRI Photometry of Stars in M31 and M33. *AJ*, 131(5):2478.

Matteucci, 1986. Some considerations on the origin of nitrogen. *Monthly Notices of the Royal Astronomical Society*, 221(4):911.

Matteucci, 2012. *Chemical Evolution of Galaxies*.

Matteucci, 2021. Modelling the chemical evolution of the Milky Way. , 29(1):5.

Matteucci, Franco, Francois, et al., 1989. Chemical evolution of disk galaxies: self-consistent structure of the disk. , 18:145.

Mattsson and Andersen, 2012. On the dust abundance gradients in late-type galaxies - II. Analytical models as evidence for massive interstellar dust growth in SINGS galaxies. *MNRAS*, 423(1):38.

McConnachie, Irwin, Ferguson, et al., 2005. Distances and metallicities for 17 Local Group galaxies. *MNRAS*, 356(3):979.

McConnachie, Irwin, Ibata, et al., 2009. The remnants of galaxy formation from a panoramic survey of the region around M31. *Nature*, 461(7260):66.

McKee and Ostriker, 2007. Theory of star formation. *Annual Review of Astronomy and Astrophysics*, 45(Volume 45, 2007):565.

Menten, Reid, Forbrich, et al., 2007. The distance to the Orion Nebula. *A&A*, 474(2):515.

Mernier, de Plaa, Pinto, et al., 2016. Origin of central abundances in the hot intra-cluster medium - ii. chemical enrichment and supernova yield models. *AA*, 595:A126.

Meyer, 1994. The r-, s-, and p-Processes in Nucleosynthesis. *Annual Review of Astronomy and Astrophysics*, 32:153.

Mo, Mao, and White, 1998. The formation of galactic discs. *MNRAS*, 295(2):319.

Mollá, Vílchez, Gavilán, et al., 2006. The nitrogen-to-oxygen evolution in galaxies: the role of the star formation rate. *Monthly Notices of the Royal Astronomical Society*, 372(3):1069.

Momcheva, Lee, Ly, et al., 2013. Nebular attenuation in h-selected star-forming galaxies at z = 0.8 from the newh survey. *The Astronomical Journal*, 145(2):47.

Monnier and Allen, 2013. Radio and Optical Interferometry: Basic Observing Techniques and Data Analysis. In Oswalt and Bond, editors, *Planets, Stars and Stellar Systems. Volume 2: Astronomical Techniques, Software and Data*, page 325.

Montuori, Di Matteo, Lehnert, et al., 2010. The dilution peak, metallicity evolution, and dating of galaxy interactions and mergers. *A&A*, 518:A56.

Moreno, Torrey, Ellison, et al., 2015. Mapping galaxy encounters in numerical simulations: the spatial extent of induced star formation. *MNRAS*, 448(2):1107.

Morisset, Delgado-Inglada, Sánchez, et al., 2016. Photoionization models of the CALIFA H II regions. I. Hybrid models. *A&A*, 594:A37.

Nagao, Maiolino, and Marconi, 2006. Gas metallicity diagnostics in star-forming galaxies. *A&A*, 459(1):85.

Nicholls, Sutherland, Dopita, et al., 2017. Abundance scaling in stars, nebulae and galaxies. *MNRAS*, 466(4):4403.

Nieten, Neininger, N., Guélin, M., et al., 2006. Molecular gas in the andromeda galaxy. *A&A*, 453(2):459.

Nieva and Przybilla, 2012. Present-day cosmic abundances. A comprehensive study of nearby early B-type stars and implications for stellar and Galactic evolution and interstellar dust models. *A&A*, 539:A143.

Nishimura, Tokuda, Kimura, et al., 2015. Revealing the Physical Properties of Molecular Gas in Orion with a Large-scale Survey in J = 2-1 Lines of ^{12}CO, ^{13}CO, and C^{18}O. *ApJ*, 216(1):18.

Nomoto, Kobayashi, and Tominaga, 2013. Nucleosynthesis in Stars and the Chemical Enrichment of Galaxies. *Annual Review of Astronomy and Astrophysics*, 51(1):457.

Osterbrock, 1989. *Astrophysics of gaseous nebulae and active galactic nuclei*.

Osterbrock and Ferland, 2006. *Astrophysics Of Gas Nebulae and Active Galactic Nuclei*. G - Reference,Information and Interdisciplinary Subjects Series. University Science Books.

Pagel, Edmunds, Blackwell, et al., 1979. On the composition of H II regions in southern galaxies – I. NGC 300 and 1365. *Monthly Notices of the Royal Astronomical Society*, 189(1):95.

Pakmor, Kromer, Taubenberger, et al., 2012. Normal Type Ia Supernovae from Violent Mergers of White Dwarf Binaries. *ApJ*, 747(1):L10.

Passot and Vázquez-Semadeni, 2003. The correlation between magnetic pressure and density in compressible MHD turbulence. *A&A*, 398:845.

Paturel, Petit, Prugniel, et al., 2003. HYPERLEDA. I. Identification and designation of galaxies. *A&A*, 412:45.

Peimbert, 1967. Temperature Determinations of H II Regions. *ApJ*, 150:825.

Peimbert and Costero, 1969a. Chemical Abundances in Galactic HII Regions. *Boletin de los Observatorios Tonantzintla y Tacubaya*, 5:3.

Peimbert and Costero, 1969b. Chemical Abundances in Galactic HII Regions. *Boletin de los Observatorios Tonantzintla y Tacubaya*, 5:3.

Peimbert and Peimbert, 2010. On the O/H, Mg/H, Si/H, and Fe/H Gas and Dust Abundance Ratios in Galactic and Extragalactic H II Regions. *ApJ*, 724(1):791.

Peimbert, Peimbert, and Delgado-Inglada, 2017. Nebular spectroscopy: A guide on h ii regions and planetary nebulae. *Publications of the Astronomical Society of the Pacific*, 129(978):082001.

Pelupessy and Papadopoulos, 2009. Molecular gas, co, and star formation in galaxies: Emergent empirical relations, feedback, and the evolution of very gas-rich systems. *The Astrophysical Journal*, 707(2):954.

Pérez-Montero, García-Benito, Hägele, et al., 2010. Disentangling the metallicity and star formation history of HII galaxies through tailor-made models. *MNRAS*, 404(4):2037.

Pettini and Pagel, 2004. [O iii]/[N ii] as an abundance indicator at high redshift. *Monthly Notices of the Royal Astronomical Society*, 348(3):L59.

Pety, Guzmán, Orkisz, et al., 2017. The anatomy of the Orion B giant molecular cloud: A local template for studies of nearby galaxies. *A&A*, 599:A98.

Pilkington, Few, Gibson, et al., 2012. Metallicity gradients in disks - do galaxies form inside-out? *AA*, 540:A56.

Pilyugin, 2001. On the oxygen abundance determination in HII regions. High-metallicity regions. *A&A*, 369:594.

Pilyugin and Grebel, 2016. New calibrations for abundance determinations in Hii regions. *Monthly Notices of the Royal Astronomical Society*, 457(4):3678.

Pilyugin, Mattsson, Vílchez, et al., 2009. On the electron temperatures in high-metallicity HII regions. *MNRAS*, 398(1):485.

Pilyugin and Thuan, 2005. Oxygen abundance determination in h ii regions: The strong line intensities-abundance calibration revisited. *The Astrophysical Journal*, 631(1):231.

Pilyugin and Thuan, 2011. Galaxy Downsizing and the Redshift Evolution of Oxygen and Nitrogen Abundances: Origin of the Scatter in the N/H-O/H Diagram. *ApJ*, 726(2):L23.

Pilyugin, Vílchez, and Thuan, 2010. NEW IMPROVED CALIBRATION RELATIONS FOR THE DETERMINATION OF ELECTRON TEMPERATURES AND OXYGEN AND NITROGEN ABUNDANCES IN h II REGIONS. *ApJ*, 720(2):1738.

Planck, 1900. Ueber irreversible Strahlungsvorgänge. *Annalen der Physik*, 306(1):69.

Planck Collaboration, Adam, Ade, et al., 2016. Planck 2015 results. X. Diffuse component separation: Foreground maps. *A&A*, 594:A10.

Pérez-Montero and Contini, 2009. The impact of the nitrogen-to-oxygen ratio on ionized nebula diagnostics based on [N ii] emission lines. *Monthly Notices of the Royal Astronomical Society*, 398(2):949.

Rice, Goodman, Bergin, et al., 2016. A uniform catalog of molecular clouds in the milky way. *The Astrophysical Journal*, 822(1):52.

Rieke, Young, Engelbracht, et al., 2004. The Multiband Imaging Photometer for Spitzer (MIPS). *ApJ*, 154(1):25.

Rolleston, Smartt, Dufton, et al., 2000. The Galactic metallicity gradient. *A&A*, 363:537.

Roy and Kunth, 1995. Dispersal and mixing of oxygen in the interstellar medium of gas-rich galaxies. *A&A*, 294:432.

Rubin, Martin, Dufour, et al., 2003. Temperature variations from Hubble Space Telescope spectroscopy of the Orion Nebula. *MNRAS*, 340(2):362.

Ruiter, Sim, Pakmor, et al., 2013. On the brightness distribution of Type Ia supernovae from violent white dwarf mergers. *MNRAS*, 429(2):1425.

Ryter, 1996. Interstellar Extinction from Infrared to X-Rays: an Overview. , 236(2):285.

Saintonge and Catinella, 2022. The cold interstellar medium of galaxies in the local universe. *Annual Review of Astronomy and Astrophysics*, 60(Volume 60, 2022):319.

Salpeter, 1955. The Luminosity Function and Stellar Evolution. *ApJ*, 121:161.

Sánchez, Rosales-Ortega, Iglesias-Páramo, et al., 2014. A characteristic oxygen abundance gradient in galaxy disks unveiled with CALIFA. *A&A*, 563:A49.

Sánchez-Menguiano., Sánchez, S. F., Pérez, I., et al., 2016. Shape of the oxygen abundance profiles in califa face-on spiral galaxies. *A&A*, 587:A70.

Sanders, Caldwell, McDowell, et al., 2012. THE METALLICITY PROFILE OF m31 FROM SPECTROSCOPY OF HUNDREDS OF H II REGIONS AND PNe. *ApJ*, 758:133.

Sandstrom, Leroy, Walter, et al., 2013. The CO-to-H_2 Conversion Factor and Dust-to-gas Ratio on Kiloparsec Scales in Nearby Galaxies. *ApJ*, 777(1):5.

Savage and Sembach, 1996. Interstellar Abundances from Absorption-Line Observations with the Hubble Space Telescope. *Annual Review of Astronomy and Astrophysics*, 34:279.

Schlegel, Finkbeiner, and Davis, 1998. Maps of Dust Infrared Emission for Use in Estimation of Reddening and Cosmic Microwave Background Radiation Foregrounds. *ApJ*, 500(2):525.

Schwarzschild, 1954. Mass distribution and mass-luminosity ratio in galaxies. *AJ*, 59:273.

Scoville, Lee, Vanden Bout, et al., 2017. Evolution of Interstellar Medium, Star Formation, and Accretion at High Redshift. *ApJ*, 837(2):150.

Scoville, Sheth, Aussel, et al., 2016. ISM Masses and the Star formation Law at Z = 1 to 6: ALMA Observations of Dust Continuum in 145 Galaxies in the COSMOS Survey Field. *ApJ*, 820(2):83.

Scoville and Solomon, 1975. Molecular clouds in the Galaxy. *ApJ*, 199:L105.

Seaton, 1979. Interstellar extinction in the UV. *MNRAS*, 187:73.

Seitenzahl, Cescutti, Röpke, et al., 2013. Solar abundance of manganese: a case for near Chandrasekhar-mass Type Ia supernova progenitors. *A&A*, 559:L5.

Shapiro and Field, 1976. Consequences of a New Hot Component of the Interstellar Medium. *ApJ*, 205:762.

Shetty, Glover, Dullemond, et al., 2011. Modelling CO emission – II. The physical characteristics that determine the X factor in Galactic molecular clouds. *Monthly Notices of the Royal Astronomical Society*, 415(4):3253.

Shirley, Nordhaus, Grcevich, et al., 2005. Modeling the Physical Structure of the Low-Density Pre-Protostellar Core Lynds 1498. *ApJ*, 632(2):982.

Simien, Pellet, and Monnet, 1979. The bulge of M31: velocity dispersions and dynamical model. *A&A*, 72(1-2):12.

Skrutskie, Cutri, Stiening, et al., 2006. The Two Micron All Sky Survey (2MASS). *AJ*, 131(2):1163.

Solomon, Rivolo, Barrett, et al., 1987. Mass, Luminosity, and Line Width Relations of Galactic Molecular Clouds. *ApJ*, 319:730.

Solomon and Sanders, 1980. Giant molecular clouds as the dominant component of interstellar matter in the Galaxy. In Solomon and Edmunds, editors, *Giant Molecular Clouds in the Galaxy*, pages 41–73.

Solomon, Sanders, and Scoville, 1979. Giant Molecular Clouds in the Galaxy; Distribution, Mass, Size and Age. In Burton, editor, *The Large-Scale Characteristics of the Galaxy*, volume 84 of *IAU Symposium*, page 35.

Spite, Cayrel, Plez, et al., 2005. First stars VI - Abundances of C, N, O, Li, and mixing in extremely metal-poor giants. Galactic evolution of the light elements. *A&A*, 430:655.

Spitzer, 1954. Behavior of Matter in Space. *ApJ*, 120:1.

Stanek and Garnavich, 1998. Distance to M31 with the Hubble Space Telescope and HIPPARCOS Red Clump Stars. *ApJ*, 503(2):L131.

Stasińska, 1978. Ionization and temperature structure of H II regions: the influence of the star, the gas density and its chemical composition. *A&A Supp.*, 32:429.

Stasińska, 2005. Biases in abundance derivations for metal-rich nebulae. *A&A*, 434(2):507.

Stasińska, Asari, Fernandes, et al., 2008. Can retired galaxies mimic active galaxies? Clues from the Sloan Digital Sky Survey. *Monthly Notices of the Royal Astronomical Society: Letters*, 391(1):L29.

Storey and Zeippen, 2000. Theoretical values for the [O iii] 5007/4959 line-intensity ratio and homologous cases. *Monthly Notices of the Royal Astronomical Society*, 312(4):813.

Strömgren, 1939. The Physical State of Interstellar Hydrogen. *ApJ*, 89:526.

Swings and Rosenfeld, 1937. Considerations Regarding Interstellar Molecules. *ApJ*, 86:483.

Symbalisty and Schramm, 1982. Neutron Star Collisions and the r-Process. , 22:143.

Tabatabaei and Berkhuijsen, 2010. Relating dust, gas, and the rate of star formation in M 31. *A&A*, 517:A77.

Tacconi, Genzel, and Sternberg, 2020. The evolution of the star-forming interstellar medium across cosmic time. *Annual Review of Astronomy and Astrophysics*, 58(Volume 58, 2020):157.

Thielemann, Eichler, Panov, et al., 2017. Neutron Star Mergers and Nucleosynthesis of Heavy Elements. *Annual Review of Nuclear and Particle Science*, 67:253.

Thomas, Maraston, Bender, et al., 2005. The Epochs of Early-Type Galaxy Formation as a Function of Environment. *ApJ*, 621(2):673.

Thompson, Moran, and Swenson, 2017. *Interferometry and Synthesis in Radio Astronomy, 3rd Edition*.

Tinsley, 1979. Stellar lifetimes and abundance ratios in chemical evolution. *ApJ*, 229:1046.

Tinsley, 1980. Evolution of the Stars and Gas in Galaxies. , 5:287.

Trimble, 1975. The origin and abundances of the chemical elements. *Reviews of Modern Physics*, 47(4):877.

Trumpler, 1930. Preliminary results on the distances, dimensions and space distribution of open star clusters. *Lick Observatory Bulletin*, 420:154.

Vargas, Geha, and Tollerud, 2014. The distribution of alpha elements in andromeda dwarf galaxies. *The Astrophysical Journal*, 790(1):73.

Viaene, Baes, M., Tamm, A., et al., 2017. The herschel exploitation of local galaxy andromeda (helga) - vii. a skirt radiative transfer model and insights on dust heating. *AA*, 599:A64.

Viaene, Forbrich, Lada, et al., 2021. Simultaneous deep measurements of CO isotopologues and dust emission in giant molecular clouds in the andromeda galaxy. *ApJ*, 912(1):68.

Vila-Costas and Edmunds, 1992. The relation between abundance gradients and the physical properties of spiral galaxies. *Monthly Notices of the Royal Astronomical Society*, 259(1):121.

Vila-Costas and Edmunds, 1993. The nitrogen-to-oxygen ratio in galaxies and its implications for the origin of nitrogen. *Monthly Notices of the Royal Astronomical Society*, 265(1):199.

Vincenzo, Belfiore, Maiolino, et al., 2016. Nitrogen and oxygen abundances in the Local Universe. *Monthly Notices of the Royal Astronomical Society*, 458(4):3466.

Vincenzo and Kobayashi, 2018. Evolution of N/O ratios in galaxies from cosmological hydrodynamical simulations. *MNRAS*, 478(1):155.

Vincenzo and Kobayashi, 2020. Stellar migrations and metal flows - Chemical evolution of the thin disc of a simulated Milky Way analogous galaxy. *MNRAS*, 496(1):80.

Vogel, Boulanger, and Ball, 1987. Giant Molecular Clouds in M31. *ApJ*, 321:L145.

Wakelam, Bron, Cazaux, et al., 2017. H2 formation on interstellar dust grains: The viewpoints of theory, experiments, models and observations. *Molecular Astrophysics*, 9:1.

Walterbos and Kennicutt, 1987. Multi-color photographic surface photometry of the Andromeda galaxy. *A&A Supp.*, 69:311.

Wenger, Balser, Anderson, et al., 2019. Metallicity structure in the milky way disk revealed by galactic h ii regions. *The Astrophysical Journal*, 887(2):114.

Whelan and Iben, 1973. Binaries and Supernovae of Type I. *ApJ*, 186:1007.

Wiescher, 2018. The History and Impact of the CNO Cycles in Nuclear Astrophysics. *Physics in Perspective*, 20(1):124.

Williams, Dalcanton, Dolphin, et al., 2015. A Global Star-forming Episode in M31 2-4 Gyr Ago. *ApJ*, 806(1):48.

Williams, Kreckel, Belfiore, et al., 2022. The 2D metallicity distribution and mixing scales of nearby galaxies. *MNRAS*, 509(1):1303.

Williams, Ortiz, Goble, et al., 2016. The 6.5-m MMT Telescope: status and plans for the future. In Hall, Gilmozzi, and Marshall, editors, *Ground-based and Airborne Telescopes VI*, volume 9906 of *Society of Photo-Optical Instrumentation Engineers (SPIE) Conference Series*, page 99060V.

Wilson, Dame, Masheder, et al., 2005. A uniform CO survey of the molecular clouds in Orion and Monoceros. *A&A*, 430:523.

Wilson, Jefferts, and Penzias, 1970. Carbon Monoxide in the Orion Nebula. *ApJ*, 161:L43.

Wilson and Rood, 1994. Abundances in the Interstellar Medium. *Annual Review of Astronomy and Astrophysics*, 32:191.

Wirth and Gallagher, 1984. The families of elliptical-like galaxies. *ApJ*, 282:85.

Wolfire, Hollenbach, and McKee, 2010. The Dark Molecular Gas. *ApJ*, 716(2):1191.

Woosley and Weaver, 1995. The Evolution and Explosion of Massive Stars. II. Explosive Hydrodynamics and Nucleosynthesis. *ApJ*, 101:181.

Xu and Helou, 1996. High-Resolution IRAS Maps and Infrared Emission of M31. I. Morphology and Sources. *ApJ*, 456:152.

Yin, Hou, Prantzos, et al., 2009. Milky Way versus Andromeda: a tale of two disks. *A&A*, 505(2):497.

Young, Bureau, Davis, et al., 2011. The ATLAS^{3D} project - IV. The molecular gas content of early-type galaxies. *MNRAS*, 414(2):940.

Young and Scoville, 1991. Molecular gas in galaxies. *Annual Review of Astronomy and Astrophysics*, 29:581.

Ysard, Köhler, Jones, et al., 2015. Dust variations in the diffuse interstellar medium: constraints on Milky Way dust from Planck-HFI observations. *A&A*, 577:A110.

Zaritsky, Kennicutt, and Huchra, 1994. H II Regions and the Abundance Properties of Spiral Galaxies. *ApJ*, 420:87.

Zinchenko, Vílchez, Pérez-Montero, et al., 2021. The dependence of the gradients of oxygen and nitrogen-to-oxygen on stellar age in MaNGA galaxies. *A&A*, 655:A58.

Zurita and Bresolin, 2012. The chemical abundance in M31 from H II regions. *MNRAS*, 427(2):1463.